MINISTRY OF EDUCATION AND TRAINING

HCMC UNIVERSITY OF TECHNOLOGY AND ENGINEERING

PHAN THANH NHAN

CHARACTERIZATION AND MODELLING VISCOELASTIC AND VISCOPLASTIC BEHAVIOR OF ASPHALT MIXTURES IN LOW STRAIN REGIME

DISSERTATION

MAJORS: MECHANICAL ENGINEERING

Ho Chi Minh City, 7/2026

MINISTRY OF EDUCATION AND TRAINING

HCMC UNIVERSITY OF TECHNOLOGY AND ENGINEERING

PHAN THANH NHAN

CHARACTERIZATION AND MODELLING VISCOELASTIC AND VISCOPLASTIC BEHAVIOR OF ASPHALT MIXTURES IN LOW STRAIN REGIME

MAJORS: MECHANICAL ENGINEERING - 9520101

Supervisor: Dr. NGUYEN HUYNH TAN TAI

Ho Chi Minh City, 7/2026

BỘ GIÁO DỤC VÀ ĐÀO TẠO TRƯỜNG ĐẠI HỌC SƯ PHẠM KỸ THUẬT THÀNH PHỐ HỒ CHÍ MINH	CỘNG HÒA XÃ HỘI CHỦ NGHĨA VIỆT NAM Độc lập – Tự do – Hạnh phúc
Số: 2329/QĐ-ĐHSPKT	*Tp. Hồ Chí Minh, ngày 28 tháng 12 năm 2021*

QUYẾT ĐỊNH

Về việc giao đề tài luận án và người hướng dẫn NCS khóa 2021 - 2024

HIỆU TRƯỞNG TRƯỜNG ĐẠI HỌC SƯ PHẠM KỸ THUẬT TP. HỒ CHÍ MINH

Căn cứ Luật Giáo dục đại học ngày 18/6/2012 và Luật sửa đổi, bổ sung một số điều của Luật Giáo dục đại học ngày 19/11/2018;

Căn cứ Nghị định 99/2019/NĐ-CP ngày 30/12/2019 của Chính phủ Quy định chi tiết và hướng dẫn thi hành một số điều của Luật sửa đổi, bổ sung một số điều của Luật giáo dục đại học;

Căn cứ Quyết định số 937/QĐ-TTg ngày 30/6/2017 của Thủ tướng Chính phủ về việc phê duyệt đề án thí điểm đổi mới cơ chế hoạt động của Trường Đại học Sư phạm Kỹ thuật TP. HCM;

Căn cứ Nghị quyết số 11/NQ-HĐT ngày 08/01/2021 của Hội đồng trường ban hành Quy chế tổ chức và hoạt động của Trường Đại học Sư phạm Kỹ thuật TP. HCM;

Căn cứ Nghị quyết số 25/NQ-HĐT ngày 29/4/2021 của Hội đồng trường về công tác cán bộ lãnh đạo của Trường Đại học Sư phạm Kỹ thuật Tp. HCM;

Căn cứ Thông tư số 08/2017/TT-BGDĐT ngày 04/4/2017 của Bộ Giáo dục và Đào tạo về việc Ban hành Qui chế tuyển sinh và đào tạo trình độ tiến sĩ;

Căn cứ Quyết định số 1557/QĐ-ĐHSPKT ngày 30/8/2017 của Trường Đại học Sư phạm Kỹ thuật TP. Hồ Chí Minh về việc ban hành Quy định đào tạo tiến sĩ của trường đại học Sư phạm Kỹ thuật Tp.HCM;

Theo nhu cầu công tác và khả năng cán bộ;

Theo đề nghị của Trưởng khoa Xây dựng và Trưởng phòng Đào tạo,

QUYẾT ĐỊNH:

Điều 1. Giao đề tài luận án tiến sĩ và người hướng dẫn cho:

Nghiên cứu sinh : ***Phan Thành Nhân***

Ngành : ***Cơ kỹ thuật*** Khoá: ***2021 – 2024***

Tên luận án : ***Phát triển phương pháp mới đánh giá khả năng kháng hằn lún vệt bánh xe của vật liệu và kết cấu bê tông át - phan***

Người HD thứ nhất (HD chính): ***TS. Nguyễn Huỳnh Tấn Tài***

Người HD thứ hai : ***TS. Trần Văn Tiếng***

Thời gian thực hiện : ***01/9/2021 đến ngày 01/9/2024***

Điều 2. Giao cho Phòng Đào tạo quản lý, thực hiện theo đúng Qui chế đào tạo trình độ tiến sĩ của Bộ Giáo dục & Đào tạo và Nhà trường đã ban hành.

Điều 3. Trưởng các đơn vị, phòng Đào tạo, các Khoa/Viện quản ngành tiến sĩ và các Ông (Bà) có tên tại Điều 1 chịu trách nhiệm thi hành quyết định này.

Quyết định có hiệu lực kể từ ngày ký./.

Nơi nhận:
- BGH (để biết);
- Như điều 2, 3;
- Lưu: VT, ĐT (4b).

PHỤ TRÁCH TRƯỜNG

BỘ GIÁO DỤC VÀ ĐÀO TẠO TRƯỜNG ĐẠI HỌC SƯ PHẠM KỸ THUẬT TP. HỒ CHÍ MINH

PGS.TS. Nguyễn Trường Thịnh

BỘ GIÁO DỤC VÀ ĐÀO TẠO
TRƯỜNG ĐẠI HỌC SƯ PHẠM KỸ THUẬT THÀNH PHỐ HỒ CHÍ MINH

CỘNG HÒA XÃ HỘI CHỦ NGHĨA VIỆT NAM
Độc lập – Tự do – Hạnh phúc

Số: 2410 /QĐ-ĐHSPKT

Tp. Hồ Chí Minh, ngày 14 tháng 8 năm 2023

QUYẾT ĐỊNH

Về việc thay đổi người hướng dẫn luận án tiến sĩ

HIỆU TRƯỞNG TRƯỜNG ĐẠI HỌC SƯ PHẠM KỸ THUẬT TP. HỒ CHÍ MINH

Căn cứ Luật Giáo dục đại học ngày 18/6/2012 và Luật sửa đổi, bổ sung một số điều của Luật Giáo dục đại học ngày 19/11/2018;

Căn cứ Nghị định 99/2019/NĐ-CP ngày 30/12/2019 của Chính phủ Quy định chi tiết và hướng dẫn thi hành một số điều của Luật sửa đổi, bổ sung một số điều của Luật giáo dục đại học;

Căn cứ Quyết định số 937/QĐ-TTg ngày 30/6/2017 của Thủ tướng Chính phủ về việc phê duyệt đề án thí điểm đổi mới cơ chế hoạt động của Trường Đại học Sư phạm Kỹ thuật TP. HCM;

Căn cứ Nghị quyết số 11/NQ-HĐT ngày 08/01/2021 của Hội đồng trường ban hành Quy chế tổ chức và hoạt động của Trường Đại học Sư phạm Kỹ thuật TP. HCM;

Căn cứ Nghị quyết số 99/NQ-HĐT ngày 21 tháng 10 năm 2022 của Hội đồng trường về công tác cán bộ lãnh đạo Trường Đại học Sư phạm Kỹ thuật TP. HCM;

Căn cứ Nghị quyết số 118/NQ-HĐT ngày 27/01/2023 của Hội đồng trường sửa đổi, bổ sung Quy chế tổ chức và hoạt động của trường Đại học Sư phạm Kỹ thuật TP. HCM;

Căn cứ Thông tư số 08/2017/TT-BGDĐT ngày 04 tháng 4 năm 2017 của Bộ Giáo dục và Đào tạo về việc Ban hành Qui chế tuyển sinh và đào tạo trình độ tiến sĩ;

Căn cứ Quyết định số 1557/QĐ-ĐHSPKT ngày 30/8/2017 của Trường Đại học Sư phạm Kỹ thuật TP. Hồ Chí Minh về việc ban hành Quy định đào tạo tiến sĩ của trường đại học Sư phạm Kỹ thuật TP.HCM;

Theo đề nghị của của NCS, Khoa quản ngành và Trưởng phòng Đào tạo.

QUYẾT ĐỊNH:

Điều 1. Đồng ý thay đổi người hướng dẫn thứ hai cho:

Nghiên cứu sinh : ***Phan Thành Nhân***
Ngành : Cơ kỹ thuật   Khoá: ***2021 – 2024***
Tên luận án : ***Phát triển phương pháp mới đánh giá khả năng kháng hằn lún vệt bánh xe của vật liệu và kết cấu bê tông át - phan***
Người HD thứ nhất (HD chính): ***TS. Nguyễn Huỳnh Tấn Tài***
Người HD thứ hai : ***không có***
Thời gian thực hiện : ***01/9/2021 đến ngày 01/9/2024***

Điều 2. Giao cho Phòng Đào tạo quản lý, thực hiện theo đúng Qui chế đào tạo trình độ tiến sĩ của Bộ Giáo dục & Đào tạo và Nhà trường đã ban hành.

Điều 3. Trưởng các đơn vị: phòng Đào tạo, khoa/viện quản ngành, phòng KHTC và các Ông (Bà) có tên ở Điều 1 chịu trách nhiệm thi hành quyết định này.

Nơi nhận:
- BGH (để chỉ đạo);
- Như điều 3;
- Lưu: VT, ĐT (3b).

KT. HIỆU TRƯỞNG
PHÓ HIỆU TRƯỞNG

TRƯỜNG ĐẠI HỌC SƯ PHẠM KỸ THUẬT TP. HỒ CHÍ MINH

PGS.TS. Lê Hiếu Giang

BỘ GIÁO DỤC VÀ ĐÀO TẠO **TRƯỜNG ĐẠI HỌC SƯ PHẠM KỸ THUẬT THÀNH PHỐ HỒ CHÍ MINH**	**CỘNG HÒA XÃ HỘI CHỦ NGHĨA VIỆT NAM Độc lập - Tự do - Hạnh phúc**
Số: 3510/QĐ-ĐHSPKT	*TP. Hồ Chí Minh, ngày 19 tháng 9 năm 2025*

QUYẾT ĐỊNH
Về việc thay đổi tên đề tài luận án tiến sĩ

HIỆU TRƯỞNG TRƯỜNG ĐẠI HỌC SƯ PHẠM KỸ THUẬT THÀNH PHỐ HỒ CHÍ MINH

Căn cứ Luật Giáo dục đại học ngày 18 tháng 6 năm 2012 và Luật sửa đổi, bổ sung một số điều của Luật Giáo dục đại học ngày 19 tháng 11 năm 2018;

Căn cứ Nghị định số 99/2019/NĐ-CP ngày 30 tháng 12 năm 2019 của Chính phủ quy định chi tiết và hướng dẫn thi hành một số điều của Luật sửa đổi, bổ sung một số điều của Luật Giáo dục đại học;

Căn cứ Quyết định số 465/QĐ-BGDĐT ngày 31 tháng 01 năm 2024 của Bộ Giáo dục và Đào tạo về việc giao quyền tự chủ tài chính giai đoạn 2023-2025 cho các đơn vị sự nghiệp công lập trực thuộc;

Căn cứ Nghị quyết số 11/NQ-HĐT ngày 08 tháng 01 năm 2021 của Hội đồng trường ban hành Quy chế tổ chức hoạt động của Trường Đại học Sư phạm Kỹ thuật Thành phố Hồ Chí Minh;

Căn cứ Nghị quyết số 118/NQ-HĐT ngày 27 tháng 01 năm 2023; Nghị quyết số 136/NQ-HĐT ngày 14 tháng 10 năm 2023; Nghị quyết số 182/NQ-HĐT ngày 28 tháng 9 năm 2024 và Nghị quyết số 212/NQ-HĐT ngày 18 tháng 12 năm 2024 của Hội đồng trường về việc sửa đổi, bổ sung Quy chế tổ chức hoạt động của Trường Đại học Sư phạm Kỹ thuật Thành phố Hồ Chí Minh;

Căn cứ Quyết định số 289/QĐ-BGDĐT ngày 24 tháng 01 năm 2025 của Bộ Giáo dục và Đào tạo về việc công nhận chức vụ Hiệu trưởng Trường Đại học Sư phạm Kỹ thuật Thành phố Hồ Chí Minh nhiệm kỳ 2020-2025;

Căn cứ Thông tư số 08/2017/TT-BGDĐT ngày 04 tháng 4 năm 2017 của Bộ Giáo dục và Đào tạo về việc ban hành Quy chế tuyển sinh và đào tạo trình độ tiến sĩ;

Căn cứ Quyết định số 1557/QĐ-ĐHSPKT ngày 30 tháng 8 năm 2017 của Trường Đại học Sư phạm Kỹ thuật Thành phố Hồ Chí Minh về việc ban hành quy định đào tạo tiến sĩ;

Xét Đơn xin thay đổi tên đề tài luận án tiến sĩ của nghiên cứu sinh;

Theo đề nghị của Trưởng phòng Đào tạo và Trưởng Khoa/Viện quản ngành.

QUYẾT ĐỊNH:

Điều 1. Thay đổi tên đề tài luận án tiến sĩ cho nghiên cứu sinh, cụ thể như sau:

Họ và tên	: **Phan Thành Nhân**	Mã NCS	: 2101001
Ngành	: **Cơ kỹ thuật**	Khóa	: **2021 - 2024**

Tên đề tài thay đổi như sau: **Phân tích và mô hình hóa ứng xử đàn hồi nhớt - dẻo nhớt của bê tông át - phan trong miền biến dạng nhỏ.**

Điều 2. Nghiên cứu sinh có tên tại Điều 1 chịu trách nhiệm thực hiện các nhiệm vụ của nghiên cứu sinh theo đúng các quy định, quy chế của Trường Đại học Sư phạm Kỹ thuật Thành phố Hồ Chí Minh.

Điều 3. Phòng Đào tạo, các đơn vị và cá nhân có liên quan chịu trách nhiệm thi hành Quyết định này./.

Nơi nhận:
- Như Điều 3;
- Lưu: VT, ĐT, PH (4).

HIỆU TRƯỞNG

BỘ GIÁO DỤC VÀ ĐÀO TẠO
TRƯỜNG ĐẠI HỌC SƯ PHẠM KỸ THUẬT TP. HỒ CHÍ MINH

PGS.TS. Lê Hiếu Giang

`

BIOGRAPHY

Thanh-Nhan Phan was born on November 3, 1982, in Binh Duong province, Vietnam. After graduating from Hung Vuong High School in 2000, he went on to the HCMC University of Polytechnics for his undergraduate degree in Civil Engineering. On completion of his undergraduate study, he attended for his Master degree in Civil Engineering with the same university in 2005. From 2009 to 2014, he is a staff of Vietnam – Korea college. From that until now, Thanh-Nhan is a lecturer at Thu Dau Mot University. In fall 2021, he enrolled at HCMC university of Technology and Education to pursue his doctoral studies in Mechanical Engineering. At HCMUTE, he studied and worked under the direction of Dr. Huynh-Tan-Tai Nguyen. His research at HCMUTE focused on characterization and modelling viscoelastic and viscoplastic behavior of asphalt mixture. He completed his dissertation in 2026.

DECLARATION

I heraby declare that I am the sole author of this research under the guidance of Dr. Nguyen Huynh Tan Tai and cited reference materials.

The data and results presented in this dissertation are accurate and have not been previously published in any other work.

Ho Chi Minh City, 10 th July 2026

Phan Thanh Nhan

`

ACKNOWLEDGEMENTS

Special thanks go to my advisor, Dr. Nguyen Huynh Tan Tai, for all of his support and guidance. Dr. Nguyen Huynh Tan Tai is not only a great teacher but also a close friend. I am so lucky and proud to be one of his students.

I would like to acknowledge the help of Mr. Phan Ba Gio from the BMT company with supporting me to prepare samples for testing. Thanks to MA. Nguyen Ngoc Hung for his help and support.

Finally, I would like to express my deepest thanks to my family for their understanding and patience over the years. Without your support this work would not have been possible.

ABSTRACT

Deformation of asphalt layers in pavement consists of viscoelastic (VE) and viscoplastic (VP) strains. Wherein, accumulated VP strains are the cause of rutting distress. A variety of predicting models have been proposed with their parameters being calibrated based on dynamic modulus, creep-recovery, repeated load permanent deformation (RLPD), or Hamburg Wheel Tracking (HWT) test, however the error of predicting and measured results remaining large. Causes to that error may be listed as follows: (i) interconversion methods linear viscoelastic properties between frequency to time domain lack of accuracy, (ii) experimental methods to determine VP strains do not ensure the homogenous applied stress in samples (e.g. HWT test) or cannot capture evolution of VP strain in time domain (e.g. RLPD test), (iii) the proposed models have not fully considered factors affecting on VP behaviors of asphalt mixture such as: the VP hardening or the ability of recovery VP strains rate in resting period. Therefore, the overall objective of this study is to accurately characterize and model the VE and VP behaviors of asphalt mixtures, key points for properly analysis and design of long-lasting pavement.

This dissertation comprises of four main tasks, which can be summarized as follows

- This dissertation proposed a novel method for calculating with high accuracy the relaxation modulus (RM) and creep compliance (CC) in the form of sum of exponential functions (SEFs) based on the input dynamic modulus (DM) master curve. First, the midpoint integration scheme was used to calculate the phase angle (PA) based on the exact relationship between the PA and DM. After that, the storage modulus (SM) and compliance were computed and decomposed with high accuracy into SEFs using a special technique. Then, the closed-form formula of the RM and CC were derived thanks to the special form function of the SM and compliance. Finally, the special technique was used once again to decompose with high accuracy the RM and CC into SEFs for possible uses in finite-element method (FEM) analysis in the time domain. The results showed that the relative errors of all LVE properties computed were lower than 0.1% at all calculating points.

- A generalized version of the CR test was proposed to investigate the permanent deformation behavior of asphalt mixtures exerted by a variety of loading patterns in the time domain. The companion back-calculation algorithm was also proposed to separate with improved accuracy and repeatability the pure VE and VP strains. First, the CC was back-calculated based only on recovery data by using an approximate analytical creep compliance function of the Huet-Sayegh model as the solution function in the optimization process. Then, the pure VE and VP strains were determined. The results show that the proposed method attains a good level of reliability although relatively short durations of the recovery period have been used.
- Based on GCR test, VP properties of asphaltic materials were determined in the next part of this dissertation. First, by conducting a series of CR tests at different temperatures and stress levels on various asphalt mixtures, master curves of CC, total and VP strains were constructed. The results showed that the time-temperature superposition principle in the VP domain was verified. In general, the shift factors were uncorrelated with each other. However, at elevated temperatures, the gaps between them became unimportant, enabling the extension of viscoelastic shift factors into the VP domain. Next, the GCR algorithm was applied to determine VE and VP strains in specimens during slope creep-recovery tests. Then, the existence of viscoplastic yield points was assessed based on the mathematical properties of the obtained VP strain curves. The results showed that VP strains occurred even at extremely low stress conditions, hence supporting the validity of the non-yielding assumption widely accepted for asphaltic materials.
- A viscoplastic behavior model was proposed and coupled with Huet – Sayegh to predict both VE, VP strains and total strains under complex historical load paths. It is worth noting that the proposed VP behavior model considered the permanent deformation hardening and the ability of recovery VP strains rate in resting period. The results showed that proposed model predicted well VE, VP and total strains not only for simple but also complex historical load paths.

The results of this work may serve as reference information for analysis and designing of long-lasting pavement

TÓM TẮT

Biến dạng của các lớp bê tông nhựa của kết cấu áo đường bao gồm biến dạng đàn hồi nhớt (VE) và biến dạng dẻo nhớt (VP). Trong đó, sự tích lũy của biến dạng VP theo thời gian là nguyên nhân gây ra hư hỏng vệt hằn lún bánh xe. Nhiều mô hình dự báo đã được đề xuất với các tham số mô hình được hiệu chỉnh dựa các thí nghiệm mô đun động, thí nghiệm từ biến – hồi phục, thí nghiệm tải trọng lặp hay thí nghiệm Hamburg Wheel Tracking, nhưng vẫn có sự sai khác tương đối lớn giữa kết quả dự báo và kết quả đo đạc. Sự sai khác này có thể do một số nguyên nhân sau: (i) phương pháp chuyển đổi các đặc trưng của biến dạng VE từ miền tần số sang miền thời gian có độ chính xác chưa cao, (ii) phương pháp xác định biến dạng VP chưa đảm bảo sự đồng nhất ứng suất trong vật liệu hay xác định được sự phát triển của biên dạng VP theo thời gian, (iii) mô hình đề xuất chưa xem xét đầy đủ các yếu tố ảnh hưởng của ứng xử của VP của hỗn hợp bê tông nhựa như: sự hóa cứng của vật liệu, khả năng hồi phục tốc độ biến dạng VP của vật liệu sau khi được dỡ tải. Vì vậy, mục tiêu tổng thể của nghiên cứu này là xác định đặc tính và mô hình hóa chính xác hơn ứng xử VE và VP của hỗn hợp bê tông nhựa, là cơ sở cho việc phân tích và thiết kế mặt đường bê tông nhựa bền lâu. Luận án này bao gồm 4 nhiệm vụ chính, cụ thể:

- Đề xuất một phương pháp lý thuyết để tính toán với độ chính xác cao mô đun dão (RM) và độ mềm từ biến (CC) dưới dạng tổng của các hàm số mũ (SEFs) dựa trên dữ liệu đầu vào là đường cong chủ của mô đun động (DM). Đầu tiên, phương pháp tích phân trung điểm được sử dụng để tính toán góc lệch pha (PA) dựa trên mối quan hệ chính xác giữa PA và DM. Sau đó, mô đun trữ (SM) và độ mềm được tính toán và phân tích với độ chính xác cao thành SEFs bằng một kỹ thuật đặc biệt. Kế tiếp, công thức cụ thể của RM và CC được suy ra nhờ vào dạng hàm đặc biệt của SM và độ mềm. Cuối cùng, kỹ thuật đặc biệt lại được áp dụng để phân tích với độ chính xác cao RM và CC thành các SEFs để cấy ghép vào phân tích trong miền thời gian bằng phương pháp phần tử hữu hạn. Kết quả cho thấy sai số tương đối của tất cả các tính chất đàn hồi nhớt tuyến tính của vật liệu được tính toán đều dưới 0,1% tại tất cả các điểm tính toán.

- Tổng quát hóa thí nghiệm từ biến hồi phục để xác định biến dạng vĩnh viễn của bê tông nhựa dưới tác dụng các kiểu tải trọng đa dạng trong miền thời gian. Một giải thuật tính ngược kèm theo cũng được đề xuất nhằm tách riêng các biến dạng VE và biến dạng VP với độ chính xác và khả năng lặp lại được cải thiện. Trước tiên, CC của vật liệu được tính ngược dựa trên dữ liệu của giai đoạn xả tải bằng cách sử dụng hàm CC xấp xỉ của mô hình Huet – Sayegh làm nghiệm của quá trình tối ưu hóa. Các CC này sau đó được so sánh và cho thấy khớp tốt với CC chuyển đổi từ dữ liệu DM bằng phương pháp đề xuất. Tiếp theo, các biến dạng VE và VP thuần được xác định. Kết quả cho thấy phương pháp đề xuất đạt được mức độ tin cậy tốt mặc dù chỉ sử dụng các khoảng thời gian xả tải tương đối ngắn.
- Xác định một số đặc tính VP của hỗn hợp bê tông nhựa. Đầu tiên, bằng cách thực hiện một loạt các thí nghiệm CR ở các nhiệt độ và ứng suất khác nhau trên nhiều hỗn hợp bê tông nhựa, các đường cong chủ của CC, biến dạng tổng và biến dạng VP được xây dựng. Kết quả cho thấy nguyên lý tương đương thời gian – nhiệt độ vẫn còn hiệu lực đối với miền biến dạng VP. Nói chung, các hệ số dịch chuyển trong miền VE và VP là không tương quan với nhau. Tuy nhiên, ở nhiệt độ cao, sự khác biệt giữa chúng là không đáng kể nên có thể sử dụng hệ số dịch chuyển VE vào miền VP. Kế tiếp, bằng cách sử dụng kiểu thí nghiệm gia tải tuyến tính, sự tồn tại của điểm chảy dẻo nhớt được đánh giá dựa trên tính chất toán học của đường cong biến dạng VP. Kết quả cho thấy biến dạng VP xuất hiện ngay cả khi ứng suất tác dụng rất bé. Kết quả này ủng hộ cho giả thuyết không có ngưỡng dẻo, một giả thuyết được chấp nhận một cách rộng rãi.
- Đề xuất một mô hình dự đoán ứng xử của biến dạng VP và kết hợp nó với mô hình Huet – Sayegh để có thể dự báo cả ứng xử của biến dạng VE, VP và biến dạng tổng dưới tác dụng của các lịch sử tải trọng tác dụng phức tạp. Cần lưu ý rằng mô hình VP đề xuất có xét đến sự phục hồi tốc độ của biến dạng VP trong giai đoạn xả tải và sự tăng cứng của biến dạng này theo sự tích lũy của nó theo thời gian. Kết quả cho thấy mô hình đề xuất dự báo tốt biến dạng VE, VP và biến dạng tổng không chỉ với các lịch sử tải trọng tác dụng đơn giản mà còn với các lịch sử tải trọng phức tạp.

Kết quả của nghiên cứu này có thể được dùng làm thông tin tham khảo cho việc phân tích và thiết kế mặt đường bền lâu.

`

TABLE OF CONTENTS

`

`

`

`

`

NOMENCLATURE AND ABBREVIATIONS

a_T	Shift factors
$\boldsymbol{\varepsilon}$	Strain tensor
$\boldsymbol{\varepsilon}^{ve}$	Recoverable strain tensor
$\boldsymbol{\varepsilon}^{vp}$	Irrecoverable strain tensor
ε_v	Vertical deformation above the base layer
$\varepsilon(t)$	Vertical strain
$\varepsilon^{ve}(t)$	Recoverable strain
$\varepsilon^{vp}(t)$	Irrecoverable strain
$\sigma(t)$	Vertical stress
$D^*(\omega)$	Complex compliance
$D^{'}(\omega)$	Storage compliance
$D^{''}(\omega)$	Loss compliance
$D(t)$	Creep compliance
$E^*(\omega)$	Complex modulus
$E^{'}(\omega)$	Storage modulus
$E^{''}(\omega)$	Loss modulus

`

$E(t)$ Relaxation modulus

F The viscoplastic potential function

f Yield surface function

$f(\sigma)^m$ The loading function

$H(t)$ Step function, Heaviside function

$h(P)$ The permanent hardening function

$\xi(s)$ The fluidity function

N The viscoplastic rate sensitivity exponent

N_r Allowed of number of cycles loading corresponding to the rut depth equal to 0.5 inch

t Time

T Temperature

T_{ref} Reference temperature

ζ The fluidity parameter

Φ The overstress function

ω Angular frequency

$\Gamma(\bullet)$ The Gamma function

$\langle\bullet\rangle$ Macaulay brackets

AACC Analytical approximate creep compliance

`

AC	Conventional mixture
CC	Complex creep compliance
CCs	Creep Compliances
CM	Complex modulus
CR	Creep recovery
DM	Dynamic modulus
FEM	Finite element method
GCR	Generalized Creep - Recovery
GM	Generalized Maxwell model
GS	Generalized sigmoid function
GVK	Generalized Kelvin - Voigt model
HiMA	High modulus mixture
HS	Huet - Sayegh model
HWT	Hamburg Wheel Tracking
LM	Loss modulus
LVE	Linear viscous elastic
MSCR	multi-stress level creep-recovery
PA	Phase angle
PD	Permanent deformation
RLPD	Repeated load permanent deformation

`

RM	Relaxation modulus.
SBS	Styrene-Butadiene-Styrene
SCC	Storage Creep Compliances
SEFs	Sums of Exponential Functions
SM	Storage modulus
SS	Standard sigmoid function
SSCR	Single-stress level creep-recovery
VE	Viscoelastic
VP	Viscoplastic
WLF	The formula of Williams – Landel – Ferry

`

LIST OF TABLES

`

`

LIST OF FIGURES

`

`

`

`

`

`

CHAPTER I
INTRODUCTION

1.1 Background

Nowadays, asphalt pavement is widely used in Vietnam because the structure is flexible, easy to construct and maintain. Moreover, asphalt pavement is flexible one so riding on it is quite comfortable. However, the quality of asphalt pavement in our country decreases quite rapidly over time due to the simultaneous harsh impact of traffic load and climate factor. It means that service life of the pavement reduces because of appearance of distresses. One of the most common distresses of asphalt pavement is rutting (see Figure 1.1), resulting in a severe decrease in traffic safety. This is a consequence of our country's specific traffic conditions where the traffic system has not been developed that makes actual traffic volume always exceed design traffic volume, causing high traffic loading and slow traffic speed. Besides that, Vietnamese climate always maintains at high temperature which causes the deformation resistance of material sharply reduced because the asphalt binder of material is softened. With the trend of global warming and current over-exploitation, the problem of rutting distress will become more and more serious.

Analysis and predicting the development of permanent deformation (rutting) of material and asphalt structure is always a challenge for scientists because asphalt material is a complex one, where the binder is not a homogeneous mono-component material. Numerous studies have shown that bitumen compounds of more than 300 to 2000 different chemical compositions (Haseeb Jamal, 2017), of which the majority are polymers with complex structures. Approximately, the chemical composition of asphalt binder can be analyzed into four main groups of substances: Saturate, Asphaltene, Resin, and Aromatic. The ratio between those groups (commonly known as SARA) plays a key

`

role in its mechanical behavior. Therefore, bitumen has the same grade, but different chemical compositions also have different mechanical behavior.

Figure 1.1. Rutting distress on entrance street of Cat Lai port, HCM City (taken in July 2021)

Furthermore, at a scale that asphalt concrete (a mixture of aggregate and binder) is considered as a homogeneous material, its behavior is further complicated by the influence of aggregate and binder interactions. A lot of studies have shown that these common properties of asphalt concrete are elastic, viscous, plastic, and fatigue (Di Benedetto et al., 2007). The material clearly shows the dependence on loading time (or loading rate) and action temperature. Thus, the theory that applies to the rate-independent material cannot be used for this material. Besides that, asphalt materials show the stress/strain-dependent behavior when the stress or strain overcomes a limit domain which is considered linearity. Based on experimental observations, Di Bendetto et al. (2007) classified the behavior of asphalt concrete into four main types depending on temperature, magnitude of strain/ stress and time (cycle) loading as follows:

- Linear viscous elastic (LVE): when the strain is small and cyclic loading is rather low (<1000 cycles);
- Nonlinear viscous elastic: when the strain is larger than the limit of the linear domain and the number cyclic loadings is low (<10 cycles);

`

- Irreversible deformation (rutting): influenced by temperature and when the number of cyclic loadings is relatively large.
- Fatigue: when the number cyclic loadings is large (>10^4 cycles).

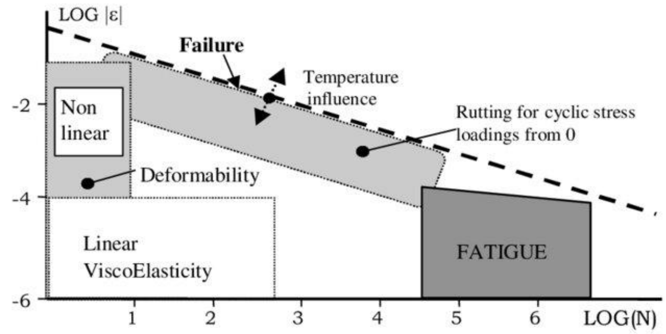

Figure 1.2. Main type behavior of asphalt concrete by Di Bendetto et al. (2007)

All the above-mentioned factors create difficulty in studying the behavior of asphalt mixture both in analyzing and modeling. Therefore, it would be too ambitious and infeasible to simultaneously investigate all forms of behavior of this material rather than seek to isolate one primary form of behavior for investigation. Based on the results of the survey of actual damage of asphalt pavement in the southern region of Vietnam, the rutting distress often appears quite soon after exploitation and the appearing time is commonly in the sunny season when the ambient temperature is high. Once the surface of the road has a high rut depth, cracking usually does not occur simultaneously. Therefore, in this study, PhD students will focus on investigating permanent (or irreversible) deformation of asphalt mixture and try to "freeze" the fatigue of the material to simplify the problem. Since the deformation of asphalt mixture includes a part of reversible deformation and a part of irreversible one, research reversible deformation or viscous elastic behavior is a necessary part of this study.

1.2 Literature review

In this section, studies for modelling to predict the permanent deformation (PD) of hot asphalt mixture pavement, laboratory testing for determining viscous elastic and

`

viscous plastic properties of material, and methods to convert viscous elastic properties from frequency domain to time domain were analyzed and synthetic.

1.2.1 PD models for hot asphalt mixture pavement.

In several decades, numerous models were proposed to predict the permanent deformation (rutting) of asphalt mixtures. They can be typically categorized into analytical and constitutive models.

1.2.1.1 Analytical models

Analytical models predict rut depths of pavement by using functions of stress/ strain which were constructed based on elastic theory or finite element method. That type of model has been proposed by plenty of studies such as AASHTO (2008), Huang (2004), IRC 37-2012 (2012), and Kenis (1978). In there, the models developed by the Shell company in 1978 and the Asphalt Institute in 1982 are considered as typical models.

In the model of Shell company, the rut depth in each layer is assumed as a function of normal stress and the total rut depth is sum of them. To calibrate the model, the uniaxial creep test was used to evaluate the stiffness of asphalt concrete. Equation (1.1) presents the formula calculating the rut depth of the model of Shell company,

$$N_r = 6.15\times10^{-7}\varepsilon_v^{\ 4.0} \tag{1.1}$$

where N_r is allowed of number of cycles loading corresponding to the rut depth equal to 0.5 inch; ε_v is vertical deformation above the base layer.

By another approach, the model of Asphalt Institute was developed based on a function of vertical strain of the asphalt concrete layers. That model is widely applied in some design standards such as AASHTO (2008) and IRC37-2012 (2012). The allowed number of cycles loading can be computed as follows:

$$N_r = 1.365\times10^{-9}\varepsilon_v^{\ -4.477} \tag{1.2}$$

where quantities are defined as like as the those of equation (1.1)

`

The parameters of the above-mentioned models were determined and calibrated by the mean value of measured data from the vehicle on the test track. These data are highly dependent on traffic and climate in the host country. Therefore, the determination of these parameters requires a lot of financial and time costs. Moreover, analytical models have clear limitations – namely: the implicit empiricism, unable to simulated load history and hardening-relaxation behavior, which can be resolve by constitutive models (Alamnie et al., 2022).

1.2.1.2 Constitutive models

Because asphalt concretes are mixture of aggregate and binder, they show many properties – namely: linear viscous elastic (LVE), nonlinear viscous elastic, viscous plastic (VP), fatigue, and rutting. Those characteristics can be determined based on amplitude of deformation and the number of load cycles acting on the material (Di Benedetto et al., 2007; Gayte et al., 2014; Neifar and Di Benedetto, 2001). Although behaviors of asphalt concretes are complex, one can simulate them with the aids of numerical methods such as finite element method. The important task is to determine constitutive law to correspond with the material's survey result.

With different approaches, several constitutive models were proposed to predict the rutting of asphalt pavement structure. In the beginning, the models were constructed based on the viscoplasticity theory (Drescher et al., 1993; Hua, 2000; Hua & White, 2002) or the elasto-viscoplasticity theory (Karrech et al., 2011; Nedjar & Nguyen, 2012; Park, 2007).

Because asphaltic materials display both viscoelastic and viscoplastic properties, those models do not predict very well the rutting of asphalt pavement. Thus, in the near decades, many authors used the viscoelastic theory coupled with the viscoplastic theory to improve the accuracy of predicting. In this approach, the total deformation was assumed that it consists of two parts: recoverable and irrecoverable deformation. Therefore, the strain tensor can be expressed as follows:

`

$$\boldsymbol{\varepsilon} = \boldsymbol{\varepsilon}^{ve} + \boldsymbol{\varepsilon}^{vp}, \tag{1.3}$$

where $\boldsymbol{\varepsilon}^{ve}$ is the recoverable strain tensor can be determined by linear viscoelastic models (e.g Huet-Sayed model) or nonlinear viscoelastic models (e.g Schapery model), $\boldsymbol{\varepsilon}^{\mathrm{vp}}$ is the irrecoverable strain tensor can be computed based on viscoplastic models (e.g Perzynal model).

To name a few works, Chehab et al. (2003) proposed a model only can be predicted the viscoplastic strain due to tensile stress by using Schapery viscoelastic-damage model (Schapery,1975) coupled to viscoplastic (Schapery, 1999). By using a Perzyna-type viscoplasticity model (Perzyna, 1971), models of Seibi et al. (2001) and Masad et al. (2005) can be simulated the vicosplastic behavior of asphalt mixtures in both tension and compression. In order to accurately predict the irreversible strain of asphalt mixtures in nonlinear domain, Perzyna viscoplastic (Perzyna, 1971) and nonlinear-viscoelastic (Schapery, 1999) models were coupled by Saadeh et al. (2007) and Huang et al. (2011a). Later, the Drucker-Prager yield surface and its modification were applied to the Perzyna viscoplastic model to develop constitutive models (Darabi et al., 2012; Nguyen, 2017). Those yield surfaces were chosen because they can be considered the effects of aggregate friction and interlocking, dilation, and pressure sensitivity (Darabi et al., 2012).

However, the above-mentioned studies determine LVE properties in frequency domain so these properties must be converted to time domain before implanting them into calculating software. This process increases the calculation costs and decreases the accuracy of LVE properties of material. Moreover, algorithms to determine irreversible strain ε_{vp} in those studies are not high accuracy which will be discussed in section 2.3 of this chapter. Therefore, the results of predicting rut depths of those models have a rather large difference with the actual measurement value.

`

1.2.2 Asphalt mixture laboratory characterization

As discussed above, deformation of asphalt pavement consists of a part of reversible deformation and a part of irreversible one. Thus, it is necessary to determine both the LVE and VP properties of asphalt mixture for analyzing and predicting the rut depth of the pavement. These characteristics are investigated by laboratory testing, so the accuracy of rut depth prediction model strongly depends on the results of experiments. It means that the laboratory testing and correspondent algorithm must be able to accurately determine these properties.

1.2.2.1 Determining LVE properties

Relaxation modulus (RM) and creep compliance (CCs) are characteristics of LVE behavior in the time domain. Meanwhile, the quantities exhibiting LVE behavior of asphalt mixture in frequency domain are complex modulus (CM) and complex creep compliance (CC). Determining the CM or CC by dynamic modulus test is easier than using relaxation test/ creeps test to investigate the RM/CCs. The reason is that at some temperature level, it is difficult to determine the pure viscous elastic (VE) deformation because the measured deformation of the experiment includes the accumulates viscous plastic deformation. Liu and You (2009) reported that irreversible deformation (viscous plastic deformation) of asphalt mixture in creep – recovery test maybe accounts for up to 80% of the total deformation at 40°C and loading time more than 10s. Thus, the result of measured deformation of asphalt mixture by relaxation test and creep test at high temperature consists of VE deformation and VP one, so the calculation of LVE properties of material based on these measurements results will lead to large errors.

In fact, Kim et al. (2008) showed that RM and CCs obtained from the relaxation test and creep test did not coincide with these convert quantities from CM. Later, by comparing the convert RM from creep test and dynamic modulus test data, Zhang et al. (2018) reported that the relative difference is up to 30% between these values. Therefore, almost standards and studies limit the temperatures of creep test under 30°C for reducing

`

the effect of VP deformation to measured data (AASHTO T 322-07, 2011; Daoudi et al., 2020; Kim et al., 2008; Lee and Kim, 1998; Richardson and Lusher, 2008; Zhang et al., 2018).

In contrast, LVE properties of material determined by data of dynamic modulus test are more reliable because VP strain does not affect to calculate the CM from the magnitude of LVE cyclic stress/strain. However, RM or CCs are required to define in most finite element programs (Abaqus, 2014; COMSOL) so the CM or CC determined from dynamic modulus test data must be converted to the time domain. Mathematically, the relaxation modulus or creep compliance can be interconverted from data of dynamic modulus test. However, proposed interconversion methods do not have high accuracy because it is difficult to directly calculate the RM/CCs from CM/CC by analytical method. Moreover, in order to construct the master curve of complex modulus, the dynamic modulus test must be conducted at various temperatures and frequencies, so it requires a lot of time and labour intensively.

Another laboratory testing that can be used to determine the LVE properties of asphalt mixture is creep–recovery test which consists of two phases: a loading period and following by unloading one. Because there is just the LVE behavior in the resting period, many calculation algorithms have been proposed for determining the LVE properties of asphalt mixture from data of the recovery phase. In the later work, nonlinear optimization algorithm was used to calculate the VE characteristic based on the data of resting period such as the study of Levenberg (2006). Later, the approach that considers the Prony series as the solution function of CCs function was applied in Abu Al-Rub et al. (2009), Bai et al. (2014), and Chen et al. (2017). With the retardation time were priori chosen, the nonlinear least-square optimization problem can turn to a simpler linear one. However, Tran et al. (2023) reported that the result of fitting the prediction by Prony series-based functions directly to the experimental data without pre-smooth treatment usually causes artificial waviness and therefore reduces accuracy. Nearly, Nguyen et al.

`

(2021) proposed a back-calculated creep compliance algorithm which can directly determine the LVE properties in the time domain even at high temperatures. In that algorithm, the derived formulation by eliminated viscoplastic strain only involves the LVE creep compliance function. The detail of that algorithm is presented in Section 2.1.1 of Chapter II.

1.2.2.2 Determining VP properties

To measure the permanent deformation of the asphalt structure, numerous procedures and algorithms were proposed. In there, Hamburg Wheel Tracking (HWT) test (AASHTO T324, 2004; EN 12697-22, 2007) is widely used for assessing the resistance of asphalt mixture to rutting. The depth of rut caused by a rolling rubber wheel to a rectangular slab with dimensions 320mm × 260mm × 60mm was measured after each load cycle. It is obvious that the stress and strain fields in the HWT are not homogenous. Therefore, using HWT data to calibrate the prediction model of rutting can be led to an overestimated result, especially in high-speed traffic areas (Nguyen, 2017).

Another test also widely used to measure the irreversible strain is repeated load permanent deformation (RLPD) test (Cao and Kim, 2022; Darabi et al., 2012; Khosravifar et al., 2014). Although the stress and strain fields in this test are homogenous, the strains measured at each cycle are not pure VP strain. The reason is the measured strains consist of a part of VE strain which is not reversible yet.

By using a two-stage process, Sun and Zhu (2013) determined the LVE of material by conducting DM test for predicting the VE creep strain. After, the creep test was performed and the VP strain evolving during the test is the difference between measure strain of creep test and predicted VE creep strain. To ensure the accuracy of calculating the master curve of CCs from the master curve of complex modulus, the DM test must be performed with a wide range of temperature and frequency while only a short portion of CC master curve at a single temperature is needed. It means that the disadvantage of two-stage process is consuming a lot of time for testing.

`

With a CR test, one can separate the VE and VP strain from the total measured strain based on two phases of that test: a loading period followed by an unloading one (Drescher et al., 1993). First, the predicted VE strain is determined based on the data in the unloading period with algorithms mentioned in subsection 2.2.1 of this chapter. Then, the VP strain can be calculated by subtracting the total measured strain to the predicted VE strain. Thus, the accuracy of computing the VP strain depends on the algorithm to determine the VE strain. All previous studies which applied the CR test just used the single-stress level except (Bai et al., 2014) wherein the authors considered a multi-stress level. In that test, they assumed that the recovery duration of each creep-recovery cycle is long enough for the VE strain to totally recover. In fact, VE strain in asphalt mixture needs an extremely long duration for recovery, especially at intermediate temperature. It means that the effect of the previous creep-recovery cycle on the present one was ignored.

In conclusion, it is necessary to develop a testing method and corresponding algorithms for determining both LVE and VP properties of asphalt mixture has a complex history of loading time and overcome the disadvantages of the previous testing methods.

1.2.3 Converting linear viscous elastic properties of material from frequency domain to time domain

In literature, various methods were proposed to convert LVE properties in the frequency domain to the time domain. It may be stated with the study of Baumgaertel and Winter (1989), the authors performed fitting the storage and loss modulus by a function equal to the function of generalized Maxwell model with the aids of an undisclosed nonlinear least-square program. Later, this approach was improved by Mead (1994). Instead of determining the relaxation time, the author chose the priori to convert the nonlinear least-square problem to the linear one that is easier to solve. Next, Mun et al. (2007) proposed only fitting the storage modulus/compliance by that of the function of generalized Maxwell model and calibrated the value of phase angle before fitting for

`

increasing the accuracy of fitting ability. For preventing a nonlinear resolution, a set of relaxation/retardation time was also pre-selected. Nearly, after pre-smoothed experimental data of dynamic modulus and phase angle by using modified sigmoid function, Zhang et al. (2018) applied generalized Maxwell model to identify both storage modulus and loss modulus. However, the authors did not discuss the satisfaction of Kramers-Kronig relative in the formulation.

In another approach, analytical approximations were used for interconverting LVE properties from the frequency domain to the time domain. The widely used formula was proposed by Schapery and Park (1999) because of simplicity and good accuracy. The approximation of storage modulus $E^{'}\left(\omega\right)$ is presented as:

$$E'(\omega)=\Gamma\left(1-n\right)\cos\left(\frac{n\pi}{2}\right)E\left(t\right), \tag{1.4}$$

where ω is the angular frequency, $t=1/\omega$, $\Gamma\left(z\right)=\int_0^\infty t^{z-1}e^{-t}dt$ is the Gamma function, and $E\left(t\right)$ is the relaxation modulus. However, like other analytical approximate formulas, the level of relative difference of this formula can be also reached to 5% (Emri et al., 2005). The same level of accuracy was also reported by Nguyen et al. (2021a, 2022) when they re-smooth the dynamic master curve data by using Huet-Sayegh model. It is easy to calculate the value of RM/CCs by applying the analytical approximate formulas. However, those formulas do not have a form of sum of exponential functions, which are suitable for constructing recursive formulas of stress and strain that can significantly improve computational efficiency.

1.3 Research objective

Today, the dynamic modulus test has been widely used to determine LVE properties of material in the frequency domain because VP strain does not affect the measured result when the action load is cyclic load. However, those properties must be interconverted to the time domain to calculate the rut depth of the asphalt pavement. It

`

means that the level accuracy of calculation of the rut depth depends on the level of accuracy of the interconversion. Meanwhile, the relative difference of proposed interconversion methods is quite high, up to 5% (Emri et al., 2005). Moreover, the interconversion must satisfy the causality principle which is not strictly ensure in previous studies. Therefore, in this study, an algorithm to convert LVE in the frequency domain to the time domain has a high accuracy and satisfies the strong form of causality principle is proposed.

To ensure that the predicting model accurately simulates the behavior of material and asphalt concrete structure, the parameter of material properties must be exactly determined. Meanwhile, each asphalt mixture has a specific set of parameters, characterizing the LVE and VP properties. Those sets of parameters are investigated by laboratory tests, therefore characterization methods play an important role in predicting the pavement behavior. However, present laboratory testing methods show limits as discussed in subsection 1.2.2. Thus, the CR test is generalized to overcome those limits for ensuring that the LVE and VP properties can be simultaneously determined with high accuracy and appropriate time costs.

In addition, a new viscoplastic model is proposed and then couple with the LVE model for predicting both LVE and VP behaviors of asphalt mixture.

Consequently, the main objectives of this work include:

- Development of an algorithm to convert LVE properties in the frequency domain to the time domain with a high accuracy and sum of exponential functions form.
- Development of a generalized CR test and a back-calculation method for determining the permanent deformation of asphalt mixture in the time domain.
- Investigating the VP properties of asphaltic material by using generalized CR tests.
- Development of a viscoplastic model for predicting the VP behavior of asphalt mixtures.

`

1.4 Research scope

A typical asphalt pavement structure consists of asphalt concrete layer, granular base, granular subbase, and subgrade (Figure 1.3). Various studies (e.g. HuiWang, 2009; Hussan S, 2013; Nathan Chilukwa, 2019, Riu Guo et al.,2020; Du Yinfei, 2018) have shown that the rut due to the irreversible permanent appears almost exclusively in the asphalt concrete layers, other layers (granular, subgrade) are almost absent. Therefore, this study just focuses on investigating the permanent strain of the asphalt concrete layers but ignores the deformation of the granular and subgrade.

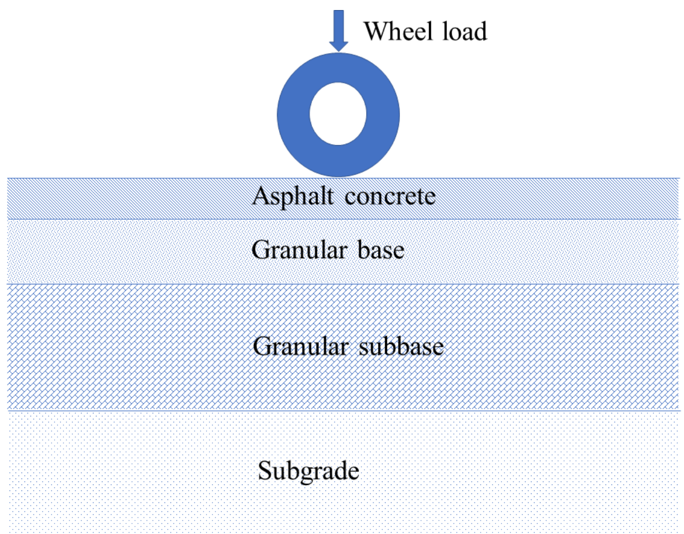

Figure 1.3. A typical asphalt pavement structure

The "low-strain regime" is defined as the region in which viscoelastic (VE) behavior remains linear. According to Nguyen et al. (2019) and Nguyen et al. (2021a), linearity is ensured when the LVE strain amplitude does not exceed 100 με in the frequency domain or 150 με in the time domain. These limits are applied only for the back-calculation of the viscoelastic properties of materials. No such restriction applies to irrecoverable deformation behavior.

The reason for limiting the strain amplitude in the low strain regime which is to ensure that the LVE theory is valid and the LVE properties in both time and frequency

`

domains can be accurately determined using fundamental procedures, based on which the reliability of the obtained results in the VP domain can be assessed.

In reality, asphalt layers are subjected to compressive pressure from wheel loads, lateral confining stresses due to restricted horizontal movement, and additional stresses caused by deformation of the underlying layers, resulting in a complex three-dimensional stress state. Unlike granular materials, asphalt concrete behavior shows less dependency on confinement conditions (Bai et al., 2014; Ossa et al., 2010). As a result, many studies ignore confinement effects when examining the behavior of asphalt mixtures, including those dealing with viscoelastic and viscoplastic behavior (Lu and Wright, 1998; Neifar and Di Benedetto, 2001; Huang et al., 2011b; Bai et al., 2014). Furthermore, equipment for creating a triaxial stress state in laboratory is not available in the faculty. Therefore, this study is limited to investigating one-dimensional behavior.

1.5 Research methodology

Three main research methods in this study are theoretical methods, experimental methods, and modeling methods.

The theoretical methods are used to synthesize the viscoelastic and viscoplastic theory. From the results of theoretical research, a method for converting LVE properties from the frequency domain to the time domain is proposed. Besides, CR test method is generalized to ensure that it can be simultaneously determined both LVE and VP properties in the time domain.

In this study, the parameters of linear viscoelastic and viscoplastic properties are determined by laboratory tests. The considered factors affected by the samples are mechanical load and environmental temperature. For asphalt mixture samples, stress controlling method and strain controlling are two widely used ones. However, this study considers the irreversible deformation of the specimen so only the stress controlling method is just chosen.

`

The linear viscoelastic can be determined in the frequency domain or the time domain by laboratory test. However, the LVE properties in the frequency domain must be converted to the time domain before they are assembled in the FEM program. This procedure increases the time costs and decreases the accuracy of the input data for simulating the behavior of asphalt mixture. Therefore, in this study, the properties of materials are directly determined in the time domain by the proposed testing method and algorithm. The characteristics of materials in the frequency domain are also identified and converted to the time domain for purposes of verification of the accuracy of the proposed testing method and algorithm.

After the linear viscoelastic and viscosplastic are determined, a newly predicting VP behavior model is proposed and then coupling with the Huet – Sayghed (HS) model, well – known predicting LVE behavior model to simulate behavior of asphalt mixtures. HS model was chosen because it has fewer input parameters but has a good fitting ability with LVE behaviors of asphalt mixtures.

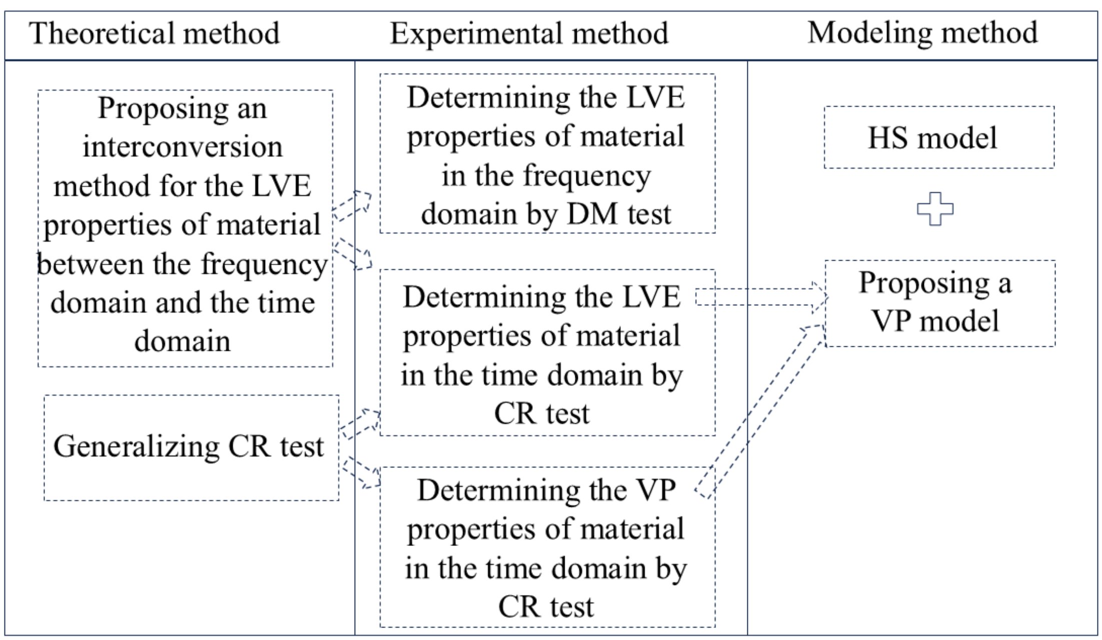

Figure 1.4. Research Framework

`

1.6 Dissertation organization

This dissertation consists of six chapters, including:

Chapter I gives a background and literature review for determining the objectives of this dissertation. Approaching and methodological research are also introduced in this chapter.

Chapter II presents a brief LVE, VP theory and synthesis the experimental methods. A proposed interconversion LVE properties in frequency domain to time domain with high accuracy also displays here. Moreover, this chapter presents a generalized CR test that can determine both pure VE, VP strain just in one test.

Chapter III, by applying the algorithm of GCR test, validates the Time-Temperature superposition still held in VP domain.

Chapter IV investigates the plastic yield point of asphalt mixtures by using slop creep-recovery test.

Chapter V characterizes and modelling VE and VP behavior of asphaltic materials

Chapter VI summarizes the findings and guide for future research.

`

CHAPTER II
THEORETICAL BACKGROUND

2.1 Theory of linear viscoelasticity and viscoplasticity

In this section, the core contents of viscoelastic, and viscoplastic theory are briefly presented as a foundation for the next contents.

2.1.1 Theory of linear viscoelasticity

2.1.1.1 Viscoelastic material

Viscoelastic material is the material that the stress – strain relation depends on loading time. With an action $\varepsilon(t)=\varepsilon_0 H(t)$ where ε_0 is the strain amplitude, and $H(t)$ is a step function, the response stress $\sigma(t)$ is a reducing function over time. For liquid, $\lim_{t\to\infty}\sigma(t,\gamma_0)=\sigma_\infty=0$, for solid, $\lim_{t\to\infty}\sigma(t,\gamma_0)=\sigma_\infty>0$. Thus, the stress of viscoelastic material can be presented as follows (Cho, 2016):

$$\sigma(t,\gamma_0)=\left[\sigma_0(\gamma_0)\phi_\lambda(t)+\sigma_\infty(\gamma_0)\right]H(t) \tag{2.1}$$

where $\dfrac{d\phi_\lambda}{dt}\le 0;\qquad \phi_\lambda(0)=1;\qquad \lim_{t\to\infty}\phi_\lambda(t)=0;\ \sigma(0,\gamma_0)=\sigma_0(\gamma_0)+\sigma_\infty(\gamma_0)$

Linear viscoelastic material is the material that the relationship between stress and strain is linear at all times. Assuming there is a relationship between stress and strain $\varepsilon(t)=T\left[\sigma(t)\right]$ then the behavior of material is linear when the function $T[\bullet]$ must be satisfied equation (2.2) with all real numbers and functions over time (Cho, 2016).

$$T\left[\alpha\sigma_1(t)+\beta\sigma_2(t)\right]=\alpha T\left[\sigma_1(t)\right]+\beta T\left[\sigma_2(t)\right]. \tag{2.2}$$

2.1.1.2 Boltzmann superposition principle

Let $D(t)$ denote the LVE creep compliance, the measured strain subject to a unit step function of stress, and the sample is applied by a stress function $\sigma(t)$ as illustrated in Figure 2.1. That stress can be considered as a sum of action constancy stress $\Delta\sigma$ in the period $\Delta\tau$.

`

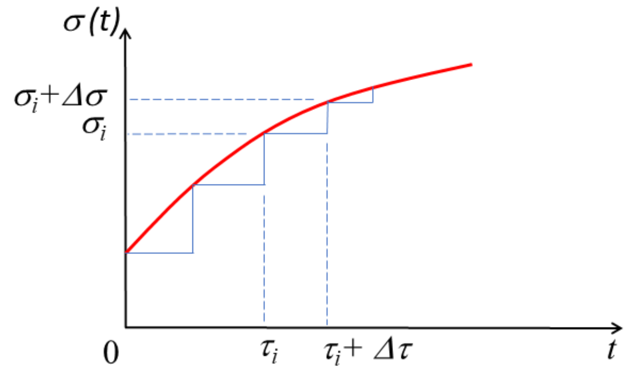

Figure 2.1. Illustration of dividing a random stress function into sum of constancy stresses.

The obtained strain under a stress increment $\Delta\sigma(\tau_i)$ is:

$$\Delta\varepsilon(\tau_i) = D(t-\tau_i)\cdot\Delta\sigma(\tau_i). \tag{2.3}$$

Because the behaviors of material are still in the LVE domain so following to equation (2.2) the strain of sample is:

$$\varepsilon = \sum_{i=1}^{n}\Delta\varepsilon(\tau_i) = \sum_{i=1}^{n} D(t-\tau_i)\cdot\Delta\sigma(\tau_i). \tag{2.4}$$

When $\Delta\tau \to 0$, the equation (2.4) can be presented as follows:

$$\varepsilon(t) = \int_0^t D(t-\tau)\cdot\frac{d\sigma}{d\tau}\cdot d\tau. \tag{2.5}$$

Besides, based on the causality principle, mathematical conditions can be added as equation (2.6)

$$D(t) = \begin{cases} D(t) \geq 0 & t \geq 0 \\ 0 & t < 0 \end{cases}. \tag{2.6}$$

Then, one can rewrite the equation (2.5) to the equation (2.7) (Tschoegl, 1989)

$$\varepsilon(t) = \int_{-\infty}^{t} D(t-\tau)\cdot\frac{d\sigma}{d\tau}\cdot d\tau. \tag{2.7}$$

Similarly, when sample is applied by a strain function depending on time, we obtained the equation (2.8) (Tschoegl, 1989)

`

$$\sigma(t) = \int_{-\infty}^{t} E(t-\tau) \cdot \frac{d\varepsilon}{d\tau} \cdot d\tau \,. \tag{2.8}$$

Both equations (2.7) and (2.8) are called Boltzmann principles.

2.1.1.3 Characteristics of viscoelastic material

a. Relaxation modulus (RM)

Let $E(t)$ denote relaxation modulus, the measured stress subject to a unit step function of strain. If the Boltzmann principle still holds, the response stress $\sigma(t)$ in material cause by an arbitrary strain history $\varepsilon(t) = \varepsilon_0 H(t)$ is given follows (Tschoegl, 1989):

$$\sigma(t) = \varepsilon_0 \int_{-\infty}^{t} E(t-\tau)\delta(t)d\tau \tag{2.9}$$

or:

$$\sigma(t) = \varepsilon_0 \cdot E(t) \,. \tag{2.10}$$

b. Creep compliance (CCs)

Let $D(t)$ denote creep compliance, the measured strain subject to a unit step function of stress. If the Boltzmann principle still holds, the response strain $\varepsilon(t)$ in material cause by an arbitrary stress history $\sigma(t) = \sigma_0 H(t)$ is given follows (Tschoegl, 1989):

$$\varepsilon(t) = \sigma_0 \int_{-\infty}^{t} D(t-\tau)\delta(t)d\tau \tag{2.11}$$

or:

$$\varepsilon(t) = \sigma_0 \cdot D(t) \,. \tag{2.12}$$

c. Dynamic moduli (DM)

Application the Boltzmann principle with a harmonic strain input $\varepsilon(t) = \varepsilon_0 \sin(\omega t)$, where ε_0 is the magnitude and ω is the angular frequency of the signal, one can obtain:

`

$$\sigma(t)=\varepsilon_0\omega\int_{-\infty}^{t}E(t-\tau)\cos(\omega\tau)d\tau\ . \tag{2.13}$$

Performing the change of variable $u=t-\tau$ in equation (2.13) gives rise to

$$\sigma(t)=\varepsilon_0\omega\cos(\omega t)\int_{0}^{+\infty}E(u)\cos(\omega u)du+\varepsilon_0\omega\sin(\omega t)\int_{0}^{+\infty}E(u)\sin(\omega u)du. \tag{2.14}$$

By convention, one defines the dynamic moduli as follows (Tschoegl, 1989):

$$\sigma(t)=E^{'}(\omega)\varepsilon(t)+\frac{E^{''}(\omega)}{\omega}\dot{\varepsilon}(t), \tag{2.15}$$

where $E'(\omega)=\omega\int_{0}^{\infty}E(u)\sin(\omega u)du=\omega\int_{0}^{\infty}E(t)\sin(\omega t)dt$ is the storage modulus, present the property of elasticity and $E^{''}(\omega)=\omega\int_{0}^{\infty}E(u)\cos(\omega u)du=\omega\int_{0}^{\infty}E(t)\cos(\omega t)dt$ is loss modulus, show the property of viscos. Storage modulus and loss modulus are two parts of the dynamic moduli (Cho, 2016).

$$\left|E^{*}(\omega)\right|=\sqrt{E^{'}(\omega)^{2}+E^{''}(\omega)^{2}}\ . \tag{2.16}$$

d. Complex moduli (CM)

Let us now study an input signal $\varepsilon(t)=\varepsilon_0 e^{i\omega t}$, and the strain is small for the Boltzmann principle is still hold. Then, the obtained stress is:

$$\sigma(t)=i\omega\varepsilon_0\int_{-\infty}^{t}E(t-\tau)e^{i\omega\tau}d\tau=E^{*}(\omega)\varepsilon^{*}(t). \tag{2.17}$$

Accomplishing the change of variable $u=t-\tau$ in equation (2.17) gives rise to

$$\sigma(t)=i\omega\varepsilon_0 e^{i\omega t}\int_{0}^{+\infty}E(u)e^{-i\omega u}du\ . \tag{2.18}$$

Let define the complex moduli as follows:

$$E^{*}(\omega)=i\omega\int_{0}^{+\infty}E(u)e^{-i\omega u}du=i\omega\int_{0}^{+\infty}E(t)e^{-i\omega t}dt\ , \tag{2.19}$$

and performing the integral, we obtain:

`

$$\sigma(t) = \varepsilon^*(t) \cdot i\omega \int_0^{+\infty} E(u) e^{-i\omega u} du = \varepsilon^*(t) \cdot E^*(\omega). \quad (2.20)$$

Applying the Euler formula $e^{i\theta} = \cos\theta + i\sin\theta$ then equation (2.20) can be rewritten as follows (Tschoegl, 1989; Cho, 2016):

$$E^*(\omega) = E'(\omega) + iE''(\omega). \quad (2.21)$$

Thus, the storage and loss modulus respectively the real and imaginary parts, dynamic moduli are the magnitude, and $\varphi_E(\omega) = \tan^{-1}\left(E''(\omega)/E'(\omega)\right)$ is phase angle of complex moduli. Then, the storage and loss modulus can be determined based on the dynamic moduli and phase angle like as:

$$E'(\omega) = |E(\omega)|\cos\varphi_E(\omega), \quad (2.22)$$

$$E''(\omega) = |E(\omega)|\sin\varphi_E(\omega). \quad (2.23)$$

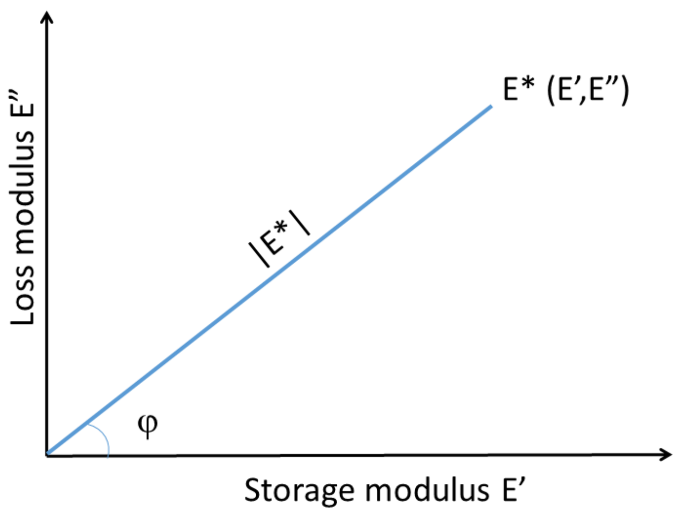

Figure 2.2. Illustration of the relation between $E^*(\omega)$, $E'(\omega)$, $E''(\omega)$, $|E^*(\omega)|$, $\varphi_E(\omega)$ in complex plane.

Similarly, those formulas relating to complex creep compliance can also be proved.

$$D'(\omega) = |D^*(\omega)|\cos(-\varphi_E(\omega)), \quad (2.24)$$

$$D''(\omega) = |D^*(\omega)|\sin(-\varphi_E(\omega)). \quad (2.25)$$

`

Because the behavior of material is unit, all its LVE properties are equivalent to each other.

2.1.1.4 The relationship of LVE properties

a. The relationship between relaxation modulus and creep compliance

As the above discussion, when the sample is applied a input strain function $\varepsilon(t) = H(t)$ where $H(\bullet)$ is a Heaviside function then the measured stress over time is creep compliance $D(t)$. In contrast, if the input signal is $\varepsilon(t) = D(t)$ then the response stress is a Heaviside function. Using Boltzmann and causality principle, one can obtain:

$$H(t) = \int_0^t E(t-\tau) \cdot \frac{dD(t)}{d\tau} \cdot d\tau . \tag{2.26}$$

Performing the Laplace transform, the equation (2.26) gives rise to:

$$\overline{E}(s) \cdot \overline{D}(s) = \frac{1}{s^2} . \tag{2.27}$$

Accomplishing the reversing of Laplace transform, the relationship between relaxation modulus and creep compliance in real space are as follows:

$$\int_0^t E(t-\tau) \cdot D(t) \cdot d\tau = \int_0^t E(t) \cdot D(t-\tau) \cdot d\tau = t . \tag{2.28}$$

b. The relationship between complex modulus and complex creep compliance

From the definition of complex modulus and complex creep compliance, the equation (2.29) and (2.30) are the result of applying the definition of the Laplace transform with $s = i\omega$.

$$E^*(\omega) = s \cdot \overline{E}(s) ; \tag{2.29}$$

$$D^*(\omega) = s \cdot \overline{D}(s) . \tag{2.30}$$

Multiplying the two sides of the equation (2.29) and (2.30), and substituting equation (2.27) in to, the relationship between complex modulus and complex compliance as below:

$$E^*(\omega) \cdot D^*(\omega) = 1 . \tag{2.31}$$

`

c. The relationship between LVE properties in the time domain and the frequency domain

From the equation of complex modulus, one can derive as follows:

$$\frac{E^*(\omega)}{i\omega} = \frac{E^{'}(\omega)}{i\omega} + \frac{E^{"}(\omega)}{\omega} = \eta^{'} - i\eta^{"}, \tag{2.32}$$

where $\eta^{'} = \frac{E^{"}}{\omega} = \int_0^{+\infty} E(t)\cdot\cos(\omega t)\cdot dt$, an odd function and $\eta^{"} = \frac{E^{'}}{\omega} = \int_0^{+\infty} E(t)\cdot\sin(\omega t)\cdot dt$, an even function are respectively real and imaginary parts of the complex number $E^*(\omega)/i\omega$. Performing the Fourier transform and using the properties of odd and even functions, the relaxation modulus can be written likes as (Lakes, 1999):

$$E(t) = \frac{2}{\pi}\int_0^{+\infty} \frac{E"(\omega)\cos(\omega t)}{\omega}\cdot d\omega = \frac{2}{\pi}\int_0^{+\infty} \frac{E'(\omega)\sin(\omega t)}{\omega}\cdot d\omega. \tag{2.33}$$

d. Kramers – Kronig relationship.

i. The relationship between storage modulus and loss modulus

Appling Laplace transform, multiplying s for two sides of the equation (2.19), and accomplishing the change of variable $\omega = w$, one can obtain:

$$s\overline{E}(s) = \frac{2}{\pi}\int_0^{+\infty} E^{'}(w)\cdot\frac{s}{s^2+w^2}\cdot dw. \tag{2.34}$$

Replacing $s = i\omega$ and substituting $s\overline{E}(s) = E^*(\omega)$, the Kramers – Kronig relation can be described as follows (Booij and Thoone, 1982):

$$E^{'}(\omega) = \frac{2\omega^2}{\pi}\int_0^{\infty}\frac{E"(w)/w}{\omega^2 - w^2}dw; \qquad E^{"}(\omega) = \frac{2\omega}{\pi}\int_0^{\infty}\frac{E'(\omega)}{w^2-\omega^2}dw. \tag{2.35}$$

ii. The relationship between dynamic moduli and phase angle

The dynamic moduli and phase angle, the two components of the complex modulus, are not independent. Their relative must obey the Kramers-Kronig to satisfy the physical causality principle (Booij and Thoon, 1982) as below:

`

$$\varphi_E(\omega) = \frac{2\omega}{\pi}\int_0^{+\infty} \frac{\ln\left|E^*(u)\right| - \ln\left|E^*(\omega)\right|}{u^2-\omega^2}du. \quad (2.36)$$

However,

$$-\frac{2\omega}{\pi}\int_0^{+\infty}\frac{\ln\left|E^*(\omega)\right|}{u^2-\omega^2}du = \frac{1}{\pi}\ln\left|E^*(\omega)\right|\int_0^{+\infty}\frac{2\omega}{\omega^2-u^2}du = \frac{1}{\pi}\ln\left|E^*(\omega)\right|\cdot\ln\left|\frac{\omega+u}{\omega-u}\right|_0^{+\infty} = 0$$

So, the relationship between the dynamic moduli and phase angle is presented in equation (2.37) (Booij and Thoon, 1982)

$$\varphi_E(\omega) = \frac{2\omega}{\pi}\int_0^{+\infty}\frac{\ln\left|E^*(u)\right|}{u^2-\omega^2}du = \frac{1}{\pi}\int_0^{+\infty}\ln\left|\frac{u+\omega}{u-\omega}\right|\frac{\ln\left|E^*(u)\right|}{d\ln u}d\ln u. \quad (2.37a)$$

$$\varphi_E(\omega) \simeq \frac{\pi}{2}\left(\frac{d\ln\left|E^*(u)\right|}{d\ln u}\right)_{u=\omega} \quad (2.38b)$$

2.1.1.5 Models of viscoelastic material

a. Mathematical models

Because LVE properties of asphaltic material are monotonic functions, the mathematical model widely used to simulate them is sigmoid function (Rowe, 2009; Tan et al., 2020; Csaba and Judit, 2010). Therefore, this study just focuses on presenting that function.

i. Standard sigmoid function (SS)

The standard sigmoid function is a symmetric function through the midpoint which has a characteristic S-shaped curve. When applying this function to asphalt mixture, a constant is added to represent the upper and lower bound of the data. Then, the equation of complex modulus of material is as shown, (Rowe, 2009):

$$\log E^*(\omega) = \delta + \frac{\alpha}{1+e^{\left[\beta+\gamma\left(\log\left(f_{red}\right)\right)\right]}}, \quad (2.39)$$

where δ is the lower bound, α is the difference of the upper bound relative to the lower bound, β, γ are the shaped parameter, f_{red} is reduced frequency.

The significance of parameter of SS function is described in Figure 2.3

`

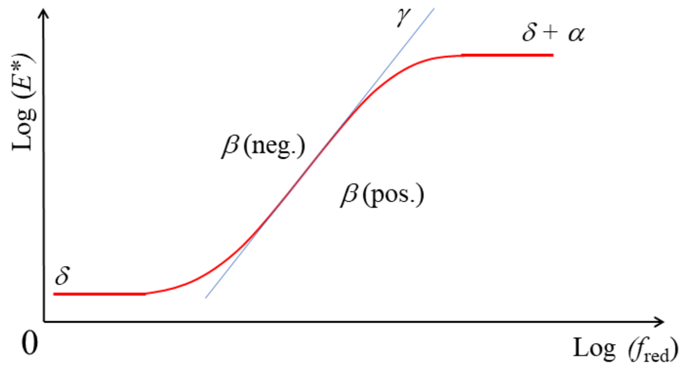

Figure 2.3. Sigmoid function shape and its parameters.

The phase angle $\varphi_E(\omega)$ in SS model can be determined by the approximately formula of Kramer – Kronig relation like this (Tan et al., 2020):

$$\varphi_E(\omega) = \frac{\pi}{2} \cdot \frac{d \log E^*}{d \log(f_{red})} = -\frac{\pi}{2} \cdot \alpha \cdot \gamma \cdot \frac{e^{\left[\beta+\gamma\left(\log(f_{red})\right)\right]}}{\left\{1 + e^{\left[\beta+\gamma\left(\log(f_{red})\right)\right]}\right\}^2}. \qquad (2.40)$$

ii. Generalized sigmoid function (GS)

Because sigmoid function is a symmetric one meanwhile the complex modulus of asphaltic material has a unsymmetric shape, so researchers developed a generalized sigmoid function based on the SS function to increase the fitting ability of the model. Then, the complex modulus of asphaltic material can be determined by equation (2.40)

$$\log E^*(\omega) = \delta + \frac{\alpha}{\left\{1 + \lambda e^{\left[\beta+\gamma\left(\log(f_{red})\right)\right]}\right\}^{1/\lambda}}. \qquad (2.41)$$

where λ is the parameter which modifies the curve of function has an unsymmetric shape.

Similarly to the SS function, the phase angle of GS function is also approximately calculated as the following (Tan et al., 2020):

$$\varphi_E(\omega) = \frac{\pi}{2} \cdot \frac{d \log E^*}{d \log \omega} = -\frac{\pi}{2} \cdot \alpha \cdot \gamma \cdot \frac{e^{\left[\beta+\gamma\left(\log f_{red}\right)\right]}}{\left\{1 + \lambda e^{\left[\beta+\gamma\left(\log f_{red}\right)\right]}\right\}^{(1+1/\lambda)}}. \qquad (2.42)$$

`

b. Rheological models

Rheological models are often used to simulate the uniaxial LVE behaviors of asphaltic materials because they automatic satisfy the thermodynamic principles. Those models are constructed based on spring, linear dashpot, and fractional dashpot element. In this section just rheological models widely used for asphaltic material are presented.

i. Generalized Maxwell model

Generalized Maxwell (GM) model consists of one stiffness E_0 spring related parallel with n Maxwell elements. In where, the m^{th} element has a stiffness E_m spring assemble in series with a linear dashpot with a viscosity coefficient η_m (Figure 2.4).

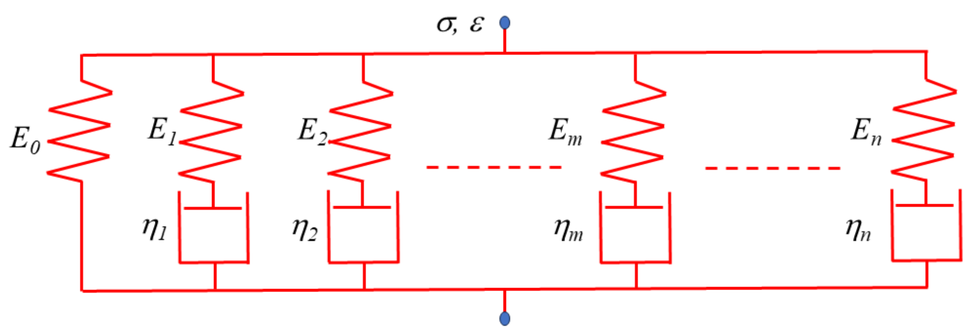

Figure 2.4. Illustration of Generalized Maxwell model

The relaxation modulus of GM is determined by Prony series as follows: (Tschoegl, 1989; Luk-Cyr et al., 2013; Cho,2016)

$$E_{GM}\left(t\right)=E_0+\sum_{m=1}^{N}E_m e^{-t/\tau_m} . \qquad (2.43)$$

ii. Generalized Kelvin – Voigt model

Different to GM model, generalized Kelvin - Voigt (GKV) model is a series of Kelvin – Voigt elements and one stiffness E_0 spring. Each Kelvin – Voigt element consists of one spring related parallel with one linear dashpot. This model is described in Figure 2.5.

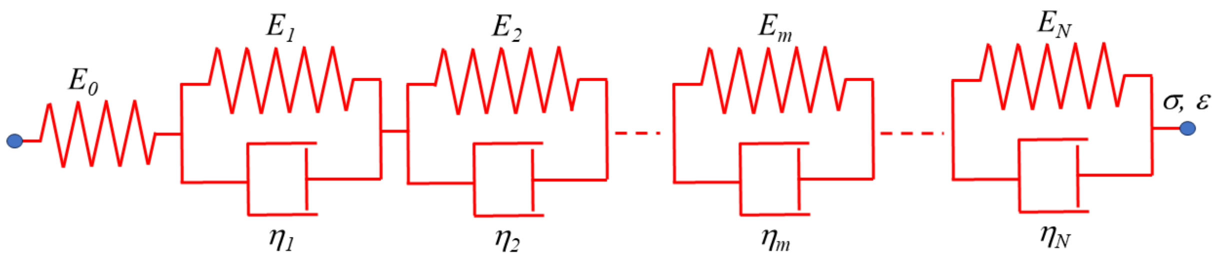

Figure 2.5. Illustration of Generalized Kelvin - Voigt model

The GKV has creep compliance in the form of Prony series, presented in equation (2.43) (Tschoegl, 1989; Luk-Cyr et al., 2013; Cho,2016)

$$D_{GKV}(t) = \frac{1}{E_0} + \sum_{m=1}^{N} \frac{1}{E_m}\left(1 - e^{-t/\tau_m}\right). \tag{2.44}$$

iii. Huet – Sayegh model

Comparison with GM and GKV models, Huet – Sayegh (HS) model has a few parameters but well fit with behaviors of asphaltic material. This model consists of one spring assembling parallel with a series of one spring and two fractional dashpots (Figure 2.6).

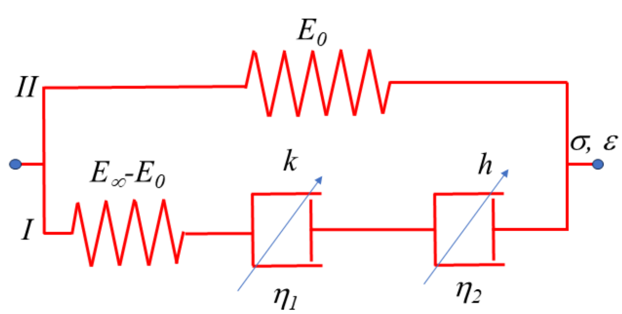

Figure 2.6. Illustration of Huet – Sayegh model

It is demonstrated that the complex modulus of HS model is as follows (Nguyen et al., 2022; Olard and Di Benedetto, 2003):

$$E^*_{HS}(\omega) = E_0 + \frac{E_\infty - E_0}{1 + \delta_1 (i\omega\tau)^{-k} + \delta_2 (i\omega\tau)^{-h}}, \tag{2.45}$$

`

where ω is angular frequency, $\delta = \tau(T)\cdot(E_\infty - E_0)/\eta_1$, $0 < k < h < 1$ are parameter of model, and E_0, E_∞ are respectively the value of $E(\omega)$ when $\omega\tau \to 0$ and when $\omega\tau \to \infty$

iv. 2S2P1D model

A modified model of HS model is 2S2P1D model which added one linear dashpot related series with one spring and two fractional dashpots (Figure 2.7).

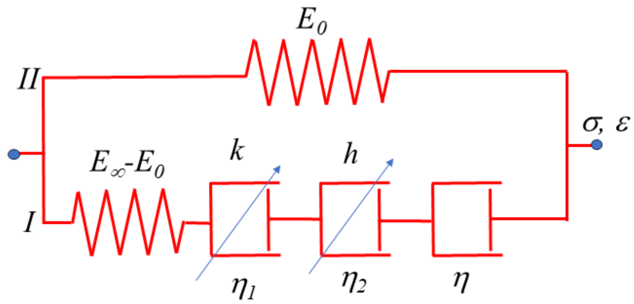

Figure 2.7. Illustration of 2S2P1D model

The complex modulus of asphaltic material is determined as below (Olard and Di Benedetto, 2003):

$$E^*_{2S2P1D}(\omega)\frac{E_\infty - E_0}{1+\delta_1(i\omega\tau)^{-k}+\delta_2(i\omega\tau)^{-h}+(i\omega\beta\tau)^{-1}}, \quad (2.46)$$

where β is material parameter, other parameters are similar to HS model.

2.1.1.6 Time-temperature superposition principle

The core of this principle is that a long period of relaxation time at low temperature is equivalent to a short period of that at higher temperature. This principle makes it possible to predict the phenomenon of LVE materials prolonged evolution by measuring them at different temperatures. Moreover, laboratory devices often have a defined measurement range, so we can expand the measurement range with this principle.

Based on this principle, the LVE properties of material can be expressed as follows:

$$D(t,T) = D(t/a_T, T_{ref}), \quad (2.47)$$

`

where a_T is the shift factor with the meaning that the behaviors of material with the loading time t at temperature T is equivalent to those with the loading time t/a_T at reference temperature T_{ref}. Thus, the value t/a_T is redemption value of loading time, is usually called reduced time at reference temperature compared to when it is conducted at a temperature T.

The value of a_T can be determined based on the formula of Williams – Landel – Ferry (WLF):

$$\log a_T = \frac{C_1\left(T - T_{ref}\right)}{C_2 - T - T_{ref}}, \tag{2.48}$$

where C_1, C_2 are the parameters of material.

2.1.2 Theory of viscoplasticity

2.1.2.1 Viscoplastic flow rule

It is defined that the rate of the viscoplastic strain $\dot{\varepsilon}_{vp}$ obeying the viscoplastic flow rule as following: (Perzyna, 1971; Heeres et al., 2002; Shakiba et al., 2013)

$$\dot{\varepsilon}_{vp} = \dot{\gamma}_{vp}\frac{\partial F}{\partial \sigma} \tag{2.48}$$

where σ is the stress vector, F is the viscoplastic potential function, and $\dot{\gamma}_{vp}$, $\frac{\partial F}{\partial \sigma}$ present the magnitude and direction of the VP strain, respectively.

Based on Perzyna model, $\dot{\gamma}_{vp}$ is determined such as (Perzyna, 1971; Heeres et al., 2002; Darabi et al., 2019)

$$\dot{\gamma}_{vp} = \zeta.\left\langle \Phi\left(f\right)\right\rangle^N \tag{2.49}$$

where ζ is the fluidity parameter, which is the inverse of viscos parameter of material, Φ represents to the overstress function, expressed as a function of f (yield surface

`

function), and N is the viscoplastic rate sensitivity exponent . It is noting that $\langle \bullet \rangle$ is the Macaulay brackets and defined as $\langle \bullet \rangle = \frac{\bullet + |\bullet|}{2}$.

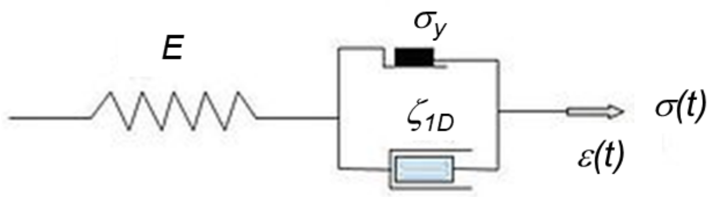

Figure 2.8. The Perzyna model (Perzyna,1966)

2.1.2.2 Yield surface function

The yield surface is the conditions under which the asphalt mixture occur the viscoplastic strain and how it accumulates as the DP in pavement. Models of yield surface proposed for asphalt mixture can be mentioned as: the Mohr-Coulomb model, Drucker-Prager and its extended model, Di Benedetto model, …Where the Drucker-Prager yield surface is widely used because it expresses by cohesion and inter friction behavior, so it is suitable for asphalt concrete. The Drucker-Prager model is presented as follows; (Drucker and Prager, 1952; Zhang, 2014)

$$\sqrt{J_2} - \alpha I_1 - \kappa_0 = 0 \qquad (2.50)$$

where I_1 are respectively the first invariant and J_2 the second invariant of the deviatoric part of the Cauchy stress vector, α and κ_0 are constant of material.

2.1.2.3 Hardening law

Under the effect of dynamic and repeated loading of vehicle, there is rearrangement of the aggregates of asphalt mixture. That rearrangement makes materials increase their resistance to PD. It means that the more increase of number of loads passes the more decrease in the cumulative VP strain rate. That phenomenon is called viscoplastic hardening of materials.

`

To model the effect of viscoplastic hardening, the yield surface functions are modified. For example, Park (2007) proposed gradually reducing the value of cohesion as the accumulation of VP strain increases, while Nedjar and Nguyen (2012) suggest increasing the viscosity of asphalt mixture when number of loads passes increases. Based on ideal of Nedjar and Nguyen (2012), Nguyen (2017) proposed to reduce the value of the fluidity parameter with increasing of accumulation of VP strain. However, with that approach, the evolution of VP strains would increase insignificantly after just a few loading cycles (Darabi et al., 2012).

2.2 Time-Frequency interconversion methods

In literature, plenty of time-frequency interconversion methods were proposed. As discussed at subsection 1.2.3, those methods are difficult to perform or unsatisfied with Kramer-Kronig relationships, or low accuracy. Therefore, in this subsection, the proposed method which fully obeys the physical causality principle and LVE theory and has a high accuracy is presented.

2.2.1 RM and CC as inverse Fourier transform of dynamic viscosity

It can be demonstrated that: (Cho, 2016)

$$\frac{E^*(i\omega)}{i\omega} = \int_0^{+\infty} E(t)\cdot\cos(\omega t)\cdot dt - i\int_0^{+\infty} E(t)\cdot\sin(\omega t)\cdot dt = \eta^{'}(\omega) - i\cdot\eta^{''}(\omega), \tag{2.51}$$

where $\eta^{'}(\omega)$ and $-\eta^{''}(\omega)$ is the real and imaginary part of the complex number $E^*(i\omega)/i\omega$, called dynamic viscosity.

Remarks 1: The real part of $E*(i\omega)/(i\omega)$ is even while the imaginary part of $E^*(i\omega)/(i\omega)$ is odd.

The RM function can be obtained by performing the inverse Fourier transform:

$$E(t) = \frac{1}{2\pi}\int_{-\infty}^{+\infty} \frac{E^{''}(\omega) - iE^{'}(\omega)}{\omega}\left(\cos(\omega t) + i\sin(\omega t)\right)d\omega, \tag{2.52}$$

`

where $E^*(i\omega)/(i\omega) = (E'' - iE')/\omega$ has been used. According to Remarks 1, E''/ω is even, $-E'/\omega$ is odd; both $E''\cos(\omega t)/\omega$ and $E'\sin(\omega t)/\omega$ are even with ω. It can be deduced that:

$$\begin{aligned} E(t) &= \frac{1}{2\pi}\int_{-\infty}^{+\infty}\frac{E''(\omega)\cos(\omega t)}{\omega}d\omega + \frac{1}{2\pi}\int_{-\infty}^{+\infty}\frac{E'(\omega)\sin(\omega t)}{\omega}d\omega \\ &= \frac{1}{\pi}\int_{0}^{+\infty}\frac{E''(\omega)\cos(\omega t)}{\omega}d\omega + \frac{1}{\pi}\int_{0}^{+\infty}\frac{E'(\omega)\sin(\omega t)}{\omega}d\omega, \end{aligned} \tag{2.53}$$

which is a real-valued function. In addition, $E(t) = 0$ for t varying from $-\infty$ to 0. Since $E''\cos(\omega t)/\omega$ is even while $E'\sin(\omega t)/\omega$ is odd with t , we have: (Lakes, 1999)

$$\int_{0}^{+\infty}\frac{E''(\omega)\cos(\omega t)}{\omega}d\omega = \int_{0}^{+\infty}\frac{E'(\omega)\sin(\omega t)}{\omega}d\omega,\ \forall t \geq 0. \tag{2.54}$$

Hence, the equation for calculating the RM is obtained: (Lakes, 1999)

$$E(t) = \frac{2}{\pi}\int_{0}^{+\infty}\frac{E'(\omega)\sin(\omega t)}{\omega}d\omega = \frac{2}{\pi}\int_{0}^{+\infty}\frac{E''(\omega)\cos(\omega t)}{\omega}d\omega,\ \forall t \geq 0. \tag{2.55}$$

And by similarity:

$$D(t) = \frac{2}{\pi}\int_{0}^{+\infty}\frac{D'(\omega)\sin(\omega t)}{\omega}d\omega = \frac{2}{\pi}\int_{0}^{+\infty}\frac{D''(\omega)\cos(\omega t)}{\omega}d\omega,\ \forall t \geq 0. \tag{2.56}$$

2.2.2 Development of a closed-form formula for the RM and CC

Due to the complexity of Kramers-Kronig relationships, the closed-form formula of the storage and loss modulus/compliance cannot be determined from the master curve of DM and compliance. In addition, the time-frequency interconversion formulas are in the form of indefinite integral whose value cannot be analytically calculated in a general manner. Therefore, in order to derive a closed-form formula of the RM and CC, the storage and loss modulus/compliance function must be approximated by some special functions for the indefinite integral to be analytically integrated. Since both equalities in equation (2.55) and (2.56) are equivalent, we will consider the first equality involving only the storage modulus and compliance.

`

In fact, the storage modulus is a monotonic increasing function, meanwhile, storage creep compliance (SCC) is a monotonic decreasing one. Those quantities tend to their asymptotes when $\omega \to \infty$. Thus, SM and SCC can be decayed into the sums of exponential functions (SEFs). Besides, the integral $\int_0^{+\infty} \left(e^{\alpha\omega} \sin(\omega t)/\omega\right) d\omega$ can be determined by the analytical resolution in case $\alpha < 0$. With that approach, the next part of this section presents the content of the interconversion method of LVE properties from the frequency domain to the time domain. That method is performed based on approximate analytical the master curve of DM into the SEFs (Phan et al., 2022).

If storage modulus can be decomposed into the SEFs as follows:

$$E^{'}(\omega) = E^{'}(\omega \to \infty) - \sum_{j=1}^{N_j} E_j^{'} e^{b_j \omega}, \tag{2.57}$$

where $b_j < 0$ are the real-valued negative decay rates; E_j are real-valued coefficients; and N_j is the number of exponential functions.

Substituting the storage modulus in the equation (2.57) into the equation (2.31), the equation (2.58) can be obtained:

$$E(t) = \frac{2E^{*}(\omega \to \infty)}{\pi} \int_0^{+\infty} \frac{\sin(\omega t)}{\omega} \cdot d\omega - \frac{2}{\pi} \int_0^{+\infty} \sum_{i=1}^{N_j} E_j^{'} e^{b_j \omega} \frac{\sin(\omega t)}{\omega} d\omega. \tag{2.58}$$

It is easy to demonstrate that the first integral in the second member is equal to the value of dynamic modulus when $\omega \to \infty$,

$$\frac{2E^{*}(\omega \to \infty)}{\pi} \int_0^{+\infty} \frac{\sin(\omega t)}{\omega} \cdot d\omega = E^{*}(\omega \to \infty), \tag{2.59}$$

The second integral in the equation (2.58) can be calculated as follows:

`

$$\frac{2}{\pi}\int_0^{+\infty}\sum_{i=1}^{N_j}E_j^i e^{b_j\omega}\frac{\sin(\omega t)}{\omega}=\frac{2}{\pi}\sum_{i=1}^{N_j}E_j^{'}\int_0^{+\infty}e^{b_j\omega}\frac{\sin(\omega t)}{\omega}d\omega$$
$$=\frac{2}{\pi}\sum_{i=1}^{N_j}E_j^{'}\int_0^{+\infty}\mathrm{L}\left\{u\left[s-\left(-b_j\right)\right]\right\}(\omega)\sin(\omega t)d\omega$$
$$=\frac{2}{\pi}\sum_{i=1}^{N_j}E_j^{'}\int_0^{+\infty}u\left[\omega-\left(-b_j\right)\right]\mathrm{L}\left\{\sin(s\cdot t)\right\}(\omega)d\omega \tag{2.60}$$
$$=\frac{2}{\pi}\sum_{i=1}^{N_j}E_j^{'}\int_0^{-b_j}u\left[\omega-\left(-b_j\right)\right]\frac{t}{\omega^2+t^2}d\omega+\frac{2}{\pi}\sum_{i=1}^{N_j}E_j^{'}\int_{-b_j}^{+\infty}u\left[\omega-\left(-b_j\right)\right]\frac{t}{\omega^2+t^2}d\omega$$

where $\mathrm{L}(\bullet)$ is Laplace transform.

Because $u(s-a)$ is a delay function,

$$\begin{cases}u(s-a)=0 & \text{when } s<a\\ u(s-a)=1 & \text{when } s\geq a\end{cases}, \tag{2.61}$$

so

$$\frac{2}{\pi}\sum_{i=1}^{N_j}E_j^{'}\int_0^{-b_j}u\left[\omega-\left(-b_j\right)\right]\frac{t}{\omega^2+t^2}d\omega=0. \tag{2.62}$$

Thus, the equation (2.60) can be rewritten as

$$\frac{2}{\pi}\int_0^{+\infty}\sum_{i=1}^{N_j}E_j^i e^{b_j\omega}\frac{\sin(\omega t)}{\omega}=\frac{2}{\pi}\sum_{i=1}^{N_j}E_j^{'}\int_{-b_j}^{+\infty}\frac{t}{\omega^2+t^2}d\omega. \tag{2.63}$$

Replacing $v=\omega/t$, the equation (2.63) becomes

$$\frac{2}{\pi}\int_0^{+\infty}\sum_{i=1}^{N_j}E_j^i e^{b_j\omega}\frac{\sin(\omega t)}{\omega}=\frac{2}{\pi}\sum_{i=1}^{N_j}E_j^{'}\int_{-b_j/t}^{+\infty}\frac{1}{v^2+1}dv=\frac{2}{\pi}\sum_{i=1}^{N_j}E_j^{'}\left[\frac{\pi}{2}-\tan^{-1}\left(\frac{-b_j}{t}\right)\right]. \tag{2.64}$$

Applying the property $\tan^{-1}(a/b)+\tan^{-1}(b/a)=\pi/2$ of $\tan^{-1}$ function, the final result is

$$E(t)=E^*(\omega\to\infty)-\frac{2}{\pi}\sum_{i=1}^{N_j}E_j^{'}\tan^{-1}\left(\frac{t}{-b_j}\right). \tag{2.65}$$

By similar procedure with storage creep compliance, we have:

`

$$D(t) = D^*(\omega \to \infty) + \frac{2}{\pi}\sum_{i=1}^{N_j} D_j^{'} \tan^{-1}\left(\frac{t}{-c_j}\right). \tag{2.66}$$

The accuracy of this method depends on the accuracy of analytical approximate the SM and SCCs into SEFs. This problem is solved thanks to the modified Dombi's algorithm proposed by Nguyen et al. (2020) (see Appendix A). That algorithm can approximate a function into SEFs better than regression or collocation methods (Phan and Nguyen, 2022). In order to facilitate the reading of this study, that algorithm is summarized as follows. First, dividing the investigated variables into small ranges and determining the decay rate for each small range by using Dombi's algorithm (Dombi, 2006). Then, eliminating coefficient has duplicate value and assembling the remaining decay rate coefficient into a set of single exponents. Finally, the coefficients of exponential functions are optimized to best fit the input data using linear least-square techniques throughout the region to be surveyed.

2.2.3 Application examples

In this subsection, two application examples were considered such that master curves of dynamic modulus of HS and GS model as input data. Those examples were performed based on the proposed algorithm to evaluate the efficiency of it. All the data was processed with the aid of the MATLAB version R2015 program operated by a Core i5 computer. For validation purposes, the obtained results will be compared with either exact solutions, analytical approximate solutions, or experimental results.

The relative error or (difference) of the computed storage or creep compliance will be determined at all calculating points by using the equation (2.67). For other quantities, the equation (2.68) will be used. It should be noted that those equations are also applied in the post section of this study.

$$\text{Err} = \max\left\{\left(1/\overline{f_i} - 1/f_i\right).f_i\right\}, \tag{2.67}$$

$$\text{Err} = \max\left\{\left(\overline{f_i} - f_i\right)/f_i\right\}. \tag{2.68}$$

`

2.2.3.1Master curves of dynamic modulus of HS model as input data

In this example, the efficiency of the proposed formulas dealing with the master curve of DM of asphalt concrete is evaluated. Because the master curve of DM derived from the HS model has the existence of exact values of LVE properties, it was used in this example for assessing the accuracy of proposed method. Although the method intends to be applied for mathematical model, the HS rheological model was still surveyed in this example for evaluating application ability of this method to rheological.

It is reminded here the complex modulus of HS model is as follows (Nguyen et al., 2022; Olard and Di Benedetto, 2003):

$$E_{HS}^{*}(\omega) = E_0 + \frac{E_\infty - E_0}{1 + \delta_1 (i\omega\tau)^{-k} + \delta_2 (i\omega\tau)^{-h}}, \tag{2.69}$$

where ω is angular frequency, $\delta = \tau(T)\cdot(E_\infty - E_0)/\eta_1$, $0 < k < h < 1$ are parameter of model, and E_0, E_1 are respectively the value of $E(\omega)$ when $\omega\tau \to 0$ and when $\omega\tau \to \infty$

Replacing $i = \cos(\pi/2) + i\cdot\sin(\pi/2) = e^{(i\pi/2)}$ into the formula of complex modulus of HS model (Equation 2.69), one can obtain:

$$E_{HS}^{*}(\omega) = E_0 + \frac{E_\infty - E_0}{A^2 + B^2}(A + B\cdot i), \tag{2.70}$$

where: $A = 1 + \delta\frac{\cos(k\pi/2)}{(\omega_T(T))^k} + \frac{\cos(h\pi/2)}{(\omega_T(T))^h}$; $B = \delta\frac{\sin(k\pi/2)}{(\omega_T(T))^k} + \frac{\sin(h\pi/2)}{(\omega_T(T))^h}$.

Next, the exact storage and loss modulus can be determined from the equation (2.70) as follows:

$$E_{HS}^{'}(\omega) = E_0 + A\frac{E_\infty - E_0}{A^2 + B^2}, \tag{2.71}$$

$$E_{HS}^{''}(\omega) = B\frac{E_\infty - E_0}{A^2 + B^2}. \tag{2.72}$$

Then, it is easy to compute the DM and phase angle (PA) from the storage and loss modulus.

`

$$\left|E_{HS}^{*}(\omega)\right| = \sqrt{\left(E_{HS}^{'}(\omega)\right)^{2} + \left(E_{HS}^{''}(\omega)\right)^{2}}, \tag{2.73}$$

$$\varphi_{E,HS}(\omega) = \tan^{-1}\left[\frac{E_{HS}^{''}(\omega)}{E_{HS}^{'}(\omega)}\right]. \tag{2.74}$$

The exact value of LVE properties in the time domain can be numerically calculated using the discrete relationships presented by Nguyen et al. (2021a, 2022).

The HS master curve of DM of the unmodified asphalt mixture studied in (Nguyen et al., 2021a) was re-used as input data for the proposed algorithm (see Figure 2.9). The best-fit HS parameters are also provided in Table 2.1. From equation (2.73), the derivative of $\left|E_{HS}^{''}(\omega)\right|$ with respect to $\ln\omega$ can be derived:

$$\frac{d\ln\left|E_{HS}^{*}(\omega)\right|}{d\ln\omega} = \frac{\omega\left(E_{\infty}-E_{0}\right)}{\left|E_{HS}^{*}(\omega)\right|^{2}}\left[E_{0}(t_{1}-t_{2})-\left(E_{\infty}-E_{0}\right)\frac{t_{2}}{2A}\right];$$
$$t_{1} = \frac{dA}{d\omega}\frac{1}{A^{2}+B^{2}};\ t_{2} = \frac{2A}{\left(A^{2}+B^{2}\right)^{2}}\left(A\frac{dA}{d\omega}+B\frac{dB}{d\omega}\right). \tag{2.75}$$

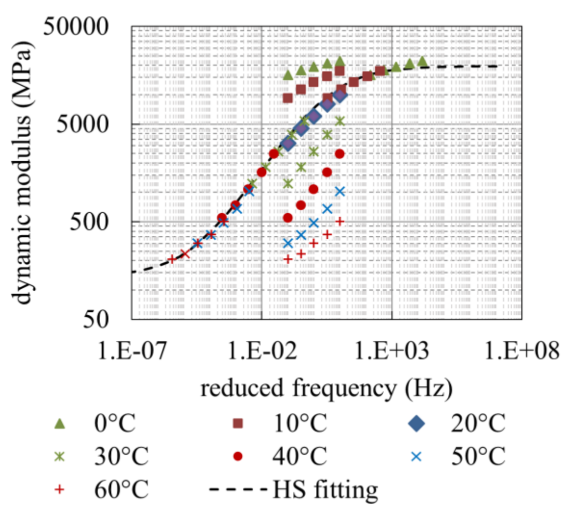

Figure 2.9. Master curve of dynamic modulus of the AC mixture studied by Nguyen et al. (2021a)

`

Table 2.1: Parameter of HS model of the conventional (AC) mixture studied by Nguyen et al. (2021a)

Properties	E_0 (MPa)	E_∞ (MPa)	k	h	δ	τ (s)	T_{ref} (°C)
Values	140	19550	0.390	0.500	12.000	20.000	20

According to the master curves of the DM, the range of frequency of interest was fixed as $\omega \in [10^{-10}, 10^{8}]$ and the range of the dummy variable was chosen larger than that range—namely, $u \in [10^{-25}, 10^{25}]$ to properly calculate the integral in equation (2.37). The number of the subintervals to discretize the dummy variable in the based 10 logarithmic scale was 50,000. The calculated results are summarized as follows.

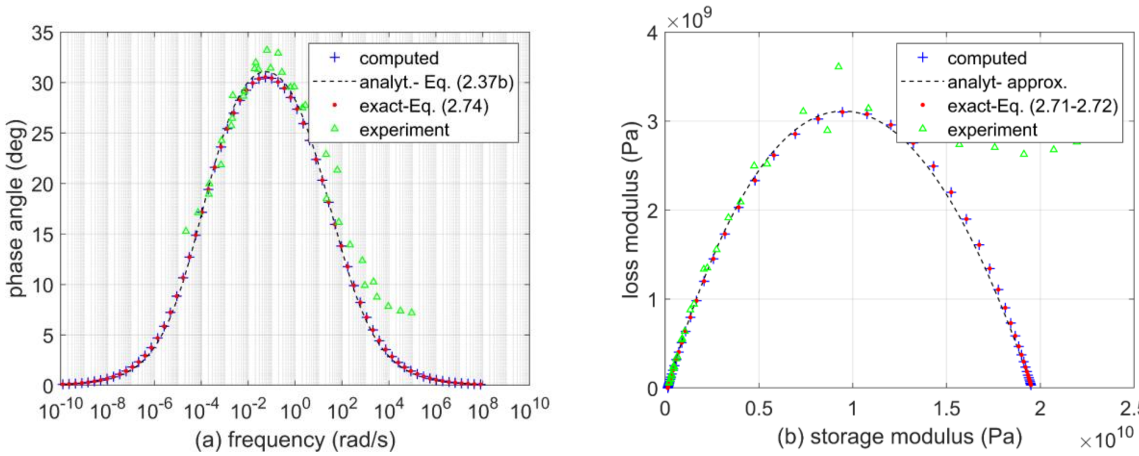

Figure 2.10. (a) Phase angles obtained from HS dynamic modulus; and (b) Cole-Cole diagram obtained from HS dynamic modulus.

The PAs versus the angular frequencies are plotted in Figure 2.10(a), in which a good agreement between the computed PAs and the exact ones can be observed. The relative errors between these values were smaller than 3.3×10^{-4} at all calculating points. As a result, the computed storage and loss moduli agreed well with the exact values as shown in the Cole-Cole diagram [Figure 2.10(b)]. In effect, the relative errors between the computed and the exact storage moduli calculated from the equation (2.71) were lower than 1.04×10^{-4}, and the relative errors between the computed and the exact loss moduli calculated from the equation (2.72) were lower than 1.75×10^{-4}.

`

By this occasion, the accuracy of the analytical approximate PAs calculated with the formulation of Booij and Thoone (1982) was also evaluated. As can be observed in Figure 2.10(a), the analytical approximate PAs were not close to the exact ones calculated from the equation (2.72). The maximal error was approximately 0.6° at the inflection point of the master curve of dynamic modulus, $\omega \approx 10^{-2.36}\,\text{rad/s}$, and the relative error at that point was 2.1×10^{-2}. Nevertheless, as the frequency approached extremely low or rather high values, the relative errors between the analytically approximated PAs and the exact values were rather large, up to 15.35%. This lack of accuracy certainly results in a shortage of accuracy of the storage and loss moduli computed, as can be seen in Figure 2.10(b).

The experimental values of the PAs are also presented in Figure 2.10(a), in which a relatively good agreement between the calculated and tested PAs at frequencies lower than 10^3 rad/s can be observed. At that frequency range, the absolute error between these PAs was lower than 6.16°, and the relative error was almost lower than 38.53%. However, the large discrepancy of the tested PAs did not allow the tested storage and loss moduli to form a reasonable master curve in the Cole-Cole diagram in Figure 2.10 (b). In effect, the errors between the experimental values and the exact ones approximately ranged from −2,000 to 3,100 MPa. In terms of relative errors, the experimental storage moduli differed <15% from the exact ones, whereas the experimental loss moduli may differ >200% from the exact ones at frequencies higher than 10^4 rad/s. This demonstrates that the PAs were more difficult to measure accurately than the DM.

An important step of the proposed method is to decompose the storage modulus and compliance into SEFs. By using the modified Dombi algorithm presented by Nguyen et al. (2022), the storage modulus and compliance were approximated with high accuracy by SEFs and are presented in Figure 2.11. It was found that the relative errors due to the

`

approximation process were extremely small, lower than 10^{-10} at all estimating points when 200 exponential functions were used in the sums, which can be neglected.

The RM and CC were computed using the closed-form formulas in the equation (2.65), the equation (2.66) and are presented in Figure 2.12. The results show that the relative errors of the obtained RM and CC were lower than 3.46×10^{-4} at all computing points. In addition, the master curve of CCs of the mixture experimentally determined by Nguyen et al. (2021a) is also shown in the figure to confirm the good agreement between the computed and experimental CCs.

For better computational efficiency of FEM analysis in the time domain, the computed RM and CC should be decomposed into SEFs. This task can be easily performed with the aid of the modified Dombi algorithm. It was shown that the relative errors between the values approximated by SEFs and the computed values were lower than 3.46×10^{-6} at every estimating point when only positive coefficients were used. Such a high level of accuracy allows one to obtain a maximal relative error of lower than 3.46×10^{-4} between the values of the SEFs and the exact values.

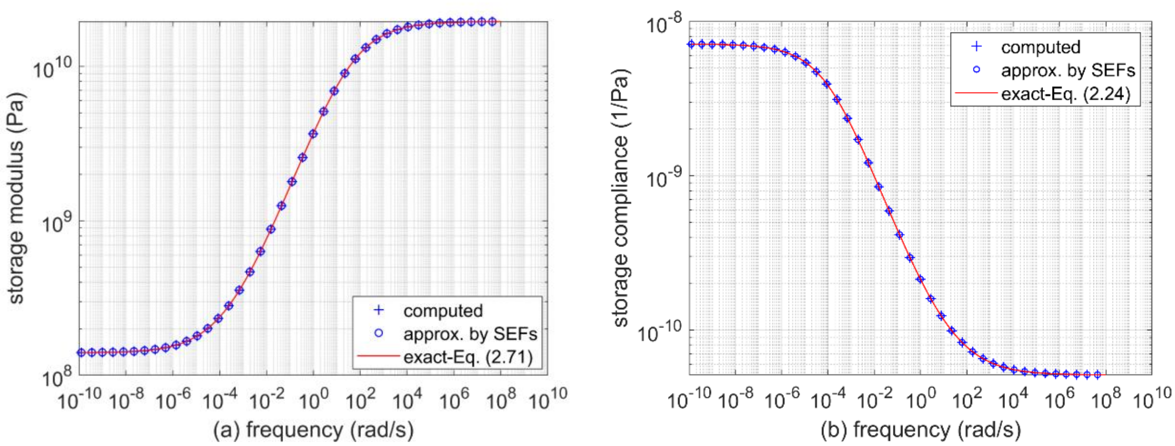

Figure 2.11. (a) Approximation by SEFs of storage moduli computed from the HS dynamic modulus; and (b) approximation by SEFs of storage compliances computed from the HS dynamic modulus.

`

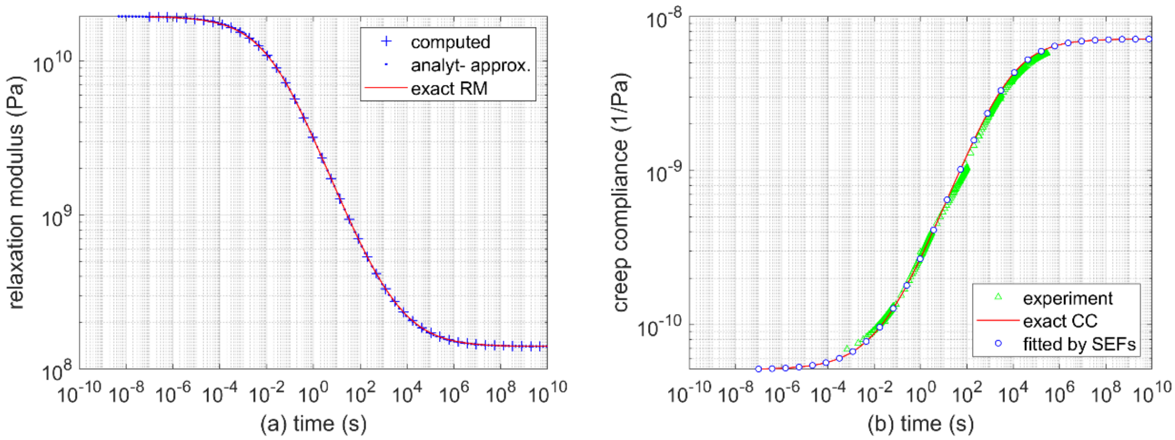

Figure 2.12. (a) Computed relaxation moduli from HS dynamic modulus and their approximations by SEFs; and (b) computed CCs from HS dynamic modulus and their approximations by SEFs.

It is obvious that the relative error of the computed RM and CC was at the same order of magnitude as that of the computed PAs. As a result, an increase in the accuracy of the computed PAs will give rise to an increase in the accuracy of the computed LVE properties.

2.2.3.2 Master curves of dynamic modulus of GS model as input data

This example is devoted to demonstrating the ability of the proposed method in dealing with the GS master curve of the DM proposed by Rowe (2009) and Rowe et al. (2009):

$$\log\left|E^*_{MS}(\omega)\right| = \delta + \frac{\alpha}{\left[1+\lambda.\exp\left(\beta+\gamma\log(\frac{\omega}{2\pi})\right)\right]^{1/\lambda}}, \quad (2.76)$$

where δ is the value of $\log\left|E^*_{MS}(\omega)\right|$ when $\omega\to 0$, $\delta+\alpha$ is the value of $\log\left|E^*_{MS}(\omega)\right|$ when $\omega\to+\infty$, λ,β and $\gamma<0$ are parameters controlling the shape of the function. The best-fit parameters of the GS master curve determined by Liu and Luo (2017) for a conventional asphalt mixture at the reference temperature (20°C) were chosen as input data for the proposed algorithm, namely δ = 2.08, α = 2.54, λ = 0.18, β = −0.98, and γ =

`

−0.41. The plot of the DM versus the angular frequency is shown in Figure 2.13(a). It should be noted that the angular frequency was used in this study instead of the frequency to maintain the consistency of the formulation throughout this section.

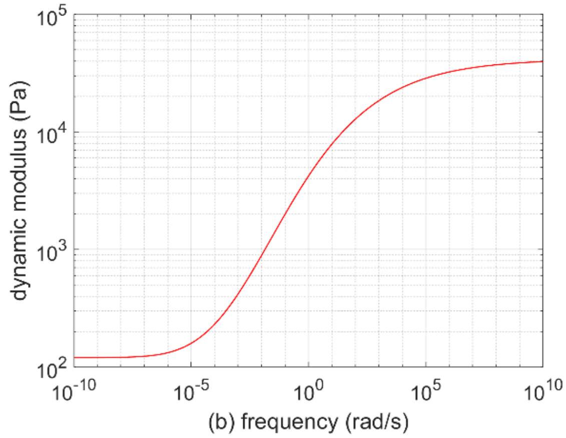

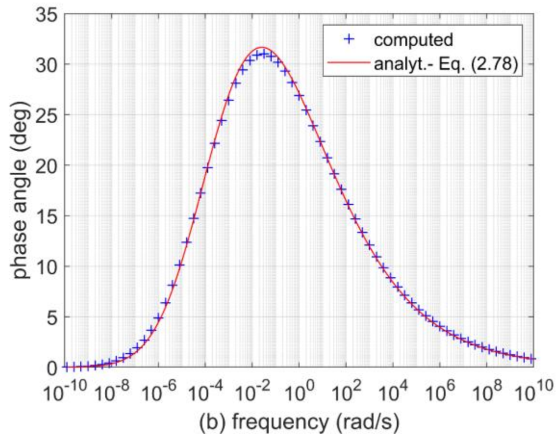

Figure 2.13. (a) MS master curve of DM data (data from Liu and Luo 2017); and (b) master curve of computed PAs from the MS master curve of DM

The corresponding LVE properties such as PA, storage modulus, RM, and CC can be analytically approximated as follows. Letting $\nu = \beta + \gamma \log(\omega/2\pi)$, the derivative of $\log\left|E(\omega)\right|$ with respect to $\log\omega$ can be derived from equation (2.76) in a straightforward manner

$$\frac{d\log\left|E_{GS}^{*}(\omega)\right|}{d\log\omega} = -\frac{\alpha\gamma e^{\nu}}{\left(1+\lambda\cdot e^{\nu}\right)^{1+1/\lambda}}. \tag{2.77}$$

The PA can be analytically approximated using the formula of Booij and Thoone (1982)

$$\varphi_{E,GS}(\omega) \simeq -\frac{\pi}{2}\frac{\alpha\gamma e^{\nu}}{\left(1+\lambda\cdot e^{\nu}\right)^{1+1/\lambda}}. \tag{2.78}$$

based on which the storage modulus and its logarithm function can be approximated by

$$E_{GS}^{'} \simeq \left|E_{GS}^{*}(\omega)\right|\cdot\cos\left(\varphi_{E,GS}(\omega)\right) \tag{2.79}$$

$$\log\left(E_{GS}^{'}\right) = \log\left(\left|E_{GS}^{*}(\omega)\right|\right) + \log\left[\cos\left(\varphi_{E,GS}(\omega)\right)\right]. \tag{2.80}$$

`

According to the work of Schapery and Park (1999), the RM and CC can be analytically approximated based on the master curve of the storage modulus

$$E_{GS}\left(t=\frac{1}{\omega}\right)\simeq\frac{E'_{GS}(\omega)}{\lambda'(\omega)};$$
$$D_{GS}\left(t=\frac{1}{\omega}\right)\simeq\frac{\sin(n\pi)}{n\pi}\frac{\lambda'(\omega)}{E'_{GS}(\omega)}; \tag{2.81}$$
$$\lambda'(\omega)=\Gamma(1-n)\cos\left(n\frac{\pi}{2}\right)$$

where $\Gamma(\bullet)$ is gamma function; and n is derivative of $\log\left(E_S(\omega)\right)$ with respect to log ω, which can be explicitly computed

$$\frac{d\log\left|E'_{GS}(\omega)\right|}{d\log\omega}=-\frac{\alpha\gamma e^{\nu}}{\left(1+\lambda\cdot e^{\nu}\right)^{1+1/\lambda}}-\varphi_E^{GS}\cdot\tan\varphi_E^{GS}\cdot\frac{\gamma}{\ln 10}\cdot\frac{\lambda\left(e^{\nu}-1\right)}{1+\lambda e^{\nu}}. \tag{2.82}$$

Owing to the lack of exact formulas for LVE properties corresponding to the GS master curve of DM, the analytical approximate values will be used as reference values to verify the reasonability of the results computed with the proposed method.

The computed results are summarized as follows. First, the PAs corresponding to the frequency of interest in the range $[10^{-10},10^{10}]$ were computed using the numerical integrate of equation (2.37) as follows. Let the range of frequency of interest be discretized by $2N+1$ equidistant points in the base 10 logarithmic scale

$$\log\omega_i=\left\{\log\omega_{-N},\ldots,\log\omega_0,\ldots,\log\omega_N\right\},\ i=-N,\ldots,N \tag{2.84}$$

The dummy variable u in equation (2.37) was also discretized by using $2M+1$ points in the base 10 logarithmic scale equally spaced at a step of $h=\left(\log\omega_M-\log\omega_{-M}\right)/2M$. By using the classical midpoint rule, the PA in equation (2.37) can be calculated

$$\varphi_E(\omega)\Big|_{i=-N,\ldots,N}\simeq\frac{h}{\pi}\cdot\sum_{j=1}^{2M-1}\ln\left|\frac{10^{\log u_{j+1/2}}+10^{\log\omega_i}}{10^{\log u_{j+1/2}}-10^{\log\omega_i}}\right|\cdot\left(\frac{d\ln\left|E^*(u)\right|}{d\ln u}\right)_{u=u_{j+1/2}} \tag{2.85}$$

`

The range of the dummy variable was chosen $u \in [10^{-25}, 10^{25}]$, which was divided into 50,000 subintervals in the base 10 logarithmic scale. The computed and the analytical approximate PAs calculated from equation (2.78) are plotted in Figure 2.16(b). It was found that the difference between these values is rather small (lower than 0.7 degree). However, the relative difference is important, which may exceed 2×10^{-1} at frequencies lower than 5×10^{-8} (rad/s). At this stage, we cannot conclude whether the computed or the analytical approximate PA is more accurate because the exact values of the PAs do not exist. Thus, the LVE properties were calculated based on both the proposed method and the analytical approximation.

The storage modulus and compliance were computed then approximated by the SEFs. The number of exponential functions used was 97 for the storage modulus and 74 for the storage compliance, which allows an extremely small relative error of lower than 8×10^{-8} at all estimating points. The RM and CC were then obtained by using the closed-form formulas in equation (2.65 and 2.66) and are presented in Figure 2.14. The analytical approximate results are also presented in the figure to verify the agreement between the results obtained with the two different approaches. It was found that the relative difference between the results is rather small, lower than 2.7×10^{-2} at all estimating frequencies. Thus, the proposed algorithm allows determining reasonable values of LVE properties based only on the master curve of the DM. Furthermore, the computed RM and CC were also decomposed with high accuracy into SEFs for better computational efficiency in FEM analysis in the time domain (see also in Figure 2.14). The error of the approximation by SEFs is very small even only positive coefficients were used—namely, the relative error is lower than 3.8×10^{-5} at all estimating frequencies.

`

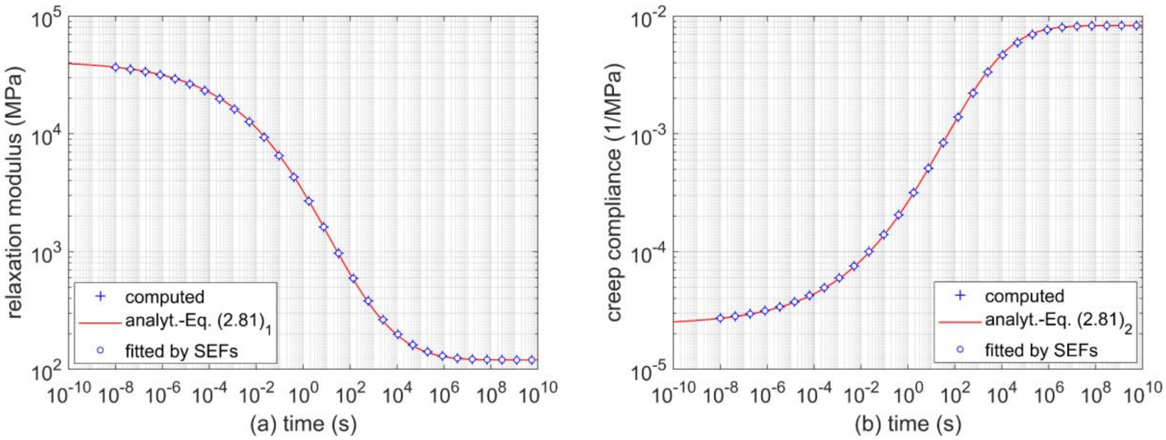

Figure 2.14. (a) Relaxation moduli computed from the GS master curve of DM and their approximations by SEFs; and (b) creep compliances computed from the GS master curve of DM and their approximations by SEFs.

In addition, the obtained RM in the form of the SEFs was used to backward compute the DM. Since the exact value of the DM is known as a priori, the accuracy of the proposed method can be verified. Because a couple of the coefficient and decay rate of the exponential functions of the RM are equivalent to the stiffness and relaxation times of one branch in the GM model, the DM can be easily interconverted from the RM. Figure 2.15 plots the dynamic moduli interconverted from the master curves of the RM against the input dynamic moduli to verify the equality. All dynamic moduli backward calculated from the relaxation moduli computed with the proposed method lie on the equality line while those interconverted from the analytical approximate relaxation moduli slightly deviate from the equality line. The relative errors between the backward calculated and the input dynamic moduli are lower than 3.4×10^{-4} when the numerical relaxation moduli were used; lower than 2.7×10^{-2} when the analytical approximate relaxation moduli were used. Thus, the proposed formulation achieves a much better level of accuracy than the analytical approximate formulation. The relative error arising

`

in the proposed algorithm is so small that it can be considered neglected and covered by the error of the process of fitting experimental data by LVE models.

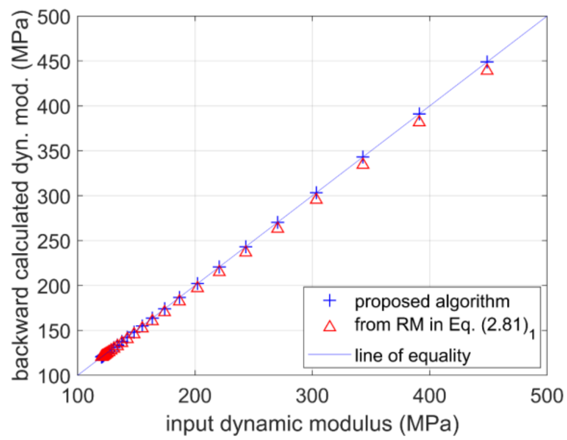

Figure 2.15. Check of equality between the input dynamic moduli and those interconverted from the relaxation modulus computed

2.2.4 Remarks

A novel method for determining with high accuracy the RM and CC of asphaltic materials in the form of SEFs based only on the master curves of DM has been successfully developed. In the formulation, the PA was numerically calculated from the DM master curve on the basis of the exact Kramers-Kronig relationships. Owing to the special form of the SEFs used for approximating with high accuracy the storage modulus and compliance, the inverse Fourier transform was analytically performed to derive the closed-form formulas of the RM and CC. Thus, the proposed formulation can be considered to fully obey the LVE theory and physical causality principle, giving rise to an excellent level of accuracy of the obtained results. The main findings of this work can be drawn as follows:

• The relative error of the PAs calculated was very small despite a rather coarse frequency step that was used, namely lower than 1.75×10^{-4} at all computing points.

`

• The maximal relative error of the approximation by SEFs using the modified Dombi algorithm was extremely small, namely lower than 8×10^{-8} when using both negative and positive coefficients, which can be considered neglected.

• The inverse Fourier transform was exactly performed to calculate the RM and CC thanks to the special form of the SEFs.

• The computed RM and CC were also approximated with high accuracy by SEFs using the modified Dombi algorithm. The maximal relative error was lower than 3.8×10^{-5} when using only positive coefficients.

The level of the overall accuracy of all computed LVE properties was dominated by that of the PA. Therefore, more accurate results can be obtained by just improving the accuracy of the numerical integration in the PA calculation step. Although the proposed algorithm for determining the RM and CC in the forms of SEFs requires more calculation steps, the obtained results are much more accurate, which will contribute to better analysis and design of asphaltic pavement, and therefore a longer service life.

2.3 Laboratory testing for determining linear viscoelastic properties.

For LVE properties of asphaltic material, they can be investigated in both the time and the frequency domain.

2.3.1 In the time domain

2.3.1.1 The relaxation test

In this test, the sample is applied to a constant VE strain ε_0, the measured stress of the sample reduces over the time (Figure 2.16).

The historical of applied deformation on the sample is defined as follows:

$$\begin{cases} \varepsilon = 0 & \text{when } t < t_0 \\ \varepsilon = \varepsilon_0 & \text{when } t \geq t_0 \end{cases}. \tag{2.86}$$

Corresponding, the measured stress in the sample is determined by:

$$\sigma = \varepsilon_0 \cdot E\left(t_0, t, \varepsilon_0\right), \tag{2.87}$$

`

where $E(t_0,t,\varepsilon_0)=0$ when $t<t_0$, and $E(t_0,t,\varepsilon_0)$ decreases over time when $t>t_0$. The function $E(t_0,t,\varepsilon_0)$ in the equation (2.87) is the relaxation modulus of LVE material.

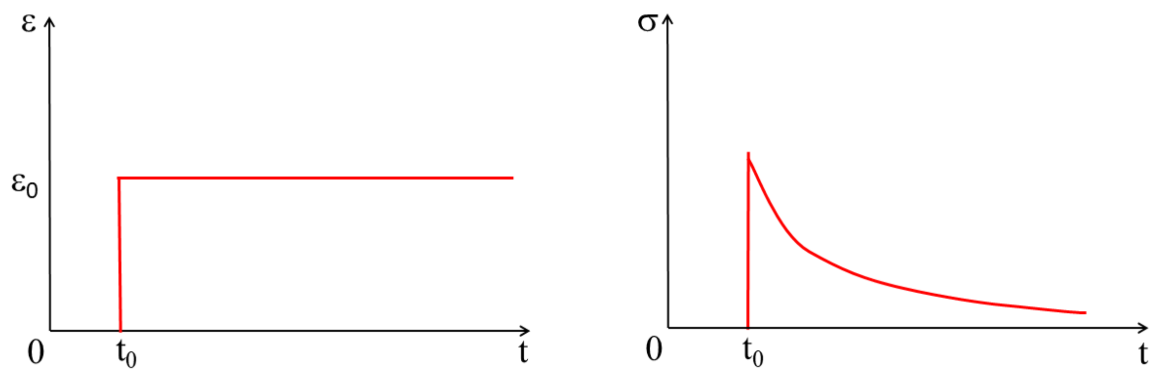

Figure 2.16. Illustration of the relaxation test

In fact, it is difficult to apply an input constant VE strain at intermediate and high temperatures for asphaltic material. The reason is the input strain creates both VE and VP strain in the sample. Therefore, directly determining RM from relaxation test at intermediate and high temperatures has a low accuracy.

2.3.1.2 Creep test

In contrast to relaxation test, the input signal in creep test is a constant stress which tents or compresses the sample. The observed strain develops over time as presented in Figure 2.17

The historical of applied stress on the sample is defined as follows:

$$\begin{cases} \sigma=0 & \text{when } t<t_0 \\ \sigma=\sigma_0 & \text{when } t\geq t_0 \end{cases}. \tag{2.88}$$

Corresponding, the measured strain in the sample is determined by:

$$\varepsilon=\sigma_0\cdot D(t_0,t,\sigma_0), \tag{2.89}$$

`

where $D(t_0,t,\sigma_0)=0$ when $t < t_0$, and $D(t_0,t,\sigma_0)=0$ increases over time when $t > t_0$. The function $D(t_0,t,\sigma_0)=0$ in the equation (2.89) is the creep compliance of LVE material.

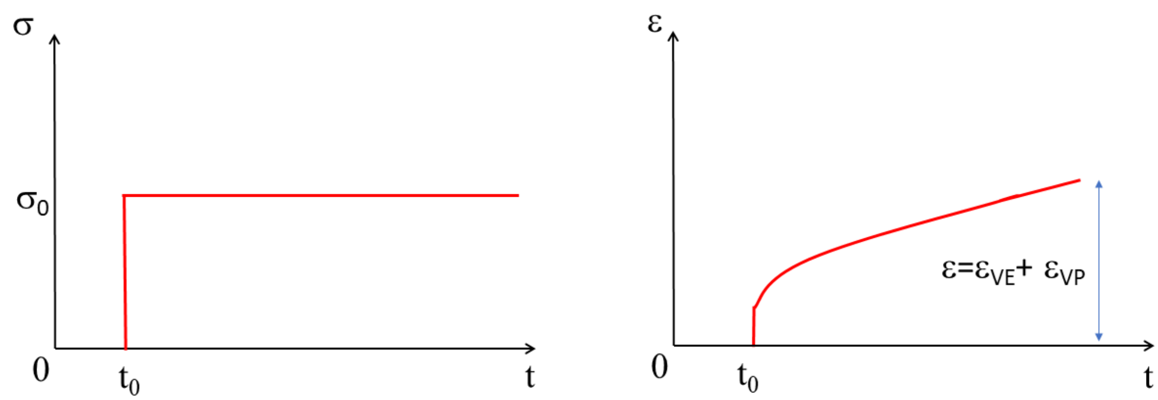

Figure 2.17. Illustration of the creep test

However, asphaltic materials are not pure LVE materials, so the measured strain at intermediate and high temperature consist of both VE and VP strain. Thus, determining the creep compliance function from measured data without eliminating the VP strain will have a large error.

2.3.1.3 Creep – Recovery test

Creep - Recovery test consists of two phases: a loading period and an unloading one as displayed in Figure 2.18. In the loading period, materials show both VE and VP characteristics meanwhile in the unloading time, only VE properties are displayed. Therefore, we can determine the VE properties of material based on the unloading period.

Plenty of algorithms were proposed to determine the LVE properties by researchers (Daver et al., 2016; Fancey, 2005; Goli et al., 2019; Liu and You, 2009, Saboo and Kumar, 2015). However, in this subsection, the algorithm which proposed by

`

Nguyen et al. (2021) is presented because that algorithm can determine the CCs of asphaltic material at intermediate and high temperatures with high accuracy.

The hypothesis of that algorithm is the measured strain in loading period consists of reversible strain ε_{ve} and permanent strain ε_{vp}. Thus, the strain at time $t_0 < t \le t_L$ is determined as follows:

$$\varepsilon(t) = \varepsilon_{ve}(t) + \varepsilon_{vp}(t), \tag{2.90}$$

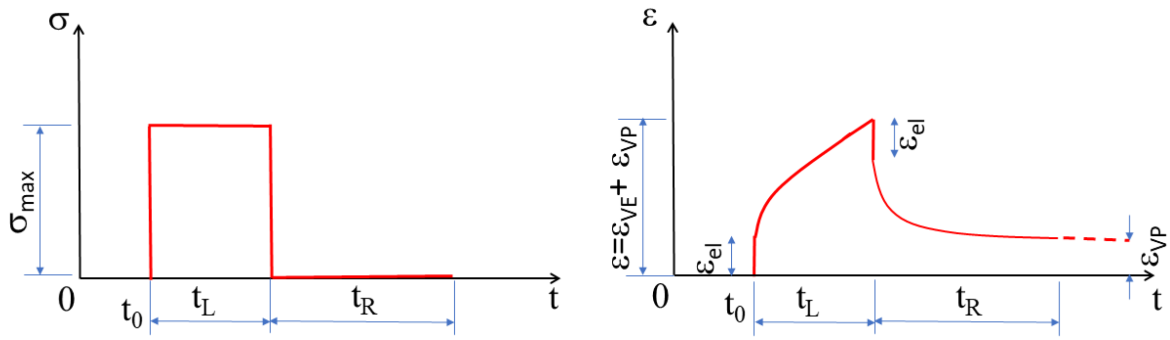

Figure 2.18. Illustration of the creep – recovery test

In unloading period, because the applied stress on the sample equal to zeros, so the accumulated permanent strain in the sample is unchanged.

$$\varepsilon_{vp}(t) = \varepsilon_{vp}(t_0 + t_L) \quad \text{when } t \ge t_0 + t_L. \tag{2.91}$$

Then, the total strain measured during the unloading time can be calculated as:

$$\varepsilon(t) = \varepsilon_{ve}(t) + \varepsilon_{vp} \quad \text{when } t \ge t_0 + t_L. \tag{2.92}$$

Besides, one can displays the maximum strain of the sample during testing by equation (2.93)

$$\varepsilon_{\max} = \varepsilon_{ve}(t_0 + t_L) + \varepsilon_{vp}. \tag{2.93}$$

By substituting both sides of the equation (2.92) and (2.93), the equation (2.94) can be obtained which eliminated the permanent strain.

$$\varepsilon_{\max} - \varepsilon(t) = \varepsilon_{ve}(t_0 + t_L) + \varepsilon_{ve}(t) \quad \text{when } t \ge t_0 + t_L. \tag{2.94}$$

In case the linear viscoelastic behavior of material is still held, the Boltzmann principle can be applied. Then, the historical of applied load on sample is divided into two phases as follows:

`

$$\begin{cases} \sigma(t) = \sigma_L(t), & \text{when } t_0 < t < t_0 + t_L \\ \sigma(t) = \sigma_L(t) + \sigma_R(t), & \text{when } t \geq t_0 + t_L \end{cases}, \quad (2.95)$$

where $\sigma_L(t) = +\sigma_{\max}$ when $t \geq t_0$ and $\sigma_R(t) = -\sigma_{\max}$ when $t \geq t_0 + t_L$.

Applying the relation of stress - strain equation with a Heaviside input function, one can obtain

$$\begin{cases} \varepsilon_{ve}(t) = D(t) \cdot \sigma_{\max}, & \text{when } t_0 < t < t_0 + t_L \\ \varepsilon_{ve}(t) = D(t) \cdot \sigma_{\max} - D(t - t_0 - t_L) \cdot \sigma_{\max}, & \text{when } t \geq t_0 + t_L \end{cases}. \quad (2.96)$$

Replacing the equation (2.96) into the equation (2.94), the obtained result is an equation of CCs function which determines based on the input stress and measured strain.

$$\frac{\varepsilon_{\max} - \varepsilon(t)}{\sigma_{\max}} = D(t_0 + t_L) - D(t) + D(t - t_0 - t_L) \quad \text{when } t \geq t_0 + t_L. \quad (2.97)$$

If the form of CCs function is known, the equation (2.97) can be solved by optimizing algorithms.

2.3.2 In the frequency domain

The dynamic modulus test is the widely used test to determine LVE properties in the frequency domain because of its stabilization and simplicity. The input signal of that test is a harmonic stress which is applied to the sample at different frequencies and temperatures (Figure 2.19).

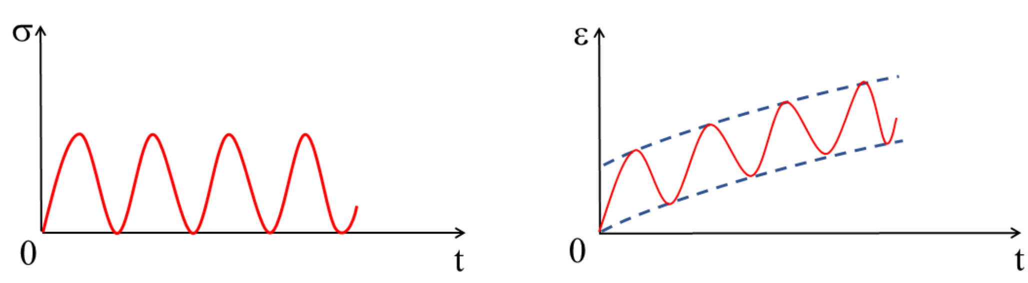

Figure 2.19. Illustration of the dynamic modulus test

`

Applied stress and measured strain of sample over time are used to calculate the dynamic moduli and phase angle by an algorithm presented in AASHTO – T342 – 11 (2011). Then, the value of dynamic moduli in range of temperatures and frequencies will be shifted to construct a master curve which represents LVE properties of asphaltic materials in the frequency domain.

2.4 Laboratory testing for determining permanent deformation

This subsection presents testing methods to investigate permanent deformation of asphaltic material.

2.4.1 Hamburg wheel tracking test

The Hamburg wheel tracking test is widely used for evaluating the resistance of asphaltic material by measuring the permanent deformation under the action of repeated wheel load at a constant temperature. The testing samples are rectangular slabs with dimensions 320 mm × 260 mm × 60 mm. The constant temperature is maintained by air conditioning or water bath. Load applies to samples by a rolling rubber wheel of 200 mm in diameter and 51 mm in width. Because the total vertical load is 710N and the contact area is 51 mm × 20 mm, the contact pressure can be calculated and equal to 0.7 MPa. The permanent deformation of samples at contact area is automatically measured and recorded after every load pass. Loading and unloading period of HWT test is displayed in Figure 2.20

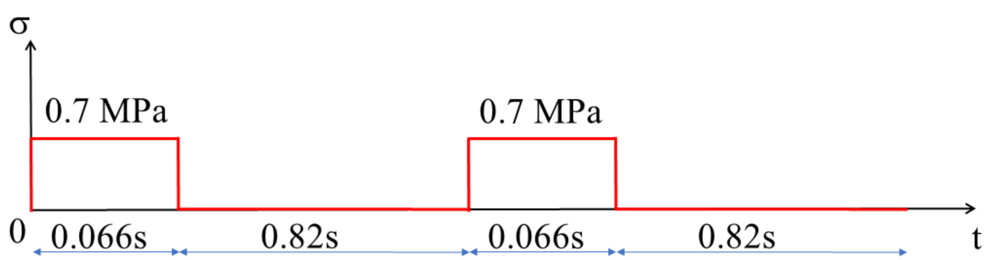

Figure 2.20. Simulating the effect of wheel load in HWT test.

`

2.4.2 ***Repeated load permanent deformation test***

Another approach to determine the properties of irreversible strain of asphalt mixture is using RLPD tests. Those tests are performed on several thousand loading cycles which consist of a haversine load followed by a resting period. The stress levels and temperatures are freely chosen by users based on the investigation purpose. Those tests can be conducted in confinement or unconfinement conditions. The cumulative permanent deformation at the end of each loading cycle is recorded as a function of the cyclic number over the test period. The input stress and response strain of the RLDP test is illustrated in Figure 2.21

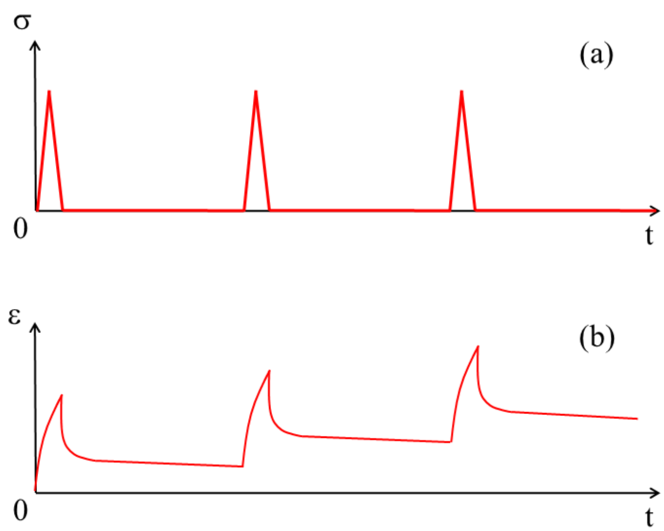

Figure 2.21. Description of RLPD test. (a) Input stress, (b) response strain.

2.4.3 Generalized Creep – Recovery test

2.4.3.1 Developing method

Assuming that the condition of the sample is under zero-strain and zero-stress at the beginning of the test. It means that,

$$\begin{cases} \sigma(t) = 0 \\ \varepsilon(t) = 0 \end{cases} \quad \text{when } t \le 0. \tag{2.98}$$

`

Then, at the time $t_{i-1} < t < t_i$ with $t_i = t_0 + \sum_{j=1}^{i} t_{L,j}$, $i \in \{1,...,n\}$, the sample is applied a step stress function $\sigma(t) = \sigma_i$. In the loading period (from t_0 to t_n), the stress applies on the sample has n steps which n is a freely chosen parameter. The time interval from t_n to $t_n + t_{uL}$ is denoted as recovery period where the applied stress on the sample equals to zero, $\sigma(t) = 0$ for $t > t_n$. Figure 2.14 illustrates a GCR test.

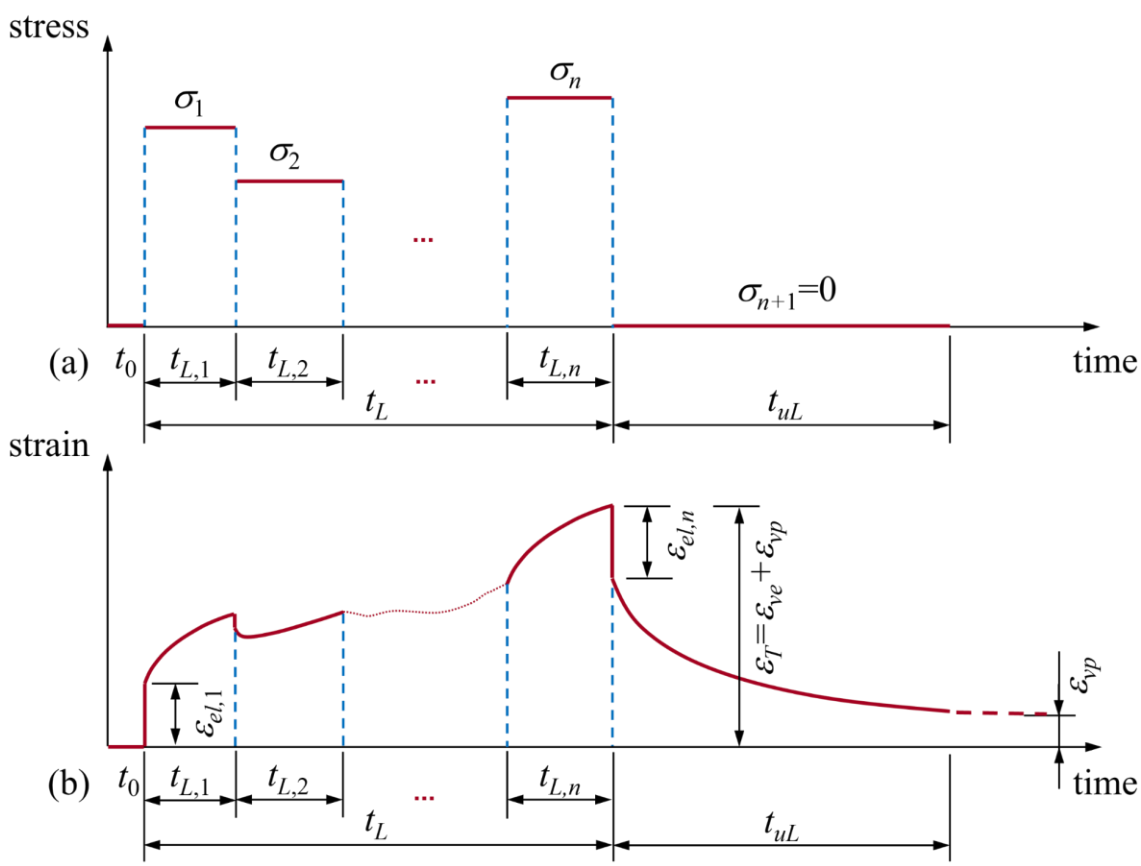

Figure 2.22. Description of the GCR test, (a) applied stress history, (b) response strain (Tran et al., 2022).

The VP strain occurs and increases even at a low temperature and stress level (Nguyen et al., 2021). Therefore, the measured strain of testing consists of VE and VP strain as equation (2.90). If the increment of the stress input at a time t_i is defined as

`

$\Delta\sigma_i = \sigma_{i+1} - \sigma_i$ with $i \in (0, n-1)$ and the Boltzmann superposition can be applied, the VE strain can be calculated as follows:

$$\varepsilon_{ve}(t) = \sum_{i=0}^{m, t_m < t \le t_{m+1}} D(t - t_i)\Delta\sigma_i, \text{ for } t_0 < t \le t_n, \tag{2.99}$$

$$\varepsilon_{ve}(t) = \sum_{i=0}^{n-1} D(t - t_i)\Delta\sigma_i - D(t - t_n).\sigma_n, \text{ for } t > t_n. \tag{2.100}$$

In the unloading period, VP strain is considered to not develop because the applied stress in that period equal to zero. It means that the value of VP strain is a constant from t_n to $t_n + t_{uL}$ and denote ε_{vp},

$$\varepsilon_{vp}(t) = \varepsilon_{vp}(t_n) = \varepsilon_{vp}, \text{ for } t \ge t_n. \tag{2.101}$$

Thus, the total strain is measured at time t in the unloading period can be displayed by a sum of $\varepsilon_{ve}(t)$ and ε_{vp},

$$\varepsilon_T(t) = \varepsilon_{ve}(t) + \varepsilon_{vp}, \text{ for } t \ge t_n. \tag{2.102}$$

Besides, the total strain at time t_n can be expressed by:

$$\varepsilon_T(t_n) = \varepsilon_{ve}(t_n) + \varepsilon_{vp}. \tag{2.103}$$

Eliminating ε_{vp} in two equation (2.102) and (2.103) by subtracting respectively two members of them, the equation (2.104) can be obtained:

$$\varepsilon_T(t_n) - \varepsilon_T(t) = \varepsilon_{ve}(t_n) + \varepsilon_{ve}(t), \text{ for } t \ge t_n. \tag{2.104}$$

Substituting equation (2.99) and (2.100) into equation (2.104), an equation just comprises the measured strain in the left member and CC function, the prescribed stress, in the right member.

$$\frac{\varepsilon_T(t_n) - \varepsilon_T(t)}{\sigma_n} = \sum_{i=0}^{n-1} D(t_n - t_i)\frac{\Delta\sigma_i}{\sigma_n} - \sum_{i=0}^{n-1} D(t - t_i)\frac{\Delta\sigma_i}{\sigma_n} + D(t - t_n), \text{ for } t \ge t_n. \tag{2.105}$$

Obviously, the left-hand side of the equation (2.105) can be easily calculated from the data of test while the number of increment stress and stress level can be chosen, so the unknown of that equation is just the CC function $D(t)$. If the form of the CC function is known the equation (2.105) can be solved by using optimization techniques. Once the

`

functional equation has been solved, the CC function can be determined. It means that the VE strain at time t can be calculated using equation (2.99) and (2.100). Thus, VP strain at that time is also computed by subtracting the total strain by the VE strain.

$$\varepsilon_{vp}(t) = \varepsilon_T(t) - \varepsilon_{ve}(t). \quad (2.106)$$

The analytical approximate CC (AACC) function derives from HS and 2S2P1D model can be used as the form of the CC function for solving the equation (2.105) (Nguyen et al., 2021).

2.4.3.2 Validation method

a. Material and sample preparation

A highly modified bitumen of PG 94 was used for preparing the high modulus mixture (HiMA). The PG 64 bitumen was modified with approximately 2% (in total weight) of styrene-butadiene-styrene (SBS) and a suitable amount of high modulus additive to obtain that bitumen. Aggregate was collected from quarries in the South of Vietnam. Its fundamental engineering characteristics were presented in Table 2.2.

Table 2.2: Fundamental properties of aggregate in this research.

Properties	Results	Limitations
Los Angeles abrasion (%)	12.3	Max 30
Flat and elongated particles (%)	≤ 6	Max 10
Water absorption (%)	1.41	Max 2
Specific gravity of coarse aggregate	2.77	-
Specific gravity of fine aggregate	2.78	-
Specific gravity of filler	2.73	-

The nominal aggregate of maximum particle size of 12.5 mm widely used in Vietnam was chosen for preparing the mixture samples. Based on the specific TCVN 13567-1(2022), the gradation curve is designed as that in (Nguyen et al., 2021a) and is shown in Figure 2.23.

`

To prepare samples for tests, the aggregate and bitumen were mixed and compacted by a roller sector compactor at 175°C to obtain a 0.32x0.26x0.08m^3 plate of mixture. After cooling down to room temperature, the plates were sawed into three prismatic samples per mixture with dimensions: 0.07x0.07x 0.15m^3.

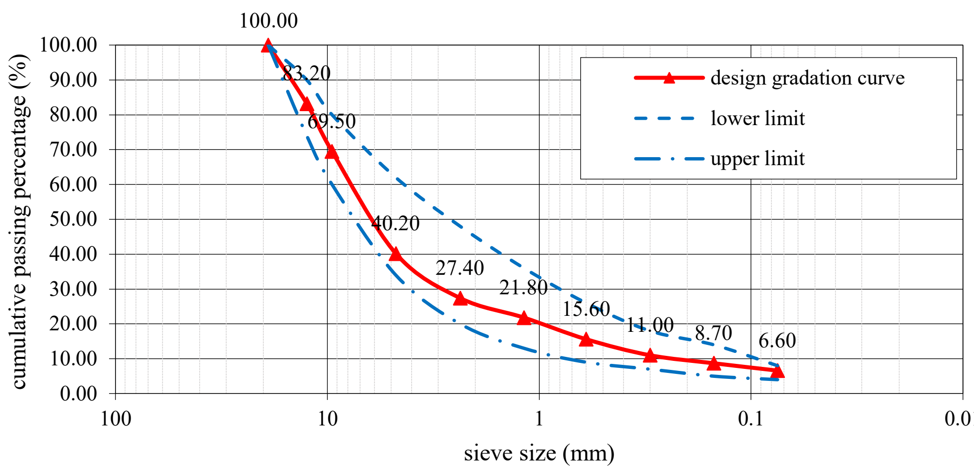

Figure 2.23. Design gradation curve used for preparing mixture

The fundamental properties of HiMA mixture are reported in Table 2.3.

Table 2.3: Fundamental properties of HiMA mixture

Engineering properties	Standards	Results
Optimum asphalt content (%)		5.0
Maximum specific gravity	ASTM D2041	2.51
Bulk specific gravity	ASTM D2726	2.36
Air void (%)	ASTM D3203	5.98
Void in aggregate (%)		15.77
Marshall stability (kN)	ASTM D6927	19.00
Marshall flow (mm)	ASTM D6927	3.10
Indirect tensile strength at 25˚C (IDTS) (MPa)	ASTM D6931	1.97

`

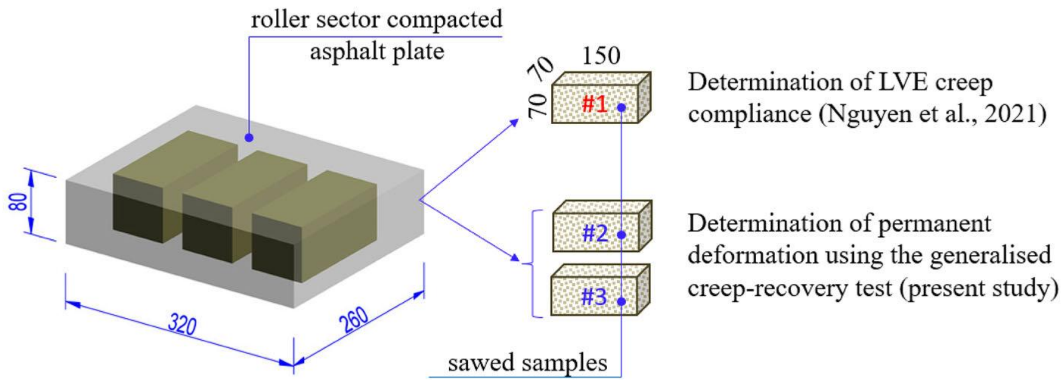

Figure 2.24. Samples preparation for the CR test studied in Nguyen et al. (2021) and for the GCR tests performed in the present research

b. Test set up

The sample was applied a controlled compressive force based on driving a lower load platen and fixing an upper one (see Figure 2.25). The relative displacement between two fixture points along to the height of sample (85mm distance) was measured by two displacement transducers. The sample was placed into a thermal chamber for maintaining temperature as constant during the test.

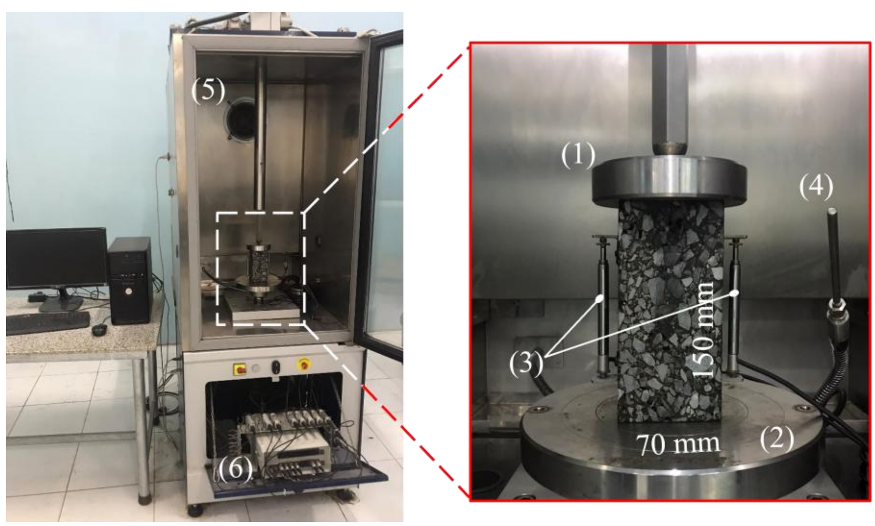

Figure 2.25. Test set-up for the GCR test: (1) Upper load platen, (2) Lower load platen, (3) Displacement transducer, (4) Control temperature sensor, (5) Thermal chamber, (6) Control and Data Acquisition System.

`

c. Experimental result

In this subsection, the GCR test results which were conducted with different number of loading intervals, loading time period or the stress levels were displayed to demonstrate the efficiency of the proposed method in characterizing simultaneously the VE and VP strain at a high temperature. The chosen temperature is 50°C because the unloading time for the specimen can recover all reversible strain is not too long at that temperature so that the test can finish within a working day and that the properties of the sample do not change much due to the cumulative permanent strain.

A single-stress level creep-recovery (SSCR) test, an increasing multi-stress level creep-recovery (MSCR) test, and a decreasing one are three conducted test derivatives. It is careful to choose the applied stress for those tests to ensure the relationship between stress and the VE strain is still linear. Thus, the chosen stress does not exceed 35.71 kPa or such that the resultant VE strain was lower than 170μm/m.

The testing program of this work is summarized in Table 2.4. The three protocols – SSCR, increasing MSCR, and decreasing MSCR – are described in detail in Subsections (i) and (ii).

Table 2.4: Summary of experimental testing program.

Test No.	Sample	Type of test	Duration of loading time (s)	Stress (kPa)	Purpose
1	2	SSCR	75	35.71	Verify the accuracy and repeatability of the obtained results
2			150		
3			300		
4			600		
5			600	23.81	Check of linearity and effect of stress level on the VP strain
6			600	11.90	
7	3	MSCR (increasing)	5 times x 100s	$5\sigma_0$ = 40.82kPa	Analyze the pure permanent deformation (PD) of the mixture when exerted by more complicated stress histories
8		MSCR (decreasing)			
9		MSCR (increasing)			
10		MSCR (decreasing)			
11		MSCR (increasing)			
12		MSCR (decreasing)			

`

It is worth noting that before performing the official tests, all specimens were conducted with three SSCR tests with a 600-s loading period for elimination the effect of post-compaction. Furthermore, the time interval between two tests should be not less than 24 hours for all resilient deformation which caused by previous test in samples can recover. Before starting each test procedure, the specimen was left in the thermal chamber for 4 hours to maintain a homogenous temperature field.

i. Single-stress level creep-recovery test (SSCR)

The results obtained from test #1 to test #4 were reported in this subsection. It is worth noting that the measured strains at the end of unloading period which is far enough for the reversible strain developed in the loading phase can most completely recover were considered 'true permanent strain' in the specimen. It leads to the variety of resting time between tests having different loading time. However, only the data acquired over a period equal to 11 times the loading time (i.e. the resting time is 10 times the loading time) were used to back-calculated for comparable results to each other. With such a ratio of loading and unloading time, obtained results have a good accuracy as will be displayed in the following paragraphs.

The result of fitting by the function described in the equation (2.105) to the measured recovery compliance in case loading time equal to 300s is good as presented in Figure 2.26(a). It can be easily seen in Figure 2.26(b) that the corresponding CCs determined with the best-fit parameters (conducted on specimen #2) and those interconverted from the complex modulus data already determined with specimen #1 in Nguyen et al. (2021) are well agreement together. The RD between these CC curves actually do not exceed 5.36%. In contrast, it can be observed in Figure 2.26(b) that the back – calculated CCs are much lower than the CCs computed from creep test data. It means that there are irreversible strains formed during the loading time as reported in Nguyen et al. (2021). It should be noted that the results in Nguyen et al. (2021) are not

`

part of this dissertation, they are used solely for comparison with the results obtained in this subsection.

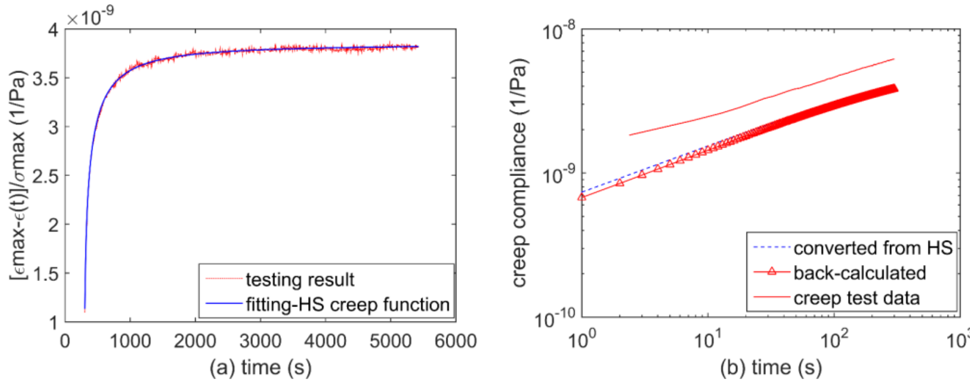

Figure 2.26. Results of the SSCR test at 50°C and t_L = 300 s, (a) Fitting results of the recovery compliance, (b) Back-calculated CC.

After determining the CC of the mixture, the VE strain can be predicted at the testing temperature and input stress level. Figure 2.27(a) showed the predicted VE strain and the measured strain in case $t_L = 300\text{s}$. It can be seen that the measured strain is larger than the VE one. The reason for this difference is the development of viscous plastic strain which is presented in Figure 2.27(b). In the loading phase, the VP strain developed at the decreasing rate and reached a value of 85.5 μm/m at the end of that phase. During a resting period, the value of the VP strain had almost no change as expected. With the maximal value of the measured strain equal to 226.13 μm/m, it can indicate that VP strain accounts for a fairly large portion of the total strain, reaches to 37.81%.

To ensure reliability of the obtained results, the back-calculated CCs based on the present algorithm were compared with the interconverted CC which was determined from complex modulus data. Figure 2.28(a) showed that both of those CCs curves agree well together. In fact, the relative differences between them do not exceed 7.47%. Moreover, the highest value of relative differences between each curve of the back-calculated CCs and the average curve of them is just 6.68%.

`

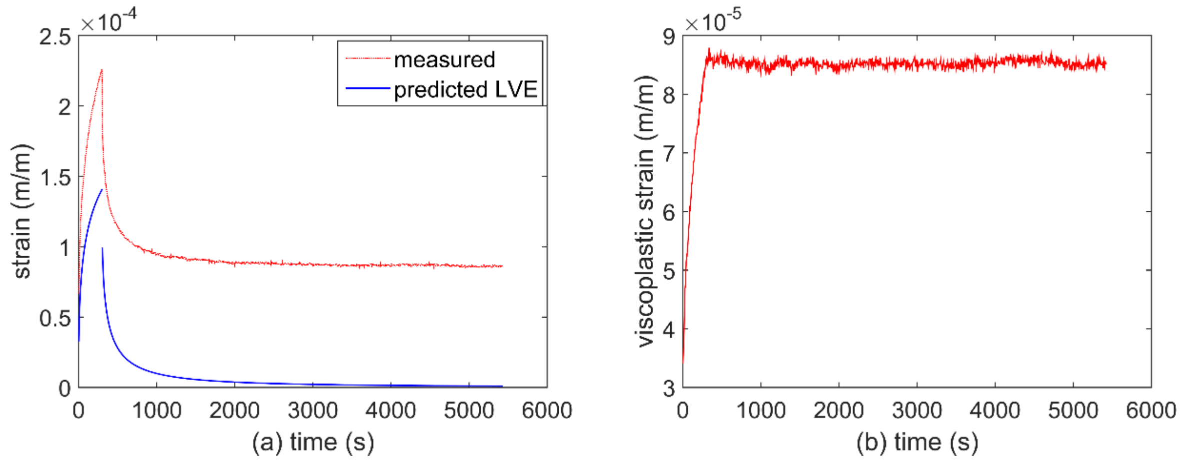

Figure 2.27. Results of the SSCR test at 50°C and $t_L = 300\mathrm{s}$, (a) Predicted VE and measured strain, (b) Computed VP strain with time.

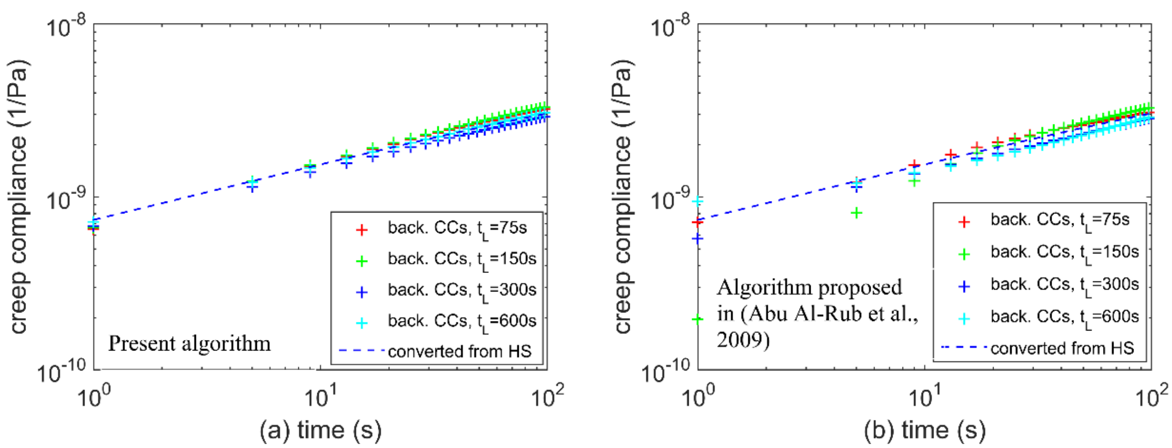

Figure 2.28. Back-calculated CCs from all test replicates at 50°C, (a) using the AACC function, (b) using the CC function in the form of a Prony series.

In this occasion, CCs computed with the algorithm of Abu Al-Rub et al. (2009) were displayed in Figure 2.28(b) to evaluate the accuracy of present algorithm. It can be seen that the algorithm of Abu Al-Rub et al. (2009) led to a lack of accuracy and repeatability of the obtained CCs, especially at small loading times (< 10s). Indeed, the overall relative errors and relative discrepancy of those CCs curves respectively 68% and 59.9% which is far higher than those obtained with the present algorithm. It means that the present algorithm determines the back-calculated CCs with more accuracy than

`

Abu Al-Rub et al. (2009)'s algorithm. This leads to values of VP strains calculated with present algorithm also more accurate than those computed with Abu Al-Rub et al. (2009)'s algorithm as shown in Figure 2.29.

Table 2.5: Assessment of the accuracy of the computed VP strains.

Loading time (s)	VP strain at time t_n		
	calculated (μm/m)	measured (μm/m)	Error (%)
Present algorithm			
75	51.94	53.82	3.49
150	70.15	70.49	0.48
300	85.72	84.29	1.69
600	119.82	119.49	0.28
Algorithm proposed in Abu Al-Rud et al. (2009)			
75	55.73	53.82	3.55
150	68.60	70.49	2.68
300	86.16	84.29	2.22
600	119.87	119.49	0.32

The results of calculated the relative errors and the standard deviation of the obtained VP strains with the present algorithm and the algorithm of Abu Al-Rub et al. (2009) were respectively presented in Tables 2.5 and 2.6. It is obvious that the relative errors of the VP strains obtained with the present algorithm (lower than 3.49%) are smaller than that one obtained with the algorithm presented in (Abu Al-Rub et al., 2009) (lower than 3.55%) and similarly for the case of the standard deviations of those algorithms (2.84 μm/m versus 4.20 μm/m). Thus, the proposed algorithm has significantly improved the reliability and performance than the algorithm in (Abu Al-Rub et al., 2009). In subsequent paragraphs, only the results obtained with the present formulation will be shown for the sake of brevity.

Table 2.6: Assessment of the repeatability of the computed VP strains.

	Computed VP strain (μm/m)					
	Test replicate number					
At time (s)	# 1	# 2	# 3	# 4	Mean	SD
Present algorithm						
10	31.85	33.37	37.33	28.48	32.76	2.84
75	51.94	55.79	57.03	54.43	54.80	1.69
150	-	70.15	70.22	70.32	70.23	0.06
300	-	-	85.72	91.12	88.42	2.20
600	-	-	-	119.82	-	-
Algorithm proposed in Abu Al-Rud et al. (2009)						
10	30.70	43.11	38.26	33.73	36.45	4.20
75	55.73	57.36	59.91	54.00	56.75	1.95
150	-	68.60	70.89	74.13	71.21	1.97
300	-	-	86.16	91.98	89.07	2.38
600	-	-	-	119.87	-	-

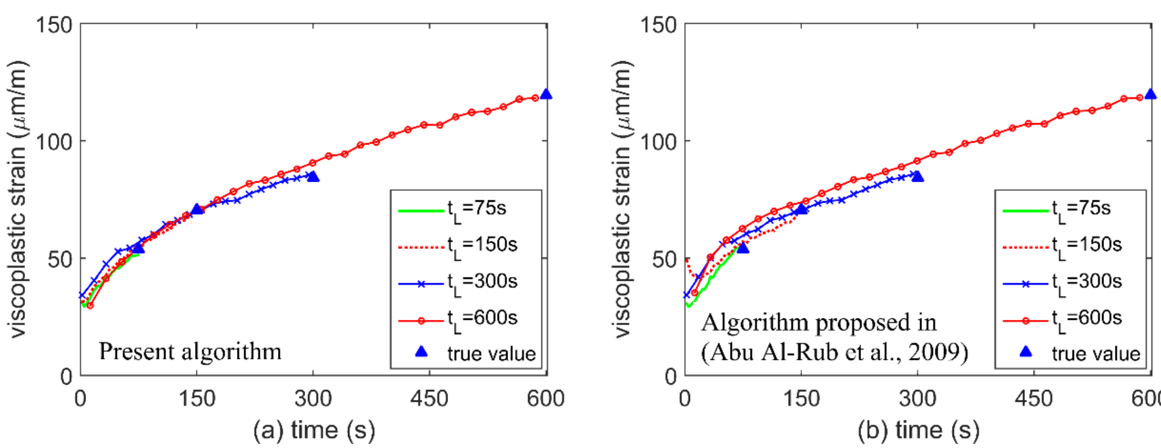

Figure 2.29. Pure VP strains obtained from all SSCR test replicates at 50°C, (a) using the AACC function, (b) using the CC function in the form of a Prony series.

`

Effect of resting time on the accuracy of VP strain

In this subsection, accuracy of the obtained VP strain with various resting time was surveyed to determine the needed time for testing which is best efficiency. For that purpose, a set of data of SSCR was created by truncating the data of SSCR test with unloading time equal to ranging from 1 to 10 times the loading time, as illustrated in Figure 2.30. Based on that set of data, the back-calculated VP strains were computed and compared to the 'true values' of the permanent strains directly measured at the end of the loading period. Therefore, the relative errors of the back-calculated and "true" VP strains were computed at time $t = t_L$.

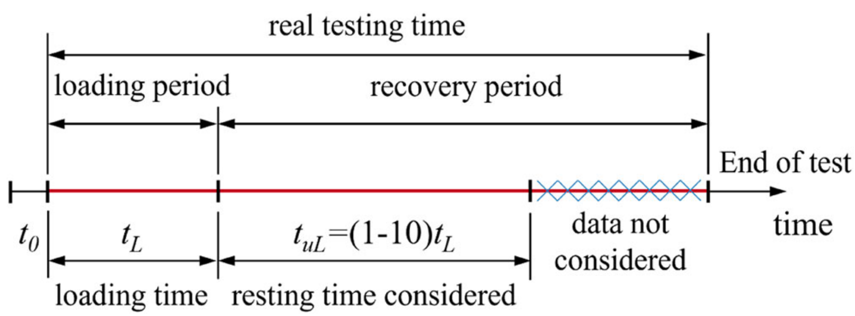

Figure 2.30. Illustration of constructing the truncated data used for the back-calculation algorithm

With directly measured VP strains, errors still in a steady decline even though the unloading time had reached 10 times the loading time. In contrast, when the ratio of unloading and loading time was increased from 1 to 5, the error of the back-calculated VP strains rapidly decreased. However, the accuracy almost was not improved with a longer resting time than that value (see Figure 2.31). Thus, with this proposed method, the best efficiency resting time is 5 times of the loading one. In fact, with ratio of resting time and loading time equal to 5, the difference between the back-calculated VP strains and the true value do not exceed 1.44%, not included case of the test with time loading is 75s. In a short loading time test, the accuracy of results was more affected by a

`

suddenly applied or removed of the stress which cause inertial effects. Despite that, the errors of obtained VP strains of that test is still lower 4.03%.

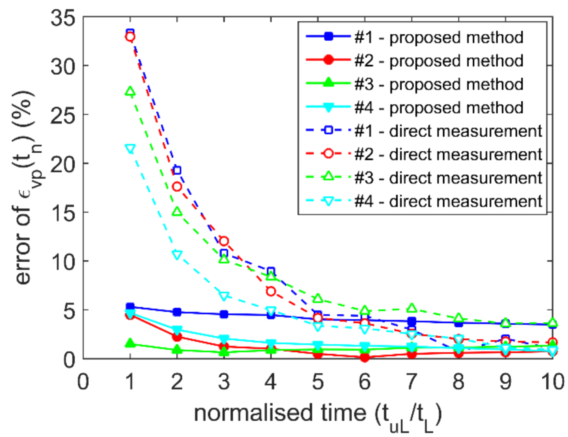

Figure 2.31. Effect of the resting time on the accuracy of VP strains obtained from all SSCR test replicates at 50°C.

It can be seen in Figure 2.31 that the proposed algorithm performs better than the direct measurements. For instance, in the case unloading time equal to loading time, the error of directly measured VP strain exceeds 21.6% whereas VP strain determined based on the present algorithm with the same data has a difference lower than 5.3% the exact value. In fact, with the short resting time, the strain measured at the end of unloading period comprised the pure VP strain and a part of VE strain has not recovered yet which led to large error of the directly measured VP strain. If the expected error for the directly measured VP strain is approximately 3%, the ratio of unloading and loading time must be larger than 7 times. Meanwhile, for achieving the same level of accuracy, the proposed algorithm just needs the resting period equal to 2 – 3 times of the loading one. Therefore, the proposed algorithm requires a shorter resting period than the direct measurement method to achieve the same level of accuracy, and the reasonable resting time for a SSCR test at 50°C ranges from 2–5 times the loading time.

Check of linearity and effect of stress level on the VP strain

`

As presented in Table 2.4, two SSCR tests were conducted on sample #2 with stress levels equal to 11.90 kPa (one-third of 35.71 kPa) and 23.81kPa (two-thirds of 35.71 kPa) respectively to check of linearity. The VE strains of all studied stress level in loading period were predicted and displayed in Figure 2.32. For checking the linearity, the predicted VE strain with stress level 35.71 kPa were divided by 3 and the predicted VE strain with stress level 23.81kPa were multiplied with one-half and all are presented in the figure.

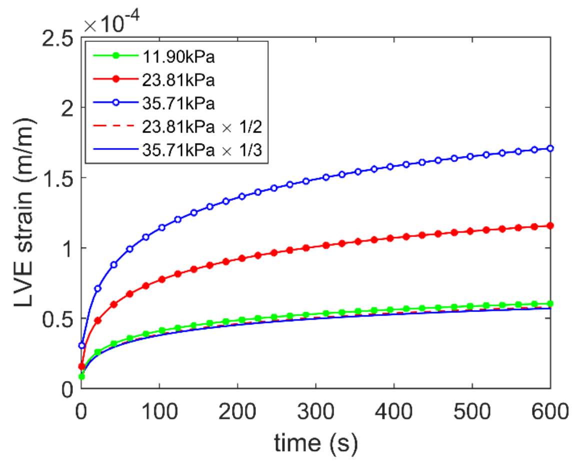

Figure 2.32. Check of linearity for VE strains at 50°C.

Figure 2.32 shows that all the scaled VE strains (i.e. by a factor of 1, 1/2, and 1/3) have a good agreement together. In fact, all scaled VE strain differ to the average VE strain do not exceed 3.95%. Therefore, it can be considered that the stress - VE strain relationship still holds the linearity at 50°C and a stress level of up to 35.71kPa or a VE strain level of up to 170µm/m. It means that the obtained results based on the proposed algorithm have a consistency with the assumption made and therefore reliable.

In this subsection, the development of VP strain in an SSCR test with various stress level was also considered. It is observed that a higher permanent in the specimen caused by a higher stress level and vice versa [see Figure 2.33(a)]. Furthermore, there is likely linearity between the increasing of the VP strain and the stress level ranging from 11.90 to 35.71 kPa [see Figure 2.33(b)].

`

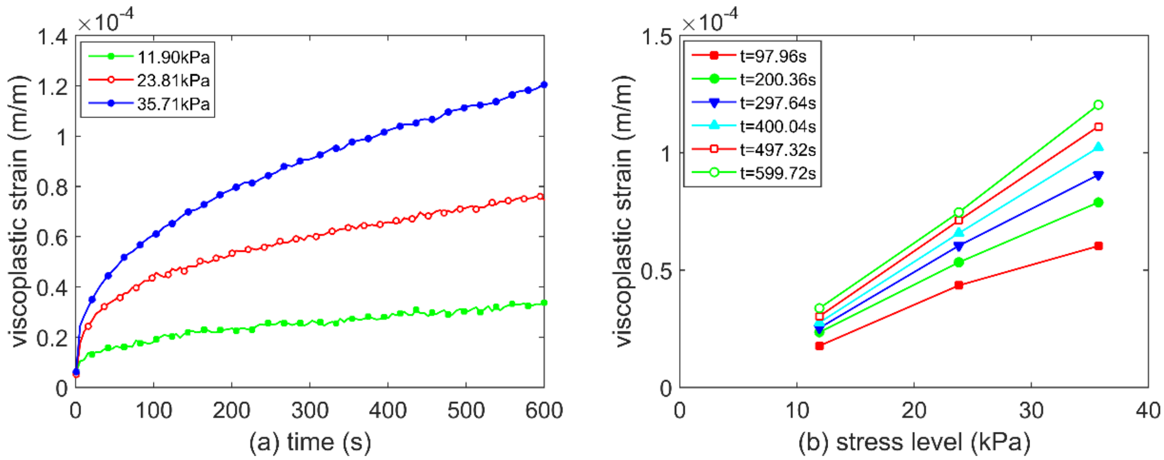

Figure 2.33. Effect of the stress level on the VP strain determined with the proposed method at 50°C.

ii. Multi-stress level creep-recovery test (MSCR)

In this subsection, ascending and descending order of a loading period of five equal time steps were investigated for verification of the performance of GCR test in handling with a complex loading history as displayed in Figures 2.34(a,b). The conducted sample, applied stress level, loading period, and order of test are presented in Table 2.4. The maximal stress equal to $5\sigma_0$ = 40.82kPa was chosen to ensure that the behavior of stress-VE strain relationship still holds linearity. Tests with two loading modes were alternately performed to reduce the influence of VP strains accumulation on the specimen behavior. One step time of loading period last 100s, and data of test was recorded to first 3000s for back-calculation VP strains then the specimen was continuously left to completely recover the VE strain for measuring the 'true value' of the VP strain in the specimen.

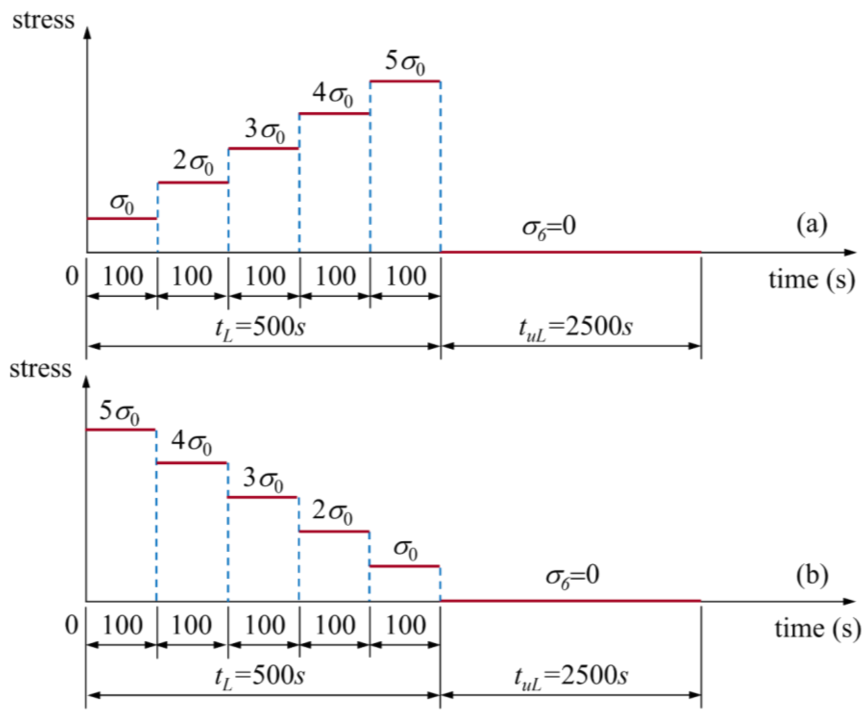

Figure 2.34. Loading patterns in (a) the increasing MSCR test and (b) decreasing MSCR test (not drawn to scale).

Increasing multi-stress level creep-recovery test

The strain directly measured, and the correspondent VE strain predicted with proposed algorithm of the test #7 (the first of MSCR test) were shown in Figure 2.35(a). Evolution trend of the measured strain and the predicted VE strain have same shape – namely, both of them have a steady increasement of their value during the loading time and then recovered during the resting period. As can be seen in Figure 2.35(b), the VP strain increases in the loading phase with a nearly constant rate and shows almost no change during the unloading period, as expected. The predicted VP strain in the test #7 can be calculated by the piece-wise linear function: $\varepsilon_{vp} = 1.81\times10^{-7} t + 4.09\times10^{-6}$ for $t \le 500\text{s}$, and $\varepsilon_{vp} = 9.31\times10^{-5}$ for $t > 500\text{s}$ with a high R^2.

`

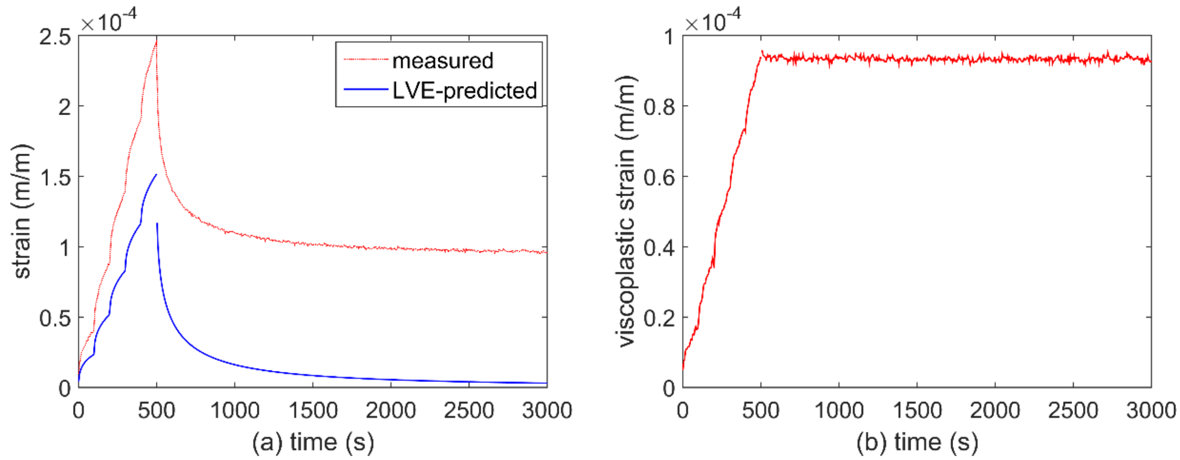

Figure 2.35. Results of increasing MSCR test replicate #1 at 50°C, (a) Predicted VE and measured strains, (b) Computed VP strain with time.

For evaluating the reliability of obtained result based on the proposed method, comparison of the back-calculated CCs and the CCs interconverted from DM data were performed. Those curves of back-calculated CCs were shown in Figure 2.36(a) and show a good agreement with each other. In fact, the maximum RD value between any CC curve and the average curve is lower than 7.19%. It means that the prediction of VE strains has a good accordance together [see Figure 2.36(b)]. According to the accuracy, the relative differences between the average curve of the back-calculated CCs and the interconverted CCs of sample #1 is approximately 17.04%, a rather large difference but is still accepted in pavement engineering because that value of RD includes the inter-sample variations.

As can be seen in Figure 2.36(b) that the VE strains have a decline after each test so there has some influence of test order on the VE characters of the mixture to the extent that the mixture may gain extra stiffness. The explanation of that is a getting closer and closer of the aggregate due to the increase of permanent contraction strain. That leads to the enhancement of interlock between the aggregate particles which increases the hardening of mixture. With the VE strain of all test replicates lower than 170 µm/m, it

`

can be ensured that the stress-VE strain relationship in the specimen was still hold in the linearity domain.

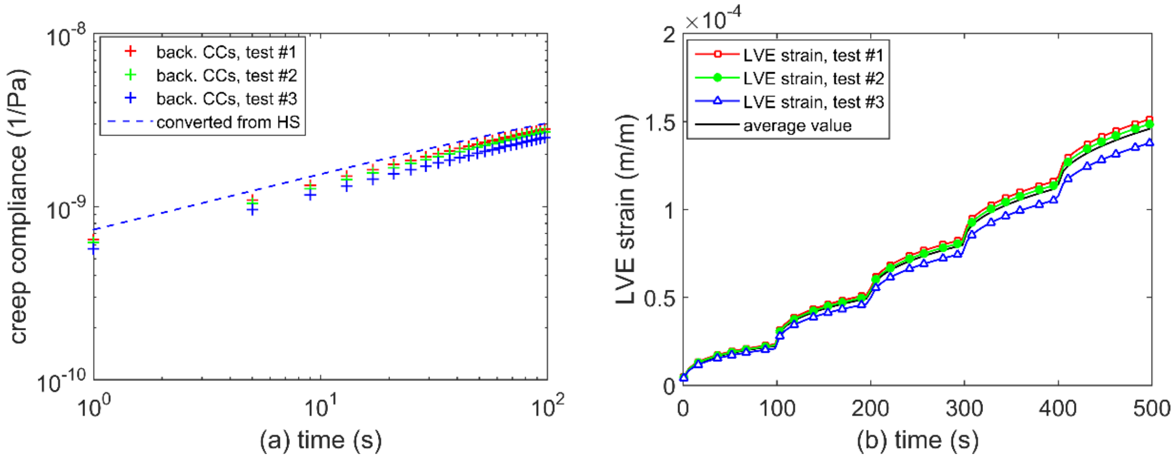

Figure 2.36. Back-calculation results of all decreasing MSCR test replicates at 50°C, (a) back-calculated CCs, (b) Predicted VE strains.

After eliminating the VE strains from the measured strains, the VP strains of all increasing MSCR test replicates were obtained and presented in Figure 2.37. The development of VP strains in test replicates #2 and #3 can also be predicted with high R^2 values by the linear functions: $\varepsilon_{vp}^{2} = 1.66\times10^{-7}t + 6.06\times10^{-6}$; $\varepsilon_{vp}^{2} = 1.52\times10^{-7}t + 2.40\times10^{-6}$ respectively. Because the initial PD behavior of the material in all test replicates is different, it cannot be basically compared the obtained VP strain to each other. However, it is still considered meaningful for comparison if the resistance of PD does not change so much. In the case of this study, the RDs do not exceed 10.91% between any curve of VP strain and the average curve, therefore, it can be considered that the calculated VP strains repeatedly. Moreover, the relative difference between the obtained VP strains and the 'true values' is lower than 4.78% which demonstrates the good reliability of VP strain values calculated based on the proposed method even with a more complicated loading history.

`

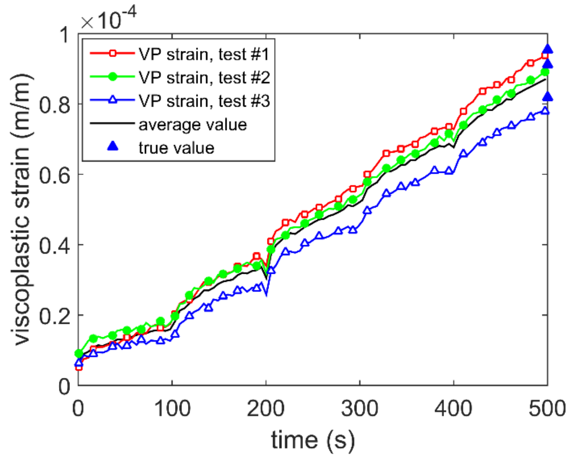

Figure 2.37. Evolution of VP strains at 50°C in sample #3 during all increasing MSCR test replicates.

It observed that the amount of PD gradually accumulated in the specimen affects the development of VP strains. The value of VP strains at the end of loading period of decreasing MSCR tests are respectively 93.82µm/m for test replicate #1, 89.15µm/m for test replicate #2, and 77.94µm/m for test replicate #3. Therefore, the accumulation of the contraction irreversible strain not only increased the stiffness but also reduced the rutting potential of the material.

Decreasing multi-stress level recovery test

Figures 2.38(a,b) show the measured strain in test replicate #4 caused by the input stress consisting of five levels in descending order: 40.82, 32.66, 24.49, 16.33, and 8.16kPa. As displayed in the figure, the response strain of the sample was rather complicated and may be summarized as follows.

In the first loading interval, the response strain drastically increased as a result of the stress that was applied at the highest level. After that, the response strain rapidly recovered at the beginning of the second loading interval due to the sudden reduction of 8.16 kPa from the current stress level. However, the recovery of the response strain lasted only in 5–10 s because the increasing rate of VP strain quickly dominated the decreasing rate. Since that moment, the response strain continuously went up until the end of the

`

second loading interval. In the third loading interval, the applied stress level was again reduced by an amount of 8.16 kPa, and therefore the strain once more started to recover for approximately 60s before resuming the increasing phase. Nevertheless, the overall tendency of the strain in this loading interval was to recover the reversible strain. Consequently, the measured strain has three peak values at t = 100, 200, and 300 s, among which the one at 200 s is the maximum (197.24μm/m). Since the onset of the fourth loading period, the measured strain has been in a steadily decreasing phase. The predicted VE strain also has the same trend of evolution as the total strain but to a lesser extent (see Figure 2.38(a)). It also had three peak values at t = 100, 200, and 300 s and reached its maximum at the second peak (153.01 μm/m).

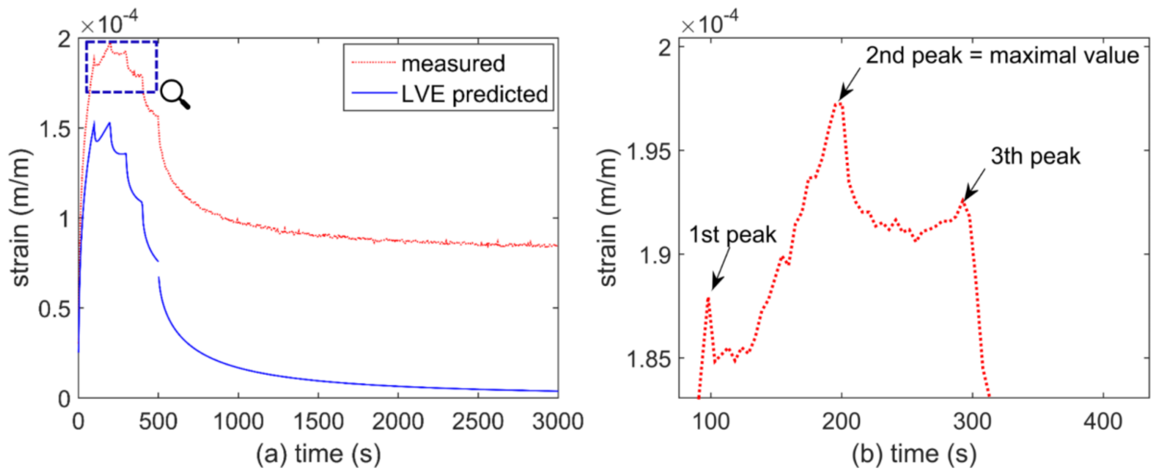

Figure 2.38. Results of decreasing MSCR test replicate #1 at 50°C, (a) Predicted VE and measured strains, (b) Zoom on the measured strain at the peak values

Interestingly, the VP strain showed a steady increase with increasing loading time and almost remained constant during the resting period even though the measured strain clearly showed a decreasing phase in the last three loading intervals (see Figure 2.39). This may be explained that the sample was not free of stress during all loading intervals, causing an irreversible strain rate in the sample and making the VP strain to grow. Moreover, compared to the total strain, the VE strain rose during the first two loading intervals with a lower overall increasing rate, while the VE strain plunged during the last

`

three loading intervals with a higher rate. Thus, the difference between these two strains certainly results in a quantity that steadily rises with an increase in the loading time.

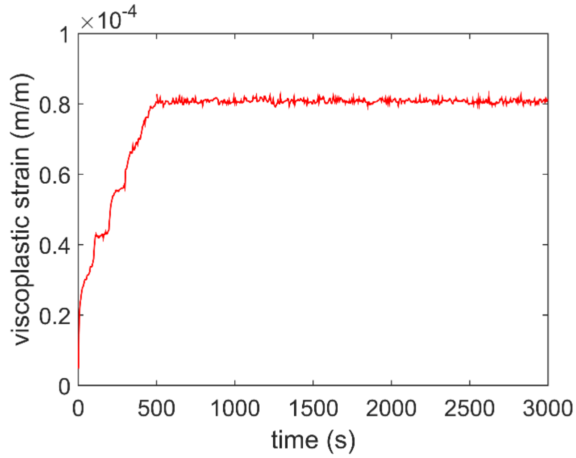

Figure 2.39. VP strain in decreasing MSCR test replicate #1 at 50°C.

Like the increasing MSCR test, the overall law of development of the VP strain in the decreasing MSCR test is likely to be linear in the loading period and almost constant in the resting period, which can be predicted with a high R^2 value by the piece-wise linear functions: $\varepsilon_{vp}^{4} = 1.2\times10^{-7}t + 2.41\times10^{-5}$ for $t \le 500s$ and $\varepsilon_{vp}^{4} = 8.05\times10^{-5}$ for $t > 500s$. When compared to the increasing MSCR test, the VP strains in the decreasing MSCR witnessed a much higher jump at the beginning of the test (approximately 4–5 times larger) and a lower growth rate (approximately 34% lower). This is because the initial stress level was higher, and the value of the stress declined with loading time.

The CCs obtained from all three decreasing MSCR test replicates were back-calculated and are shown in Figure 2.40(a). All the CC curves agree relatively well with each other – namely, the relative difference between any curve of CC and the average curve is lower than 8.18%. As a result, there was also relatively good agreement between all the predicted VE strains [see Figure 2.40(b)]. In terms of accuracy, the average curve of the back-calculated CCs differs approximately 10.11% from the interconverted CCs of sample #1, which is an acceptable value.

`

Similar to the increasing multi-stress level creep-recovery test, the order of testing also influences the VE characteristics of the studied mixture. In fact, the VE strain in test replicate #4 is the highest, followed by that in test replicate #5, and the VE strain in test replicate #6 is the smallest as shown in Figure 2.40(b). As discussed above, the aggregate was rearranged under the effects of the cumulative permanent contraction strain, and therefore the mixture hardened. In all decreasing multi-stress level creep-recovery test replicates, the maximal value of the VE strain did not exceed 170 µm/m; therefore, a linear stress-VE strain relationship was also ensured.

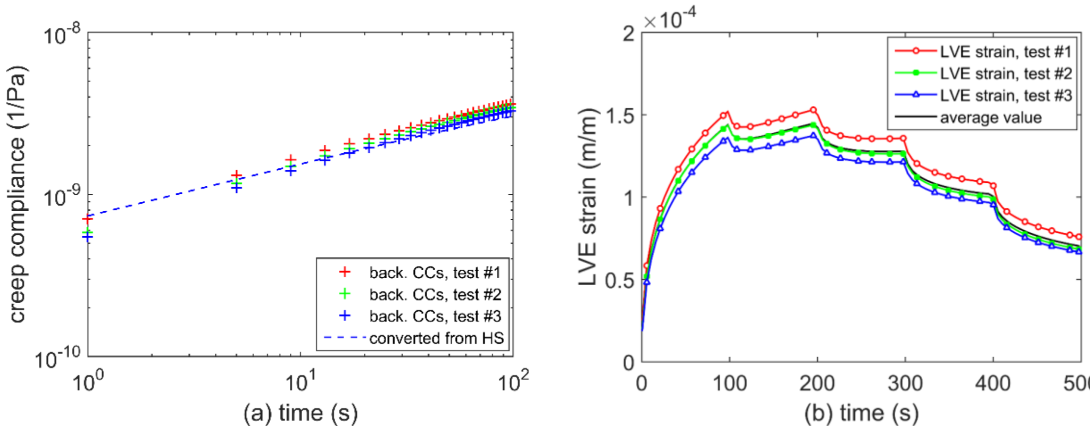

Figure 2.40. Back-calculation results of all decreasing MSCR test replicates at 50°C, (a) Back-calculated CCs, (b) Predicted VE strains.

Figure 2.41 shows the VP strains determined from the data of all decreasing MSCR test replicates. The DR between any curve of VP strain and the average curve is lower than 4.35%. In addition, the computed VP strains differ less than 4.41% from the 'true values'. Therefore, the proposed method is capable of determining reliable VP strains even with a complicated loading condition like that in the decreasing MSCR test.

The VP strain at 500s in test replicate #4 is the highest (80.53µm/m), followed by that in test replicate #5 (75.62µm/m), and that in test replicate #6 is the smallest (72.38 µm/m), proving that the cumulative contraction permanent strain had an impact on the resistance to rutting as already observed in the increasing multi-stress level creep-

`

recovery tests. However, the overall variations of VP strains obtained from all test replicates are still small (< 4.35%); therefore, the bias could be considered small and did not affect much the agreement between the obtained results.

It remains for us to respond to the question raised in the introduction of the MSCR test. Based on the results obtained in the increasing and decreasing MSCR test replicates, one can conclude that the loading pattern does affect the amount of VP strain accumulated in the sample. In fact, the average value of VP strains at the end of the loading period obtained in the decreasing MSCR test is 76.18 µm/m while that obtained in the increasing MSCR test is 86.97 µm/m, which is 14.16% higher.

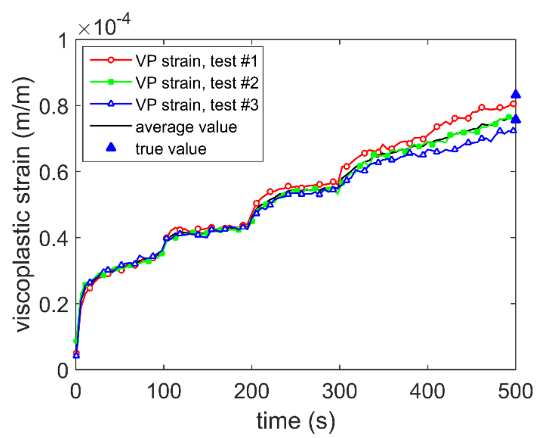

Figure 2.41. Evolution of VP strains at 50°C in sample #3 during all decreasing MSCR test replicates.

2.4.3.3Remarks

A generalized version of the CR test procedure has been proposed to examine the PD of asphalt mixtures exerted by any complex loading history in the time domain. The results of the GCR test were successfully used to characterize both the VE and PD behavior of the material at 50°C without conducting DM tests. Owing to the present back-calculation algorithm, the CCs were determined with a good level of accuracy and repeatability, based on which the viscoplastic strains could be accurately determined even with short recovery periods. The main findings can be drawn as follows:

`

• The AACC function derived from the HS model outperforms the Prony series CC function when used to fit the recovery compliance data. The CCs obtained with the latter function deviated far from the exact CCs, especially at low loading times, while those obtained with the creep function derived from the HS model showed a good agreement with the exact CCs.

• The duration of the recovery period has a significant impact on the directly measured VP strains at 50°C; however, it does not affect much the back-calculated VP. In fact, a resting time equal to 2–3 times the loading time could lead to an accuracy level of roughly 3% for the back-calculated VP strains. Therefore, a ratio of resting time to loading time ranging from 2 to 5 was sufficient for the back-calculation algorithm to give reliable results for tests at 50°C. Conversely, a much longer resting period was needed for the direct measurement to achieve good results at the same testing temperature, at least 7 times the loading time.

• At a high temperature (50°C), permanent strains account for an important part of the total strains, which suggests that a mixture with higher stiffness may have a higher resistance to rutting.

• When the resting time equals 5 times the loading time, the relative errors of the VP strain are lower than 4.78% while any curve of VP strain differs < 10.91% from the average curve, which proves that the back-calculation algorithm is reliable at the high testing temperature (50°C).

• The loading history does affect the development of VP strain. With the same number of loading intervals, duration of loading period, and maximal level of the applied stress, the VP strain obtained in the increasing MSCR test was larger than that obtained in the decreasing MSCR test, approximately 14.16% higher in the conditions studied.

According to the obtained results, the proposed test procedure allows determining with good accuracy and repeatability the pure permanent deformation of asphalt

`

mixtures. Therefore, the results can be used to calibrate predictive models as well as to evaluate the rutting potential of asphalt mixtures.

2.5 Conclusions of Chapter II

In this chapter, linear viscoelastic and viscoplastic theories were summarized, based on which two new theories were proposed—namely:

- A new approach has been successfully developed to determine the RM and CC of asphaltic materials in the form of SEFs based solely on the master curves of DM. Since the proposed formulation fully adheres to the LVE theory and the principle of physical causality, it achieves a high level of accuracy as demonstrated in the results obtained.
- A generalized CR test procedure and a back-calculation algorithm have been proposed to evaluate the LVE and PD of asphalt mixtures under complex loading histories in the time domain without requiring DM data. The obtained results achieve good level of accuracy and repeatability, enabling accurate determination of VP strains with relatively short recovery periods.

`

CHAPTER III

VERIFICATION OF TIME-TEMPERATURE SUPERPOSITION PRINCIPLE FOR VISCOPLASTIC STRAINS OF ASPHALT MIXTURES

3.1 Introduction

In the linear viscoelastic (LVE) domain, the response of asphalt mixtures caused by a longer duration of the load and at a lower temperature is equivalent to that caused by a shorter loading time and at a higher temperature, called time-temperature superposition principle (TTSP) (Ferry, 1980; Tschoegl, 1989). It is well-known that asphalt mixtures are thermo-rheological simple materials in the LVE domain. Consequently, the master curve of LVE properties can be constructed by using horizontal shifting techniques (Forough et al., 2014; Qian et al., 2008). Similarly, asphalt mixtures were demonstrated to remain thermo-rheological simple in the nonlinear viscoelastic region with or without growing damage, and fatigue behavior (Boussabnia et al., 2023;Bradaietal.,2022; Chehab et al., 2002; Nguyen et al., 2009; Nguyen et al., 2013b; Nguyen et al., 2013a; Schapery, 1997; Schapery, 1999; Schwartz et al., 2002).

Zhao and Kim (2003) conducted constant strain rate tests at various temperatures to show that TTSP still holds in the VP domain with growing damage by constructing stress-log reduced-time master curves. With this approach, the mastercurves of VP strain, or the curve of VP strain caused by the same stress level in a wide range of time of interest, were not able to be constructed. Moreover, RLPD tests with the same loading conditions at 25, 40, and 55°C were additionally performed by Zhao and Kim (2003). The testing times were chosen such that the reduced times calculated with VE shift factors were the same. The strains obtained at different temperatures were then all plotted versus the reduced time to demonstrate the agreement, hence the validity of TTSP in the

`

VP domain. The approach was then adopted by Yun et al. (2010) to validate TTSP in the VP domain in considering the effect of the confining stress. Later, in an attempt to build the master curve of PD over a wide range of the reduced time, Khosravifaretal. (2014) performed RLPD tests at three temperatures per mixture with the same testing time and the obtained PD at each temperature was shifted using the shift factors determined from dynamic modulus tests. Since the steps between the investigating temperatures were rather large, there were no overlap portions in the mastercurves of the PD obtained, and thus the characteristics of the master curve were not assessed. Recently, Cao and Kim (2022) proposed a method to determine VP shift factors by determining the value of a temperature-related parameter in the prediction of PD obtained from triaxial RLPD tests. However, the construction of the VP strain master curve was not considered by the authors. In the above-mentioned works, the application of TTSP in the VP domain was partially demonstrated. Either the appropriate VP shift factors or the master curves of VP strains have not been yet investigated.

Therefore, the objective of this work is to adequately verify the applicability of TTSP in the VP domain within the low-strain regime. The reason for limiting the strain amplitude is to ensure that the LVE theory is valid and the LVE properties in both time and frequency domains can be accurately determined using fundamental procedures, based on which the reliability of the obtained results in the VP domain can be assessed. The specific objectives of this work are defined as follows:

- Investigating the pure VP strains in the low-strain regime of a variety of asphalt mixtures caused by several stress levels and temperatures using CR tests;
- Developing new theoretical formulations to quantitatively estimate the influences of various factors causing biases in the obtained results;
- Examining the extension of existing LVE shifting techniques into the total and VP strains and developing a new shifting method to reliably determine the shift factors;

`

• Analyzing the properties of the obtained master curves and their corresponding shift factors to theoretically demonstrate the applicability of TTSP in the VP domain;

• Applying a simple VP model for predicting their irreversible strains of all studied mixtures to demonstrate the efficiency of the master curve of VP strains and the companion VP shift factors in characterizing and predicting the PD behavior of asphalt mixtures, based on which the TTSP in the VP domain can be experimentally validated.

3.2 Material and method

3.2.1 Material and test set up

In this section, the application of TTSP in LVE and VP domain of three asphalt mixtures including a conventional mixture (AC), a polymer-modified bitumen (PMB) asphalt mixture, and a highly modified asphalt mixture (HiMA) were examined. The AC mixture was prepared with a neat bitumen of grade PG 64 and the PMB mixture was produced with a polymer-modified bitumen. The PMB was a blend of the neat bitumen and 4% ÷ 5% (in total weight) of styrene-butadiene-styrene (SBS) such that its performance grade attained PG 76. In order to prepare the HiMA mixture, a highly modified bitumen of PG 94 was used. It was obtained by modifying the PG 64 bitumen with approximately 2% (in total weight) of SBS and a suitable amount of high modulus additive. The fundamental properties of studied binders are presented in Tables 3.1 and 3.2. All mixtures were made of andesite aggregates, which were collected in the south of Vietnam. The nominal maximum aggregate size of all mixtures is 12.5 mm and the proportions of all aggregates were chosen similar to those in (Nguyen et al., 2021a) and are reported in Figure 2.23. The fundamental properties of all mixtures are reported in Table 3.3.

In order to prepare specimens for tests, the mixtures were compacted by a roller sector compactor at 145, 160, and 175°C to obtain three plates of AC, PMB and HiMA mixtures, respectively. The dimensions of the plates were 0.32x0.26x0.08m^3. After cooling down to room temperature, the plates were sawed into three prismatic samples

`

per mixture with dimensions: 0.07x0.07x 0.15m^3 and labelled – namely: 1.1, 1.2 and 1.3 for AC mixture; 2.1, 2.2 and 2.3 for PMB mixture; and 3.1, 3.2, 3.3 for HiMA mixture as shown in Figure 3.1. Test set up in this section are similar to one in Subsection 2.4.3.2.

Table 3.1: Engineering properties of the neat binders (AC mixture).

Engineering properties	Standards	Results	Specification limit
Softening point (˚C)	ASTM D36	48.7	Min 46.0
Penetration at 25 ˚C (0.1mm)	ASTM D5	64.5	60.0–70.0
Ductility at 25 ˚C (cm)	ASTM D116	>140	Min 100
Specific gravity at 25 ˚C	ASTM D70	1.04	1.00–1.05

Table 3.2: Engineering properties of the PMB and HiMA binders.

Engineering properties	Standards	Results	
		PMB	HiMA
Softening point (˚C)	ASTM D36	85	N/A(*)
Penetration at 25 ˚C (0.1mm)	ASTM D5	54.7	N/A(*)
Viscosity (Pa.s)	ASTM D4402	2.43 (at 135 ˚C)	0.621 (at 180 ˚C)
Elastic recovery (%)	ASTM D6084	90	N/A(*)

(* Non-Disclosure Agreement)

Table 3.3: Engineering properties of the studied asphalt mixtures.

Engineering properties	Standards	Results		
		AC	PMB	HiMA
Optimum asphalt content (%)		4.8	5.0	5.0
Maximum specific gravity	ASTM D2041	2.52	2.51	2.51
Bulk specific gravity	ASTM D2726	2.39	2.38	2.36
Air void (%)	ASTM D3203	5.16	5.18	5.98
Void in aggregate (%)		14.02	15.06	15.77
Marshall stability (kN)	ASTM D6927	10.60	15.50	19.00
Marshall flow (mm)	ASTM D6927	3.50	3.40	3.10
Indirect tensile strength at 25˚C (IDTS) (MPa)	ASTM D6931	0.98	1.24	1.97

Figure 3.1. Preparation of samples for AC, PMB, HiMA mixtures.

3.2.2 Determination of VP strain using single stress level creep-recovery (SSCR) test

With the SSCR test is illustrated as Figure 2.18, the VP strain can be calculated using the algorithm presented in subsection 2.4.3 which is comprised of three steps: (*i*) determination of creep compliance function, (*ii*) prediction of viscoelastic (VE) strain, and (*iii*) calculation of VP strain. It should be noted that the creep compliance function for single stress level creep – recovery test (see Figure 3.2) is:

$$\frac{\varepsilon_T(t_1)-\varepsilon_T(t)}{\sigma_1}=D(t_1-t_0)-D(t-t_0)+D(t-t_1),\ \text{for } t>t_1. \quad (3.1)$$

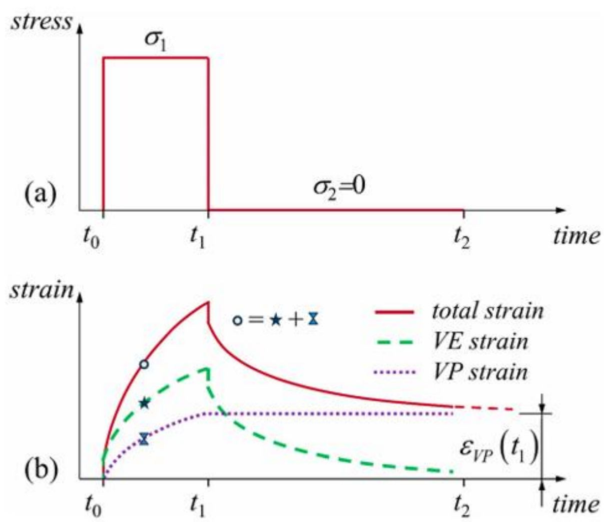

Figure 3.2. Illustration of the stress history (a) and response strain (b) in an SSCR test.

`

3.3 Experimental result and analysis

Table 3.4. Summary of experimental testing programme.

Test No.	Sample	Type of test	Temperature (°C)	Stress (kPa)	Purpose
AC-1,2,3,4	1.1	SSCR	17.5; 25; 32.5; 40	23.81	check TTSP
AC-5,6,7,8	1.2	SSCR	17.5; 25; 32.5; 40	35.71	check TTSP
AC-9	1.2	DM	-	-	check time-frequency agreement
AC-10,11,12,13	1.3	SSCR	17.5; 25; 32.5; 40	53.57	check TTSP
AC-14,15,16	1.3	SSCR	25, 25, 25	53.57	check replication
AC-17,18,19	1.3	SSCR	32.5, 32.5, 32.5		
AC-20,21,22	1.3	SSCR	40, 40, 40		
PMB-1,2,3,4	2.1	SSCR	27.5; 35; 42.5; 50	23.81	check TTSP
PMB-5,6,7,8	2.2	SSCR	27.5; 35; 42.5; 50	35.71	check TTSP
PMB-9,10,11,12	2.3	SSCR	27.5; 35; 42.5; 50	53.57	check TTSP
PMB -13	2.3	DM	-	-	check time-frequency agreement
PMB-14,15,16	2.1	SSCR	35, 35, 35		check replication
PMB-17,18,19	2.1	SSCR	42.5, 42.5, 42.5	23.81	
PMB-20,21,22	2.1	SSCR	50, 50, 50		
HiMA-1,2,3,4	3.1	SSCR	40; 47.5; 55; 62.5	23.81	check TTSP
HiMA-5	3.1	DM	-	-	check time-frequency agreement
HiMA-6,7,8,9	3.2	SSCR	40; 47.5; 55; 62.5	35.71	check TTSP
HiMA-10,11,12,13	3.3	SSCR	40; 47.5; 55; 62.5	53.57	check TTSP
HiMA-14,15,16	3.3	SSCR	47.5, 47.5, 47.5		check replication
HiMA-17,18,19	3.3	SSCR	55, 55, 55	53.57	
HiMA-20,21,22	3.3	SSCR	62.5, 62.5, 62.5		

In this subsection, the results of twenty-one SSCR test for each mixture were used to verify the TTSP in viscoplastic domain and to check replicate of the results. Each

`

SSCR test consisted of 150s loading time and 3000s resting one. Each sample was applied one stress level (23.81, 35.71, or 53.57MPa) at four different temperatures to eliminate the effects of the heterogeneity of asphalt mixture on obtained results. Testing temperatures are 17.5, 25, 32.5, and 40°C for AC mixture; 27.5, 35, 42.5, and 50°C for PMB mixture; and 40, 47.5, 55, and 62.5 for HiMA mixture. Those level stress and temperatures were chosen to ensure that the Boltzmann superposition can be applied to the VE strain. It should be noted that all tests were performed from the lowest to the highest temperature to reduce the effect of the accumulated VP strains of preceding tests to the evolution of VP strains of subsequent tests. To facilitate the reader, list of tests was presented in Table 3.4.

3.3.1 Measured strains, CCs, and irreversible strains obtained from SSCR

This section presents results of measured strain (total strain), VE strain (or back-calculated of CCs), and irreversible strains (VP strain) at single temperatures of all mixtures. Creep compliances were back-calculated based on the algorithm proposed by Nguyen et al. (2021) with the AACC function derives from HS was used as the form of the CC function. Then, VP strains were computed by using the algorithm in Tran et al. (2022).

The obtained results of SSCR test performed on sample 1.2 at 32.5°C and σ = 35.71 kPa , were chosen to illustrate the data processing of SSCR tests, are presented in Figure 3.3. The fitting result of the experimental recovery compliance by using the AACC function derived from HS model is good and showed in Figure 3.3(a). The CC of sample presented in Figure 3.3(b) was calculated with the best-fit AACC function parameters. After computing the CC, the VE strain in the loading time was predicted and displayed in Figure 3.3(c). It can be observed that the measured strain is larger than the predicted VE one. It means that using only creep test data can lead to large errors for determining the CC (Nguyen et al., 2021b). Viscoplastic strain was obtained by subtracting the total measured strain to the predicted VE strain and showed in Figure

3.3(d). Because the VP strain continuously develops in the loading phase and has constant value during the unloading one, so just VP strain in the loading phase will be shown in upcoming paragraphs.

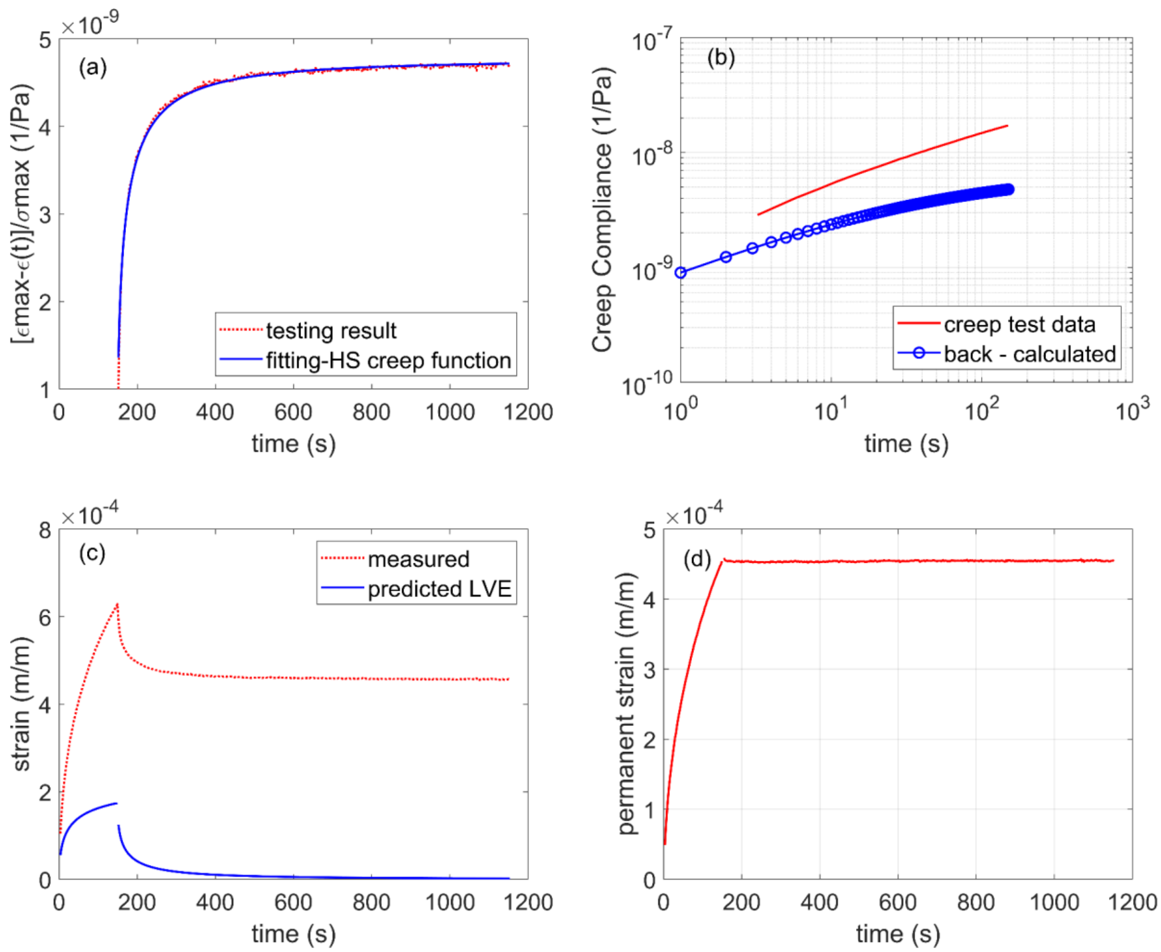

Figure 3.3. Results of the SSCR test at 32.5°C and σ = 35.71 kPa of AC: (a) Fitting results of the recovery compliance, (b) Back calculated CC, (c) Measured strains and predicted VE strains, and (d) computed VP strain.

Total strains (measured strains) evolute during loading periods of SSCR tests of all AC, PMB, and HiMA samples are respectively presented in Figures. 3.4, 3.5, and 3.6. It is easy to observe that an increased temperature or stress level led to an increase measured strain.

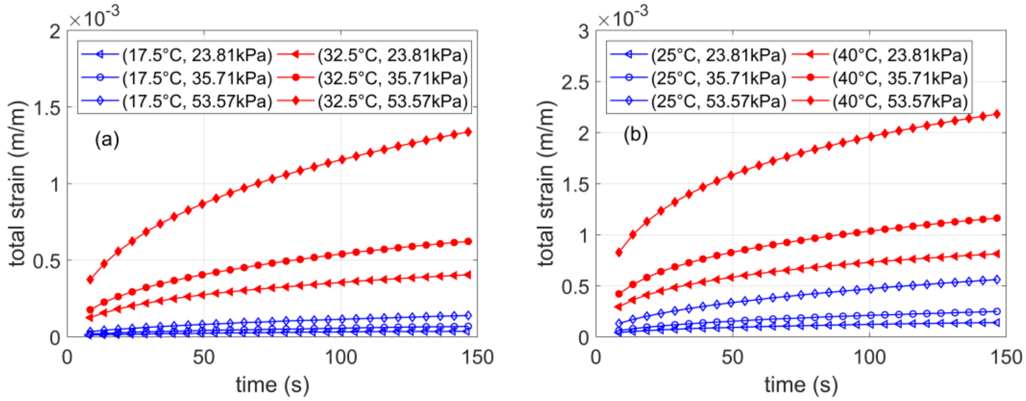

Figure 3.4. Measured strains (total strains) of AC samples at different temperatures and stress levels: (a) 23.81kPa, (b) 35.71kPa, and (c) 53.57kPa.

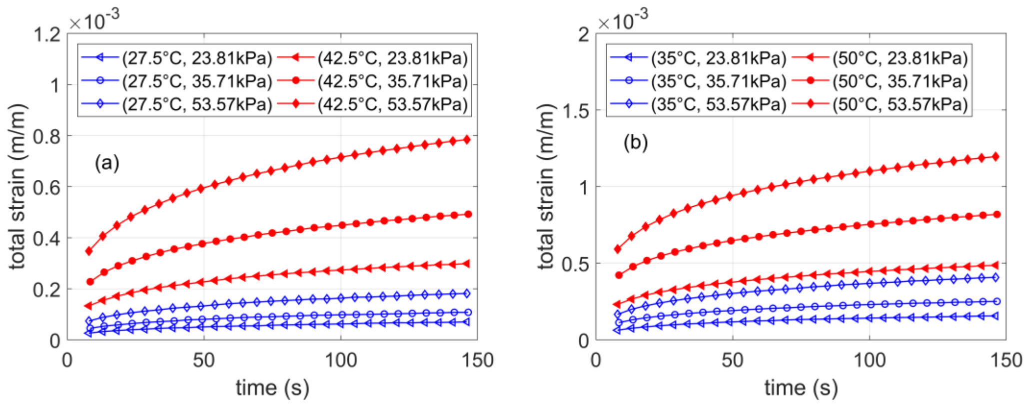

Figure 3.5. Measured strains (total strains) of PMB samples at different temperatures and stress levels: (a) 23.81kPa, (b) 35.71kPa, and (c) 53.57kPa.

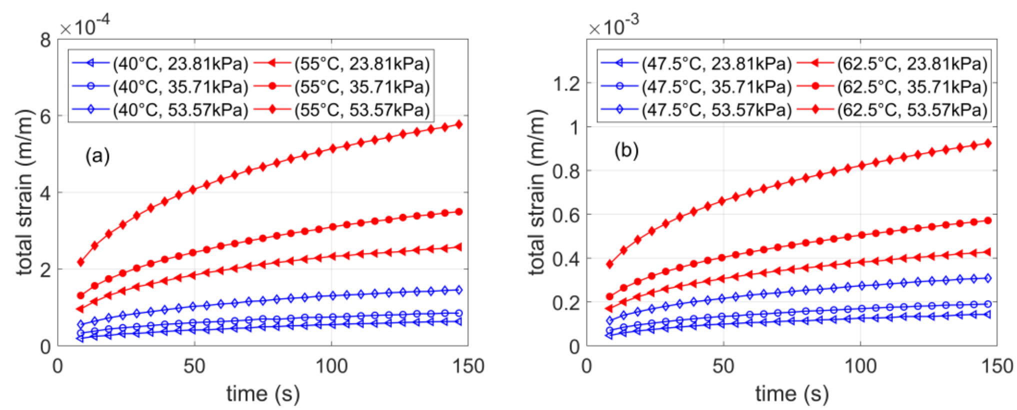

Figure 3.6. Measured strains (total strains) of HiMA samples at different temperatures and stress levels: (a) 23.81kPa, (b) 35.71kPa, and (c) 53.57kPa.

`

The back calculated creep compliance of all mixtures at all testing temperatures with different stress levels are shown in Figures 3.7 (a), (b), and (c). Based on the back calculated CCs, VE strains were predicted. Then, VP strains were calculated by eliminating VE strains from measured strains and displayed in Figures 3.8, 3.9, and 3.10. Because the deformation of AC mixture at 17.5°C and at 23.81 kPa was too small for the displacement transducers can accurately capture so the VP strain at those testing conditions were not presented. It can be seen that all VP strains continuously develop in loading time. Moreover, it is different effect between stress level and temperature to an increase of VP strain. There is a steady impact of stress level on VP strain while temperature dramatically promotes the development of VP strain.

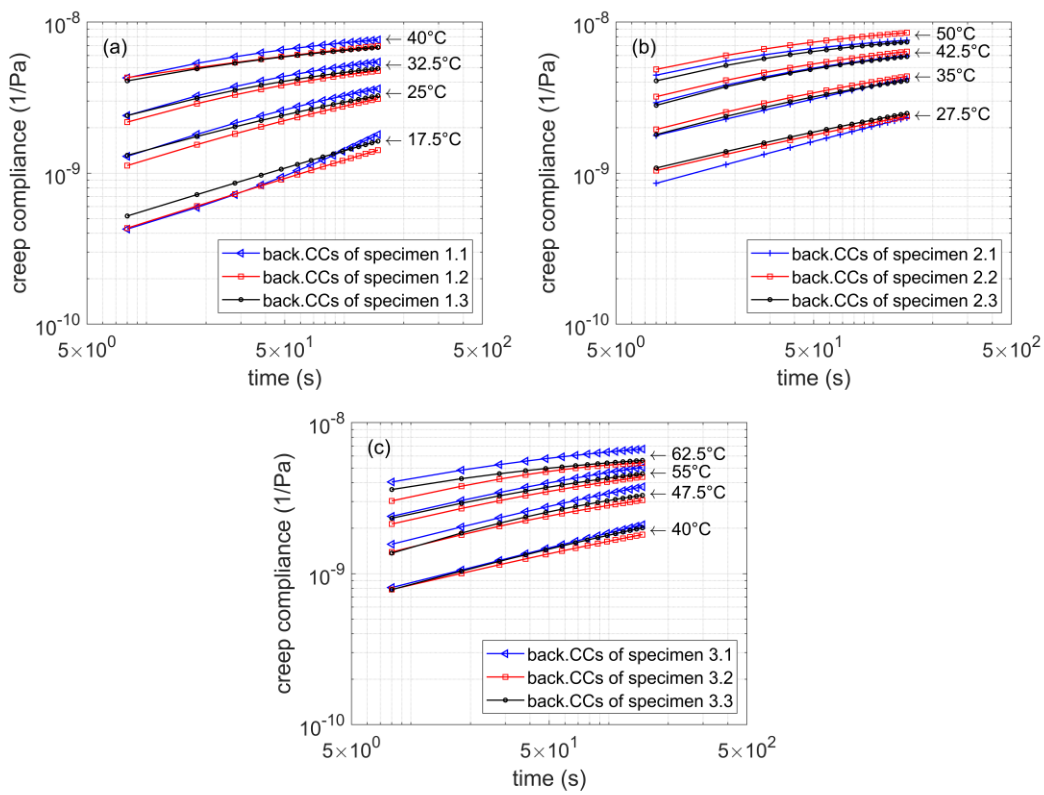

Figure 3.7. Back calculated creep compliance of asphalt mixtures at different temperatures: (a) AC mixtures, (b) PMB mixtures, and (c) HiMA mixtures.

`

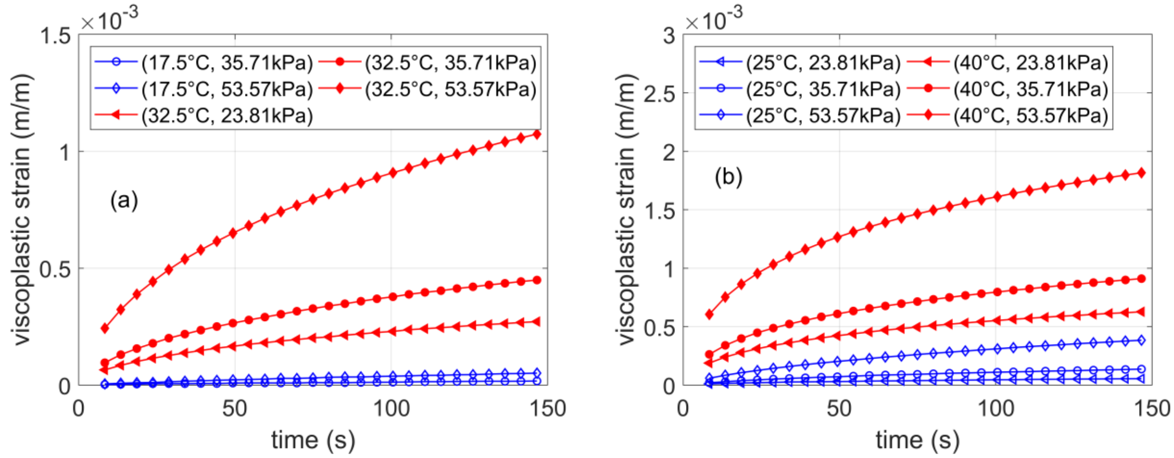

Figure 3.8. Comparison the effects of stress level and temperature on the evolution of VP strains of AC mixtures in SSCR tests. (a) 17.5°C compared with 32.5°C. (b) 25°C compared with 40°C.

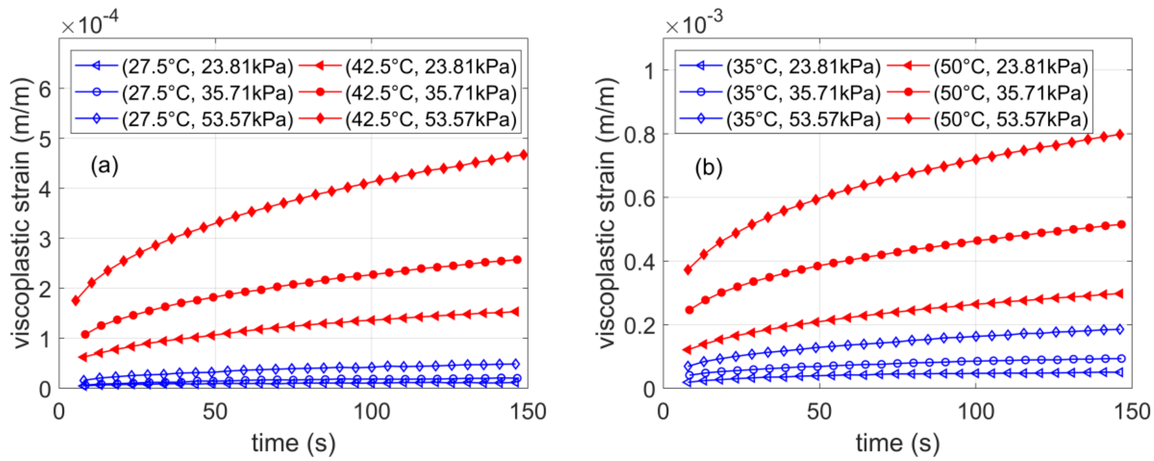

Figure 3.9. Comparison the effects of stress level and temperature on the evolution of VP strains of PMB mixtures in SSCR tests. (a) 27.5°C compared with 42.5°C. (b) 35°C compared with 50°C.

`

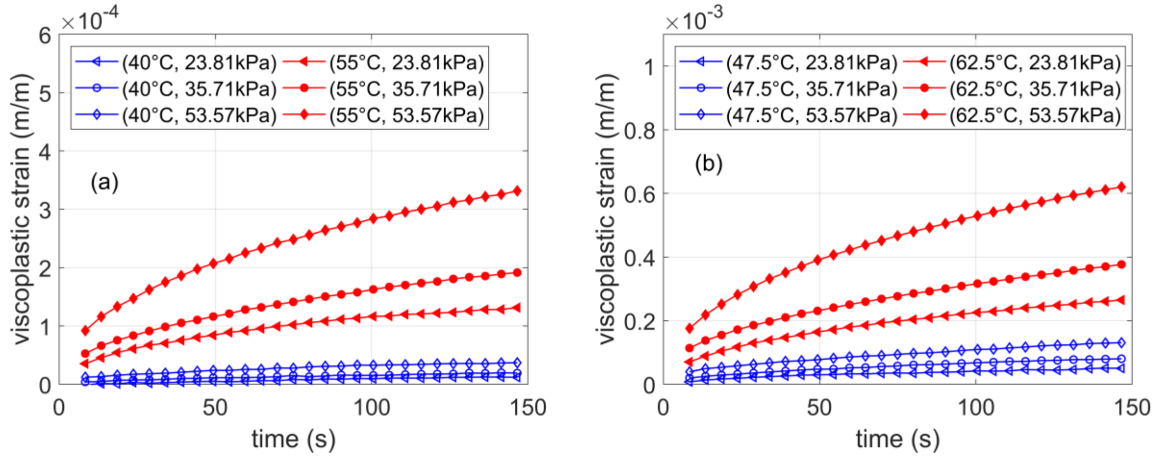

Figure 3.10. Comparison the effects of stress level and temperature on the evolution of VP strains of HiMA mixtures in SSCR tests. (a) 40°C compared with 55°C. (b) 47.5°C compared with 62.5°C.

3.3.2 Construction of master curves of total strains, CCs, and VP strains

TTSP says that the LVE property of a thermo-rheological simple material at a temperature T_1 and loading time t_1 is equivalent to that at temperature $T_1 > T_2$ and at loading time $t_2 < t_1$, and vice-versa. In other words, the loading time at a lower temperature (T_1) is 'reduced' by a factor equal to $a_T = t_2/t_1$ when converted to that at a higher temperature (T_2). Consequently, by choosing an arbitrary temperature as the reference temperature (T_{ref}) and shifting the LVE properties at all temperatures to those at T_{ref}, the master curve of the LVE characteristics can be obtained (Chailleux et al., 2006; Cho,2016; Tschoegl,1989). By following the same process, the mastercurves of the total and pure VP strains were also constructed.

3.3.2.1Master curve of CCs, total, and VP strains

Creep compliances, total and VP strains of samples at different temperature was shifted by using the modified method of HonerKamp and Weese which proposed in previous subsection to construct their master curves and determine their shift factors. It can be observed that CCs of three samples of each mixture agree well together (see

`

Figure 3.12, 3.13 and 3.14). The maximal value of RDs between all master curves of CC and their average curve is 11.80% (for AC mixture). The largest RD of shift factors is 5.96% (see Table 3.5) for all mixtures. Those RDs include the inter-sample heterogeneity because those master curve of CCs and shift factor were constructed with different samples and applied stress levels. It means that those tests have good repeatability, and the inter-sample heterogeneity does not affect much to the testing results. Thus, it can be considered that all samples remain their behavior in LVE domain with the applied stress levels.

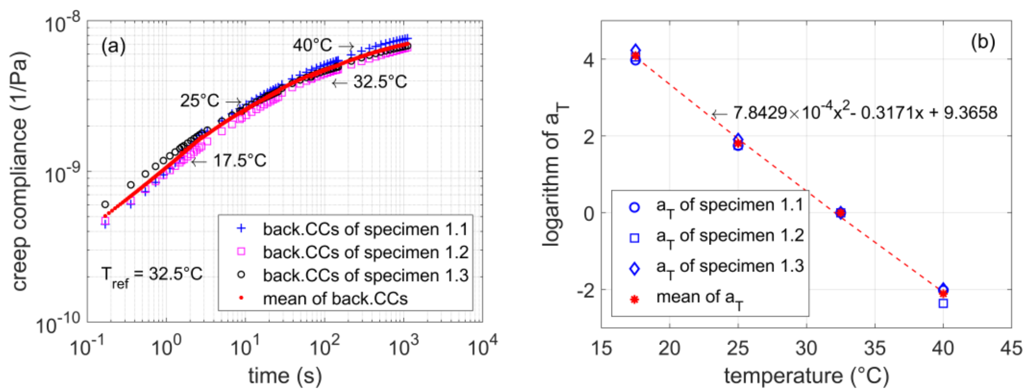

Figure 3.12. Master curves of all back-calculated CCs of AC mixtures (a) and their corresponding shift factors (b).

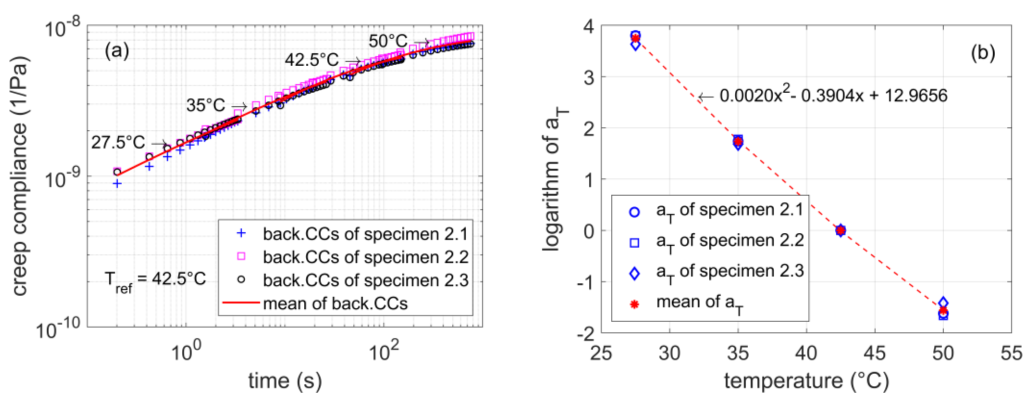

Figure 3.13. Master curves of all back-calculated CCs of PMB mixtures (a) and their corresponding shift factors (b).

`

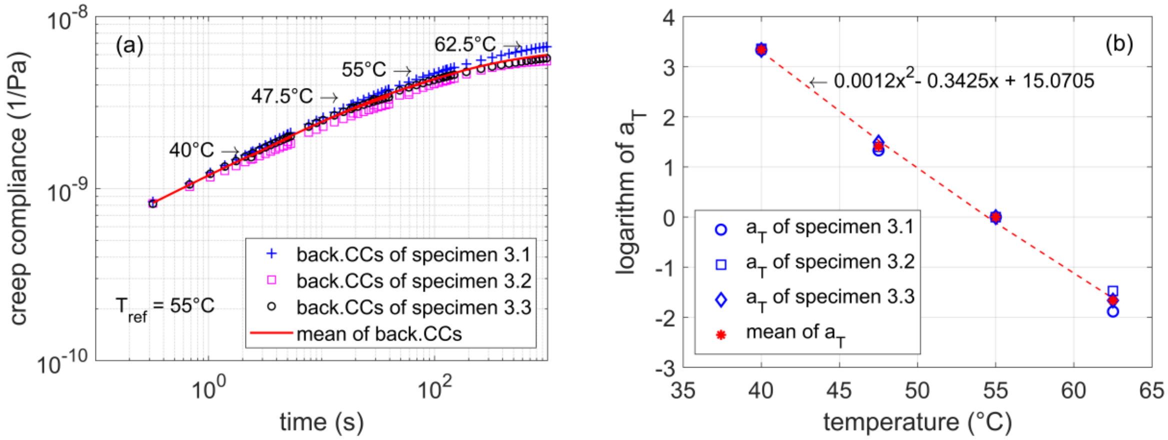

Figure 3.14. Master curves of all back-calculated CCs of HiMA mixtures (a) and their corresponding shift factors (b).

Table 3.5: The relative differences of CCs and VE shift factors.

Mixture	Sample code	RDs of CCs	RDs of a_T
AC	1.1	0.0903	0.0324
	1.2	0.0940	0.0522
	1.3	0.1180	0.0416
PMB	2.1	0.0652	0.0180
	2.2	0.0432	0.0274
	2.3	0.0323	0.0428
HiMA	3.1	0.0497	0.0596
	3.2	0.0627	0.0471
	3.3	0.0147	0.0204

Figures 3.15 - 3.20 present shifted curves of measured strain and VP strains of investigated mixtures and their corresponding shift factors noted as $a_{T,T}$, $a_{T,VP}$. Figures 3.15 – 3.20 (a) showed that form of those curves are relatively smooth and unique. Moreover, with the monotonous shapes, those curves satisfy a unique relationship between time and measured or VP strain. Therefore, it can be considered that the shifted

curves of measured and VP strains are their master curves at the reference temperature. Furthermore, Figures 3.15 – 3.20 (b) show that all shift factors ensure an injective relationship between temperature and $a_{T,T}$ or $a_{T,VP}$ because their functions are also monotonous functions. It means that TTSP can be applied on both measured and VP strains of study mixtures.

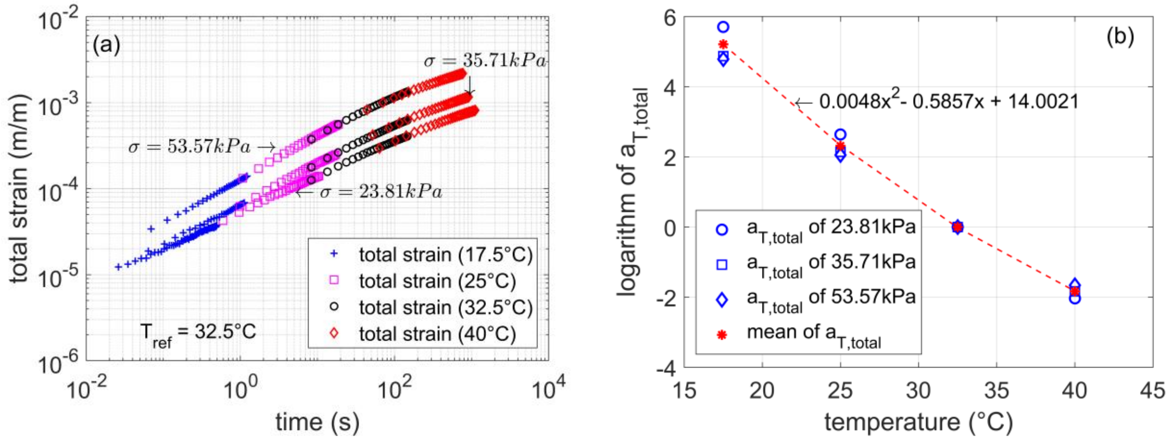

Figure 3.15. Master curves of total strains of AC mixtures (a) and their corresponding shift factors (b).

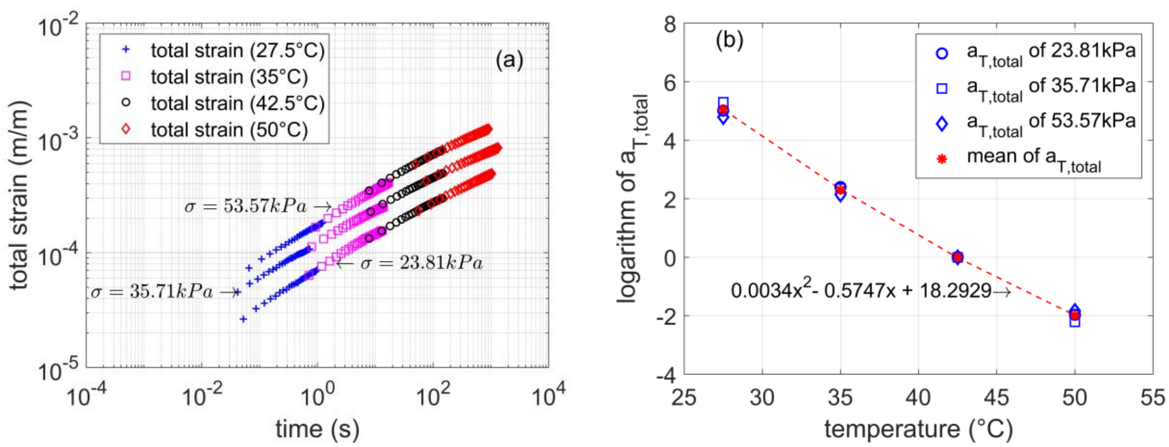

Figure 3.16. Master curves of total strains of PMB mixtures (a) and their corresponding shift factors (b).

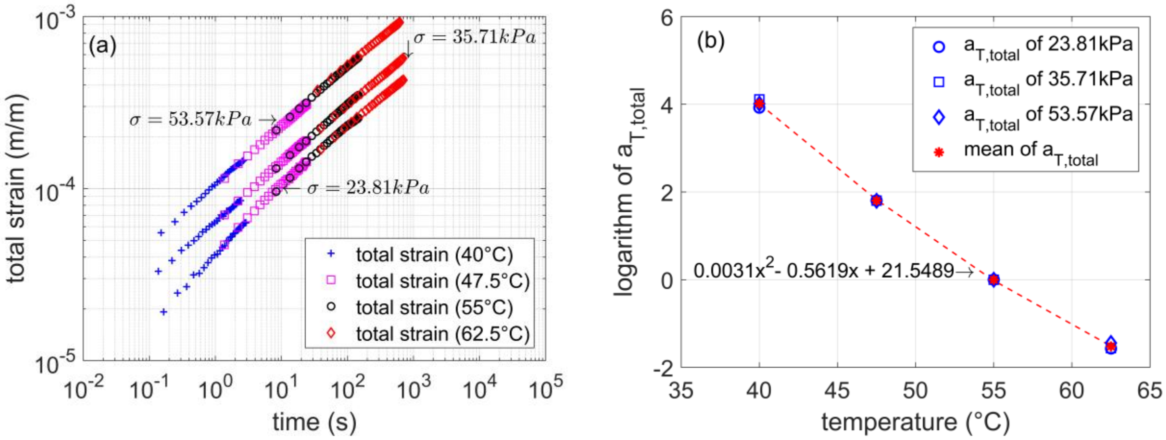

Figure 3.17. Master curves of total strains of HiMA mixtures (a) and their corresponding shift factors (b).

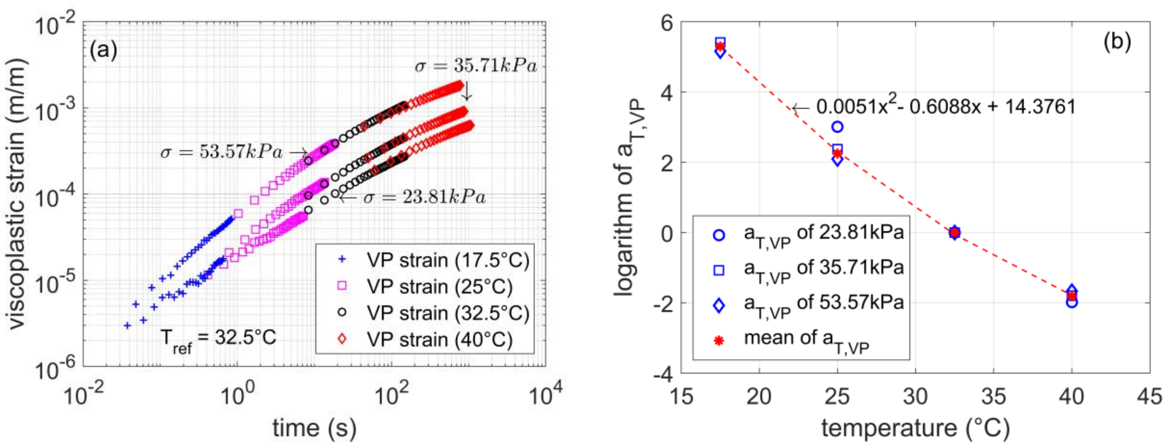

Figure 3.18. Master curves of all VP strains of AC mixtures (a) and their corresponding shift factors (b).

To evaluate effect of stress level to the values total and VP shift factors, the relative differences between each their value to their average values were computed. The largest value of RDs is 11.04% for $a_{T,T}$ and 13.50% for $a_{T,VP}$ (for all investigated mixtures). It is worth to note that those values include the inter-sample variation, so those values are still small and can be accepted in pavement engineering. Thus, values of $a_{T,T}$ and $a_{T,VP}$ can be considered independent on stress level.

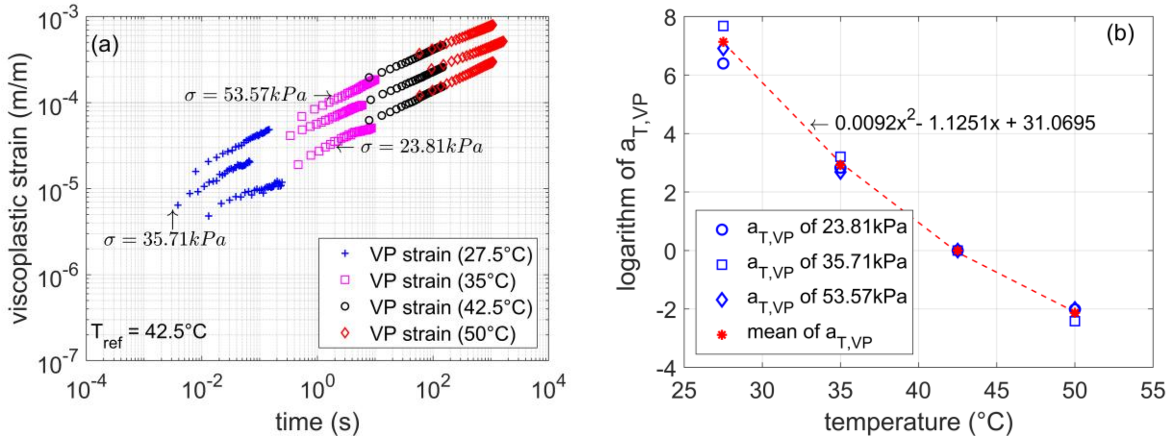

Figure 3.19. Master curves of all VP strains of PMB mixtures (a) and their corresponding shift factors (b).

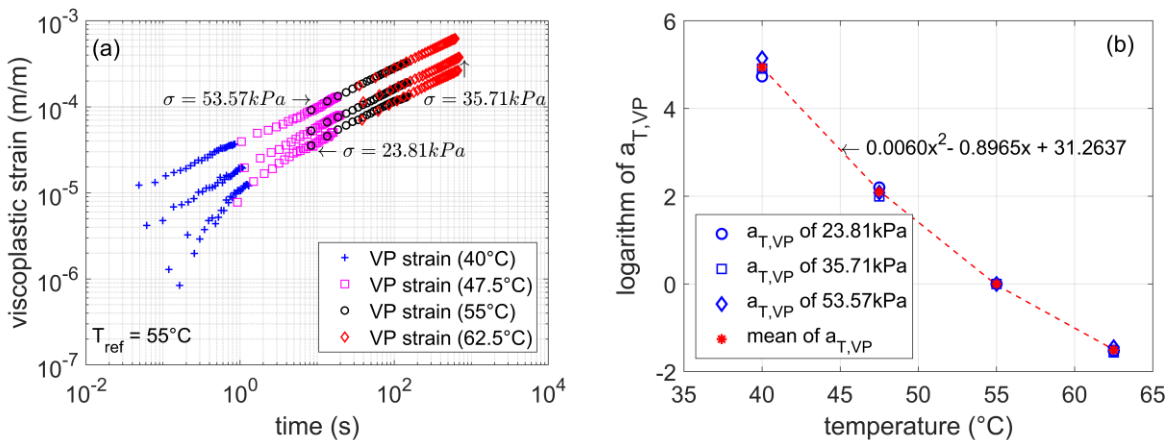

Figure 3.20. Master curves of all VP strains of HiMA mixtures (a) and their corresponding shift factors (b).

3.3.2.2Horizontal shifting methods

The shift factors can be determined by simply adjusting adjacent isotherms (Ferry, 1980; Goodrich, 1988); however, the obtained results depend on the experience of the person processing the data (Cho, 2016). In order to ensure the objectivity of the shift factors computed, Honerkamp and Weese (1993) used a nonlinear regression method to calculate the shift factors from the storage modulus data. First, the authors approximated

\`

the storage modulus $E'_{T_{ref}}(\omega)$ at the reference temperature by an *N*-order polynomial of $\log(\omega)$:

$$\log\left(E'_{T_{ref}}(\omega)\right) \approx \sum_{k=0}^{N} a_k \log(\omega)^k \quad (3.2)$$

Then, the shift factors were determined by minimizing the value of:

$$\chi^2 = \sum_{j=0}^{m}\sum_{i=1}^{n}\left[\log\left(E'_{T_j}(\omega_i)\right) - \sum_{k}^{N} a_k \left(\log(\omega_i) + \log a_T(T_j)\right)^k\right]^2, \quad (3.3)$$

where $E'_{T_j}(\omega_i)$ is the storage modulus measured at temperature T_j and frequency ω_i; $a_T(T_j)$ is the shift factor used to convert $E'_{T_j}(\omega_i)$ to that at the reference temperature, and m, n are the number of testing temperatures and frequencies. As suggested by the authors, the order of the polynomial should be chosen in the range of $\sum_{j=0}^{m} n_j / 20 \le N \le \sum_{j=0}^{m} n_j / 4$. However, according to the work of Cho (2016), the order of the polynomial should be around 10 for the computed shift factors to be independent of the polynomial order. This value is quite high, requiring more data points at one testing temperature so that the approximation by the high-order polynomial could be properly performed. Moreover, in the case where temperature T_j and the reference temperature have a large difference, the determination of shift factors may encounter large errors. This is because the two sets of data do not have an overlap; thus, the calculation of shift factors must be based on the extrapolated data of the storage modulus at the reference temperature. By using a different approach, Chailleux et al. (2006) proposed a formula to calculate the shift factor based on the dynamic modulus and phase angle data at two close temperatures:

$$\log\left(a_{(T_1,T_2)}\right) = \frac{\pi}{2}\frac{\log\left(\left|E^*(T_1,\omega)\right|\right) - \log\left(\left|E^*(T_2,\omega)\right|\right)}{\bar{\varphi}^{(T_1,T_2)}(\omega)} \quad (3.4)$$

`

where $a_{(T_1,T_2)}$ is the shift factor applied for isotherm T_2 according to temperature T_2; $\left|E^*(T_1,\omega)\right|$, $\left|E^*(T_2,\omega)\right|$ are respectively the dynamic modulus at temperatures T_1, T_2 at a chosen angular frequency ω; and $\overline{\varphi}^{(T_1,T_2)}(\omega)$ is the average of the two phase angles measured at frequency ω and at temperatures T_1, T_2. The accuracy of the shift factor computed from equation (3.4) depends strongly on that of the phase angle which is a quantity more difficult to be measured (Rowe et al., 2009; Zhang et al., 2020; Phan et al., 2022). Based only on the dynamic modulus data, Cho (2009) proposed to minimise the sum of distances called "arc length" formed by the shifted data points obtained at two close temperatures. Based on our observations, the method only works well when the two isotherms have large enough overlaps or the slope of the curve is not too flat.

All the above-mentioned methods were originally oriented to be used in the frequency domain. Some of them can be extended into the time domain such as those of HonerKamp and Weese (1993) and Cho (2009). As the arc length method is more susceptible to the characteristics of the overlap of the two isotherms, we considered only the method of HonerKamp and Weese (1993). A modification of this method was proposed to reduce the order of the polynomial and avoid extrapolating data, as shown in Algorithm 1 and graphically illustrated in Figure 3.11.

Algorithm 1. Algorithm for determining the shift factor

Step 1: Determine the shift factor $\left(a_T^{n+1,n}\right)$ applied for $(n+1)^{th}$ isotherm according to n^{th} isotherm

- Fitting each data set by a (quadratic) polynomial, noted $f_n\left[\log(t)\right]$; $f_{n+1}\left[\log(t)\right]$
- Given an initial value of $a_T^{n,n+1}$, calculating the value of $f_{n+1}\left[\log\left(t / a_T^{n+1,n}\right)\right]$
- Determining $a_T^{n+1,n}$ by minimising:

`

$$\Delta f^2 = \sum_{j=j_1}^{j_2} \left\{ f_n\left(t_j\right) - f_{n+1}\left[\log\left(t_j\right) - \log\left(a_T^{n+1,n}\right)\right] \right\}^2,$$

wherein $f_n\left[\log\left(t_{j_1}\right)\right]$ and $f_n\left[\log\left(t_{j_2}\right)\right]$ define the potential overlap region of the two isotherms

Step 2: Determining the shift factor applied for an arbitrary isotherm according to the isotherm at T_{ref}

- Let the k^{th} isotherm be the reference isotherm, the shift factor applied for an arbitrary n^{th} isotherm according to the isotherm at T_{ref} :

$$a_T^{n,k} = \prod_{i=k}^{n} a_T^{i,i+1} \text{ if } n \geq k;\; a_T^{n,k} = \prod_{i=n}^{k} a_T^{i,i+1} \text{ if } n < k.$$

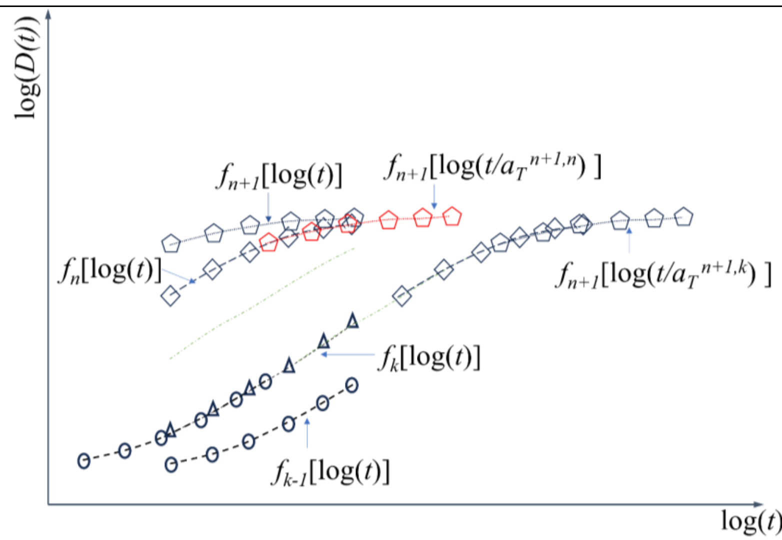

Figure 3.11. Illustration of the proposed shifting method.

3.3.2.3Comparison of total, VE, and VP shift factors

Figure 3.21 plotted the values of $a_{T,T}$, a_T, and $a_{T,VP}$ together for comparing them. Effect of cumulative VP strain and non-instantaneous applied load in the loading period of CR test were also investigated to determine the reliable intervals of the shift factors. The error bars of $a_{T,T}$ and $a_{T,VP}$ display limit region of their value. The upper

`

and lower bounds of VE shift factor are just the SD of the set of three values of a_T obtained from SSCR tests with three stress levels.

It can be observed in Figure 3.21 that value of $a_{T,T}$ and $a_{T,VP}$ seem to be similar to value of a_T at high temperatures (as depend on the behavior of the investigated mixture, e.g. ≥32.5°C for AC mixture, ≥42.5°C for PMB mixture, and ≥55°C for HiMA mixture). The result of computation the mean of relative differences between the $a_{T,T}$ versus a_T , and the $a_{T,VP}$ versus a_T (13.758% and 14.949% for AC mixture, 26.975% and 35.713% for PMB mixture, and 7.037% and 11.726% for HiMA mixture) shows that gaps of shift factors of AC and HiMA mixtures estimated at high temperatures are rather small. This explains why many authors suggest extending the validity of VE strain shift factor into the VP domain.

Nevertheless, it is easy observed that values of total strain or VP strain shift factors are not similar to values of VE strain shift factors in the full range of study temperatures. In fact, the RDs for BMP mixture are respectively 33.744% and 82.440% between the mean values of $a_{T,T}$ and a_T, and $a_{T,VP}$ and a_T (see Table 3.6). In case eliminating all of factors causing biases to values of shift factor, between $a_{T,T}$ and a_T, and between $a_{T,VP}$ and a_T still exist clearly recognizable gaps. As reported in Table 3.7, the possible minimal gaps between $a_{T,T}$ and a_T are 11.419% for AC mixture, 23.367 % for PMB mixture, and 14.932% for HiMA mixture, while the potential shortest distances between $a_{T,VP}$ and a_T are much larger, respectively 18.947% , 60.156%, and 35.366% for AC, PMB, and HiMA mixture. It means that the $a_{T,T}$ and $a_{T,VP}$ are independent on a_T as suggested by Cao & Kim (2022).

It should note that although the RD between $a_{T,T}$ and $a_{T,VP}$ of the AC mixture is only 4.487%, this character does not infer a dependence between $a_{T,T}$ or $a_{T,VP}$ with a_T.

Apart from this case, obvious gaps exist between $a_{T,T}$ and $a_{T,VP}$, so it is necessary to use independent values of the total, VP, and VE shift factors for characterizing and modelling the behavior of asphalt mixture in the full-range of PD.

Table 3.6: Relative differences between mean values of shift factors.

RD | Mixture	AC	PMB	HiMA
$a_{T,T}$ vs. a_T (%)	25.639	33.744	20.034
$a_{T,VP}$ vs. a_T (%)	29.528	82.440	44.007
$a_{T,VP}$ vs. $a_{T,T}$ (%)	4.487	36.907	20.876

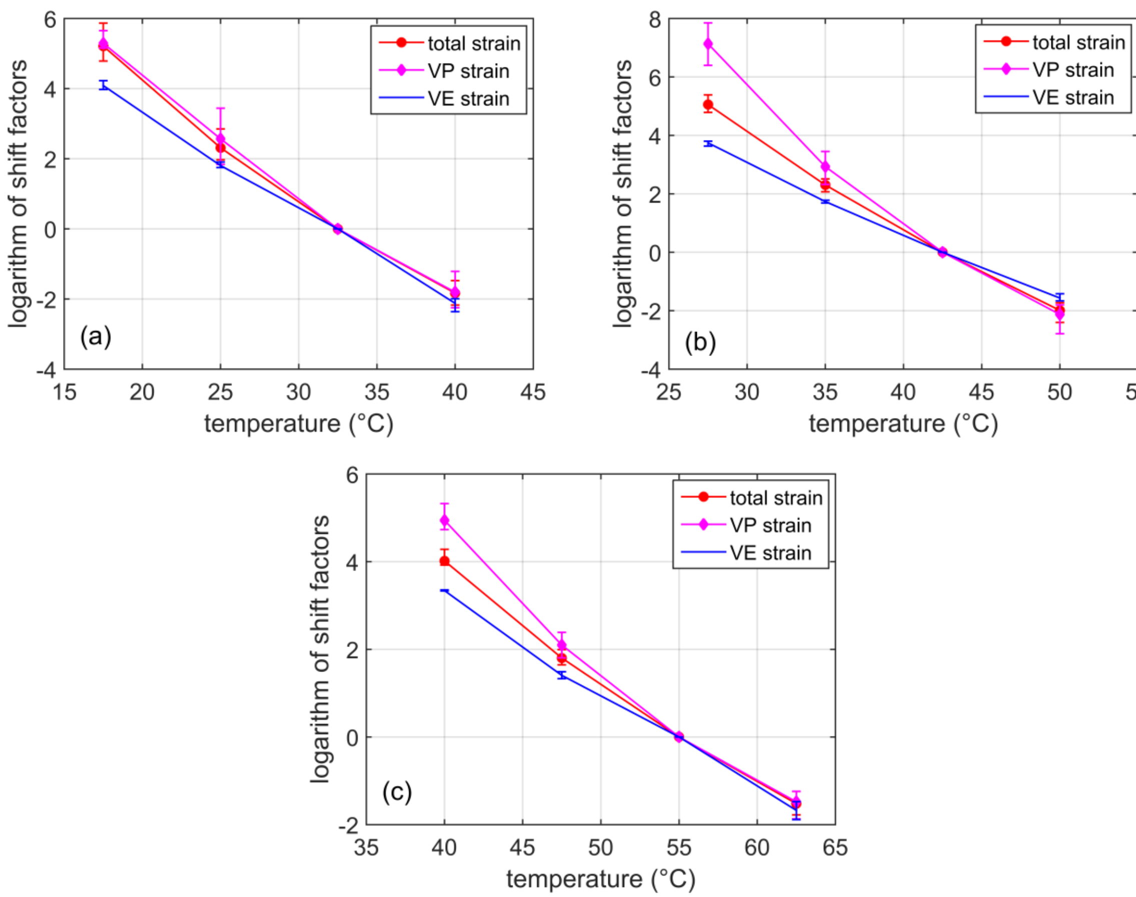

Figure 3.21. Shift factors of total, VE, and VP strains obtained with (a) AC, (b) PMB, and (c) HiMA samples.

`

The error bars in the graphs of $a_{T,T}$ and $a_{T,VP}$ indicate the reliable interval of shift factors at a testing temperature considering biases caused by accumulated permanent contraction strains while the error bars in the graphs of a_T show the variation of a_T obtained from CR test with different stress levels.

Table 3.7: Potential lowest RDs between shift factors.

RD | Mixture	AC	PMB	HiMA
$a_{T,T}$ vs. a_T (%)	11.419	23.367	14.932
$a_{T,VP}$ vs. a_T (%)	18.947	60.156	35.366

3.3.3 Factors causing biases in the obtained results

3.3.3.1 Effects of non-instantaneous application of stress

With a hydraulic servo actuator, the instantaneous stress cannot be exactly applied. In fact, the true creep loading history was approximated by applying a ramp loading function during a short period, called loading ramp time, prior to the application of a constant loading function [see Figure 3.22(a)]. This means that the response strains measured including VE and VP components are significantly lower than the true values at the beginning of the test. Owing to the viscous properties of the materials studied, the effects of the non-instantaneous application of loading rapidly attenuate, and the measured strain approaches its true value as the creep time exceeds some moment, noted as t_c. Therefore, the response strains measured at $t < t_c$ are less reliable and need to be cut off from the results

According to the results reported in Appendix II, in order to ensure the tolerance of 2% for the obtained results, the cut-off times for VE component range from 6.46 to 11.83 times t_0 while the cut-off times for VP strain are slightly higher, varying from 9.51 to 15.15 times t_0. Therefore, with the loading ramp time being set to 0.5s in this study,

`

the measured data before 7.5s were cut off to mitigate the effects of the non-instantaneous application of the stress on the obtained results..

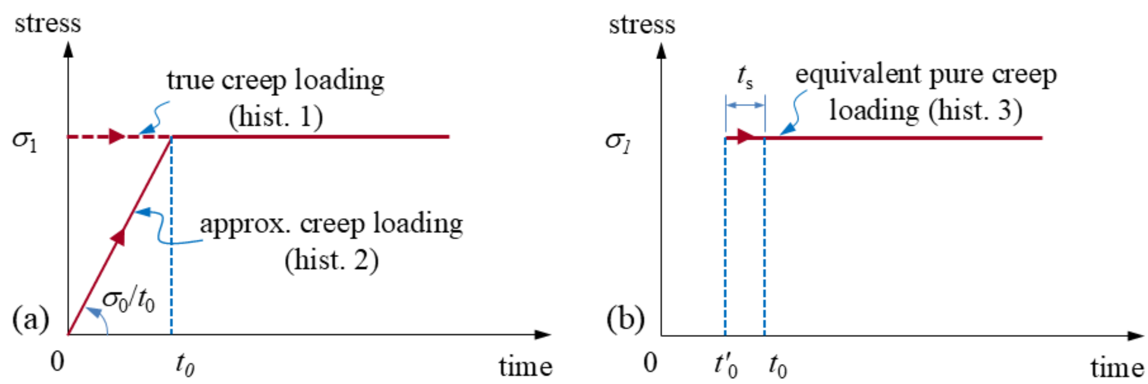

Figure 3.22. Illustration of the applied creep loading history at the beginning of an SSCR test. (a) ramp stress history created by the hydraulic servo actuator used. (b) conversion of ramp stress history into a pure creep stress history.

3.3.3.2 Replication of VP strains and effects of accumulated permanent contraction strain on the measured total and VP strains ,and their companion shift factors

In this study, the determination of VP strains at four temperatures in ascending order caused by one stress level was performed on one single specimen instead of four different virgin specimens. Before running an SSCR test, the specimens were left free of stress for approximately 20h at room temperature for the material to restore as much as possible to its initial conditions, and the LVDTs were reset to zero so that the measured response strain of the specimen in an SSCR test can be considered independent on those obtained in other SSCR tests. With this approach, the effect of inter-specimen heterogeneity is eliminated, and the experimental cost is significantly reduced. However, the VP strain accumulated during preceding SSCR tests certainly affects the development of VP strain in subsequent ones as already pointed out in (Tran et al., 2023). In fact, after performing an SSCR test, the permanent contraction strain inside the specimen increases by an amount equal to the VP strain developed in that SSCR test,

`

which enhances the aggregate interlock and makes the material harden. In other words, the material of the specimen is not virgin before running SSCR tests except the test at the lowest temperature, which makes the measured total and VP strains lower than their true values except the one obtained at the lowest temperature as illustrated in Figure 3.23. This phenomenon certainly causes biases in the construction of the master curves of total and VP strain.

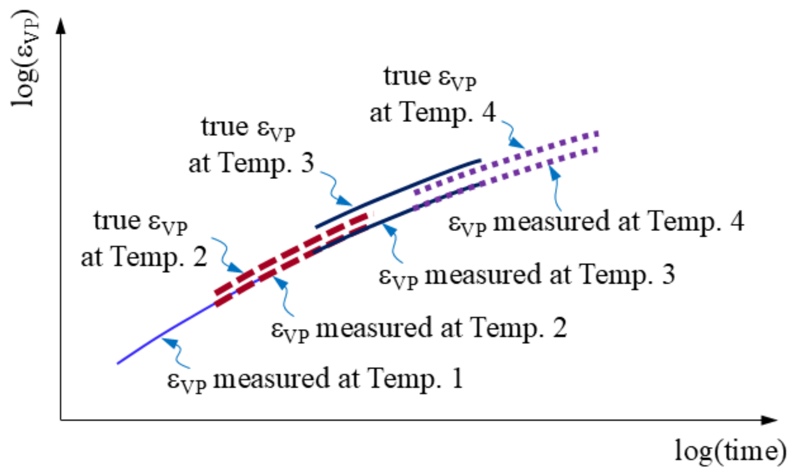

Figure 3.23. Illustration of the effect of cumulative permanent contraction strain on the measured strains.

Therefore, tests were consecutively performed from the lowest to the highest temperatures without alternating repeatability tests to minimize the influence of the cumulative permanent strain on the obtained results. Instead, the replication of the total and VP strains under the same testing conditions was assessed after all SSCR tests had been finished. Three replicate tests for three mixtures were carried out on specimens 1.3, 2.1, and 3.3 to assess the extent of reduction in the total and VP strain induced by the non-virgin conditions of the material before conducting SSCR tests. Since VP strains obtained at the lowest temperatures were not affected by the accumulated permanent contraction strain, no replicate test was conducted at that temperature. The results of the total and VP strains gained in replication tests are all presented in Figures 3.24 – 3.26, which clearly show a considerable reduction in their values as compared with initial

`

SSCR tests due to the extremely high amount of the permanent strain already accumulated in the specimens.

It can be seen in Figure 3.24 – 3.26 that the total and VP strains developed in a subsequent SSCR test are lower than those in preceding SSCR tests due to mechanical hardening effects as previously mentioned. Let r_i^T and r_i^{VP} be the reduction ratios of the total and VP strains at a testing temperature defined as the average ratios of the total and VP strains measured in test replicate i to those measured in test replicate $(i+1)$. As a result, the average reduction ratios of the total and VP strains at that temperature after one cycle of CR test were calculated as $r^{-T} = \Sigma r_i^T/2$, $r^{-VP} = \Sigma r_i^{VP}/2$, and are reported in Table 3.8. The data show that the values of r^{-T} and r^{-VP} are relatively small, respectively lower than 1.08 and 1.25, proving the relatively good level of repeatability of the measured total and VP strains.

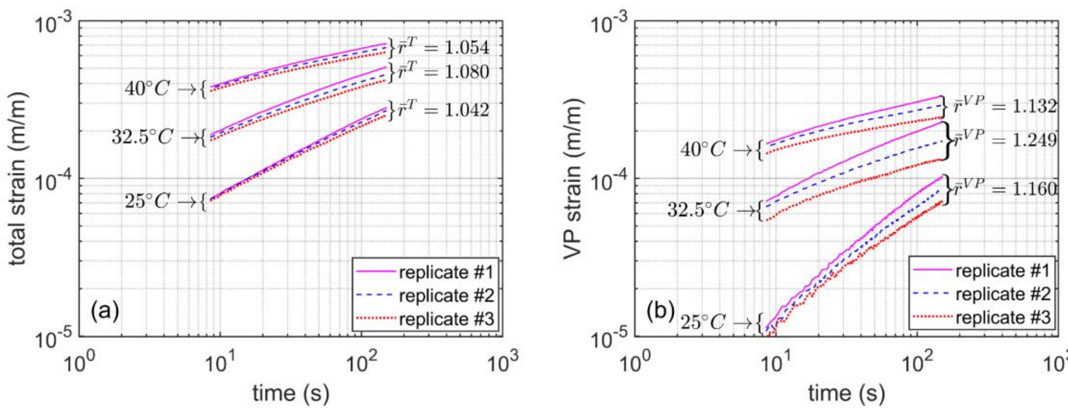

Figure 3.24. Results of replication test of AC mixture at 25, 32.5, and 40°C. (a) Total strains, (b) VP strains.

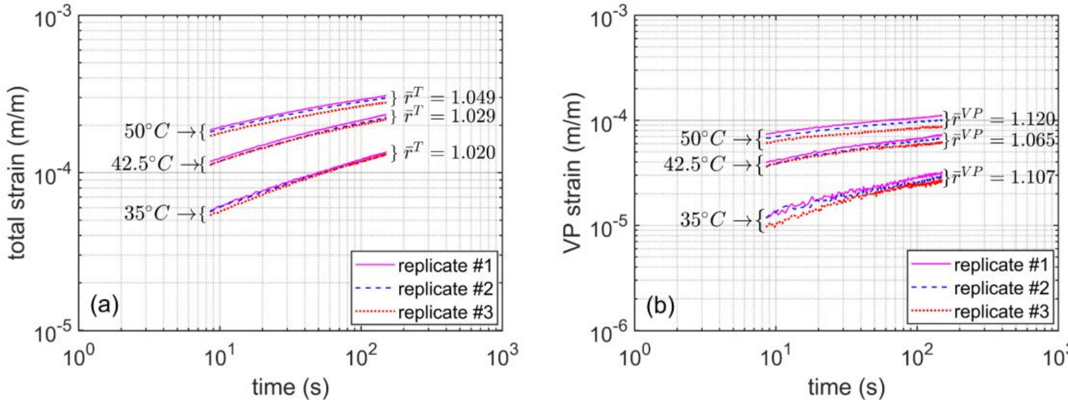

Figure 3.25. Results of replication test of PMB mixture at 35, 42.5, and 50°C. (a) Total strains, (b) VP strains.

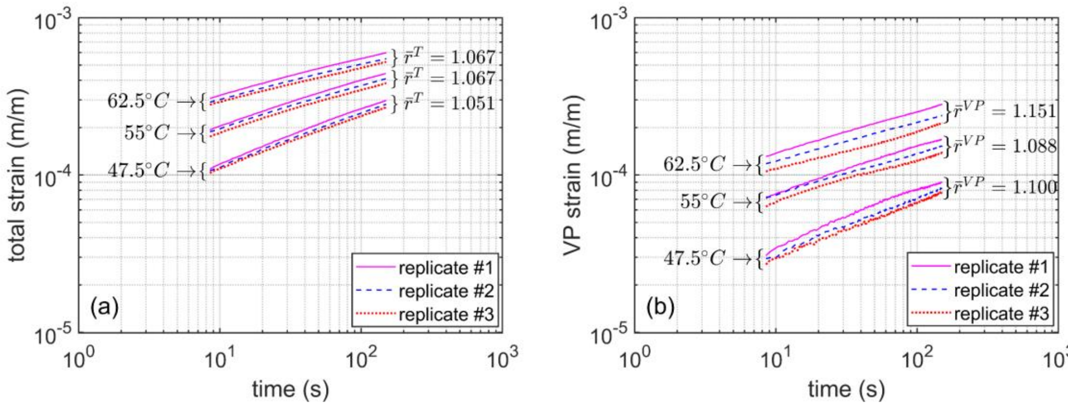

Figure 3.26. Results of replication test of HiMA mixture at 47.5, 55, and 62.5°C. (a) Total strains, (b) VP strains.

Table 3.8: Reduction ratios of VP and total strains.

Mixture	AC			PMB			HiMA		
Temp.(°C)	25	32.5	40	35	42.5	50	47.5	55	62.5
r^{-T}	1.042	1.08	1.054	1.020	1.029	1.049	1.051	1.067	1.067
r^{-VP}	1.116	1.249	1.132	1.107	1.065	1.120	1.100	1.088	1.151

Let us now respectively define R^T and R^{VP} as the average ratio of the true total and VP strains to the measured ones at a testing temperature. Since the values of VP strain at the end of an SSCR test are almost greater than the amount of the cumulative

`

VP strains gained in all previous SSCR tests (see Figure 3.24 –3.26), one can assume that $R^{T} \le r^{-T}$ and $R^{VP} \le r^{-VP}$. With this assumption in hand, the reliable intervals of shift factors for the total strains at a testing temperature T_j can be estimated:

$$\log\left(a_{T,T}\right)\text{-}\ \frac{\log\left(R^{T}\left(T_j\right)\right)}{m_s} \le \log\left(a_{T,T}\right) \le \log\left(a_{T,T}\right)+\ \frac{\log\left(R^{T}\left(T_{ref}\right)\right)}{m_s}, \text{ if } T_j{>}T_{ref}. \quad (3.5)$$

$$\log\left(a_{T,T}\right)\text{-}\ \frac{\log\left(R^{T}\left(T_{ref}\right)\right)}{m_s} \le \log\left(a_{T,T}\right) \le \log\left(a_{T,T}\right)+\ \frac{\log\left(R^{T}\left(T_j\right)\right)}{m_s}, \text{ if } T_j{<}T_{ref}. \quad (3.6)$$

where m_s is the average slope coefficient of $\log\left(\varepsilon_T\right)$ versus $\log\left(t\right)$ in the overlapping region of the two isotherms. The equations for VP shift factors are similar to equations 3.5 and 3.6 and will not be presented here for the sake of brevity. The lower and upper bounds of $a_{T,T}$ and $a_{T,\mathrm{VP}}$ were calculated and are all presented in Figure 3.21. The largest discrepancies of the total and VP shift factors were respectively ±23.17% and ±34.05% (of the mean values) for AC mixture, ±20.07% and ±31.04% for PMB mixture, and ±18.37% and ±26.32% for HiMA mixture.

3.3.4 Agreement between the results of LVE characteristics obtained in the time and frequency domain

To ensure the accuracy of computed VP strain, the LVE characteristics of investigated mixtures determined in time domain were compared to the interconverted one obtained in frequency domain. Dynamic modulus tests were conducted after performing SSCR tests to characterize the LVE properties of the mixture in frequency domain. Just one specimen per mixture was used for testing (specimens 1.2, 2.3, and 3.1) because of well-known and widely used dynamic modulus test. Based on proposed shifting technique in subsection 3.3.2.1, the master curves of DM and PA were constructed and then predicted with HS model. The interconverted CC function determined from the complex modulus function by using the algorithm proposed in

`

subsection 2.2. Then, the interconverted CCs and the back-calculated CCs obtained from SSCR tests were plotted together to consider the agreement between them.

3.3.4.1 Dynamic modulus test

All mixtures were tested at -10, 0, 10, 20, 30, 40, and 50°C and one more temperature (60°C) was performed for HiMA mixture. The considered frequencies at each testing temperature were 0.033, 0.1, 0.33, 1, and 3.33Hz. To compute the DM and PA, the algorithm presented in (AASHTO T342-11, 2011) were used to process the raw data. The temperature equal to 20°C was chosen as the reference temperature for all mixtures.

The master curves of DM and PA of AC, PMB, and HiMA mixtures are respectively showed in Figures 3.27 - 3.29a,b and their shift factors are displayed in Figure 3.30. Meanwhile, the Cole-Cole and Black diagram are respectively presented in Figures 3.27 - 3.29c,d. Because all components of the complex modulus formed a single and relatively smooth curves, so investigated mixtures obey TTSP in the LVE domain.

Regarding determination the HS parameters for predicting the LVE properties of study mixtures, parameters k, h, as suggested by many studies, were chosen based on Cole-Cole diagrams. We observed that value of E_0 affects a little to the errors between the predicted and experimental dynamic moduli yet the effect of it to the time-frequency interconverted results is much larger. Thus, the values E_0 of all mixtures were determined by using static modulus tests to ensure objectivity. Those tests were respectively performed at 55°C, 60°C and 65°C for AC, BMP, and HiMA mixtures. The period of loading time is 300s and the unloading one is 1500s. To computed values of E_0, the formula $E_0 = \sigma / \Delta\varepsilon$ was used, where σ and $\Delta\varepsilon$ are respectively denoted for the stress level applied to the specimen and the recovered strain during the resting period. The remaining parameters of HS model were determined by minimum the error between the predicted and experimental dynamic moduli. All the parameters are presented in

Table 3.9. It should be noted that the stiffness of the HiMA mixture (sample 3.1) obtained in this chapter is slightly lower than that obtained in chapter II (sample 1)–namely, E_0, and E_∞ decrease by 13-18%. This can be explained by variations in stiffness of aggregates as they were exploited at different depths of the quarry.

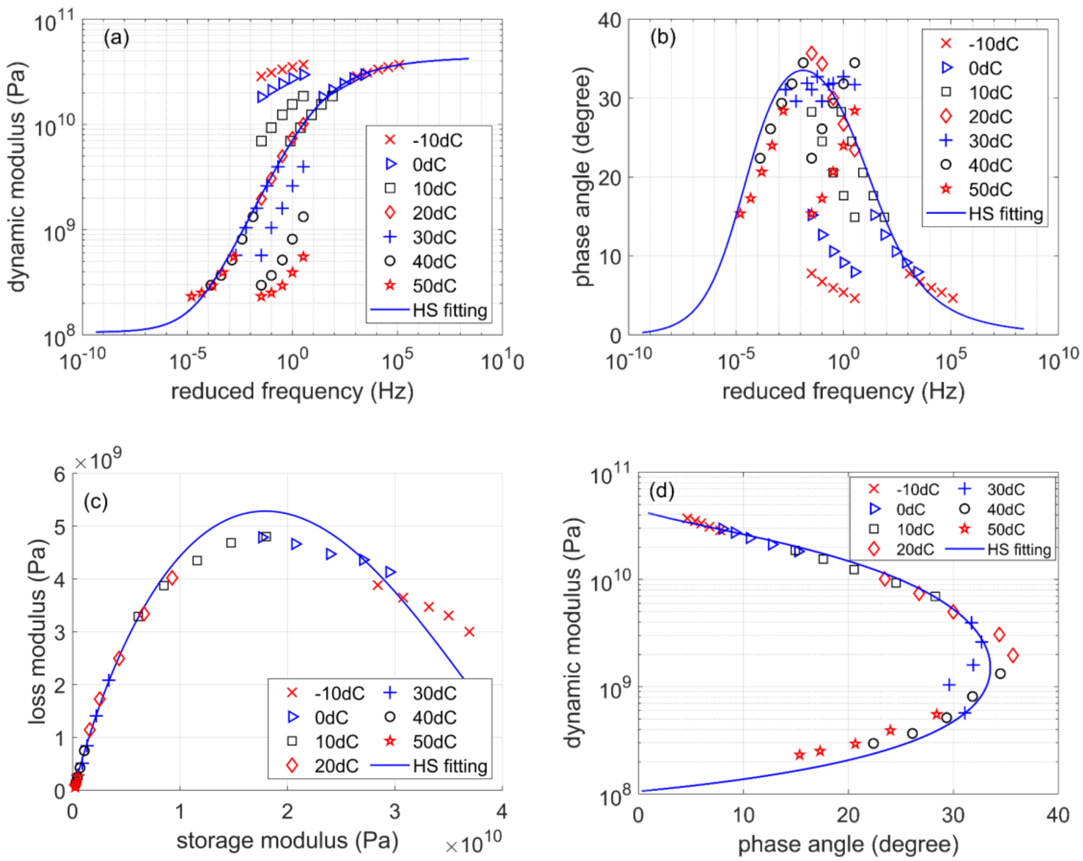

Figure 3.27. Results of LVE characterization of AC mixture. (a) Dynamic moduli (b) phase angles, (c) Cole – Cole diagram, and (d) Black diagram.

Table 3.9:Huet-Sayegh parameters of all studied mixtures.

Mixture	E_0 (MPa)	E_∞ (MPa)	k	h	δ	τ (s)	T_{ref} (°C)
AC	105.923	44232.438	0.170	0.435	0.770	0.005	20
PMB	98.834	31107.174	0.170	0.375	0.611	0.006	20
HiMA	115.355	39509.649	0.180	0.430	3.121	1.925	20

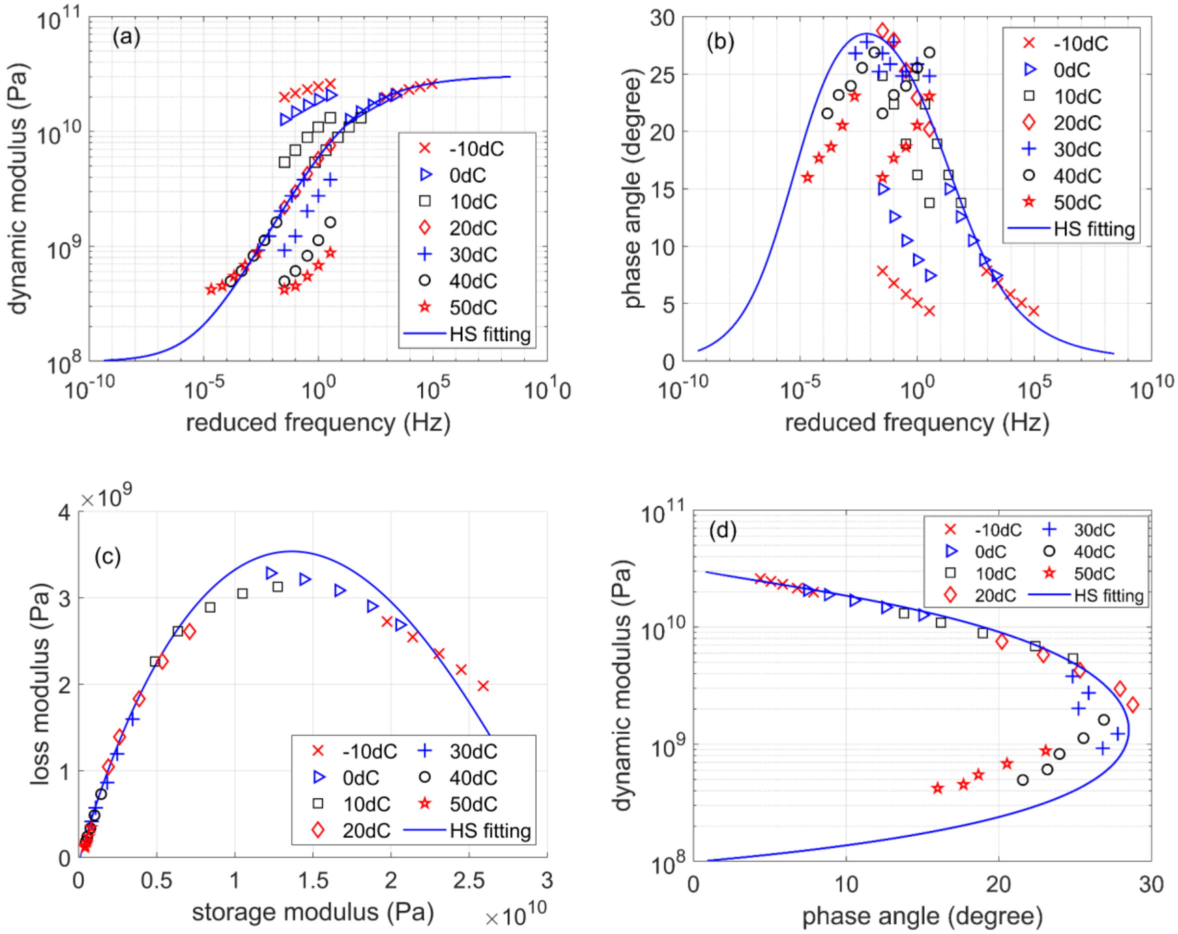

Figure 3.28. Results of LVE characterization of PMB mixture. (a) Dynamic moduli (b) phase angles, (c) Cole – Cole diagram, and (d) Black diagram.

Figures 3.27 - 3.29 show that the HS model can predict very well the LVE properties of all mixtures. In fact, the maximum RE between the predicted and experimental respectively are just 2.94% and 12.12% for DM and PA for all investigated mixtures (see Table 3.10). It is obvious that the RE of predicted PA is higher than the RE of predicted DM for all mixtures which involves it is more difficult to measure the PA than the DM as reported in (Rowe, 2009; Zhang et al., 2020; Phan et al., 2022).

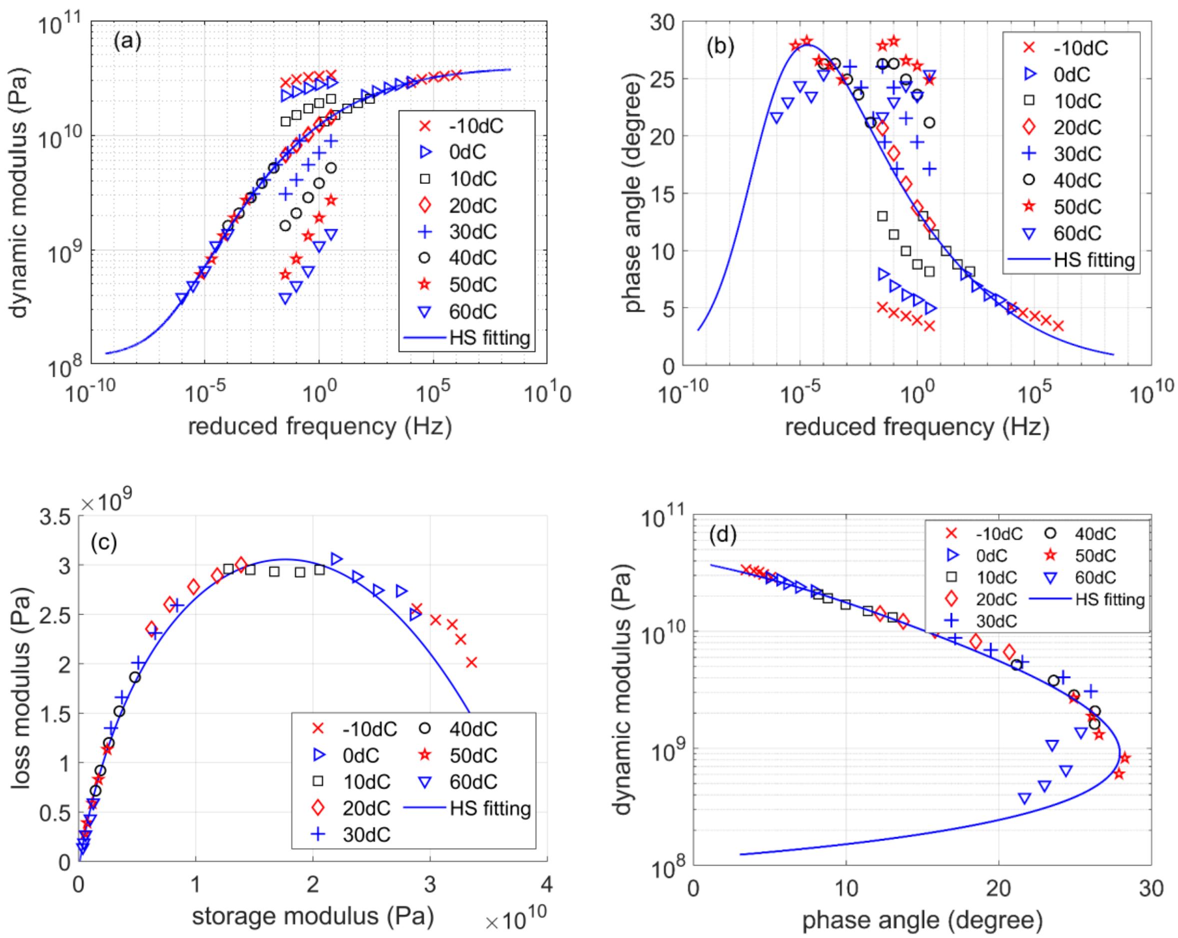

Figure 3.29. Results of LVE characterization of HiMA mixture. (a) Dynamic moduli (b) phase angles, (c) Cole – Cole diagram, and (d) Black diagram.

Table 3.10: The relative errors (RE) between the experimental and predicted master curve of dynamic modulus and phase angle.

Mixture	$RE^{\lvert E^{*}\rvert}$ (%)	RE^{φ} (%).
AC	2.937	9.714
PMB	2.866	12.117
HiMA	2.352	7.602

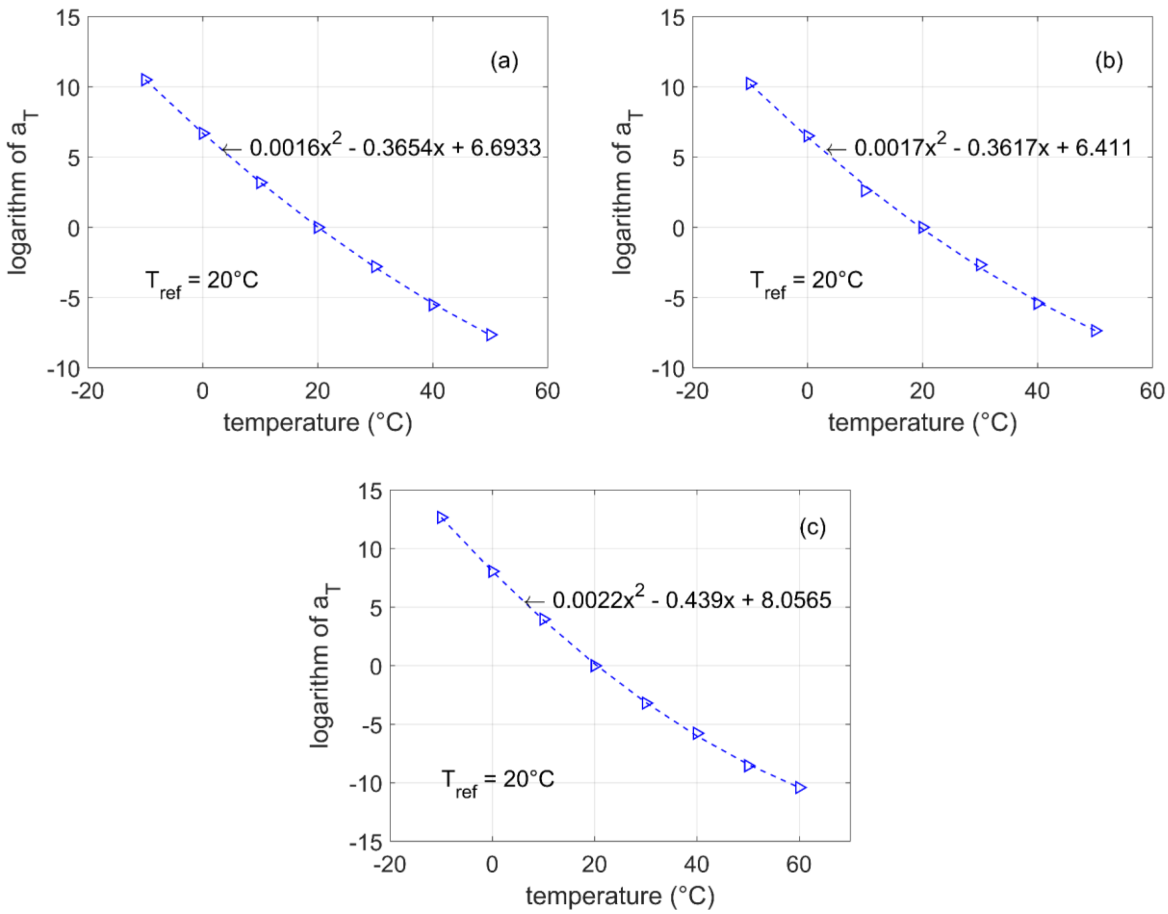

Figure 3.30. VE shift factors of (a) AC mixture, (b) PMB mixture, and (c) HiMA mixture.

3.3.4.2 Comparison of shift factors in the frequency and time domain

For avoiding interpolation, the value of shift factors in both domain (frequency and time) was shifted to one common temperature at which both they were experimentally determined. Those chosen reference temperatures are respectively 40°C, 50°C, and 40°C for AC, PMB, and HiMA mixture. Figure 3.31 shows that it agrees well between the shift factor in frequency and time domain. In fact, relative differences between them are respectively 17.94%, 4.75%, and 5.97% for AC, PMB, and HiMA mixtures.

`

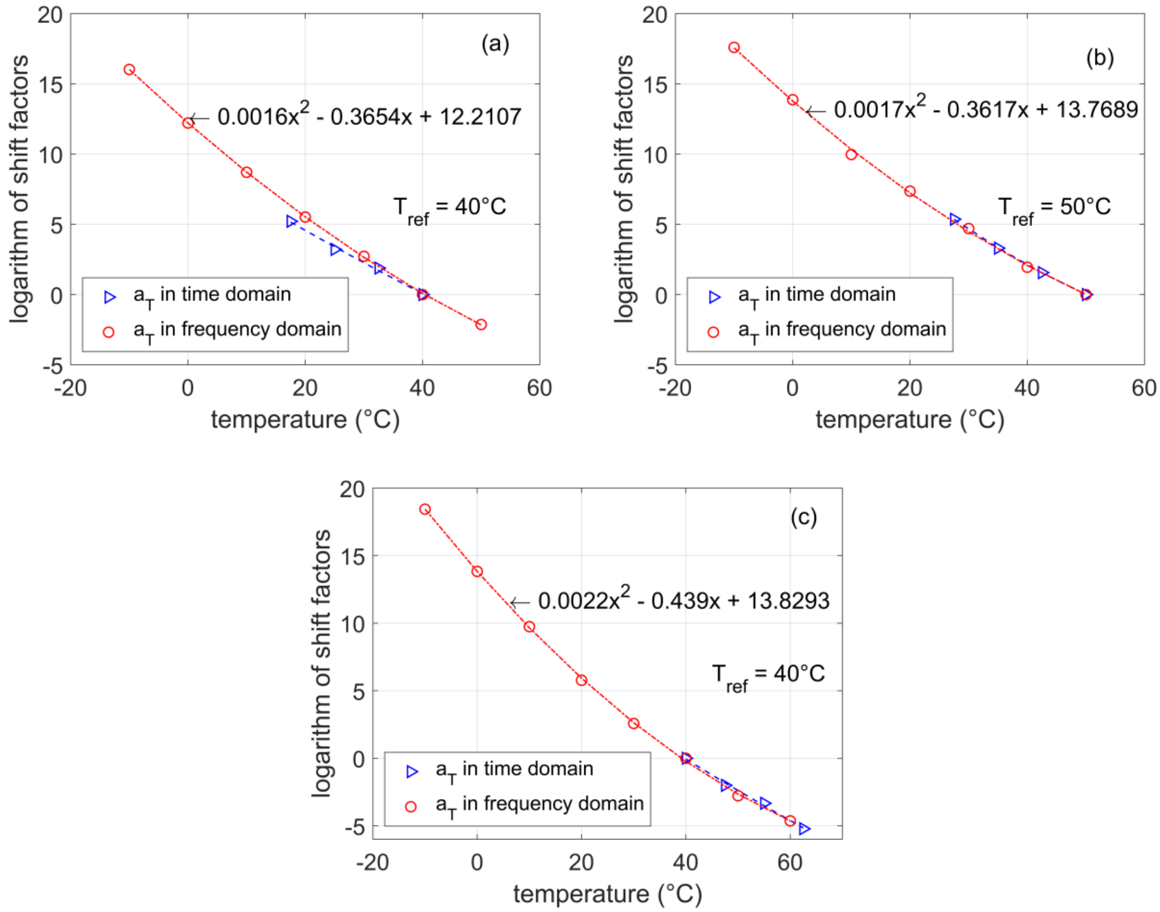

Figure 3.31. Comparison of shift factors in frequency and time domain. (a) AC mixture, (b) PMB mixture, and (c) HiMA mixture.

3.3.4.3 Comparison of creep compliances

Figure 3.32 plotted both back-calculated CCs from SSCR test and interconverted CCs from data of DM test of specimens 1.2, 2.3, and 3.1 to evaluate relative difference between them. It can be seen that both of them agree well together. The maximum RD of all mixtures is just 8.38% (for BMP mixture) show that the results of computed LVE characters from SSCR tests are reliable. It means that the obtained VP strains are validity.

`

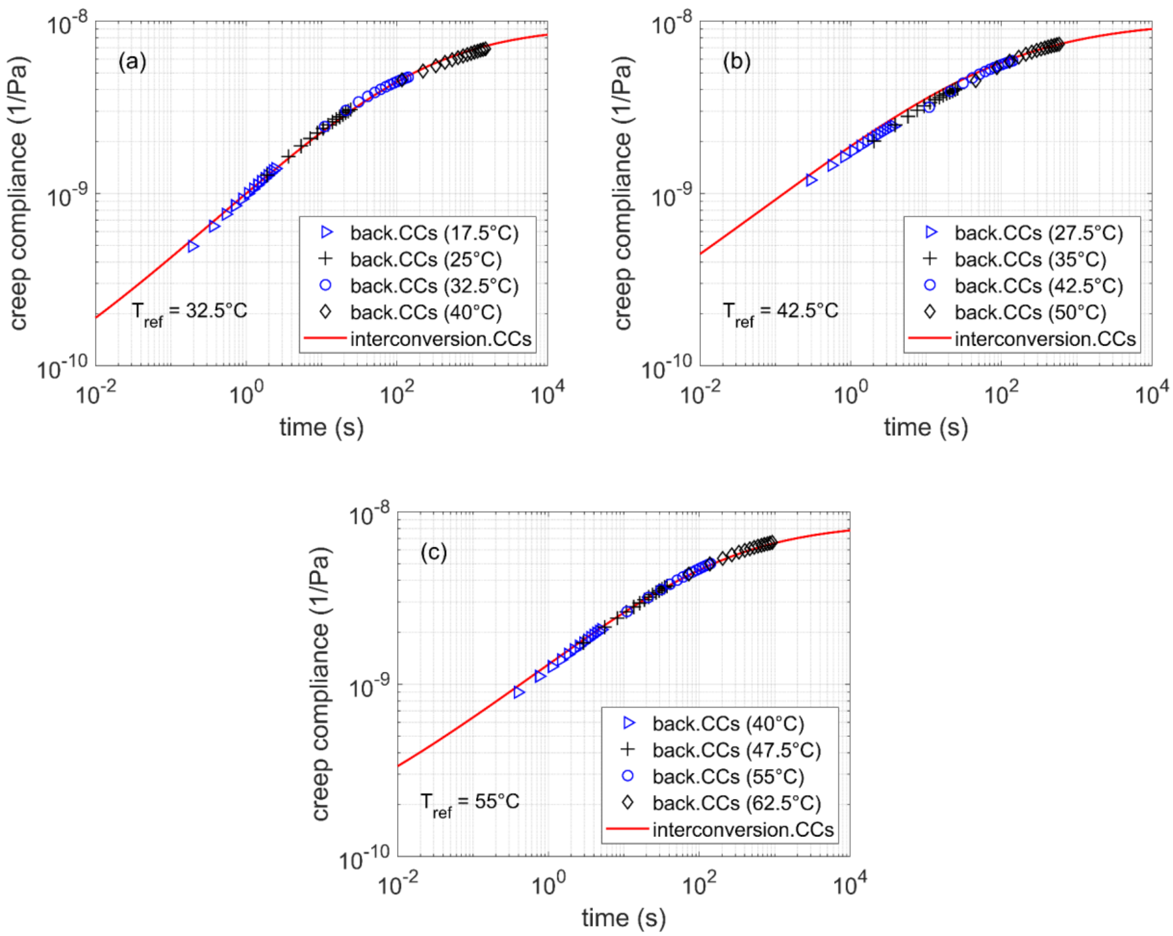

Figure 3.32. Back calculated CCs versus interconverted CCs. (a) specimen 1.2, (b) specimen 2.3, and (c) specimen 3.1.

3.3.5 Application of TTSP to characterize and predict the permanent deformation behavior of AC, PMB, and HiMA mixtures

3.3.5.1 Comparison of the resistance to PD of mixtures

For comparison the resistance to PD of the investigated mixtures, the VP strain master curves caused by the same stress levels applied and at the same reference temperature (40°C) of those mixtures were plotted in the same Figure 3.33. Overall, it can be ranked the resistance to PD of three mixtures in ascending order as follows: AC, BMP, and HiMA mixtures. Case in point of $\sigma = 23.81\ \text{kPa}$, the loading periods was approximately 2.57s, 101.6s and 7922s for AC, PMB, and HiMA mixtures for VP strain achieved a value of $10^{-4}(\text{m/m})$ (see Figure 3.52 a). Another exemplification, with the same value of loading time equal to 100s and value of applied stress equal to 53.57 kPa, the accumulated VP trains were $1.61\times10^{-3}(\text{m/m})$ for AC mixture, 3.28×10^{-4} for PMB mixture, and 3.28×10^{-5} for HiMA mixture. It is obvious that the resistance to permanent deformation between all mixtures is large enough differences, so the ranking is effective.

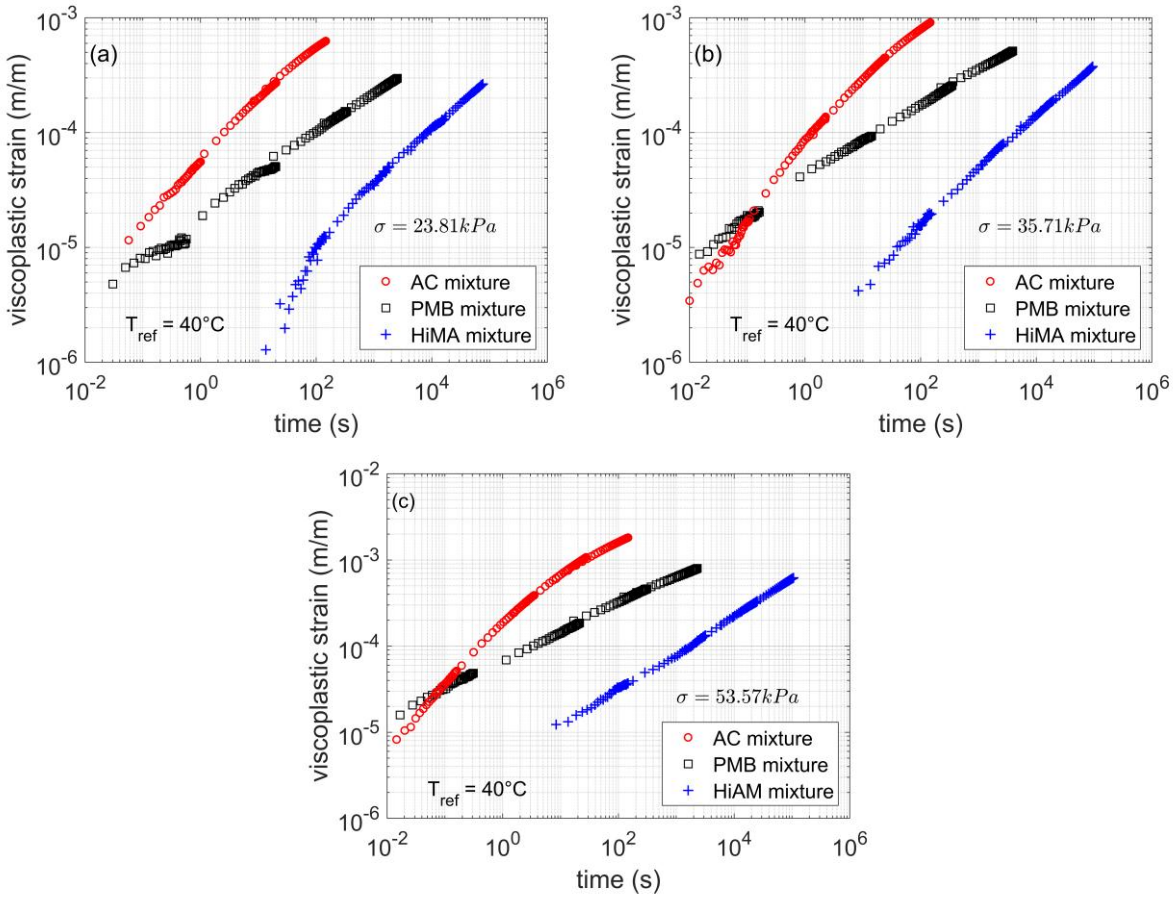

Figure 3.33. Comparison of the resistance to PD of all mixtures at different stress levels: (a) 23.81 kPa, (b) 35.71 kPa, and (c) 53.57 kPa.

In fact, at a loading time is shorter than 0.12s and stress levels of 35.71 and 53.57kPa, the obtained VP strain of AC mixtures are smaller than those of PMB mixtures (see Figures 3.33b,c). With those conditions, the values of the obtained VP strains are too small, approximately $10^{-5}(\text{m/m})$, so the errors of measurement devices may cause

`

this observation. Therefore, it does not ensure that the resistance to PD of AC mixtures is better than PMB mixture at an extremely short loading time.

3.3.5.2Characterizing and predicting the permanent deformation behaviour of AC, PMB, and HiMA mixtures

In this subsection, the applied of VP strains master curves was performed to characterize and predict the permanent deformation behavior of investigated mixtures. To monitor the development of VP strain in the sample subjected to pure creep loading, the adopted model is the simple power law one proposed in (Hua, 2000):

$$\dot{\varepsilon}_{VP}(t) = Abt^{b-1}\sigma^m,\ \varepsilon_{VP}(t) = \int_0^t \dot{\varepsilon}_{VP}(\tau)d\tau = At^b\sigma^m, \tag{3.7}$$

where b is the slope coefficient of the predicted VP strain curve in the double logarithmic scale, m controls the nonlinear effect of stress level, and A is just a correcting factor. For calibrating the model of each mixture, the used master curves of VP strain are the master curves caused by the highest and lowest stress levels. The result of prediction was compared to the remaining master curve of VP strain for assessing the accuracy. By using the Solver toolbox of MS Excel software, the parameters of model were determined by minimizing the sum of squared errors between the predicted and measured VP strains in the double logarithmic scale. The best-fit model parameters were presented in Table 3.11.

Table 3.11: Best-fit model parameters for predicting VP strains of all mixtures exerted by a pure creep loading (the stress and time are in SI unit).

Mixture	A	b	m
AC	7.296×10^{-12}	0.538	1.459
PMB	6.454×10^{-11}	0.319	1.298
HiMA	2.498×10^{-10}	0.454	1.080

The experimental and computed, with the best-fit parameters, VP strains at the reference temperature caused by the stress levels of 23.81 and 53.57kPa of AC, PMB, and HiMA mixtures were presented respectively in Figures 3.34. It can be seen that the

`

computed VP strains of PMB and HiMA mixtures agree well with the experimental those. Meanwhile, the prediction of VP strains of AC mixture is less accurate because the master curve of that mixture is more complex in double logarithmic scale plots. Indeed, although the coefficients of determination of all mixtures are high $\left(R^2 > 0.974\right)$, the REs between the best-fit and experimental master curves of vicous plastic strain of AC mixture surpasses 16.151% while that of PMB and HiMA mixtures do not exceed 4.732%, and 9.747%.

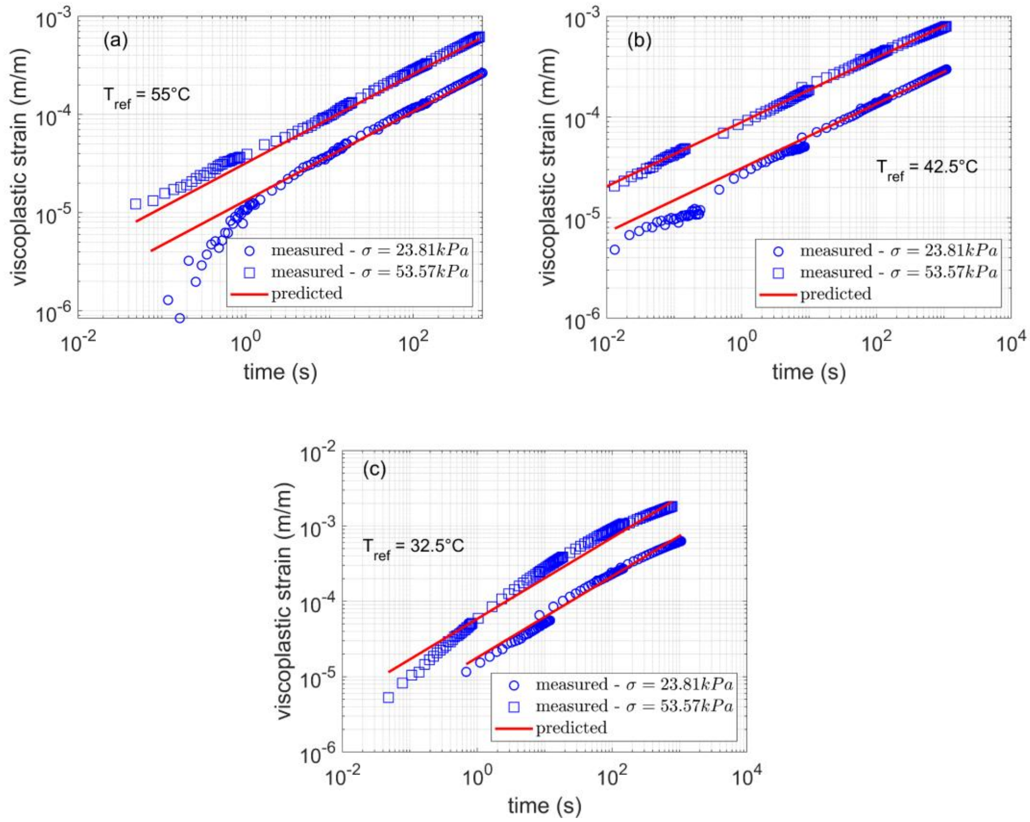

Figure 3.34. Determination of model parameters based on the master curve of VP strains at the reference temperature equal 32.5°C caused by stress levels equal 28.81 and 53.57kPa: (a) HiMA mixture, (b) BMP mixture, (c) AC mixture

The evolutions of VP strains of investigated mixtures at various testing temperature and stress level 35.71 kPa were predicted by using the obtained best-fit parameters. Then, at any temperature, the VP strain can be determined as follows:

$$\varepsilon_{VP}\left(t,T\right) = A\cdot\left(t/a_{T,VP}\left(T\right)\right)^{b}\sigma^{m}. \tag{3.8}$$

where $a_{T,VP}$ is called VP reduce time which is used to convert the real loading time at a temperature into the equivalent one at the reference temperature. Those shift factors are the average of those determined from tests with the stress levels 23.81 and 53.57kPa. The results prediction of VP strain at investigate temperatures of each mixture were presented in Figures 3.35.

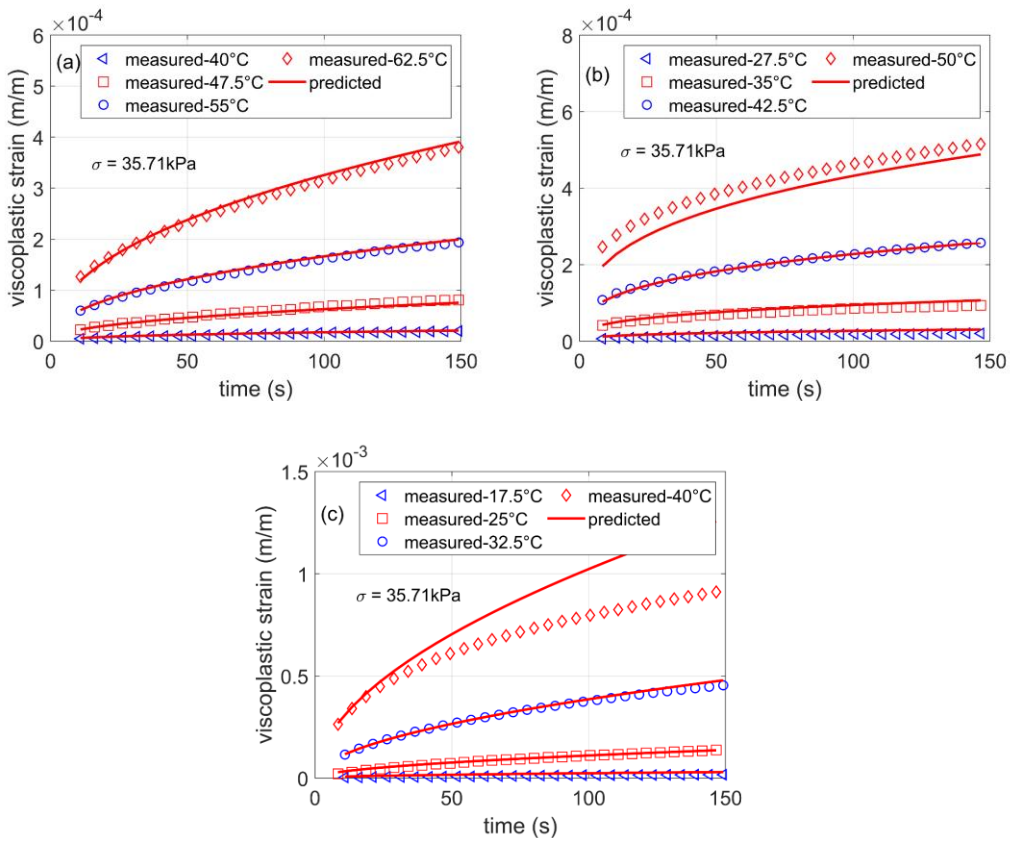

Figure 3.35. Prediction of VP strains caused by the stress level 35.71kPa at various temperatures: (a) HiMA mixture, (b) BMP mixture, (c) AC mixture

`

Table 3.12: Relative errors of the prediction of VP strains of AC, PMB, and HiMA specimens caused by stress level 35.71kPa

AC mixture		PMB mixture		HiMA mixture	
Temp. (°C)	RE (%)	Temp. (°C)	RE (%)	Temp. (°C)	RE (%)
17.5	80.820	27.5	48.724	40.0	12.034
25.0	3.544	35.0	11.188	47.5	6.574
32.5	3.162	42.5	0.848	55.0	3.017
40.0	27.937	50.0	8.499	62.5	2.944

Because the VP strains were computed by eliminating the VE strains from the measured data, the accuracy of predicted VP strains should be verified by comparing a predicted quantity with a directly measured one. For that purpose, the prediction of total strains of investigated mixtures in SSCR test were calculated at all testing temperatures and the stress level 35.71kPa. It is worth noting that the predicted total strains were determined by summing the predicted VP and VE strains, computed with the average CC function obtained from the recovery data of tests with the stress levels 23.81 and 53.57kPa. The results of predicted total strains are plotted together with the measured one in Figure 3.36 – 3.38 showed that both are good agreement, not including the high error cases of the predicted VP strain (AC sample at 17.5°C and 40°C and PMB sample at 27.5°C) as above mentioned. The REs between the predicted and measured total strains of all samples were calculated and presented in Table 3.13 The results showed that they are rather small in most cases, ranging from 1.724 to 28.141%. It proved that pure PD behavior of the studies mixtures can be characterized by the constructed master curves of VP strains and their companion VP shift factors.

`

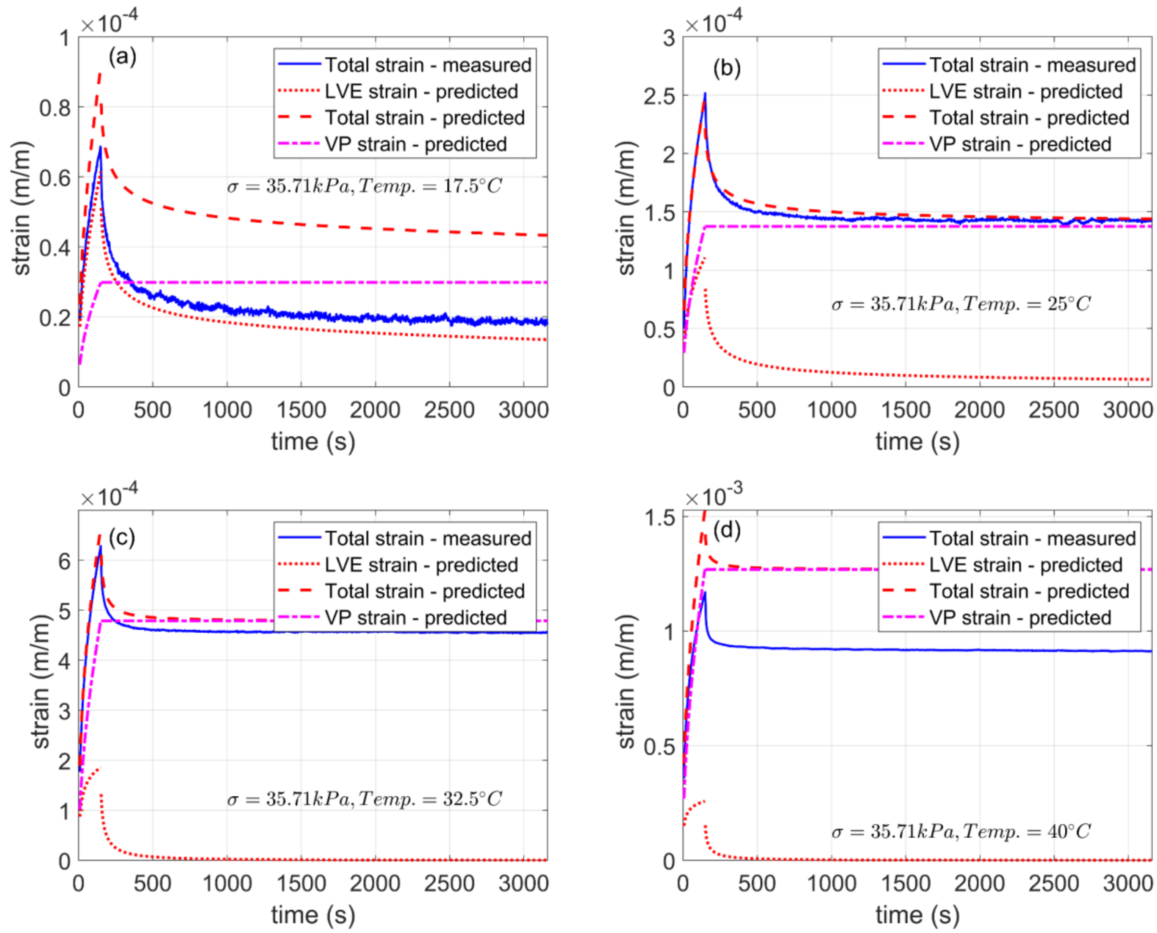

Figure 3.36. Comparison of the predicted total strain with the measured strain at various temperatures of AC mixture.

It is worth noting that the total strains of the samples cannot be predicted with just VE component because the predicted VE strains tended to zero with enough unloading time. Moreover, there is agreement between the prediction values at the end of the loading phase of VP strains and the asymptotic values of the measured strains. In fact, the relative differences did not almost exceed 12.52% between them so the predicted VP with the best-fit parameters well described the development of the real PD in the samples. This confirms that the irreversible strain in the sample did not change during the unloading time is an appropriate assumption. Therefore, the total strain at least

`

comprises of two components, an able to recovery one being the VE strain, and an unable to recovery one mainly constituted by the VP strain as assumed above.

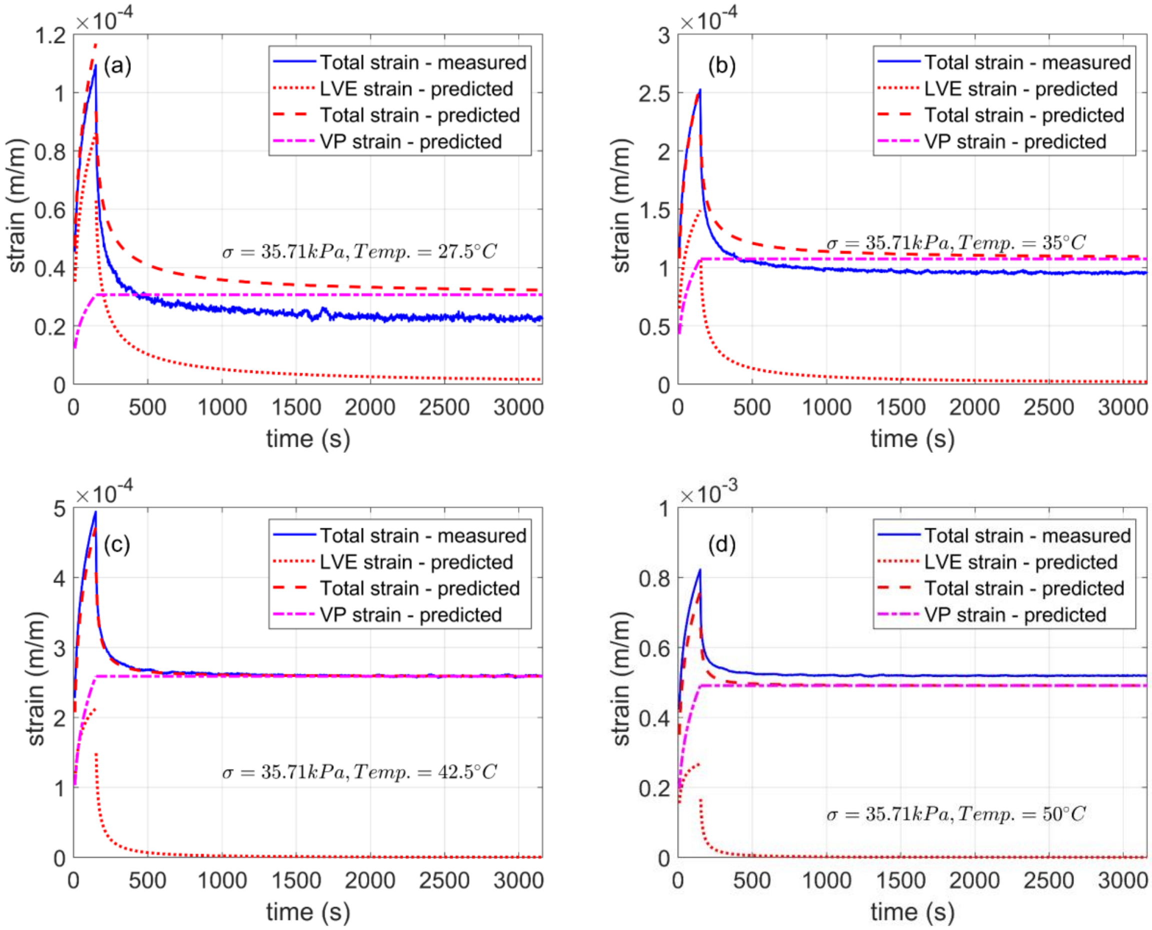

Figure 3.37. Comparison of the predicted total strain with the measured strain at various temperatures of PMP mixture.

`

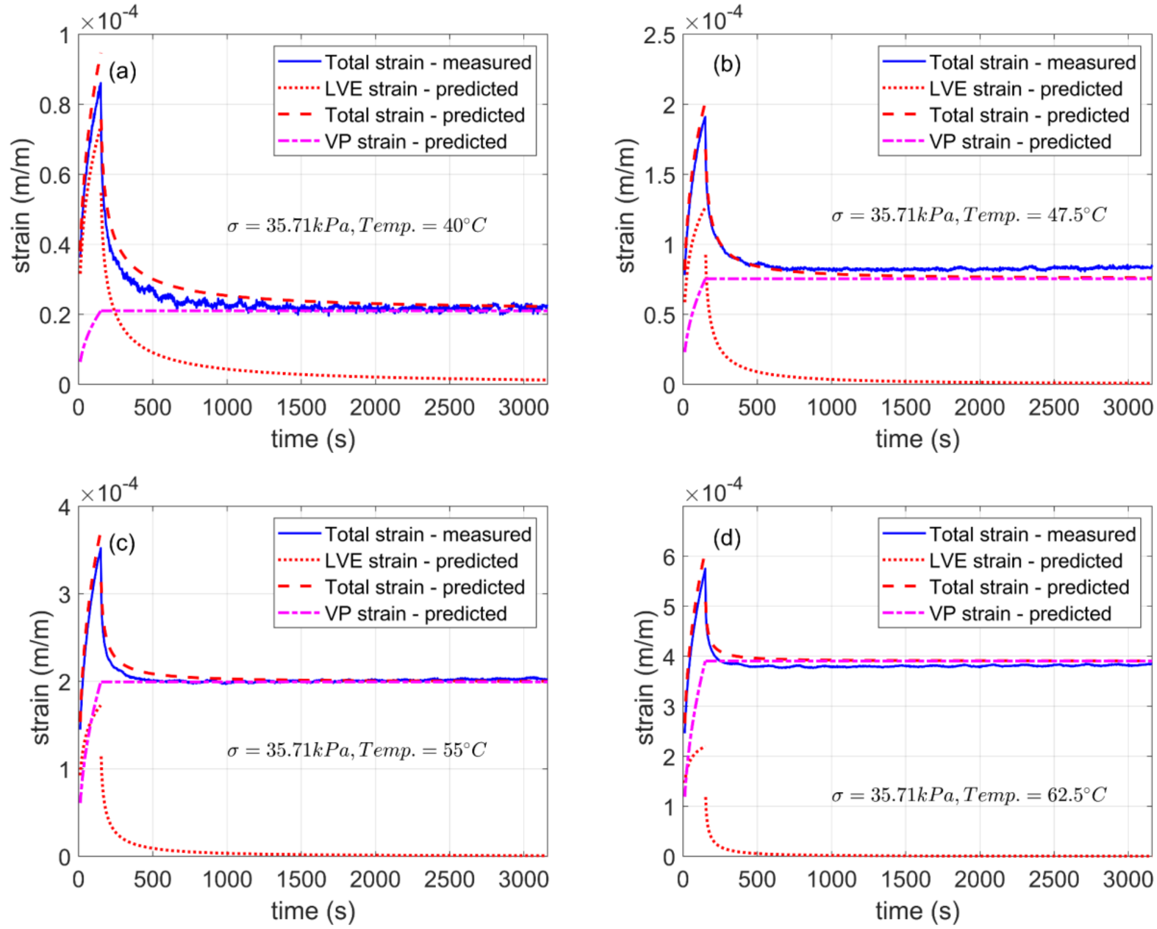

Figure 3.38. Comparison of the predicted total strain with the measured strain at various temperatures of HiMA mixture.

Table 3.13: Relative errors of the prediction of total strains of AC, PMB, and HiMA specimens caused by stress level 35.71kPa

AC mixture		PMB mixture		HiMA mixture	
Temp. (°C)	RE (%)	Temp. (°C)	RE (%)	Temp. (°C)	RE (%)
17.5	113.405	27.5	38.906	40.0	11.252
25.0	10.085	35.0	28.141	47.5	13.140
32.5	5.076	42.5	1.724	55.0	2.797
40.0	37.703	50.0	5.903	62.5	3.460

`

3.4 Conclusions of Chapter III

In this chapter, VE and VP behavior of three asphalt mixtures including AC, PMB and HiMA mixtures were successfully characterized using SSCR tests and the companion back-calculation algorithm. Owing to the proposed shifting method, the VE and VP shift factors were separately identified and demonstrated to be obviously different. With the obtained shift factors, the master curves of CCs and VP strains were constructed. The results showed that the CCs obtained with SSCR test agreed well with those interconverted from dynamic modulus data, which confirms the reliability of the obtained VP strains. All master curves of VP strain were relatively smooth and monotonous, ensuring an injective relationship between time and VP strain. In addition, all VP shift factors were independent of the stress levels applied and injective with the temperatures. Therefore, TTSP still holds in VP domain, at least with the examined asphalt mixtures.

Owing to the results of this work, the VP behavior of asphalt mixtures can be investigated over a wide range of loading time by conducting a series of SSCR tests with reasonable testing times instead of performing extremely long-time SSCR tests. Once the master curves of VP strain are constructed, the resistance to PD of asphalt mixtures will be assessed with high sensitivity. In fact, AC mixture was demonstrated to be the most vulnerable to PD, compared to PMB mixture and HiMA mixture. Furthermore, the master curves of VP strain can be used to calibrate rutting prediction models, which will be carried out in future works.

`

CHAPTER IV

CHARACTERIZATION OF ASPHALT MIXTURE VISCOPLASTIC YIELDING

4.1 Introduction

For modeling and predicting this behavior in asphalt concrete layers, many models have been proposed based on coupled viscoelastic and viscoplastic theories. Since the separation point between reversible and irreversible behavior in stress–strain curves of asphalt concretes are unclear, some models were proposed without incorporating the yield surface of asphalt concrete (Lu and Wright, 1998; Cao and Kim, 2022;…), while other authors implemented a yield surface in their models (Nguyen, 2017; Darabi et al., 2019; …). Therefore, the characteristic of the yield surface applied to asphalt concrete is crucial to properly predict the accumulation of permanent deformation strain.

By performing creep–recovery tests at 25°C with different stresses, Perl et al. (1983) established the relationship between plastic strain and applied stress, then they reported that the yield stress of sand–asphalt mixture does not exist. However, the authors did not disclose how to determine the instantaneous strain at the moment of applying and removing the load. Later, due to equipment limitation, Drescher et al. (1993) suggested that strains at the first ten seconds of the loading and resting period in a creep–recovery test can be considered the instantaneous parts of the total and elastic strains, respectively. Their study indicated that the plastic strain is a linear function of stress, similar to the total strain and elastic strain. In other words, there is no yield stress for the investigated asphalt material.

Saadeh et al. (2007) reported that it highly depends on the test set-up and the selected time for what is considered "instantaneous" response to determine the

`

instantaneous strain and decouple it from the time-dependent strain. Therefore, several authors used monotonic strain rate tests to identify the yield stress of asphalt mixtures (Zhang et al.,2013; Darabi et al.,2019). However, the applied strains in those tests are not in a low–train regime. Moreover, those studies do not specify a clear definition of the separation point in the stress-strain curve for asphaltic materials (Nguyen, 2017; Cao and Kim, 2022). Thus, the yield stress identification methods are controversial and do not convince readers. Therefore, the objective of this section is to propose a method capable of identifying the viscoplastic yield stress—if it exists—within the low-strain regime.

4.2 Theoretical framework

In this section, the slope creep-recovery (SCR) test was used to characterize the viscoplastic yield stress of an asphalt concrete (AC) mixture. The applied stress history in an SCR test is illustrated in Figure 4.1. A ramp function of the stress was applied during a certain duration before being removed, for the strain to recover a part of its reversible part. Typical response strain histories in an SCR test are illustrated in Figure. 1(b) and (c).

As mentioned in subsection 2.3.1.3, VP strain can be computed as follows

$$\varepsilon_{vp}(t) = \varepsilon_T(t) - \varepsilon_{ve}(t) \; . \qquad (4.1)$$

Since the recovery period is a purely viscoelastic process, the VE behavior of the material can be extracted with high accuracy based on the recording data during this period (Nguyen et al., 2021; Tran et al., 2023). The VE strain during the loading phase can be predicted. Then, the VP strain can be computed using equation 4.1.

Let us assume that the material exhibits a viscoplastic yield point noted as σ_y, then the following equation holds:

$$\begin{cases} \dot{\varepsilon}_{vp}(t) = 0, \ \text{for} \ \sigma \le \sigma_y \\ \dot{\varepsilon}_{vp}(t) > 0, \ \text{for} \ \sigma > \sigma_y \end{cases} . \qquad (4.2)$$

`

Consequently, the VP strain curve follows the typical shape as illustrated in Figure 4.1(b), wherein an observable "plateau zone" of zero VP strain will be observed. Otherwise, the VP strain evolves regardless of the applied stress level, and $\sigma_y = 0$ in this case.

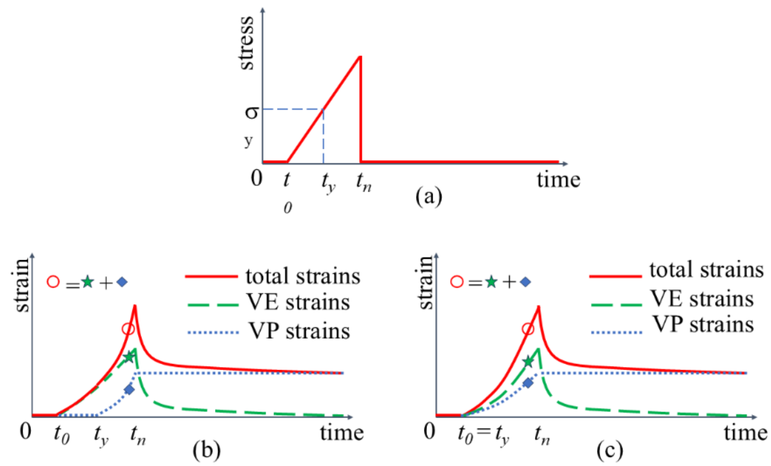

Figure 4.1. Description of SCR test: (a) applied stress history, (b) response strain in case viscoplastic yield stress exists, and (c) response strain in case viscoplastic yield stress does not exist.

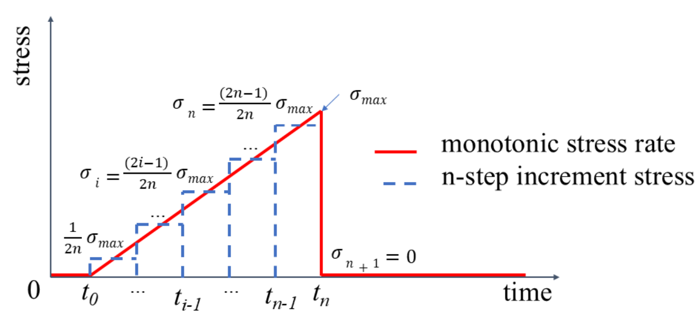

Figure 4.2. Discretization of the stress history used in the GCR algorithm.

The generalized creep-recovery (GCR) algorithm proposed in subsection 2.4.3 was used to post-process SCR test data, which can be summarized as follows. Let the loading period of the stress history be divided by *n* subintervals as illustrated in Figure

`

4.2. As a result, the discretized stress value at a time $t_i = t_0 + i*(t_n - t_0)/n$ is $\sigma_i = (2i+1)\cdot\sigma_{\max}/(2n)$.

Assuming that VE strains are still in the low-strain regime, the Boltzmann superposition principle is applied (Tschoegl, 1989; Cho, 2016):

$$.\sigma(t) = \int_{-\infty}^{t} E(t-\tau)\dot{\varepsilon}(\tau)d\tau; \quad \varepsilon(t) = \int_{-\infty}^{t} D(t-\tau)\dot{\sigma}(\tau)d\tau \ . \tag{4.3}$$

Applying time discretization, the VE strains can be computed by using the following formulas:

$$\begin{aligned}\varepsilon_{ve}(t) &= D(t-t_0)\frac{\sigma_{\max}}{2n} + \sum_{i=1}^{m\le n-2} D\left[t - t_0 - \frac{i(t_n - t_0)}{n}\right]\frac{\sigma_{\max}}{n} \\ &+ D\left[t - t_0 - \frac{(n-1)(t_n - t_0)}{n}\right]\frac{\sigma_{\max}}{2n}, \text{for } t_0 < t \le t_n\end{aligned} \tag{4.4}$$

$$\begin{aligned}\varepsilon_{ve}(t) &= D(t-t_0)\frac{\sigma_{\max}}{2n} + \sum_{i=1}^{n-2} D\left[t - t_0 - \frac{i(t_n - t_0)}{n}\right]\frac{\sigma_{\max}}{n} \\ &+ D\left[t - t_0 - \frac{(n-1)(t_n - t_0)}{n}\right]\frac{\sigma_{\max}}{2n} - D(t - t_n)\sigma_{\max}, \text{for } t > t_n.\end{aligned} \tag{4.5}$$

It is worth noting that the VP strains do not develop in the unloading period:

$$\varepsilon_T(t) = \varepsilon_{ve}(t) + \varepsilon_{vp}, \text{ for } t \ge t_n, \tag{4.6}$$

where ε_{vp} is the accumulated VP strain at the end of the loading period. As a result,

$$\varepsilon_T(t_n) = \varepsilon_{ve}(t_n) + \varepsilon_{vp}. \tag{4.7}$$

Subtracting both sides of equation (4.7) from those of equation (4.6) to eliminate the contribution of VP strain, one has:

$$\varepsilon_T(t_n) - \varepsilon_T(t) = \varepsilon_{ve}(t_n) - \varepsilon_{ve}(t), \text{ for } t \ge t_n. \tag{4.8}$$

Then, by substituting the values of VE strain calculated from equation (4.4) and equation (4.5) into equation (4.8), one gains:

`

$$\frac{\varepsilon_T(t_n)-\varepsilon_T(t)}{\sigma_{\max}}=\frac{1}{2n}\left\{D\left(t_n-t_0\right)+D\left[t_n-t_0-\frac{\left(n-1\right)\left(t_n-t_0\right)}{n}\right]-D\left(t-t_0\right)\right.$$
$$\left.-D\left[t-t_0-\frac{\left(n-1\right)\left(t_n-t_0\right)}{n}\right]\right\}+\frac{1}{n}\left\{\sum_{i=1}^{n-2}D\left[t_n-t_0-\frac{i\left(t_n-t_0\right)}{n}\right]\right. \quad (4.9)$$
$$\left.-\sum_{i=1}^{n-2}D\left[t-t_0-\frac{i\left(t_n-t_0\right)}{n}\right]\right\}+D(t-t_n),\ \text{for } t>t_n.$$

It is worth mentioning that equation (4.9) is a functional equation of an unknown $D(t)$, and it is free of VP strain. Thus, it can be solved by optimization techniques provided that the form function $D(t)$ is known as a priori. According to (Nguyen et at., 2021; Tran et al., 2023), the analytical approximate creep compliance (AACC) function derived from the Huet-Sayegh (HS) model can be used as a good solution to equation (4.9) for its excellence in predicting the linear VE behavior of asphaltic materials.

4.3 Experimental program and analysis of results

4.3.1 Materials, sample preparation, and test arrangement

In this section, AC mixture was chosen for investigating the viscoplastic yielding because it is widely used for the road system in Vietnam. AC samples were prepared and all SCR tests were set up as same as subsection 3.2.1 except strains inside the specimen were measured by four LVDT, which were installed on four side planes of the specimen.

To facilitate the reading of this section, the experimentation program with testing conditions and purposes was summarized in Table 4.1.

The loading rates and durations were chosen to ensure that the stress–strain behavior of the specimens still lies in the linear viscoelastic domain for the validity of the theoretical formulation proposed.

Table 4.1: Summary of the experimentation program

Test No.	Sample	Loading duration (s)	Loading rate (N/s)	Testing temperature (°C)	Purpose
T1	1	100	2	30	Check linearity and repeatability
T2		125	2	30	
T3		165	2	30	
T4	2	100	3	30	Characterize the viscoplastic yield point
T5		140	3	25	
T6		200	3	20	
T7		300	3	15	
T8		150	6	15	

4.3.2 Convergence of the GCR algorithm

Before moving on to the assessment of viscoplastic yield stress, we performed a quick analysis on the convergence of the GCR algorithm to determine a balanced level of discretization in terms of accuracy and computational cost. Therefore, only the results provided by the GCR algorithm in dealing with T1, T5, and T7 test data were selected for the analysis.

For illustration purposes, the results obtained from T1 test data with the number of subintervals n being chosen equal to 320 steps were displayed in Figure 4.3. As can be observed, the AACC function derived from the HS model allowed a good fitting of the experimental recovery compliance in the resting period [see Figure 4.3(a)]. The CCs calculated with the best-fit parameters are displayed in Figure 4.3(b), and the predicted VE strains computed using equation 4.4 and 4.5 are presented in Figure 4.3(c). It can be observed that the measured strains are much larger than the VE strains, confirming the existence of VP strains inside the specimen. The VP strain was computed using equation 4.1 and is presented in Figure 4.3(d) to illustrate the evolution of permanent deformation of the specimen during the ramp loading and resting conditions.

`

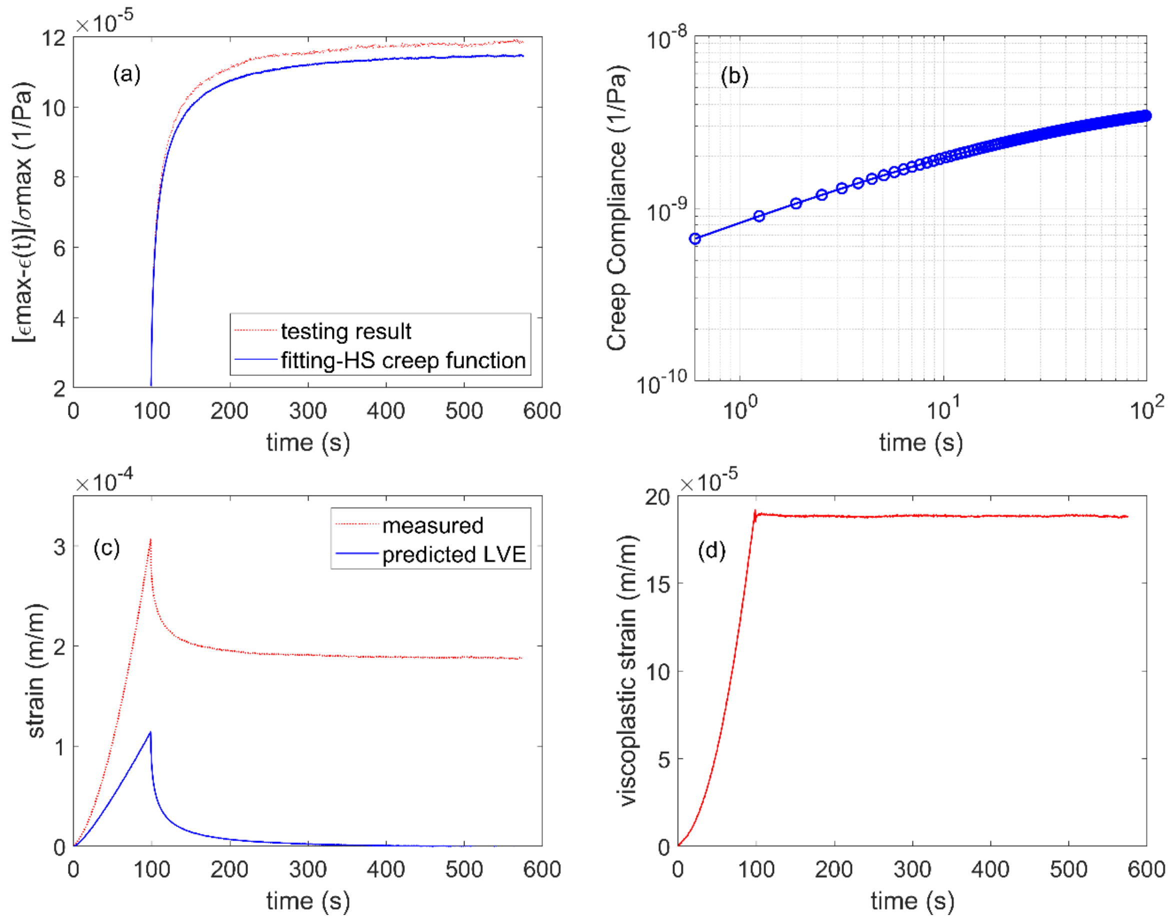

Figure 4.3. Results of the SCR test at 30°C, stress rate equal to 2N/s, and loading time equal to 100s. (a) Fitting results of the recovery compliance with n=320; (b) Back-calculated CC; (c) Predicted VE and total strains; and (d) Computed VP strain

It can be seen in Figure 4.3c, the VP strain continuously developed in the loading period and maintained its stable values in the resting phase, as assumed. Therefore, in the upcoming sections, only VP strains in the loading periods were shown in the figures.

To verify the convergence of the GCR algorithm, the influence of discretization fineness on the obtained results was considered. As can be observed in Figure 4.4(a), the relative errors exhibit a decreasing trend with an increasing number of subintervals. In terms of computing time, a finer discretization clearly requires a longer computation time to complete the calculation, as shown in Figure 4.4(b). According to the results obtained, a discretization using 320 subintervals appeared sufficient to ensure both numerical

`

accuracy and computational efficiency, as supported by the findings of Do et al. (2025). Higher values of n yielded only marginal improvements in accuracy; therefore, $n = 320$ was selected for post-processing all testing data in this project.

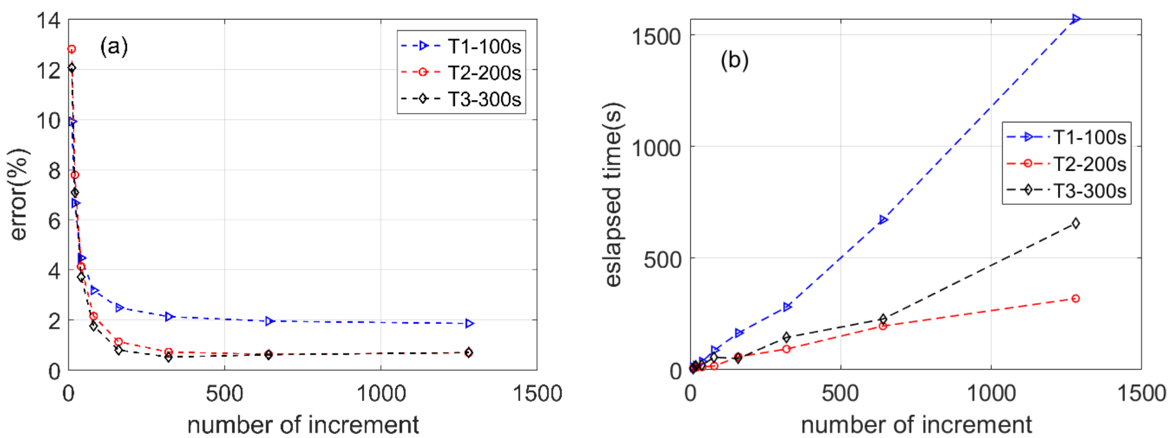

Figure 4.4. Effect of the discretization fineness on (a) the accuracy of the results obtained with the GCR algorithm, and (b) elapsed time for post-processing.

4.3.3 Verification of linearity and repeatability

Figure 4.5 presents CCs and VP strains of specimen # 1, determined from tests T1, T2, and T3. It is obvious that the obtained CC curves are close to each other. In fact, the maximum relative difference between them and the mean of back-calculated CCs does not exceed 5.82% when calculated over the first 100s of the loading time. Regarding VP strains, the relative differences between consecutive tests can reach 17.90%. However, this variability is mainly caused by the mechanical hardening effects of the material as the aggregates come closer to each other under the effect of the contractive permanent deformation strain. In addition, this level of variation is still small and widely acceptable in pavement engineering. Thus, the results obtained with the SCR test can be considered repeatable.

Regarding the evolution of VP strains, it can be observed in Figure 4.5(b) that all VP strain curves continuously increased from the onset of stress application. This may suggest that the material does not exhibit viscoplastic yield points at 30 °C. However,

`

the yield stress at this temperature may be extremely low, falling below the detection threshold of the testing equipment. Therefore, this hypothesis will be further examined in the next subsection, where the material behavior at temperatures lower than 30 °C is investigated.

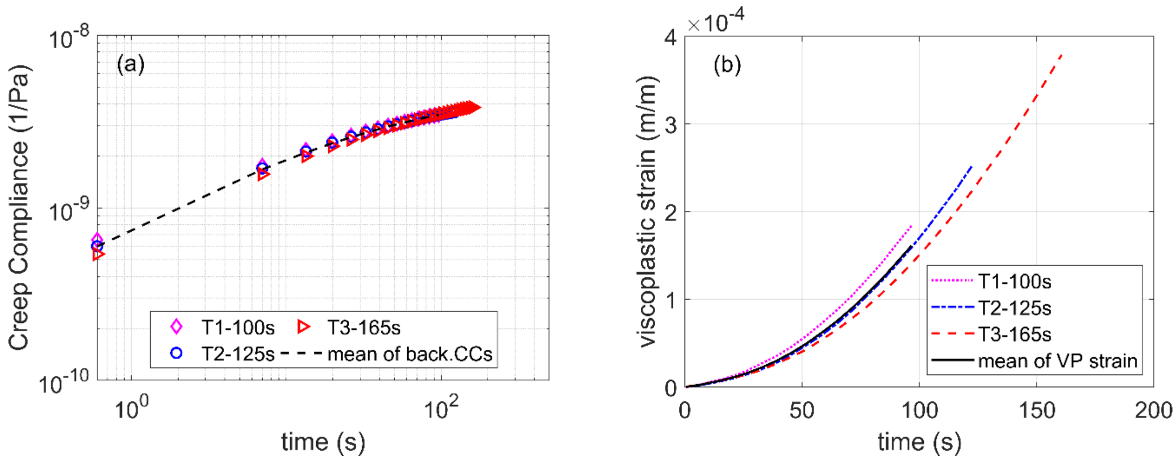

Figure 4.5. Back-calculation results of all tests performed on sample #1: (a) Back-calculated creep compliances; (b) Evolution of VP strains.

4.3.4 Verification of the non-existence of viscoplastic yield point

In this subsection, additional tests at lower temperatures - namely 25, 20, and 15°C were conducted to verify whether viscoplastic yield points exist or not. Tests were conducted on specimen # 2.

Figure 4.6(a,b) displays the obtained CCs and VP strains. It is evident that the material is stiffer at lower temperatures, complying with LVE theory. In addition, the rates of VP strain at a higher temperature are also greater than those at a lower one. Although the rates of accumulation of VP strains are different at different temperatures, most VP strains tend to increase continuously with the loading time due to increases in the stress magnitude applied, except for the VP strain obtained at 15°C with a loading rate of 3N/s. At this testing condition, the VP strain curve seems to have a "plateau region" for the loading time lower than or equal to 30s. This may indicate the presence of a viscoplastic yield point of approximately 90N, beyond which the VP strain started to grow.

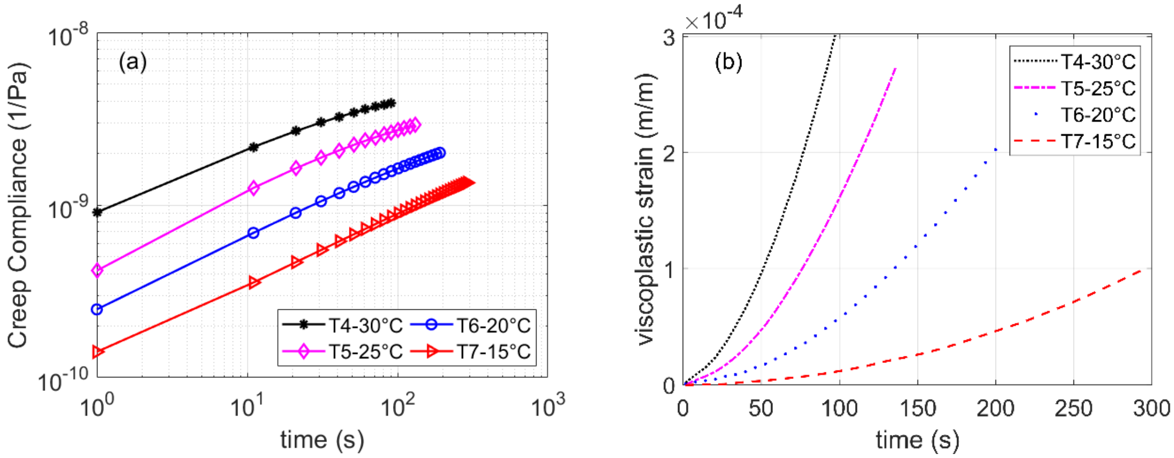

Figure 4.6. Back-calculation results of all tests performed on sample #2, (a) Back-calculated CCs, (b) Evolution of VP strains.

To verify if there exists a viscoplastic yield point for the studied mixture at 15 °C, an additional test (T8) was conducted at the same temperature but with a higher loading rate of 6 N/s, which is twice the rate used in test T7. In the case that the viscoplastic yield point exists, there must be a "plateau region" in the VP strain curve obtained for the loading time ranging from 0 to 15s.

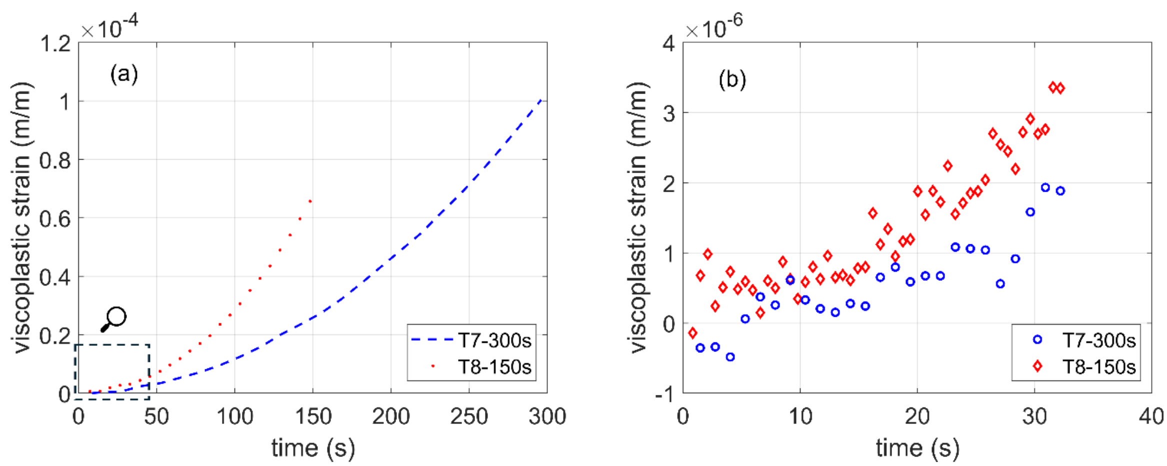

Figure 4.7. Evolution of VP strains at 15°C (a) and zoom of accumulated VP strains in the first 30s of the loading periods (b).

`

The resulting VP strain curve from test T8 is plotted alongside that of test T7 in Figure 4.7(a) for comparison. In addition, zoomed-in views of the accumulated VP strains during the first 30 seconds are presented in Figure 4.7(b) to facilitate the observation. In both tests, the VP strains showed an increasing trend despite relatively large oscillations. This proves that the viscoplastic yield point of the investigated mixture at 15 °C—if it exists—is extremely small and can therefore be considered negligible.

4.4 Conclusions of Chapter IV

The viscoplastic yield point of a conventional asphalt mixture was successfully characterized by using slope creep-recovery tests in the low-strain regime. It is efficient to apply the generalized creep-recovery algorithm for separating viscoelastic and viscoplastic behavior of the specimen from slope creep-recovery test data. Based on the identified VP strain curves, the material did not show any observable separation point between reversible and irreversible regions within the testing temperatures, ranging from 15°C to 30°C. This finding is in line with the assumption made by many other authors, yet has not been properly verified. The results of this study will support the development of permanent deformation behavior models based on non-yielding viscoplastic theory.

`

CHAPTER V

MODELING THE BEHAVIOR OF ASPHALT MIXTURE UNDER UNIAXIAL COMPRESSIVE STRESS

5.1 Introduction

Asphaltic materials are composite ones, created by mixing graded aggregate and binder. Because asphalt mixture has viscosity, owing to binder, its response shows dependence on time/ temperature/ rate and historical applied stress. In the small strain regime, the total strain of asphalt mixture under uniaxial compressive stress can be decomposed into VE and VP strains, in which VE strain is the recoverable components and VP strain is the irreversible one. The accumulated VP strain is the primary cause of rutting, one of the most critical distresses in asphalt pavements. Therefore, predicting the evolution of VP strain play a crucial role in analysis and design of asphalt pavements.

The prediction of VP behavior can be grouped into two main types: analytical, and constitutive approaches. Analytical models are developed using regression techniques based on data collected from test tracks, which require long testing periods and high-cost field acquisition equipment. Furthermore, these data strongly depend on traffic and climatic conditions in the host country, while physical factors such as loading and rest durations, applied stress magnitude, and temperature are inherently mixed in the measurements. Therefore, in addition to regression-based models, constitutive models have been developed to address these limitations.

Darabi et al. (2012) reported that if viscoplastic properties of materials remain constant during the resting period, the predicted permanent deformation of the classical hardening Perzyna-type viscoplastic model will saturate after a few cycles. The deviation

`

between the model predictions and experimental results becomes significant at a large number of cycles. Thus, the classical hardening Perzyna-type viscoplastic models are not suitable to predict the evolution of permanent deformation of asphalt mixture under repeated load as well as complex loading paths. To overcome that problem, Darabi et al. (2012) proposed to control the saturation limit of the hardening function for capturing the hardening – relaxation effect which is the phenomenon where the material can recover its VP strain development ability after unloaded. However, because the studied asphalt mixture does not show viscoplastic yielding (see Chapter V), the model seems not appropriate for predicting the behavior of the studied mixture.

Based on the observation that the nonlinear stress–strain curve of asphalt mixture does not have a certain separation point, another approach to establishing viscoplastic deformation models is to use convolution integral form. A model with such an approach has been proposed by Subramanian et al. (2013), assuming that the hardening and the viscoplastic strain functions are similar to viscoelastic strain functions. However, only the hardening in load pulses was implanted into the model while the softening effect was not considered yet. Inspired by that idea, Cao and Kim (2016) modified the model by deriving the computation into three steps: loading half pulse in the first cycle, unloading half pulse in the first cycle and unloading period, and loading half pulse after the first cycle scenario. The softening of VP strains was considered in the unloading half pulse in the first cycle and in the unloading period. This implies that VP strains are assumed to be non-increasing during the unloading half-cycle, an assumption that is only valid for short loading durations. However, our observations indicate that rutting, i.e., the accumulation of VP strains, occurs predominantly at intersections, where wheel loads are applied over extended periods ranging from several tens to hundreds of seconds.

In this chapter, permanent hardening law and the characteristics of materials which recover its ability to develop VP strains in resting period are investigated before

`

a new model is proposed for effectively predicting the evolution of VP strains under complex applied stress paths.

5.2 Experiment measurements

As concluded in Chapter III, the three mixtures including unmodified and modified mixtures manifest similar behavior in VP domain. The VP strain is increasing with increases in stress magnitude, loading time, and temperature. In addition, all mixtures obey the TTSP in VP domain, allowing good prediction of permanent deformation caused by creep loadings at different temperature. The effects of physical hardening effects and time-related relaxation were not yet considered in the previous chapter, which will be deeply investigated in this chapter. Therefore, only unmodified mixture, the most frequently used one, was chosen in the experimentation campaign. Since TTSP is valid in VP domain, tests were conducted at one single temperature to reduce the overall testing time.

The investigated specimens were fresh ones, which were prepared following the process reported in chapter III. As a results, the engineering properties of the studied mixtures are similar to those presented in Table 3.3. Tests were conducted on two samples, named as #1, #2. Results of tests which were obtained from sample #1 were used for calibrating the model, while results of sample #2 were used to check the repeatability of material's behavior and validating model. All of tests were conducted at 32.5°C which suitable with environmental conditions of Vietnam. Four types of tests were performed in this study, namely: single stress creep – recovery, two cycle creep – recovery, various applied stress and loading time creep – recovery and slope creep – recovery tests.

5.2.1 Single stress creep – recovery test (SSCR)

The single stress creep – recovery test was performed with 150s loading time with a following 1500s rest period. Two stress levels were applied on the samples respectively

`

30.61 and 40.81kPa to check the VE behavior of mixture still in linear regime and determine the parameters of nonlinear of VP strain parameters.

5.2.2 Two-cycle creep - recovery test (GCR-TC)

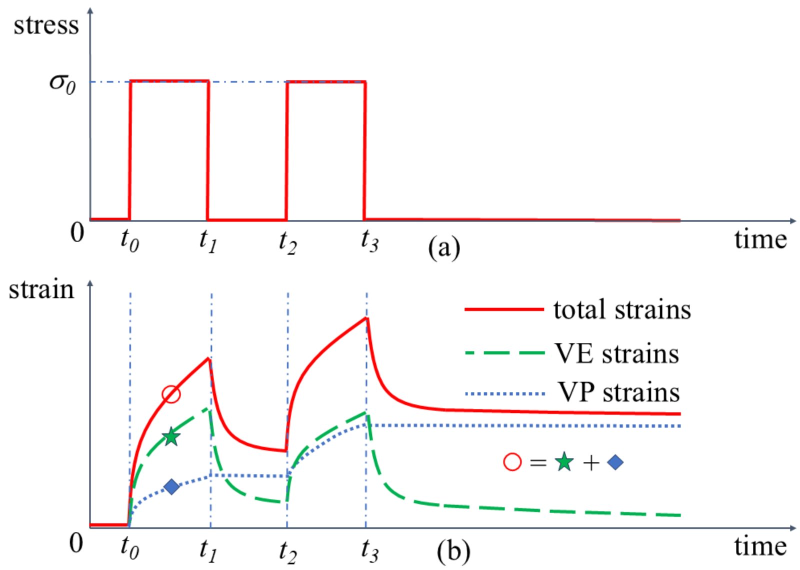

Figure 5.1. Description of GCR-TC test: (a) applied stress history, (b) response strain

Figure 5.1 illustrates applied stress and response strain histories of typical GCR-TC test. The GCR-TC test was conducted with constant applied stress ($\sigma_0 = 20.41kPa$) and 150s loading time for two cycles. Resting period of 1st cycle was surveyed from 0 second to 24 hours. The purpose of this test is to characterize the parameters of VE and VP model.

5.2.3 Various applied stress and loading time creep - recovery test (GCR-VLT)

This test was performed with applied stress level, loading time, and rest period between two cycles which were randomly chosen to validate the proposed model. In this study, applied stress historied namely as Figure 5.2 and detail in Table 5.1.

5.2.4 Slope creep - recovery test (SCR)

This test comprised one loading period with a constant stress rate following by a rest period. (see Figure 4.1 in subsection 4.2). In this study, a 0.408 kPa/s stress rate was

`

applied on samples in 100s and the unloading period lasted in 300s. This test is also used for validating proposed models.

Table 5.1: Loading conditions of various loading and time CR test

Cycle	1	2	3	4	5
Creep stress (kPa)	10.20	24.49	20.41	15.31	30.61
Creep duration (s)	100	80	120	100	150
Recovery duration (s)	200	100	0	150	2600

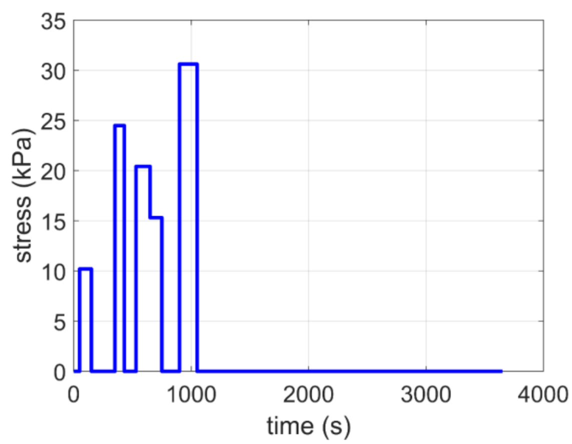

Figure 5.2. Loading history of GCR-VLT test

List of tests conducted on two specimens was summarized in Table 5.1 and 5.2. It is worth noting that some tests have two replicates to ensure that the results obtained are objective.

Table 5.2: List of tests conducted on sample #1

No	Test label	Type of test	t_{L1} (s)	t_{uL1} (s)	t_{L2} (s)	t_{uL2} (s)
1	TC-50s-R1	GCR-TC	150	50	150	1500
2	TC-300s-R1	GCR-TC	150	300	150	3000
3	TC-300s-R2	GCR-TC	150	300	150	3000
4	TC-50s-R2	GCR-TC	150	50	150	1500
5	TC-0s-R1	GCR-TC	150	0	150	1500

6	TC-0s-R2	GCR-TC	150	0	150	1500
7	TC-1800s-R1	GCR-TC	150	1800	150	4200
8	TC-1800s-R2	GCR-TC	150	1800	150	4200
9	TC-24h-R1	GCR-TC	150	86400	150	1500
10	TC-24h-R2	GCR-TC	150	86400	150	1500
11	TC-3h-R1	GCR-TC	150	10800	150	1500
12	TC-3h-R2	GCR-TC	150	10800	150	1500
13	TC-6h-R1	GCR-TC	150	21600	150	1500
14	TC-6h-R2	GCR-TC	150	21600	150	1500
15	SS-200N-R1	SSCR	150	1500	-	-
16	SS-150N-R1	SSCR	150	1500	-	-
17	SS-150N-R2	SSCR	150	1500	-	-
18	SS-200N-R2	SSCR	150	1500	-	-

Table 5.3: List of tests conducted on sample #2

No	Test label	Type of test	t_{L1} (s)	t_{uL1} (s)	t_{L2} (s)	t_{uL2} (s)
1	TC-225s	GCR-TC	150	225	150	3000
2	TC-900s	GCR-TC	150	900	150	3000
3	TC-1h	GCR-TC	150	3600	150	3000
4	TC-2h	GCR-TC	150	7200	150	3000
5	TC-4h	GCR-TC	150	14400	150	1500
6	TC-8h	GCR-TC	150	28800	150	1500
7	TC-16h	GCR-TC	150	57600	150	1500
8	TC-24h	GCR-TC	150	86400	150	1500
9	GCR-VLT-R1	GCR-VLT				
10	GCR-VLT-R2	GCR-VLT				

11	SCR-R1	SCR
12	SCR-R2	SCR

5.3 Proposed viscoplastic model

The additive decomposition of total strain is illustrated in Figure 5.3. For VE behavior, two springs and two parabolic dashpots arranged as suggested by Huet and Sayegh (1969) are enough to represent the complicated behavior of asphaltic materials. Regarding VP behavior, the stress-VP strain is too complex to be represented by traditional rheological elements. Therefore, we propose in this study a VP block consisting of one PD element as illustrated in Figure 5.3. The following equations hold:

$$\varepsilon(t) = \varepsilon_{ve}(t) + \varepsilon_{vp}(t); \ \sigma(t) = \sigma_{ve}(t) = \sigma_{vp}(t) \tag{5.1}$$

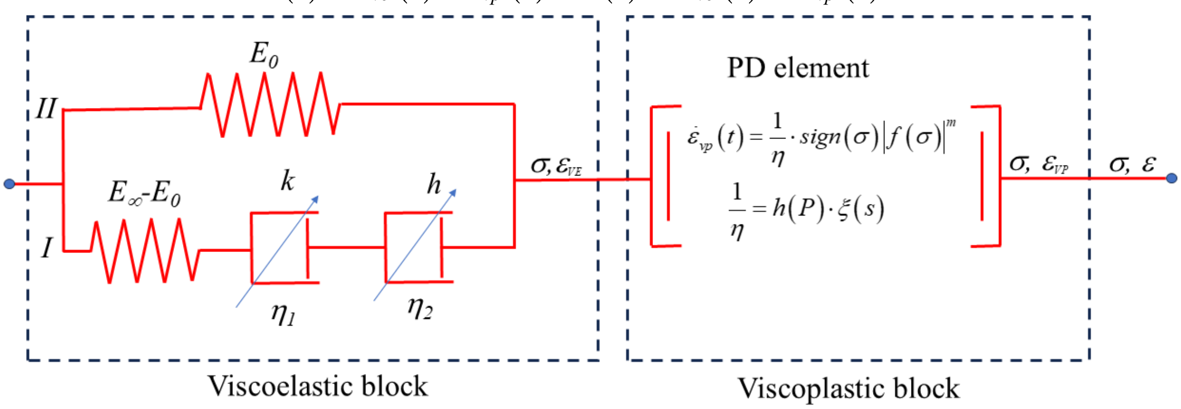

Figure 5.3. Representation of strain decomposition and modeling.

The PD element is in fact a non-linear dashpot governing the evolution of viscoplastic strain:

$$\dot{\varepsilon}_{VP}(t) = \frac{1}{\eta} \cdot sign(\sigma) \cdot |f(\sigma)|^m \tag{5.2}$$

where η is the "viscosity" of the material, σ is the induced stress, and m is a coefficient accounting for stress-dependence. Based on observations in subsequent sections, the viscoplastic strain rate varies with accumulated permanent deformation strain, noted as $P = \int_0^t d\varepsilon_{VP}$, as well as the actual relaxation state of the material, noted s.

`

The more PD is accumulated and the more the material is stressed, the less the VP rate is. Therefore, the fluidity, or the inverse of viscosity, is modeled by the product of a function of P and a function of s:

$$\dot{\varepsilon}_{VP}(t) = h(P)\cdot\xi(s)\cdot sign(\sigma)\cdot\left|f(\sigma)\right|^{m} \tag{5.3}$$

And the resulting VP strain is computed by:

$$\varepsilon_{VP}(t) = \int_0^t \dot{\varepsilon}_{VP}(\tau)\,d\tau, \tag{5.4}$$

In equation (5.3) $h(P)$ is a decreasing function of P representing the "permanent mechanical hardening" effect, $\xi(s)$ is a decreasing function of s representing the "actual capability" of the material in producing the rate of viscoplastic strain, called the "time-related relaxation" phenomenon, and $\left|f(\sigma)\right|^{m}$ is the loading function as proposed by Perzyna (1966). Here, the stress state is in uniaxial condition, $\left|f(\sigma)\right|$ is just the magnitude of the stress.

The permanent hardening law can be predicted by the following equation:

$$h(P) = h_1 + \frac{h_2}{1 + h_3\cdot \mathrm{e}^{h_4 P}}, \tag{5.5}$$

where h_1 contribute to the fluidity in the long-term of the material where P tends to infinity. At that stage, the aggregates in the mixture are compacted to their maximum density and cannot be further compacted. As a result, the physical hardening becomes unchanged. Parameters h_2, h_3, h_4 decide the evolution of hardening law as P increases and can be separately identified through a series of two-cycle CR tests. It is worth mentioning that $h(P)=1$ at the initial stage of the material where $P=0$; thus,

$$h_1 + \frac{h_2}{1+h_3} = 1. \tag{5.6}$$

`

In terms of time-related relaxation effect, experimental results (as will be reported in subsequent section) shows strong dependence of VP strain rate on the loading time as well as on the time the material is permitted to relax before applying a stress. Therefore, we introduce a novel state variable s defined as:

$$s = \int_0^t D_s(t-\tau)\dot{\sigma}d\tau \tag{5.7}$$

wherein σ is the stress history applying to the VP block, $D_s(t)$ is a function describing the evolution of s variable:

$$D_s(t) = A_1 t^{q_1} + A_2 t^{q_2} \ . \tag{5.8}$$

It should be mentioned that $D_s(t)$ has dimension of a compliance and thus s has a dimension of a strain. The purpose is to introduce a state variable that is increasing with a constant or increasing stress histories and decreasing as stress is declining or equal to zero. Accordingly, $\xi(s)$ is a decreasing function with s, defined as:

$$\xi(s) = \xi_1 + \frac{\xi_2}{1+\xi_3 \cdot s^n} \tag{5.9}$$

At the initial stage where the material is at rest, or $s=0$, the fluidity is at its maximal value, showing its highest potential to a viscoplastic flow rate. During the loading phase where the stress is held constant or kept increasing, variable s is in increasing trend, giving rise to a decreasing trend of the fluidity. Parameters ξ_1, ξ_2, ξ_3, ξ_4 and A_1, q_1, A_1, q_2 are just model's parameters determined by minimizing the differences between prediction and measurement performed at different resting times.

The relaxation phenomenon can be traced back to the observations of Darabi et al. (2012) and was later discussed by Cao and Kim (2016). It was initially termed as "hardening–relaxation mechanism" and subsequently referred to as "softening during rest periods" by Cao and Kim (2016). According to Darabi et al. (2012), the phenomenon can be explained by the rearrangement of aggregates, which increases interlocking and

`

thereby reduces the viscoplastic (VP) strain rate. During the loading phase, the bitumen within the aggregate network becomes pressurized, generating internal residual stresses. When the load is removed, the bitumen recovers its LVE strain and partially pushes the aggregates back toward their initial positions. As a result, the material partially regains its capacity for the development of VP strain. However, this mechanism does not adequately explain the experimental results obtained in this study. Specifically, the time-dependent relaxation process cannot be fully attributed to the relaxation of linear viscoelastic (LVE) strain, and the permanent hardening law depends solely on the accumulated permanent deformation (PD) strain (as will be shown in subsequent sections). Therefore, this study proposes to separate the hardening process from the hardening–relaxation process, as formulated in equations. (5.1)–(5.9).

It has been observed by many authors and confirmed via experiments in this work that asphalt mixture does not show obvious viscoplastic strength yield as demonstrated in chapter IV; thus, the loading function can be written as:

$$f(\sigma)^m = \begin{cases} \dfrac{\sigma}{\sigma_L}, \text{ for } \sigma \leq \sigma_L \\ \left(\dfrac{\sigma}{\sigma_L}\right)^m, \text{ for } \sigma > \sigma_L \end{cases}, \tag{5.10}$$

where $m > 1$ is a parameter used to represent the nonlinearity effect of the stress on the evolution of VP strain beyond a certain magnitude, noted σ_L. It should be mentioned that m can also be a stress-dependent parameter. For instance, the following model was used to predict the dependency of power coefficient m

$$m = \begin{cases} 1+n, \text{ for } \sigma \leq \sigma_L \\ 2+n-\dfrac{1}{1+m_1\sigma^{m_2}}, \text{ for } \sigma > \sigma_L \end{cases}, \tag{5.11}$$

where n is the power coefficient in equation 5.8.

In order to illustrate better the model, we study two typical cases:

`

(i) $\sigma \neq 0$ for time ranging from 0 to t_1:

$$\dot{\varepsilon}_{VP}(t) = h(P) \cdot \xi(s) \cdot sign(\sigma) \cdot |f(\sigma)|^m$$

the VP strain continues to grow following the direction of the driving stress and obeying the hardening and time-related relaxation laws. Assuming that σ is constant, s increases with time, giving rise to a decreasing trend of the predicted VP strain rate.

(ii) $\sigma = 0$ for time $t > t_1$, $\dot{\varepsilon}_{vp} = 0$, thus, the VP strain in the PD element is unchanged during $t > t_1$. Furthermore, s decline during this period following equation (5.7); the material then recovers its potential in developping VP strain rates in the subsequent loading cycle.

5.4 Model calibration

This section presents a systematic analysis procedure to calibrate both VE and VP models. Raw obtained data of tests were analyzed based on algorithms proposed in subsection 2.4.3. Back calculated CCs were used to calibrate parameters of VE model (HS model) while parameters of VP model were determined based on the computed VP strain.

5.4.1 Identification of HS model

In this subsection, parameters of HS model were calibrated by fitting $D(t)$ function of HS model to the average CC which is mean of back-calculated CCs. The results were shown in Figure 5.4, and the specific value of the model parameters are presented in Table 5.4. It can be seen that all of back-calculated CCs are convergency together. The relative difference between the average CC and another CC does not exceed 17.41%. It means that the obtained parameters of HS model are reliable. Moreover, Figure 5.4(c) shows that back-calculated CCs of three levels of applied stress agree together so materials still have VE behavior in the linear regime suitable with the initial hypothesis.

`

Table 5.4:Parameters of HS model

Param	E_0(MPa)	E_∞(MPa)	h	k	δ	τ
Value	109.929	38319.305	0.525	0.435	912.613	0.185

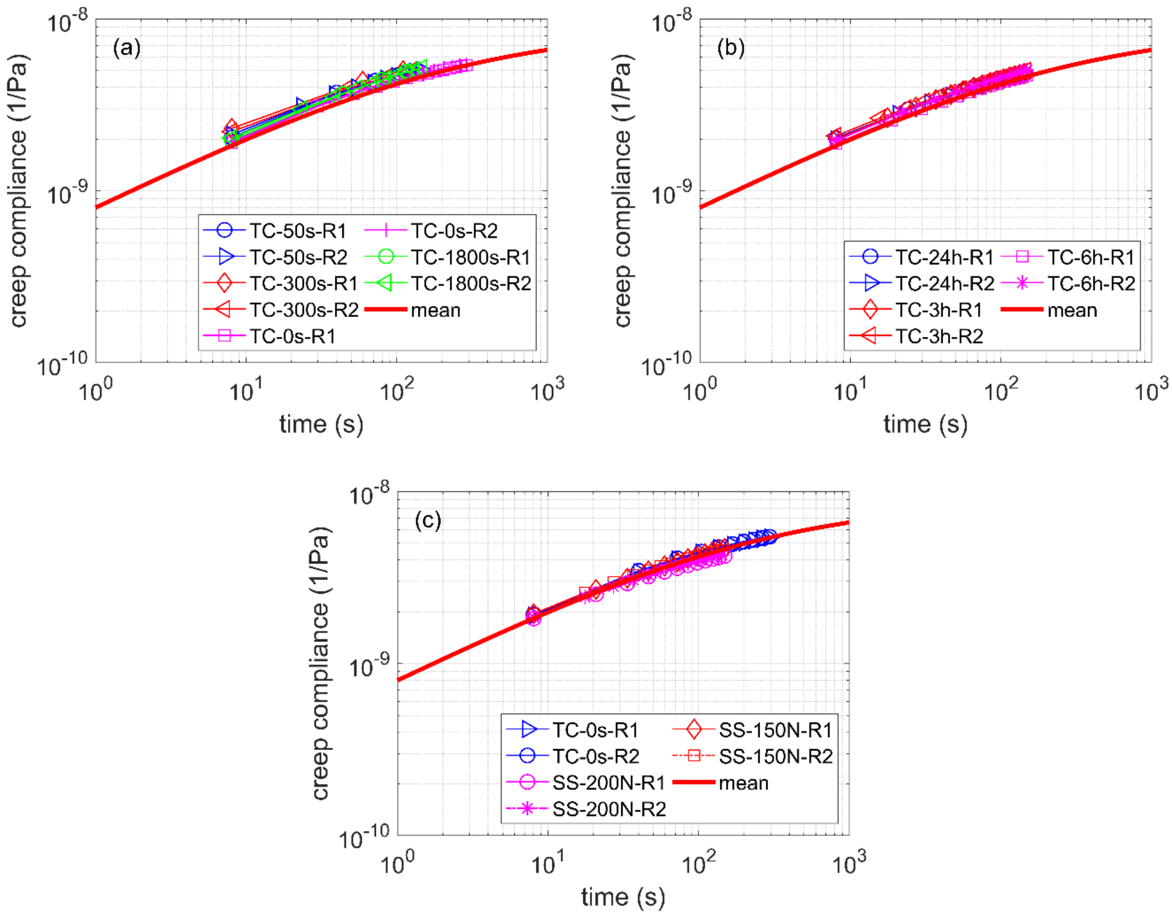

Figure 5.4. Back-calculated creep compliances and the average creep compliance. (a, b) back-calculated creep compliances of GCR-TC tests, (c) back-calculated creep compliances of SSCR tests.

5.4.2 Identification of the parameters of VP model from two cycle CR test

The proposed VP model is superposition of hardening function, fluidity function, and loading function. Parameters of each function are respectively identified in following paragraphs.

`

5.4.2.1 Parameters of permanent hardening function

In experimental observation, permanent hardening behavior is dependent on accumulation of VP strain. To survey that behavior, the evolution of VP strain during the first loading period of each GCR-TC test was compared with the one of the first test. It worths to note that the sample should be rested at least 24 hours after each test to eliminate the effect of time-related relaxation. The results presented in Figure 5.5(a) showed that the development of VP strain decreases with an increase in accumulate VP strain. Thus, the chosen function to represent the permanent hardening law such as equation (5.5)

Parameters of permanent hardening function $h(P)$ were identified by fitting with experimental result. With obtained parameters (see Table 5.5), the predicted of $h(P)$ was determined and plotted with experimental one in Figure 5.5(a). It is obvious that both predicted and measured curves agree well together. The relative error approximate 6.35% to indicate that the chosen function for permanent hardening law is suitable. Then, all data was normalized to represent the rule of material [see Figure 5.5(b)].

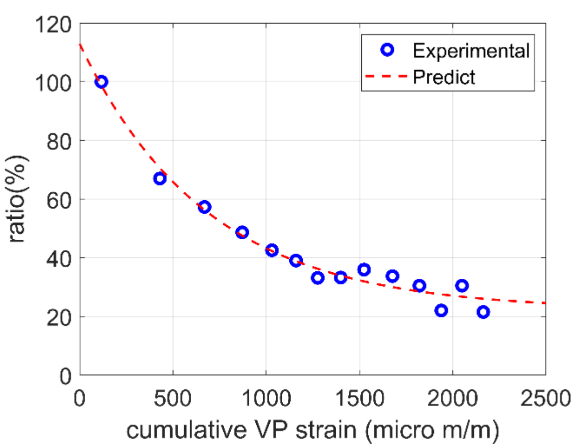

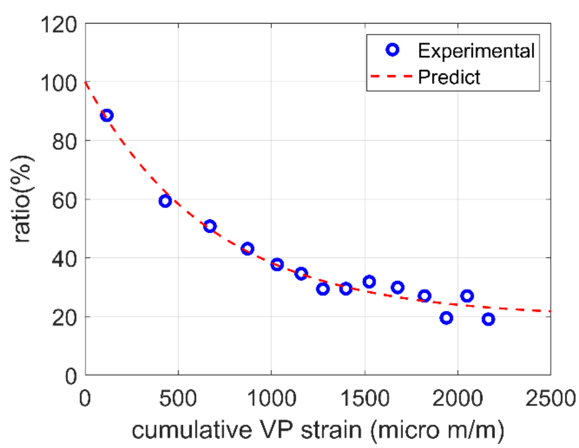

Figure 5.5. Predicted versus experimental permanent hardening curve of sample #1. (a) unnormalized, (b) normalized.

`

Table 5.5: Parameters of $h(P)$ obtained from tests on sample # 1

Param	h_1	h_2	h_3	h_4
Unnormalized	0.222	1620.758	1786.121	1462.376
Normalized	0.196	1435.441	1786.121	1462.376

To ensure that above function is a property of material, the repeatability of permanent hardening law was checked with tests on sample #2. By similar process, parameters of permanent hardening function were determined and presented in Table 5.6 It can be seen in Figure 5.6 that the predicted curve fitting well with the experimental one (RE = 2.88%). The relative difference between two permanent hardening functions obtained from sample #1 and #2 is 5.52% (see Figure 5.7) which include variation of sample and error of measurement indicates obtained permanent hardening function is a characteristic of material.

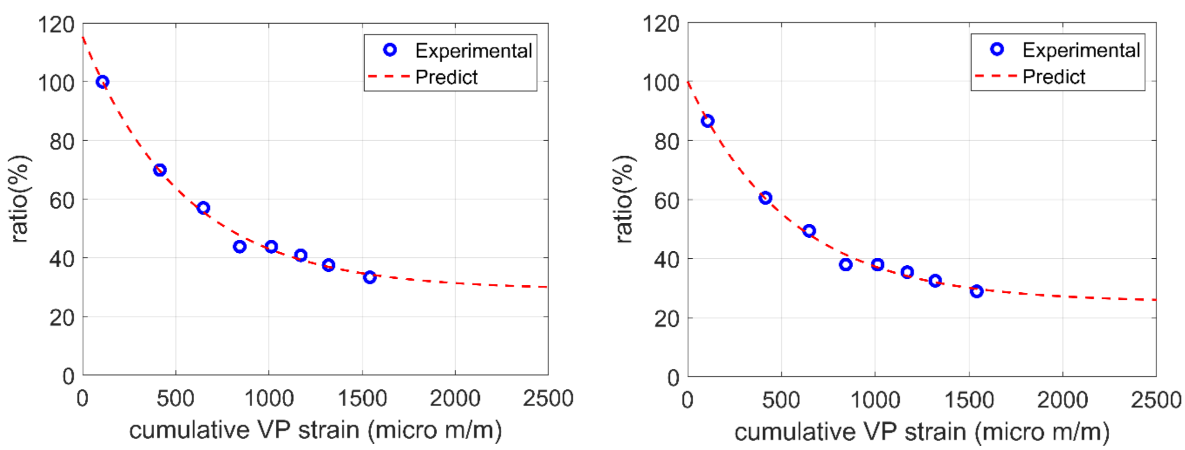

Figure 5.6. Predicted versus experimental permanent hardening curve of sample #2. (a) unnormalized, (b) normalized.

`

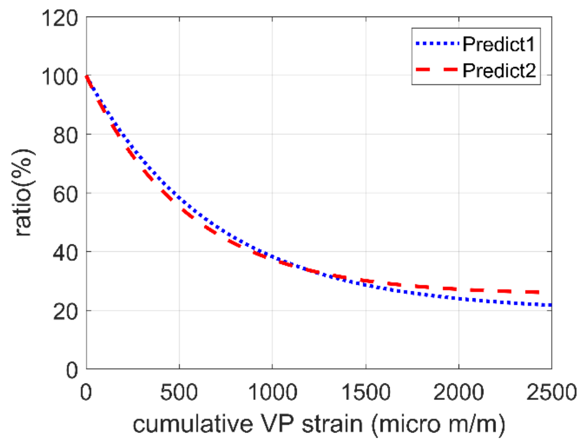

Figure 5.7. Predicted permanent hardening curve of sample #1 versus sample #2.

Table 5.6: Parameters of $h(P)$ obtained from tests on sample #2.

Param	h_1	h_2	h_3	h_4
Unnormalized	0.291	1303.614	1510.009	1824.939
Normalized	0.252	1129.460	1510.009	1824.939

5.4.2.2 Time-related relaxation parameters and nonlinear parameters of VP strain

Observe VP strain obtained from GCR-TC tests, it is easy to see that the ratio between evolution of VP strain in the second and the first cycle depends on resting period of the first cycle. Cause of that phenomenon is changing of material's microstructure in the unloading period that makes its status differ with it's at the end of the first loading period (Darabi et al., 2012). Results of survey the effect of resting period of first cycle on the evolution of VP in second cycle was presented in Figure 5.8. Obviously, there is a repeatability of obtained results from two specimens, the relative difference between two curves is so small. Although VP strains values do not eliminate effect of permanent hardening behavior, it can be seen in Figure 5.9 that with more last of first cycle's resting period, asphalt mixture evolutes more VP strains in second loading period. That behavior is referred to as time-related relaxation.

`

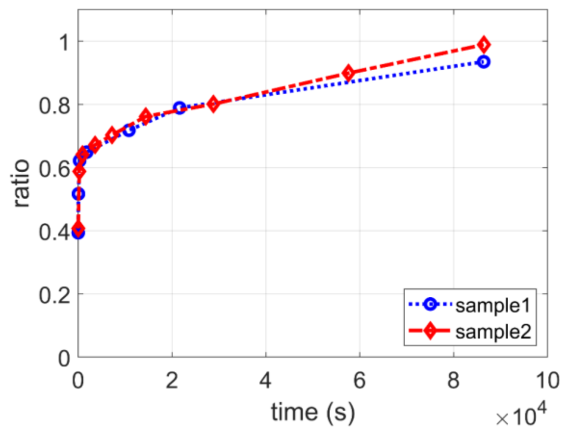

Figure 5.8. Effect of the first cycle's resting period on ability of development VP strains in second loading period of GCR-TC test.

Function's parameters of time-related relaxation behavior and nonlinear parameters of VP strains are identified by minimizing the total errors by using equation (5.3) simultaneous fit to calculated VP strains of test #1÷8 and #15÷18 conducted on sample #1. Obtained parameters were presented in Table (5.7 - 5.8) and fitting results are showed in Figure 5.9. It can be seen that the proposed VP model fits well with almost calculated VP strains. In fact, the maximum error is just 14.32% in case of test label TC-0s-R1 that can be accepted in pavement engineering.

Table 5.7: Parameters of time-related relaxation function

Param	ξ_1	ξ_2	ξ_3	A_1	q_1	A_2	q_2
Value	0	9.684×10^{-6}	7.297	1.039×10^{-5}	0.613	1.128×10^{-5}	0.9

Table 5.8: Parameters of *m* and nonlinear of VP strains

Param	m_1	m_2	n
Value	1.127	1.144×10^{-3}	0.5

`

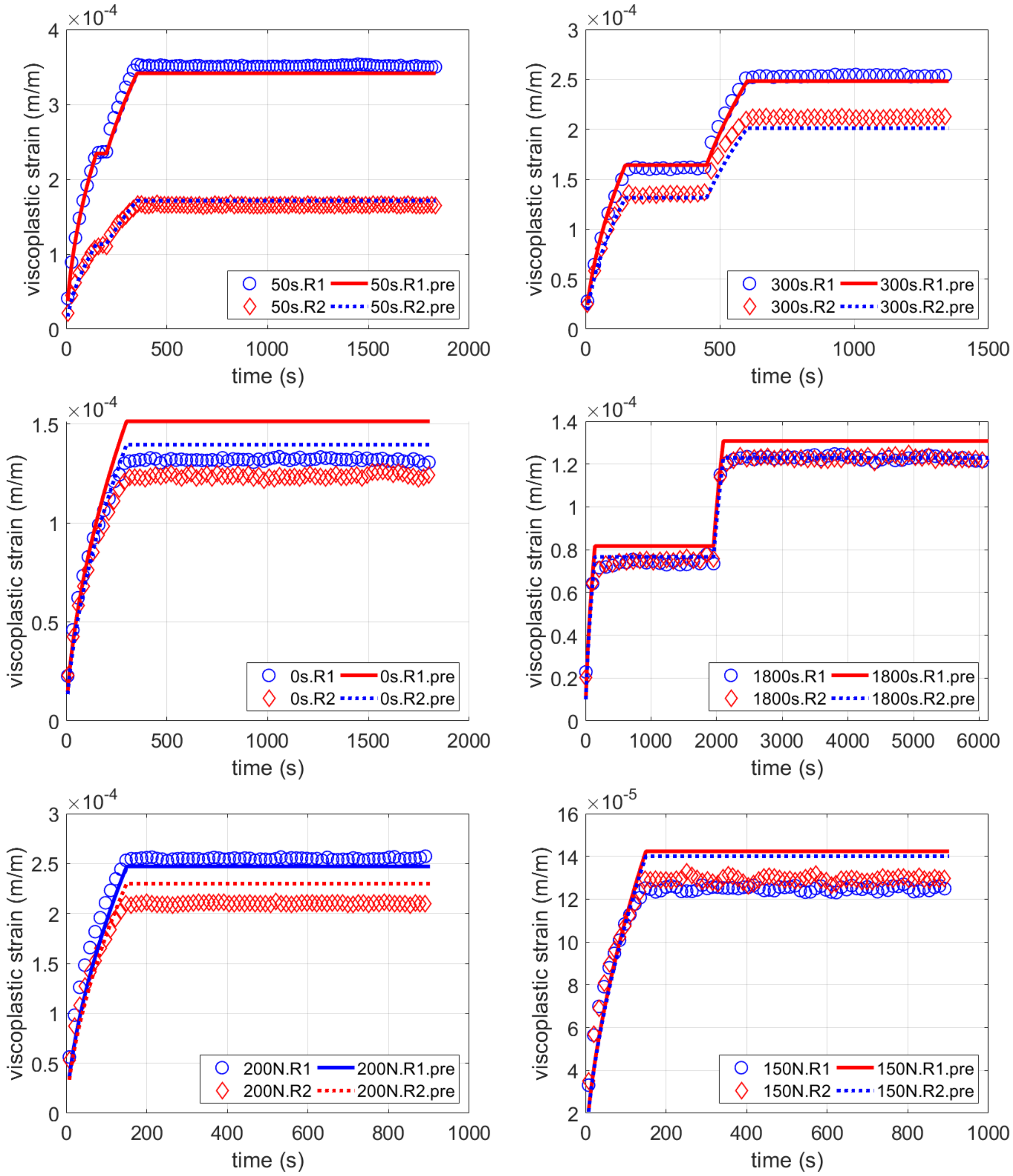

Figure 5.9. Results of fitting equation 5.3 to calculated VP strain performed on sample #1

5.5 Model validation

Once the LVE and VP model parameters are determined from data test conducted on sample #1, the predictions of model will be compared with independent laboratory test results performed on sample #2 for evaluation of the efficacy of the model.

It is demonstrated the prediction of proposed model for GCR-TC tests with first resting period 225, 900, and 3600s, respectively in Figure 5.10(a-c). Those figures indicate that the model has reasonable predictions with experimental measurements for different unloading times. In fact, the maximum relative errors of total strains, VE strains, and VP strains are 4.39, 13.96, and 4.42%, respectively.

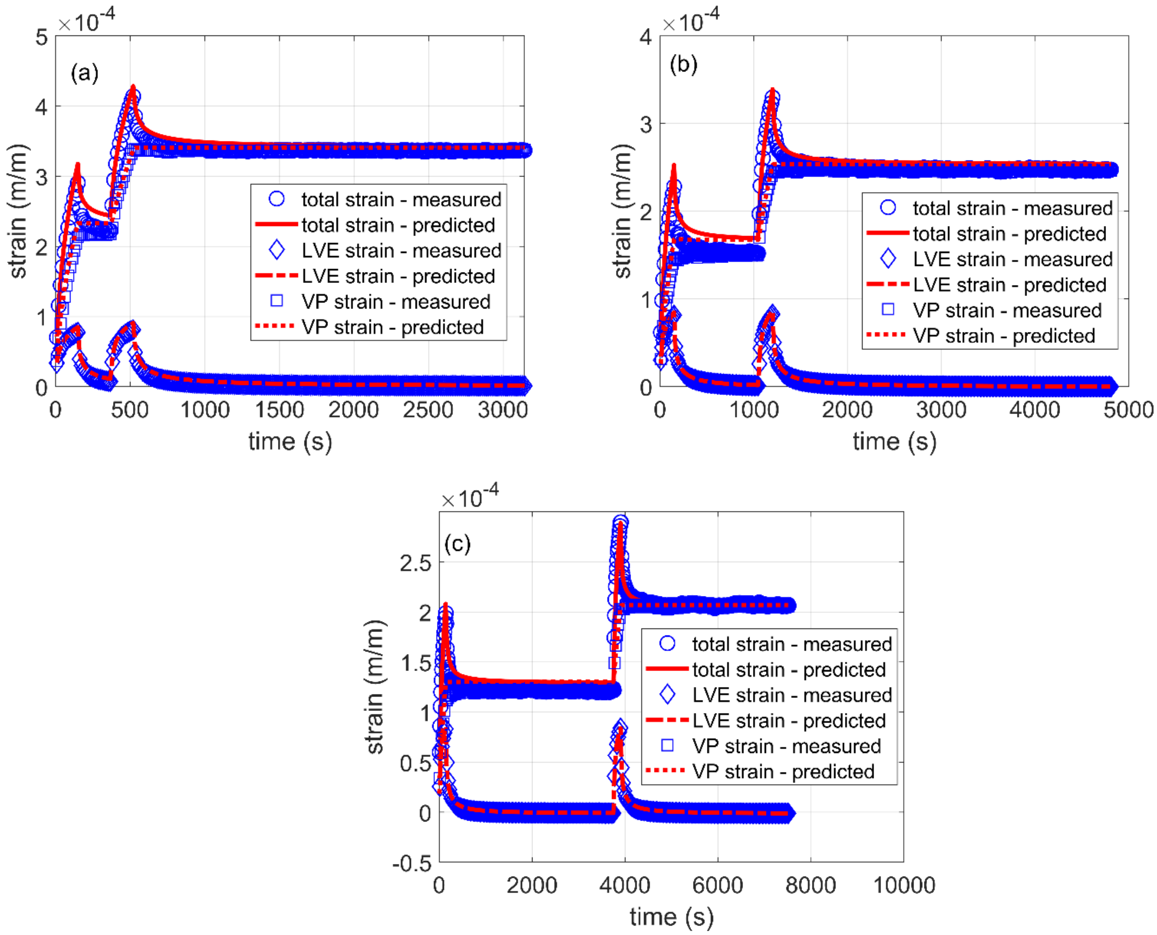

Figure 5.10. The comparison between model predictions and experimental measurements for GCR-TC test. (a) test GCR-TC-225s, (b) test GCR-TC-900s, (c) test GCR-TC-1h.

In Figure 5.11, prediction of model was compared with experimental measurements for GCR-VLT tests. It can be seen that the proposed model agrees well with experimental measurements, and it can describe response of material for not only

`

different loading and unloading period but also variable applied stress. It is worth noting that the maximum relative errors of total strains, VE strains, and VP strains are 8.40, 3.35, and 11.13%, respectively.

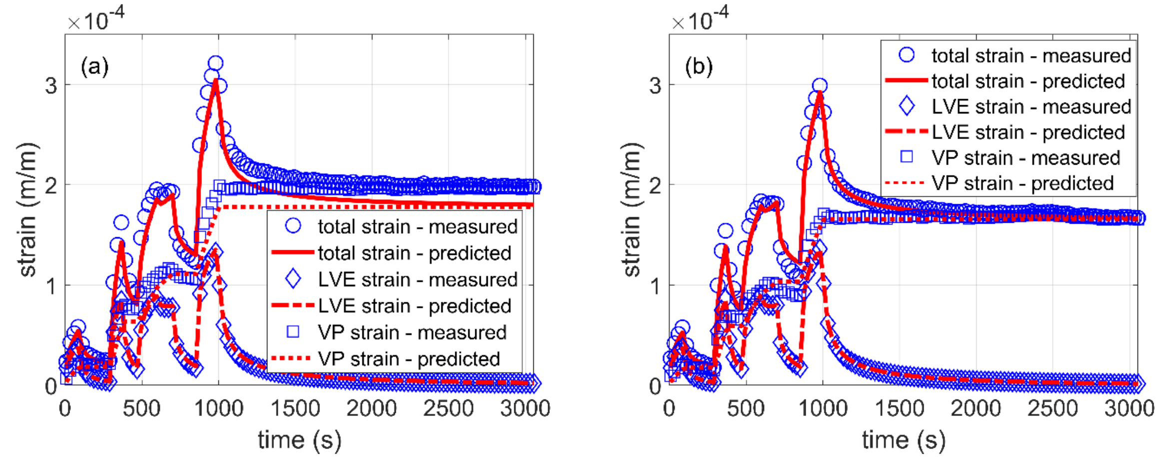

Figure 5.11. The comparison between model predictions and experimental measurements for GCR-VLT tests. (a) test GCR-VLT-R1, (b) test GCR-VLT-R2.

The validation results for SCR tests were presented in Figure 5.12 and it also displays a good agreement with the result of experiment. With the RE does not exceed 5.42% for the total strain, it is obvious that the proposed model can predict response of asphaltic materials at a linear applied stress.

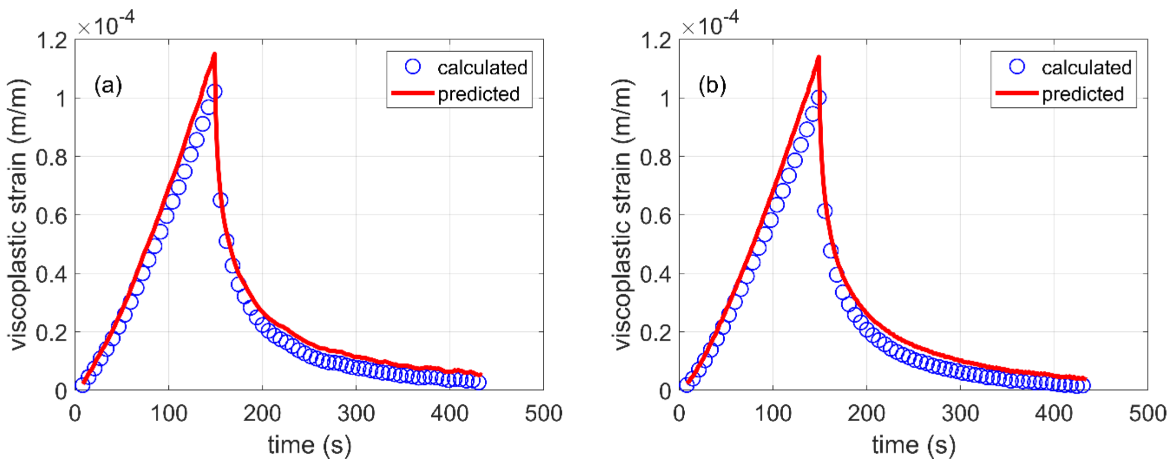

Figure 5.12. The comparison between model predictions and experimental measurements for SCR tests. (a) test SCR- R1, (b) test SCR- R2.

`

Obtained results of this chapter validated that proposed model could represent the response of asphaltic materials with uniaxial compressive stress. The model shows good ability for predicting response of asphalt mixtures under various complex types of loading paths. It is worth noting that model parameters are identified with simple tests and the proposed analysis procedure can sufficiently identify the material characteristics (e.g., VE, VP, permanent hardening, time – related relaxation).

5.6 Conclusions of Chapter V

This study successfully proposes a model to predict the behavior of the considered asphalt mixture (AC) at 32.5 °C under uniaxial compressive stress, with the following contributions: (1) identifying the material's permanent hardening law based on experimental data; (2) investigating the time-related relaxation phenomenon for VP strain; and (3) developing a novel viscoplasticity model for asphalt materials in compression that incorporates permanent hardening and time-related relaxation functions.

Two cycle CR, various applied stress and loading time CR, and slope CR tests were applied to validate the model at 32.5°C shows that the proposed model has ability to predict the behavior of the studied asphalt mixture under complex loading paths. Like other predicted models, the applicability of this model is only valid within the investigating ranges of applied stress, loading and unloading period, and temperature wherein model parameters were identified. Although only one mixture was chosen in this chapter, the process was performed in a general manner and therefore the extension of the proposed method to other mixtures and temperatures could be performed in a similar manner, which will be demonstrated in future works.

`

CHAPTER VI

CONCLUSIONS AND RECOMMENDATIONS

6.1 Main conclusions

In this research, the behavior of VE and VP of asphalt mixture were successfully characterized by using generalized creep recovery test and well predicted by a newly proposed model. The main findings of this work can be drawn as follows:

First, the dissertation has successfully developed a novel method for interconverting the relaxation modulus and creep compliance of asphaltic materials in the form of SEFs based solely on the master curves of dynamic modulus. The proposed method not only shows an excellent level of accuracy but also fully obeys the LVE theory and physical causality principle. Consequently, the validity of VP strains can be confirmed.

Second, the creep-recovery test procedure was generalized for determining both the viscoelastic and permanent deformation behavior without conducting dynamic modulus tests. It is worth noting that the proposed procedure can be applied to identify the permanent deformation of asphalt mixtures exerted by any complex loading history in the time domain, with which the VP behaviors of asphalt mixtures can be investigated.

Third, applying the single stress creep-recovery test with three stress levels and four temperatures on three asphalt mixture, the obtained VP strains were horizontally shifted with the aid of a modified shifting method. The results show that these are relatively smooth and monotonous for all master curves of VP strain, ensuring an injective relationship between time and VP strain. Moreover, it is demonstrated that the stress levels applied do not effect on the VP shift factors and they are independent of temperature. Therefore, time-temperature superposition principle was still hold in VP domain, at least with the examined asphalt mixtures.

`

Fourth, slope creep–recovery tests conducted in the low-strain regime, combined with the GCR algorithm, enabled successful characterization of the viscoplastic yield point of the studied conventional asphalt mixture. Analysis of the resulting VP strain curves showed no clear distinction between reversible and irreversible regions across the testing temperature range (15–30 °C). This observation supports a common assumption in the literature that has not been thoroughly validated. These findings contribute to advancing VP models based on non-yielding viscoplastic theory.

Finally, a new viscoplastic model was proposed and coupled with Huet-Sayegh model to predict the behavior of an asphalt mixture under uniaxial compression state. The model incorporates permanent hardening law and time – related relaxation properties; thus, it is demonstrated that the model can predict the behavior of the investigated asphalt mixture at 32.5°C caused by complex loading histories in the low strain regime.

The results of this work rely on the following assumptions: (i) the VE behavior of materials remains within LVE domain, which restricts the application of large stress/strain magnitude; (ii) the total (measured) strains are additively decomposed into reversible and irreversible components. For the first assumption, nonlinear VE theory could be considered in the formulation to extend the applicability of the proposed method into large strain domain. Although the validity of the additive decomposition of strain was verified in the small strain regime, its extension into large strain domain should be verified in future works. Furthermore, the multiplicative decomposition of reversible and irreversible deformation gradient tensor, which is commonly used in large deformation for metallic materials, should be investigated.

6.2 Recommendations

Based on the results of this research, there are a few recommendations for future studies to expand the implication of this work as follows:

`

- The procedure of GCR test is limited to low strain regime so that the Boltzmann principle still validate for LVE behavior of material. Hence, it should be developed a suitable procedure for nonlinear viscoelastic behavior of asphalt mixture.
- The stress states of all tests in this research are uniaxial while the stress states of asphalt concrete layers are not the case. Thus, it is required to consider the effects of confining pressure in future works to predict the rutting depth in real pavement.
- The proposed model was calibrated and validated solely using tests on an AC mixture at a single temperature (32.5°C). To confirm its broader applicability, it is important to evaluate the model with different mixtures, including variations in binder types, aggregate gradations, and viscosity properties.

`

REFERENCES

[1] AASHTO. *Mechanistic-empirical pavement design guide – a manual of practice*. Washington, DC: American Association of State Highway and Transportation Officials. 2008.

[2] AASHTO T322-07. *Determining the creep compliance and strength of hot mix asphalt (HMA) using the indirect tensile test device*. American Association of State Highway and Transportation Officials. 2011.

[3] AASHTO – T324. *Hamburgwheel-track testing of compacted hot mix asphalt*. American Association of State Highway and Transportation Officials. 2004.

[4] AASHTO T342-11. *Standard method of test for determining dynamic modulus of hot mix asphalt (HMA).* American Association of State Highway and Transportation Officials. 2011.

[5] Abaqus. Abaqus analysis user's guide. Internet: https://www.sharcnet.ca/Software/Abaqus/6.14.2/v6.14/books/usb/default.htm?startat = pt05ch22s07abm13.html#usb-mat-cfreqvisco. 2014

[6] Abu Al-Rub, R. K., Masad, E. A., & Huang, C.-W. Improving the sustainability of asphalt pavements through developing a predictive model with fundamental material properties (Research Report Number SWUTC/09/476660-00007-1). *Texas Transportation Institute*. 2009.

[7] Alamnie, M.M., Taddesse, E., Hoff, I. Advances in Permanent Deformation Modeling of Asphalt Concrete—A Review. *Materials*, 15, 3480. https://doi.org/10.3390/ma15103480. 2022.

[8] Bai, F., Yang, X., & Zeng, G. Creep and recovery behavior characterization of asphalt mixture in compression. *Construction and Building Materials*, 54, 504–511. https://doi.org/10.1016/j.conbuildmat.2013.12.088. 2014.

`

[9] Baumgaertel, M., and H. H. Winter. Determination of discrete relaxation and retardation time spectra from dynamic mechanical data. *Rheol. Acta 28 (6):* 11–519. https://doi.org/10.1007/BF01332922 . 1989.

[10] Booij, H. C., and G. P. J. M. Thoone. Generalization of KramersKronig transforms and some approximations of relations between viscoelastic quantities. *Rheol. Acta 21 (1):* 15–24. https://doi.org/10.1007/BF01520701. 1982.

[11] Boussabnia, M. M., Perraton, D., Di Benedetto, H., Lamothe, S., & Proteau, M. (2023). Validation of time-temperature superposition principle for high modulus asphalt concrete in the linear viscoelastic and fatigue domains. *Fatigue and Fracture of Engineering Materials and Structures*, 46, 80–95. https://doi.org/10.1111/ffe.13849Bradaietal.,2022.

[12] Cao, W. & Kim, Y. R. (2022). A triaxial viscoplastic model with temperature dependence for asphalt concrete permanent deformation. *International journal of applied mechanics*. DOI: 10.1142/S1758825122500235.

[13] Cardona, D. A. R., Pouget, S., Di Benedetto, H., & Olard, F. Viscoelastic behaviour characterization of a gap-graded asphalt mixture with SBS polymer modified bitumen. *Materials Research*, 18(2),373–381. https://doi.org/10.1590/1516-1439.332214. 2015

[14] Chailleux, E., Ramond, G., Such, C., & de la Roche, C. A mathematical-based master-curve construction method applied to complex modulus of bituminous materials. *Road Materials and Pavement Design*, 7(S1), 75–92. https://doi.org/10.1080/14680629.2006.9690059. 2006.

[15] Chehab, G. R., Kim, Y. R., Schapery, R. A., Witczak, M. W., and Bonaquist, R. Time-Temperature Superposition Principle for Asphalt Concrete Mixtures with Growing Damage in Tension State. *Journal of the Association of Asphalt Paving Technologists*, Vol. 70, 2002.

`

[16] Chen, F., Balieu, R., & Kringos, N. Thermodynamics-based finite strain viscoelastic-viscoplastic model coupled with damage for asphalt material. *International Journal of Solids and Structures*, 129, 61–73. https://doi.org/10.1016/j.ijsolstr. 2017.09.014. 2017.

[17] Cho, K. S. *Viscoelasticity of polymers*. Theory and numerical algorithms. Dordrecht, Netherlands: Springer. 2016.

[18] Cho, K. S. Geometric interpretation of time-temperature superposition. *Korea-Australia Rheology Journal*. Vol. 21, No. 1, 13-16. 2009.

[19] Csaba & Judit. Determination of master curves for asphalt mixtures by means of IT-CY tests. *Periodical polytechnical Civil Engineering* 54/2 (2010) 137–142 doi: 10.3311/pp.ci.2010-2.09. 2010.

[20] Daoudi, A., Perraton, D., Dony, A., & Carter, A. From complex modulus E∗ to creep compliance D(t): Experimental and modeling study. *Materials*, *13*(8), 1945. https://doi.org/10.3390/ma13081945 . 2020.

[21] Darabi, M. K., Abu Al-Rub, R. K., Masad, E. A., Huang, C. W., & Little, D. N. A modified viscoplastic model to predict the permanent deformation of asphaltic materials under cyclic-compression loading at high temperatures. *International Journal of Plasticity*, *35*, 100–134. https://doi.org/10.1016/j.ijplas.2012.03.001. 2012.

[22] Darabi, M. K., C-W. Huang., M. Bazzaz., E. A. Masad., D. N. Little. Characterization and validation of nonlinear viscoselastic-viscoplastic with hardening-relaxation constitutive relationship for asphalt mixtures. *Construction and Building Materials*, 216, (2019), pp. 648–660.

[23] Daver, F., Kajtaz, M., Brandt, M., & Shanks, R. A. Creep and recovery behaviour of polyolefin-rubber nanocomposites developed for additive manufacturing. *Polymers*, 8(12), 1–13. https://doi.org/10.3390/polym812043. 2016.

`

[24] Di Benedetto, H., Mondher, N., Sauzéat, C., & Olard, F. Three-dimensional thermo-viscoplastic behaviour of bituminous materials: The DBN model. *Road Materials and Pavement Design*, 8, 285–315. https://doi.org/10.1080/14680629.2007.9690076 . 2007.

[25] Dombi.J. Approximation and interpolation sum of exponential functions. http://www.inf.u-szeged.hu/ dombi/.2006.

[26] Dong, N., Ni, F., Li, S., Jiang, J., & Zhao, Z. Characterization of permanent deformation performance of asphalt mixture by multi-sequenced repeated load test. *Construction and Building Materials*, 180, 425–436. https://doi.org/10.1016/j.conbuildmat.2018.06.003. 2018.

[27] Do, T.T., T.N. Phan., N.H. Nguyen., T.A. Pham., V.T. Tran., H.T.T. Nguyen. Definition and application of linear viscoelastic unit slope response functions for efficiently dealing with piecewise linear excitations on asphaltic materials. *Material civil engineering*, 37(5), http://doi.org/10.1061/JMCEE7.MTENG-19208. 2025.

[28] Drescher, A., Kim, J., & Newcomb, D. Permanent deformation in asphalt concrete. *Journal of Materials in Civil Engineering*, *5*, 112–128. doi:10.1061/(ASCE)0899-1561(1993)5:1(112). 1993.

[29] Drucker, D.C. and Prager, W. Soil mechanics and plastic analysis for limit design. *Quarterly of Applied Mathematics*. 10 (2). 157-165. 1952.

[30] Du Yinfei, Chen Jiaqi, Han Zheng, Liu Weizheng. A review on solution for improving rutting resistance of asphalt pavement and test method. *Construction and Building Materials, 168, 893–905*. https://doi.org/10.1016/j.conbuildmat.2018.02.151. 2018.

[31] Emri, I., B. S. Bernstorf, R. Cvelbar, and A. Nikonov. Re-examination of the approximate methods for interconversion between frequency- and time-dependent

`

material functions. *J. Non-Newtonian Fluid Mech*. 129 (2): 75–84. https://doi.org/10.1016/j.jnnfm.2005.05.008. 2005.

[32] EN 12697-22. *Bituminous mixtures: Test method for hot mix asphalts-Part 22: Wheel tracking*. Brussels: European Standard. 2007.

[33] Fancey, K. F. A mechanical model for creep, recovery and stress relaxation in polymeric materials. *Journal of Materials Science*, 40(18), 4827–4831. https://doi.org/10.1007/s10853-005-2020-x. 2005.

[34] Fang, H., Liu, Q., Mo, L., Javilla, B., Shu, B., & Wu, S. Characterization of three-stage rutting development of asphalt mixtures. *Construction and Building Materials*, 154, 340–348. https://doi.org/10.1016/j.conbuildmat.2017.07.222. 2017.

[35] Ferry, J. *Viscoelastic properties of polymers (3rd ed.)*. John Wiley. 1980.

[36] Forough, S. A., Nejad, F. M., & Khodaii, A. (2014). A comparative study of temperature shifting techniques for construction of relaxation modulus master curve of asphalt mixes. *Construction and Building Materials*, 53, 74–82. https://doi.org/10.1016/j.conbuildmat.2013.11060

[37] Gayte, P., Di Benedetto, H., & Sauzéat, C. *Three dimensional behaviour of bituminous mixtures in the linear viscoelastic and viscoplastic domaines: The DBN model*. In Y. R. Kim (Ed.), Proceedings of ISAP conference (pp. 1079–1090). Taylor & Francis Group. 2014.

[38] Goli, A., Baditha, A., Muppireddy, A. R., & Pandey, B. B. Comparison of various rutting parameters and modelling of creep and recovery behaviour of high modulus bituminous binders. *International Journal of Pavement Research and Technology*, 12(6), 648–658. https://doi.org/10.1007/s42947-019-0077-1. 2019.

[39] Goodrich, J. Asphalt and polymer modified asphalt properties related to the performance of asphaltic concrete mixes. *Association of asphalt paving*

`

technologists Proc (Vol. 57, pp. 116–175), MN, Association of Asphalt Paving Technologists (AAPT). 1988.

[40] Haseeb, J. Chemical and physical composition of bitumen. https://www.aboutcivil.org/Composition%20and%20Properties%20of%20Bitumen.html, 2017.

[41] Heeres .O. M., Akke S.J.S., Rene .D.B. A comparison between the Perzyna viscoplastic model and the consistency viscoplastic model. *Euro Journal of Mechanics A/Solid*, 21, 1-12. 2002.

[42] Honerkamp, J., & Weese, J. A note on estimating mastercurves. *RheologicalActa*, 32, 57–64. 1993.

[43] Hornych, P., Kerzrého, J. P., & Salasca, S. Prediction of the behaviour of a flexible pavement using finite element analysis with non-linear elastic and viscoelastic models. *Proceedings of 9th International Conference on Asphalt Pavements*. 2002. pp. 511–529.

[44] Hua, J. *Finite element modelling and analysis of accelerated pavement testing devices and rutting phenomenon* (Ph.D. thesis). Purdue University, West Lafayette, IN. 2000.

[45] Hua, J., & White, T. A study of nonlinear tire contact pressure effects on HMA rutting. *International Journal of Geomechanics*, *2*, 353–376. 2002.

[46] Huang, Y. H. *Pavement analysis and design* (2nd ed.). Upper Saddle River, NJ: Pearson Prentice Hall. 2004.

[47] Huang, C., Abu Al-Rub, R., Masad, E., & Little, D. Three-dimensional simulations of asphalt pavement permanent deformation using a nonlinear viscoelastic and viscoplastic model. *Journal of Materials in Civil Engineering*, *23*, 56–68. doi:10.1061/(ASCE)MT.1943-5533.0000022. 2011a.

[48] Huang, C., Abu Al-Rub, R., Masad, E., Little, D. & Airey. G.D. Numerical implementation and validation of a nonlinear viscoelastic and viscoplastic model

`

for asphalt mixes, *International Journal of Pavement Engineering*, 12:4, 433-447.2011b.

[49] Hui Wang; Qisen Zhang; & Jiqing Tan. Investigation of Layer Contributions to Asphalt Pavement Rutting. *Journal of Materials in Civil Engineering,* 21(4): 181-185. DOI: 10.1061/(ASCE)0899-1561(2009)21:4(181). 2009.

[50] Hussan S., Kamal M. A., Khan M. B, Irfan M, Hafeez I. Determining the Contribution of Different Structural Layers of Asphalt Pavement System to Rutting Using Transverse Profile Analysis. *Journal of Civil Engineering and Architecture, 2013, Vol. 1, No. 6, 174-180.* DOI:10.12691/ajcea-1-6-7. 2013.

[51] IRC 37-2012. *Guidelines for the design of flexible pavements*. New Delhi: Indian Road Congress. 2012.

[52] Isailovic, I., Wistuba,M., &Augusto,C.F. Permanent deformation of hot mix asphalt under compression and tension. *6th Eurasphalt & Eurobitume Congress*. https://doi.org/10.14311/EE.2016.401. 2016.

[53] Khan, S., Nagabhushana, M. N., Tiwari, D., & Jain, P. K. Rutting in flexible pavement: Approach of evaluation with accelerated pavement testing facility. *2nd conference of transportation research group of India*. Procedia- Social and Behavioral Sciences, 104. 2013. pp. 149–157. https://doi.org/10.1016/j.sbspro.2013.11.107

[54] Karrech, A., Seibi, A., & Duhamel, D. Finite element modelling of rate-dependent ratcheting in granular materials. *Computers and Geotechnics*, *38*, 105–112. doi:10.1016/j.compgeo.2010.08.012, 2011.

[55] Kenis, W. J. *Predictive design procedures-VESYS users manual* (Report No. FHWA-RD-77-154). Washington, DC: Federal Highway Administration, 1978.

[56] Khosravifar, S., Haider, I., Afsharikia, Z., & Schwartz, C. W. Application of time - temperature superposition to develop master curves of cumulative plastic strain in

repeated load permanent deformation tests. *International journal of pavement engineering*. 16:3, 214-223. DOI: 10.1080.10298436.2014.937810. 2014

[57] Kim, J., Sholar, G. A., & Kim, S. Determination of accurate creep compliance and relaxation modulus at a single temperature for viscoelastic solids. *Journal of Materials in Civil Engineering*, 20(2), 147–156. https://doi.org/10.1061/(ASCE)0899-1561(2008)20:2(147), 2008.

[58] Lai, J. S., and D. Anderson. Irrecoverable and recoverable non-linear viscoelastic properties of asphalt concrete. *Highway Res. Rec*, 468 (Jan), pp. 73–88. 1973.

[59] Lake, R. S. *Viscoelastic solids*. Boca Raton, FL: CRC Press, 1999.

[60] Lagos-Varas, M., Movilla-Quesada, D., Raposeiras, A. C., Castro-Fresno, D., Muñoz-Cáceres, O., Andrés-Valeri, V. C., & Rodríguez-Esteban, M. A. Viscoelasticity modelling of asphalt mastics under permanent deformation through the use of fractional calculus. *Construction and Building Materials*, 329, Article 127102. https://doi.org/10.1016/j.conbuildmat.2022.127102. 2022

[61] Laukkanen, O.-V., Soenen, H., Pellinen, T., Heyrman, S., & Lemoine, G. Creep-recovery behavior of bituminous binders and its relation to asphalt mixture rutting. *Materials and Structures*, 48(12), 4039–4053. https://doi.org/10.1617/s11527-014-0464-7. 2015

[62] Lee, H. J., & Kim, Y. R. Viscoelastic constitutive model for asphalt concrete under cyclic loading. *Journal of Engineering Mechanics*, 124(1), 32–40. https://doi.org/10.1061/(ASCE)0733-9399(1998)124:1(32),1998.

[63] Levenberg, E. *Constitutive modeling of asphalt-aggregate mixes with damage and healing*. PhD thesis, Technion– Israel Institute of Technology, 2006.

[64] Liu, H., and R. Luo. Development of master curve models complying with linear viscoelastic theory for complex moduli of asphalt mixtures with improved accuracy. *Constr. Build. Mater. 152* (Oct):259–268. https://doi.org/10.1016/j.conbuildmat.2017.06.143, 2017.

`

[65] Liu, Y., & You, Z. Determining Burger's model parameters of asphalt materials using creep-recovery testing data. *Proceeedings of Symposium on Pavement Mechanics and Materials at the Inaugural International Conference of the Engineering Mechanics Institute,* American Society of Civil Engineers, 18-21 May 2009. pp. 26–36.

[66] Lu, Y. and Wright, P.J. Numerical approach of visco-elastoplastic analysis for asphalt mixtures. *Computer and Structures*, 69, pp. 139–147. 1998.

[67] Luk-Cyr, J., Crochon, T., Li, C. Interconversion of linearly viscoelastic material functions expressed as Prony series: a closure. *Mech Time-Depend Mater,* . 17: 53-82.2013.

[68] Masad, E., Tashman, L., Little, D., Zbib, H. Viscoplastic modeling of asphalt mixes with the effects of anisotropy, damage, and aggregate characteristics. *Journal of Mechanics of Materials* 37, 1242–1256. 2005.

[69] Mead, D. W. Numerical interconversion of linear viscoelastic material functions. J. *Rheol. 38 (6)*: 1769–1795. https://doi.org/10.1122/1.550526, 1994.

[70] Mun, S., Chehab, G. R., & Kim, R. R. Determination of time-domain viscoelastic functions using optimized interconversion techniques. *Road Materials and Pavement Design, 8*(2), 351–365. https://doi.org/10.1080/14680629.2007.9690078, 2007.

[71] Nathan Chilukwa & Richard Lungu. Determination of Layers Responsible for Rutting Failure in a Pavement Structure. *Infrastructures*, 4, 29. doi:10.3390/infrastructures4020029, 2019.

[72] Neifar, M., & Di Benedetto, H. Thermo-viscoplastic law for bituminous mixes. *Road Materials and Pavement Design*, 2(1), 71–95. https://doi.org/10.1080/14680629.2001.9689894, 2001.

`

[73] Nedjar, B., & Nguyen, D. T. On a simple cyclic plasticity modeling with implicit kinematic hardening restoration. *Annals of Solid and Structural Mechanics*, *4*, 33–42. doi:10.1007/s12356-012-0031-2, 2012.

[74] Nahi, M. H., Ismail, A., & Ariffin, A. K. Analysis of asphalt pavement under nonuniform tire pavement contact stress using finite element method. *Journal of Applied Sciences*, 11, 2562–2569. https://doi.org/10.3923/jas.2011.2562.2569. 2011.

[75] Nguyen, H. T. T. Modelling the mechanical behaviour of asphalt concrete using the Perzyna viscoplastic theory and Drucker–Prager yield surface. *Road Materials and Pavement Design*, 18(S2), 264–280. https://doi.org/10.1080/14680629.2017.1304255, 2017.

[76] Nguyen, H. T. T., Do, T. T., Tran, V. T., Phan, T. N., Pham, T. A., & Nguyen, M. L. Determination of creep compliance of asphalt mixtures at intermediate and high temperature using creep-recovery test. *Road Materials and Pavement Design*, 22(Sup1), S514–S535. https://doi.org/10.1080/14680629.2021.1908407. 2021

[77] Nguyen, H. T. T., Nguyen, D. L., Tran, V. T., & Nguyen, M. L. Finite element implementation of Huet–Sayegh and 2S2P1D models for analysis of asphalt pavement structures in time domain. *Road Materials and Pavement Design*, https://doi.org/10.1080/14680629.2020.1809501, 2021a.

[78] Nguyen, H. T. T., Nguyen, D. L., Tran, V. T., & Nguyen, M. L. Finite element implementation of Huet–Sayegh and 2S2P1D models for analysis of asphalt pavement structures in time domain. *Road Materials and Pavement Design*, 23(1), 22–46. 2022. https://doi.org/10.1080/14680629.2020.1809501.

[79] Nguyen, Q. T., Nguyen, M. L., Di Benedetto, H., Sauzéat, C., Chailleux, E., & Hoang, T. T. N. Nonlinearity of bituminous materials for small amplitude cyclic loadings. Road Materials and Pavement Design, 20(7), 1571–1585. 2019. https://doi.org/10.1080/14680629.2018.1465452

`

[80] Olard, F., & Di Benedetto, H. General '2S2P1D' model and relation between the linear viscoelastic behaviours of bituminous binders and mixes. *Road Materials and Pavement Design*, 4, 185–224. https://doi.org/10.1080/14680629.2003.9689946, 2003.

[81] Ossa EA, Deshpande VS, Cebon D. Triaxial deformation behavior of bituminous mixes. *Journal of Materials Civil Engineering*, 22(2),124 – 35. 2010

[82] Park, D. W. Simulation of rutting profiles using a viscoplastic model. *KSCE Journal of Civil Engineering*, *11*, 151–156. doi:10.1007/BF02823895, 2007.

[83] Perl, M., J. Uzan, and A. Sides. Visco-elasto-plastic constitutive law for a bituminous mixture under repeated loading. *Transportation Research Record*, 911, pp. 20–27. 1983.

[84] Perzyna, P. Fundamental problems in viscoplasticity. In Chernyi, G.G. (Ed.), *Advanced Applied Mechanics* (pp. 243-377). New York: Academic Press. 1966.

[85] Perzyna, P. Thermodynamic theory of viscoplastcity. *Advances in Applied Mechanics* 11, 313–354. 1971

[86] Phan, T.N.; Nguyen, D.L.; Vu, T.V.; Tran, V.T.; Nguyen, H.T.T; and Nguyen, M.L. Determining with High Accuracy the Relaxation Modulus and Creep Compliance of Asphaltic Materials in the Form of Sums of Exponential Functions from Mathematical Master Curves of Dynamic Modulus. *Journal of Materials in Civil Engineering 34(9): 04022219.* DOI: 10.1061/(ASCE)MT.1943-5533.0004366, 2022.

[87] Phan, T.N.& Nguyen, H.T.T. Comparison the accuracy of approximate methods by sums of exponential using real-valued coefficients. *Proceedings of 11th national mechanics conference.* 2022. pp. 513-521.

[88] Phan, T.N., N.H. Nguyen, T.D. Do, H.T.T. Nguyen, M.L. Nguyen. Verification of time-temperature superposition principle for viscoplastic strains of asphalt mixtures obtained from creep-recovery tests in the low-strain regime. *Road*

`

Materials and Pavement Design, 26(5), pp. 958-995, http://doi.org/ 10.1080/14680629.2024.2390156. 2025.

[89] Pronk,A.C. The Huet-Sayegh model: A simple and excellent rheological model for mastercurves of asphaltic mixes. *Proceedings of the R.Lytton Symposium on Mechanics of Flexible Pavements*. American Society of Civil Engineers. 1–3 June 2005. pp.73–82.

[90] Qian, G., Zheng, J. & Wang, Q. Calculating thermal stresses of asphalt pavement in environmental conditions. *Pavements and materials*. pp.78-87. 2008.

[91] Richardson, D., & Lusher, M. *Determination of creep compliance and tensile strength of hot-mix asphalt for wearing courses in Missouri (Technical Report No. MoDOT OR08-018)*. Missouri University of Science and Technology, USA. 2008.

[92] Rowe, G. Phase angle determination and interrelationships within bituminous materials. *In Proc., Advanced Testing and Characterization of Bituminous Materials, London: Taylors and Francis,* 2009. pp. 43–52.

[93] Rowe, G., G. Baumgardner, and M. Sharrock. Functional forms for master curve analysis of bituminous materials. *In Proc., Advanced Testing and Characterization of Bituminous Materials, London: Taylor and Francis*, 2009. pp. 81–91.

[94] Rui Guo, Tengfei Nian, Fei zhou. *Analysis of factors that influence anti-rutting performance of asphalt pavement*. Construction and Building Materials 254, https://doi.org/10.1016/j.conbuildmat.2020.119237, 2020.

[95] Saadeh, S., Masad, E., Little, D. Characterization of hot mix asphalt using anisotropic damage viscoelastic–viscoplastic model and repeated loading. *ASCE Jouranl of Materials in Civil Engineering* 19, 912–924. 2007

[96] Saboo, N., & Kumar, P. A study on creep and recovery behavior of asphalt binders. *Construction and Building Materials*, 96, 632–640. https://doi.org/10.1016/j.conbuildmat.2015.08.078, 2015.

`

[97] Sayegh, G. *Contribution à l'étude des propriétés visco-élastiques des bitumes purs et des bétons bitumineux (Doctoral dissertation)*. Paris: Sorbonne University, France, 1965.

[98] Schapery, R.A. A theory of crack initiation and growth in viscoelastic media, Part I: Theoretical development, Part II: Approximate methods of analysis, Part III: Analysis of continuous growth. *International Journal of Fracture* 11, 141159. 369–388, 549–562. 1975.

[99] Schapery, R.A. Nonlinear viscoelastic and viscoplastic constitutive equations with growing damage. *International Journal of Fracture* 97, 33–66. 1999.

[100]Schapery, R. A., & Park, S. W. Methods of interconversion between linear viscoelastic material functions. Part II – An approximate analytical method. *International Journal of Solids and Structures*, 36(11), 1677–1699. https://doi.org/10.1016/S0020-7683(98)00060-2, 1999.

[101]Schwartz, C. W., Gibson, N., & Schapery, R. A. Time– temperature superposition for asphalt concrete at large compressive strains. *Transportation Research Record*, 1789(1), 101–112. https://doi.org/10.3141/1789-11. 2002.

[102]Seibi, A.C., Sharma, M.G., Ali, G.A., Kenis, W.J. Constitutive relations for asphalt concrete under high rates of loading. *Transportation Research Record* 1767, Transportation Research Board, Washington, DC, pp. 111–119. 2001.

[103]Shakiba .M., Darabi .M.K., Abu Al-Rub .R.K., Masad .E.A., Little .D.N. Microstructure modeling of asphalt concrete using a coupled moisture-mechanical constitutive relationship. *International Journal of Solid and Structures*, 51, 4260-4279. 2014.

[104]Shume, H. *Loading conditions in the triaxial test for the characterisation of the resistance to permanent deformation of asphalt mixtures (Technical report)*. Delft University, Delft, Netherlands. 2002.

`

[105]Subramanian, V., Guddati, M. N. and Kim, Y. R. A viscoplastic model for rate dependent hardening for asphalt concrete in compression. *Mechanics of Materials*, 59, 142–159. 2013.

[106]Sun, L., & Zhu, Y. A serial two-stage viscoelastic–viscoplastic constitutive model with thermodynamical consistency for characterizing time-dependent deformation behavior of asphalt concrete mixtures. *Construction and Building Materials*, 40, 584–595. https://doi.org/10.1016/j.conbuildmat.2012.10.004, 2013.

[107]Tan, G., W. Wang, Y. Cheng, Y. Wang, and Z. Zhu. Master curve establishment and complex modulus evaluation of SBS-modified asphalt mixture reinforced with basalt fiber based on generalized sigmoidal model. *Polymers 12 (7):* 1–17. https://doi.org/10.3390/polym12071586, 2020.

[108]Institute of transport science and technology. *TCVN 13567-1. Hot Mix Asphalt Pavement Layer - Construction and Acceptance - Part 1: Dense - Graded Asphalt Concrete*. Hanoi: Construction, 2022.

[109]Tran, V.T., Phan, T.N., Tran, V.T., Do, T.T., Nguyen, H.T.T. & Nguyen, M.L. Development of a generalised creep-recovery test and a back-calculation method for determining the permanent deformation of asphalt mixtures inthe time domain, *Road Materials and Pavement Design*, DOI: 10.1080/14680629.2023.2180291. 2023

[110]Tschoegl, N. W. *The phenomenological theory of linear viscoelastic behavior: An introduction*. New York: Springer, 1989.

[111]Xu, T. and Huang, X. Investigation into cause of in-place rutting in asphalt pavement. *Construction and Building Materials*, 28(2012), 525-530. doi:10.1016/j.conbuildmat.2011.09.007. 2012.

[112]Yun, T., Underwood, B. S., & Kim, Y. R. Time-Temperature superposition for HMA with growing damage and permanent strain in confined tension and compression.

`

Journal of Materials in Civil Engineering, 22(5), 415–422 .https://doi.org/10.1061/(ASCE)MT.1943-5533.000003. 2010.

[113]Zahid, H., Debaroti, G., & Musharraf, Z. Use of the multiple stress creep recovery (MSCR) test method to characterize polymer-modified asphalt binders. *Journal of Testing and Evaluation*, 44(1S), Article 20140061. https://doi.org/10.1520/jte20140061. 2016.

[114]Zhang, Y., Luo, R. and Lytton, R. L. Characterization of viscoplastic yielding of asphalt concrete. *Construction and Building Materials*, 47, pp. 671–679. 2013.

[115]Zhang, Y., Bernhardt, M., Biscontin, G., Luo, R., and Lytton, R. L. A generalized Drucker-Prager viscoplastic yield surface model for asphalt concrete. *Materials and Structures*. DOI 10.1617/s11527-014-0425-1.2014

[116]Zhang, F., Wang, L., Li, C., and Xing, L. Predict the phase angle master curve and study the viscoelastic properties of warm mix crumb rubber-modified asphalt mixture. *Materials* 13 (21): 5051. https://doi .org/10.3390/ma13215051. 2020.

[117]Zhang, W., Cui, B., Gu, X., & Dong, Q. Comparison of relaxation modulus converted from frequency and time dependent viscoelastic functions through numerical methods. *Applied Sciences*, 8, 2447. https://doi.org/10.3390/ app8122447. 2018.

[118]Zhao, Y., & Kim, Y. R. Time-Temperature superposition for asphalt mixtures with growing damage and permanent deformation in compression. *Transportation Research Record* 1832. 03-3903. 161-172. 2003.

`

LIST OF PUBLICATIONS

1. Phan, T.N.; Nguyen, D.L.; Vu, T.V.; Tran, V.T.; Nguyen, H.T.T; and Nguyen, M.L. Determining with High Accuracy the Relaxation Modulus and Creep Compliance of Asphaltic Materials in the Form of Sums of Exponential Functions from Mathematical Master Curves of Dynamic Modulus. Journal of Materials in Civil Engineering 34(9): 04022219. DOI: 10.1061/(ASCE)MT.1943-5533.0004366, 2022.

2. Phan, T.N.& Nguyen, H.T.T. Comparison the accuracy of approximate methods by sums of exponential using real-valued coefficients. Proceedings of 11th national mechanics conference. 513-521, 2022.

3. Tran, V.T., Phan, T.N., Tran, V.T., Do, T.T., Nguyen, H.T.T; and Nguyen, M.L. Development of a generalised creep-recovery test and a back-calculation method for determining the permanent deformation of asphalt mixtures in the time domain. Road Materials and Pavement Design. DOI: 10.1080/14680629.2023.2180291. 2023.

4. Nguyen, N.H., Phan, T.N., Do, T.T., and Nguyen, H.T.T. Evaluating the accuracy of linear viscoelastic properties in the time domain analytically approximated from complex modulus data . Proceedings of national mechanics conference for 45th anniversary of The Institute of Mechanics. 103-110, 2024.

5. Phan, T.N., Nguyen, N.H., Do, T.T., Nguyen, H.T.T; and Nguyen, M.L. Verification of time–temperature superposition principle for viscoplastic strains of asphalt mixtures obtained from creep-recovery tests in the low-strain regime. Road Materials and Pavement Design. DOI: 10.1080/14680629.2024.2390156. 2024

`

6. Phan, T.N.& Nguyen, H.T.T. Characterizing the creep compliance of a conventional asphalt mixture using creep-recovery test. Proceedings of the 4th Annual International Conference on Material, Machines, and Methods for Sustainable Development (MMMS2024). 141-148, 2025.

APPENDIX

Appendix I. Modified Dombi Algorithm

Let $f(t)$ be a decaying function in the time range of interest $[0, t_n]$, which is divided by n equidistant time steps $[0, t_n] = \bigcup_{i=0}^{n-1} [t_i, t_{i+1}]$, $\Delta t = t_{i+1} - t_i$. The approximated value of $f(t)$ at time t_i is:

$$\overline{f}(t_i) = \sum_{j=1}^{m} a_j e^{b_j(i\Delta t)} = \sum_{j=1}^{m} a_j \left(e^{b_j \Delta t}\right)^i . \quad \text{(I-1)}$$

Let $q_j = e^{b_j \Delta t}$, $j = 1..m$. It can be demonstrated that if $q_1, q_2, .., q_m$ are the root of the m-order polynomial ($2m \le n$)

$$q^m + s_1 q^{m-1} + s_2 q^{m-2} + ... + s_m = 0 , \quad \text{(I-2)}$$

then the coefficients of the m-order polynomial are the root of the following equations: (Dombi, 2005)

$$\begin{cases} \overline{f}_1 s_m + \overline{f}_2 s_{m-1} + ... + \overline{f}_m s_1 + \overline{f}_{m+1} = 0 \\ ... \\ \overline{f}_m s_m + \overline{f}_{m+1} s_{m-1} + ... + \overline{f}_{2m-1} s_1 + \overline{f}_{2m} = 0 \\ ... \\ \overline{f}_{n-m} s_m + \overline{f}_{n-m+1} s_{m-1} + ... + \overline{f}_{n-1} s_1 + \overline{f}_n = 0 \end{cases} . \quad \text{(I-3)}$$

The decay rates of the exponential functions can be simply calculated by:

$$b_j = \ln(q_j) / \Delta t . \quad \text{(I-4)}$$

Once the decay rates have been determined, the coefficients of the exponential functions can be optimized using linear least-square techniques to best fit the input data.

Since the original method of Dombi (2005) works only with a constant time step, the method cannot be directly applied to LVE functions, which must be evaluated over several decades. Therefore, Nguyen et al. (2020) have proposed a modified version of the original Dombi algorithm. The time range was divided into several smaller intervals of time and the appropriate decay rates in each single time interval were determined. The "appropriate decay rates" of the input function over the entire time range of interest is just the combination of all obtained suitable decay rates.

Another remark is that the algorithm works only with decaying functions. Therefore, the following pre-treatments to the input function should be done before performing the decomposition algorithm to ensure numerical convergence:

$$E^{'}(\omega) = E^{*}(\omega \to \infty) - E^{'}(\omega);\ D'(t) = D^{'}(\omega) - D^{*}(\omega \to \infty)\,, \tag{I-5}$$

$$E(t) = E(t) - E^{*}(t \to 0);\ D(t) = D^{*}(t \to \infty) - D(t)\,. \tag{I-6}$$

The obtained approximations by sums of exponential functions are, therefore:

$$E^{'}(\omega) = E^{*}(\omega \to \infty) - \sum_{j=1}^{N_j} E^{'}_j e^{b_j \omega};\ D'(t) = \sum_{j=1}^{N_j} D^{'}_j e^{c_j \omega} - D^{*}(\omega \to \infty)\,, \tag{I-7}$$

$$E(t) = E(t \to 0) + \sum_{j=1}^{N^{'}_j} E_j e^{b'_j t};\ D(t) = D(t \to \infty) - \sum_{j=1}^{N^{'}_j} D_j e^{c'_j t}\,. \tag{I-8}$$

Appendix II. Estimation of cut-off time for CCs and VE strains obtained from SSCR tests

The objective of this section is to analytically estimate the value of the cut-off time so that the obtained VE and VP strains are reliable. Since the time range of interest in this analysis is relatively short, the creep compliance function at all testing temperatures can be approximated by the power law in Eq. (II-1) to facilitate the analytical investigation:

$$D(t) \approx D_1 t^{\alpha_1}\,. \tag{II-1}$$

The VE strain at $0 < t \le t_0$ caused by stress histories 1 and 2 (see Figure 3.22) can be easily computed by:

$$\varepsilon_{VE,1}(t) = D_1 t^{\alpha_1} \cdot \sigma_1\,, \tag{II-2}$$

$$\varepsilon_{VE,2}(t) = \frac{D_1 t^{\alpha_1 + 1}}{\alpha_1 + 1} \cdot \frac{\sigma_1}{t_0}\,. \tag{II-3}$$

It is clear that $\varepsilon_{ve,2}(t)$ is less than $\varepsilon_{ve,1}(t)$ for $\alpha_1 > 0$ and $t \le t_0$. As a result, there exists a time, noted t_s, such that the VE strain caused by stress history 1 at t_s is equal to the VE strain caused by stress history 2 at time t_0:

$$\frac{t_s}{t_0} = (\alpha_1 + 1)^{-\frac{1}{\alpha_1}}. \quad \text{(II-4)}$$

Consequently, the ramp loading history can be approximated by a pure creep loading history in which the applied stress is delayed by an amount of time equal to $t_0^{'} = t_0\left[1 - (\alpha_1 + 1)^{-1/\alpha_1}\right]$. With the aid of the equivalent loading history (stress history 3 in Figure 3.22), the VE strain caused by the true creep loading history and the real ramp loading history at any time greater than can be computed:

$$\varepsilon_{VE,2}(t) = D_1\left(t - t_0^{'}\right)^{\alpha_1} \cdot \sigma_1. \quad \text{(II-5)}$$

Let TOL be the acceptable value of the relative tolerance, one can estimate the cut-off time as follows:

$$\frac{t_c}{t_0} = \frac{1 - (\alpha_1 + 1)^{-1/\alpha_1}}{1 - (1 - TOL)^{1/\alpha_1}}. \quad \text{(II-6)}$$

With the TOL chosen equal to 2%, the estimation of cut-off times for VE strains (and CCs) of all mixtures at all testing temperatures were calculated and are reported in Table II-1.

Table II-1. Estimation of cut-off times for VE strain of all mixtures

Mixture	Temperature (°C)	α_1	t_s / t_0	t_c / t_0
AC	17.5	0.411	0.433	11.830
	25.0	0.378	0.428	10.982
	32.5	0.311	0.419	9.254
	40.0	0.211	0.404	6.535
PMB	27.5	0.304	0.418	9.044
	35.0	0.292	0.416	8.749
	42.5	0.270	0.413	8.156
	50.0	0.223	0.405	6.867
HiMA	40.0	0.328	0.421	9.694
	47.5	0.327	0.421	9.670
	55.0	0.299	0.417	8.917
	62.5	0.208	0.403	6.460

According to the data reported in Table II-1, the cut-off time varied with testing temperature and material type, ranging from 6.460 to 11.830 times t_0. However, the value of t_s did not change much and its average value is approximately $2t_0/5$. Thus, the average value of the delayed time $t_0^{'}$ was nearly $3t_0/5$.

Appendix III. Estimation of cut-off time for VP strains obtained from SSCR tests

Let us now compute the VP strains caused by the two loading histories as illustrated in Figure 3.22:

$$\varepsilon_{VP,1}\left(t\right)=At^b\sigma_1^m, \quad \text{(III-1)}$$

$$\varepsilon_{VP,2}\left(t\right)\approx A\left(t-\frac{3t_0}{5}\right)^b\sigma_1^m, \quad \text{(III-2)}$$

By applying the same approach, the cut-off times of VP strain can be estimated:

$$\frac{t_{c,VP}}{t_0}=\frac{3}{5}\left[1-\left(1-TOL\right)^{\frac{1}{b}}\right]^{-1}. \quad \text{(III-3)}$$

With the same value of the tolerance and the values of b given in Table 3.9, the estimated cut-off times of VP strain of AC, PMB, and HiMA mixture respectively equal to 15.152, 9.510, and 13.815 times t_0.